

Collective Microswimmer Motility in Complex Environments

Dissertation

zur Erlangung des mathematisch-naturwissenschaftlichen Doktorgrades

Doctor rerum naturalium

der Georg-August-Universität Göttingen

im Promotionsprogramm Physics of Biological and Complex Systems (PBCS)
der Georg-August University School of Science (GAUSS)

vorgelegt von

Fabian Jan Schwarzendahl

aus Gütersloh

Göttingen, August 2018

Betreuungsausschuss:

Prof. Dr. Marco G. Mazza,
Research Group “Nonequilibrium Soft Matter”,
Department “Dynamics of Complex Fluids”,
Max Planck Institute for Dynamics and Self-Organization

Prof. Dr. Annette Zippelius,
Research Group “Statistical Physics and Complex Systems”,
Institute for Theoretical Physics,
Georg-August-Universität Göttingen

Prof. Dr. Jörg Enderlein,
Research Group “Single Molecule Spectroscopy and Imaging for Biophysics and Complex Systems”,
Drittes Physikalisches Institut,
Georg-August-Universität Göttingen

Mitglieder der Prüfungskommission:

Prof. Dr. Marco G. Mazza,
Research Group “Nonequilibrium Soft Matter”,
Department “Dynamics of Complex Fluids”,
Max Planck Institute for Dynamics and Self-Organization

Prof. Dr. Annette Zippelius,
Research Group “Statistical Physics and Complex Systems”,
Institute for Theoretical Physics,
Georg-August-Universität Göttingen

Weitere Mitglieder des Prüfungsausschuss:

Dr. Michael Wilczek,
Max-Planck Research Group “Theory of Turbulent Flows”,
Max Planck Institute for Dynamics and Self-Organization

Prof. Dr. Stefan Klumpp,
Research Group “Theoretical Biophysics Group”,
Institute for Nonlinear Dynamics,
Physics Department, Georg-August-Universität Göttingen

Prof. Dr. Matthias Krüger,
Research Group “Non-equilibrium Statistical Physics”,
Institute for Theoretical Physics,
Georg-August-Universität Göttingen

Tag der mündlichen Prüfung: 28. September 2018

“We wander around strictly as amateurs equipped only with some elementary physics even if we don’t throw much light on the other subjects.”

Edward Mills Purcell (Life at Low Reynolds Number)

Abstract

This thesis deals with the collective motility of microswimmers in complex environments. We study the motility of a single alga in complex environments, the hydrodynamic interactions between microswimmers, the collective effects of the run-reverse-flick swimming strategy, and the statistical effects of an active Brownian particle exhibiting two motility stages.

We investigate the swimming behavior of the green alga *Chlamydomonas reinhardtii* in confinement and find an increased probability of the cell swimming close to the confining wall. We discovered that the near-wall swimming probability scales with the local wall curvature. The model that we propose, consisting of an asymmetric dumbbell, describes the near-wall swimming accurately and does not require any fitting parameter. In fact, we found that the important ingredient to the curvature-guided navigation is the torque stemming from the asymmetry of the organism.

Hydrodynamic interactions between microswimmers can also play an important role in their collective behavior. To investigate the effects of hydrodynamic interactions we propose a new model based on an asymmetric dumbbell that takes into account the hydrodynamic flow fields of puller- or pusher-type microswimmers. We explore the corresponding nonequilibrium phase diagram and find density heterogeneities in the configuration of swimmers. In fact, we find a maximum heterogeneity at intermediate filling fractions and high Péclet number. Using simulations with only hydrodynamic and only steric interactions between the swimmers we show that the maximum in heterogeneities of swimmers stems from a competition of hydrodynamic and steric interactions. This result is supported by an analytical theory that we propose. Importantly, this maximum represents an optimum for microswimmers' colonization of their environment.

Bacteria have different swimming strategies for finding nutrition. *Escherichia coli* bacteria follow a run and tumble strategy, whereas *Vibrio alginolyticus* bacteria have a run-reverse-flick pattern. We study the collective effects of the run-reverse-flick strategy from a theoretical point of view using molecular dynamics simulations and analytical theory. We present the collective diffusion coefficient of the system and find using both approaches that there is maximum in collective diffusion at a forward-to-backward runtime ratio of 1.2. Intriguingly this is the same runtime ratio that was found experimentally for *Vibrio alginolyticus*.

We study the statistical effects of a microswimmer that can switch from a highly motile state to a low motility state. By solving the underlying Fokker-Planck equation we find the mean square displacement as well as the intermediate scattering function analytically, which we verify using Brownian dynamics simulations. We find an interesting subdiffusive behavior of the mean square displacement and point out implications for experimental systems. The intermediate scattering function that we find shows non-ergodic effects that resemble the properties of a supercooled liquid.

Contents

Abstract	vii
List of Figures	xiii
List of Tables	xvii
1 Introduction	1
1.1 Motivation	1
1.2 Swimming at low Reynolds number	5
1.2.1 Examples of biological microswimmers	6
Puller-type swimmer	6
Pusher-type swimmer	7
Mono-flagellated swimmer	8
1.3 Literature review	8
1.4 Scope and main results of the thesis	10
1.4.1 Main results	11
2 Theoretical background	13
2.1 Stokes equation	13
2.1.1 Swimming at low Reynolds numbers	15
2.1.2 Stokeslet solution and multipole expansion	16
2.1.3 Model flow fields	17
2.2 Overdamped dynamics	19
2.2.1 Brownian particle	19
2.2.2 Active Brownian particle	20

2.2.3	Motility-induced phase separation	22
3	Computational methods	27
3.1	Molecular dynamics simulations	27
3.1.1	Neighbor list	28
3.1.2	Brownian dynamics	28
3.1.3	Quaternion dynamics	29
3.2	Multiparticle collision dynamics	31
3.2.1	Conservation laws	32
	Multiparticle collision dynamics with angular momentum con- servation	34
3.2.2	Boundaries in MPCD	34
3.2.3	Forced flow	35
3.2.4	Rigid objects immersed in an MPCD fluid	36
	Simulation details	37
	Laminar flow around sphere and dumbbell	37
	Equipartition theorem	37
	Stokes drag of a sphere	39
	Diffusion of a sphere	40
3.2.5	Computational complexity of MPCD	40
4	Microswimmer motility in complex environments	43
4.1	<i>Publication:</i> Curvature-Guided Motility of Microalgae in Geometric Confinement	46
4.2	<i>Supplemental Material to Publication:</i> Curvature-Guided Motility of Microalgae in Geometric Confinement	53
5	Implications of hydrodynamics on microswimmer dynamics	69
5.1	<i>Publication:</i> Maximum in density heterogeneities of active swimmers .	72
5.2	<i>Supplementary Information to Publication:</i> Maximum in density het- erogeneities of active swimmers	87
6	Swimming strategies of microorganisms	97
6.1	Run and tumble strategy	97
6.2	Run-reverse-flick strategy	99
6.3	Numerical implementation of run-reverse-flick	100
	Overdamped Langevin run-reverse-flick	100
	Squirmer run-reverse-flick	101
6.3.1	Single particle statistics	101
6.4	Analytical treatment of run-reverse-flick	102
6.4.1	Moment expansion	104
6.5	Maximum in collective diffusion of run-reverse-flick particles	105

7 Motility states of active particles	107
7.1 Intermediate scattering function of two active motility states	108
7.2 Simulation of two active motility states	111
7.3 Mean square displacement of two active motility states	112
7.4 Intermediate scattering function of two motility states	113
8 Conclusions and outlook	117
8.1 Conclusions	117
8.2 Outlook	119
Appendix	123
Bibliography	133
Acknowledgements	149

List of Figures

1.1	(a) Dense suspension of <i>Bacillus subtilis</i> showing bacterial turbulence; yellow lines show the flow field of bacteria. Reprinted from [1]. (b) Turbulent vorticity field obtained from the flow field in (a). Reprinted from [1]. (c) Rippling structure of <i>Myxococcus xanthus</i> preying on an <i>Escherichia coli</i> colony. Reprinted from [2] Copyright 2008 National Academy of Sciences. (d) Example of a bioconvection pattern of <i>Euglena gracilis</i> . Reprinted from [3].	3
1.2	(a) Algal bloom of phytoplankton, around the Swedish island Gotland in the Baltic Sea. [4] (b) Biofilm in a hydrothermal hot spring. (Biscuit Basin, Yellowstone National Park, USA) Reprinted by permission from Springer Nature, Nature Reviews Microbiology, [5], Copyright 2004, Springer Nature.	4
1.3	(a) Scanning electron microscopy image of <i>Chlamydomonas reinhardtii</i> algae. [6] (b) Hydrodynamic flow field around a <i>Chlamydomonas reinhardtii</i> alga. Reprinted with permission from [7] Copyright 2010 by the American Physical Society.	6
1.4	(a) Transmission electron microscopy image of an <i>Escherichia coli</i> bacterium. [8] (b) Hydrodynamic flow field around an <i>Escherichia coli</i> bacterium. Reprinted from [9].	7
1.5	Transmission electron microscopy image of a <i>Vibrio alginolyticus</i> cell. Reprinted from [10].	8

2.1	Sketch of the flow fields produced by (a) a pusher-type swimmer and (b) a puller-type swimmer. Black arrows are a sketch of the fluid velocity around the swimmers and gray arrows show the direction of motion.	18
2.2	The solid lines show the MSD [Eq. (2.37)] of an active Brownian particle. The dotted line shows a linear scaling, and the dashed-dotted line a quadratic scaling.	22
2.3	Representative snapshot of a simulation of active Brownian particles (reprinted with permission from [11] Copyright 2010 by the American Physical Society.) showing motility-induced phase separation. A clear separation between dense and gas phases can be seen.	23
3.1	Sketch of MPCD particles inside cells. The gray and black grids represent the position of the grid used in the collision step before and after the grid shift.	32
3.2	Parabolic flow profile from a forced flow simulation (squares) and theoretical prediction (line) between two walls.	36
3.3	Two-dimensional cross section in the $z = 0$ plane of a sphere inside a 3d plug flow. The white arrows show the flow direction and the color code shows the magnitude of the flow velocity. It can be seen that the no-slip boundary condition on the sphere is well achieved.	38
3.4	Two-dimensional cross section in the $z = 0$ plane of a dumbbell inside a 3d plug flow. The white arrows show the flow direction and the color code shows the magnitude of the flow velocity. It can be seen that the no-slip boundary condition on the dumbbells surface is well achieved.	39
3.5	Velocity of a spherical particle slowing down due to Stokes' drag. Circles represent MPCD simulations and line show the theoretical prediction from Eq. (3.41).	40
3.6	MSD of a spherical particle inside an MPCD fluid. Squares show the results of the MPCD simulations and the line shows the theoretical prediction from Eq. (3.42).	41
4.1	Simulated trajectories (top) and probability distributions (bottom) of an active Brownian particle. The radius of the particle is $1\mu\text{m}$ and the circular confinement $20\mu\text{m}$. The self-propulsion speed is (a) $v_0 = 0\mu\text{ms}^{-1}$, (b) $v_0 = 5\mu\text{ms}^{-1}$ and (c) $v_0 = 10\mu\text{ms}^{-1}$. Reprinted with permission from [12] Copyright 2010 by the American Physical Society.	44
5.1	(a) Puller-type squirmer with $\beta = 5$, (b) neutral squirmer, (c) pusher-type squirmer with $\beta = -5$ [13].	70
5.2	The force-counterforce model: one force acts on the spherical body, the second force on the fluid. Reprinted with permission from [14] Copyright 2010 by the American Physical Society.	70

6.1	Run and tumble trajectory of an <i>Escherichia coli</i> bacterium. Reprinted by permission from Springer Nature, Springer eBook, [15], Copyright Springer-Verlag New York, Inc. 2004.	98
6.2	Experimental observation of the run-reverse-flick trajectory of a <i>Vibrio alginolyticus</i> bacterium. Green lines mark the forward running state, red lines mark the backward running state, and the black circles show a flick event. Reprinted from [16].	99
6.3	(a) Comparison of MSD from simulations (orange circles) to analytical prediction (blue line) [Eq. (6.2)]. (b) Relative error of simulation to theoretical prediction.	102
6.4	Comparison of the diffusion coefficient from simulations (squares for 2d, circles for 3d) to analytical prediction (line for 2d, dotted line for 3d) Eq. (6.6).	103
6.5	Nonequilibrium phase diagram for two dimensional interacting run-reverse-flick particles. The normalized diffusion constant D/D_0 is shown for different runtime ratios τ_f/τ_b and filling fractions ϕ (color code). For fixed filling fraction a maximum at $\tau_f/\tau_b \sim 1.2$ is found. The black line shows the theoretical prediction of the maximum from Eq. (6.26). . . .	106
7.1	Schematic representation of a <i>Chlamydomonas reinhardtii</i> cell in a quasi two dimensional confinement with different motility stages: (a) performing the highly motile breaststroke motion; (b) the less motile gliding motion on the surface of a substrate.	108
7.2	MSD of an active particle with two motility states. Data points show the simulations and lines show the analytical results Eq. (7.34). Different colors show the MSD with different switching times τ , the dotted line shows a linear and the dashed-dotted shows a quadratic scaling. The inset shows a zoom of the data, where a plateau of the MSD can be seen. This is related to the switching of the motility state.	113
7.3	Intermediate scattering function (ISF) for different switching times τ . For each switching time a range of wavevectors $k^* = kv_h/\tau$ is shown (color code). The data points show simulations and the lines show the analytical calculation from Sec. 7.1. The leveling off in the ISF is induced by the switching of motility states.	115
8.1	Probability flux of a <i>Chlamydomonas reinhardtii</i> cell inside a quasi two dimensional elliptical confinement. Top panel shows the experimental data and bottom panel the simulations (see also Chapter 4). The apparent loops in the probability flux are a hallmark of nonequilibrium behavior. The figure was kindly provided by Jan Cammann.	119

- 8.2 Phase diagram of run-reverse-flick model of active particles in two dimensions. The abscissa shows the runtime ratio and the ordinate shows the packing fraction. Blue symbols indicate a homogeneous particle configuration, red symbols show dynamic clusters. No large scale clusters as in motility induced phase separation are found. The figure was kindly provided by Arghadwip Paul. 121

List of Tables

7.1	Parameter values used for the MSD in Fig. 7.2 and the ISF in Fig. 7.3, where σ is the particle radius and v_h is the particle velocity in the high motility state.	112
-----	---	-----

List of Abbreviations

PDE	P artial D ifferential E quation
MSD	M ean S quare D isplacement
MIPS	M otility I nduced P hase S eparation
MD	M olecular D ynamics
MPCD	M ultiparticle C ollision D ynamics
MPCD-AT	M ultiparticle C ollision D ynamics - A ndersen T hermostat
MPCD-AT+a	M ultiparticle C ollision D ynamics - A ndersen T hermostat a ngular
GPU	G raphics P rocessing U nit
WCA	W eeks- C handler- A nderson
ISF	I ntermediate S cattering F unction
DLVO	D erjaguin- L andau- V erwey- O verbeek
2d	two d imensional
3d	three d imensional

Chapter 1

Introduction

1.1 Motivation

Microorganisms, such as bacteria or microalgae, form the largest amount of biological mass on our planet and are ubiquitous in our environment. It has been estimated that in total there are approximately 5×10^{30} bacteria on our planet [17]. In the body of a human alone, one can find about 3.8×10^{13} bacteria [18], which is similar to the number of human cells in a body ($\sim 3.0 \times 10^{13}$).

A large amount of bacteria are found in the planktonic state, i.e., they freely swim within a fluid, in wet soil, lakes, or oceans. Bacteria in the planktonic state can only react to local stimuli such that the ecologically relevant interactions have also a local character. Hence, the motion of a bacterium is not only governed by their biological nature, but is largely affected by physical or chemical interactions. Physically, steric and hydrodynamic interactions play an important role in their motile behavior, but also chemical gradients of, for example, nutrients effect the motility of bacteria. These interactions are especially important when dense collections of bacteria are investigated and can lead to fascinating effects.

Figure 1.1(a)-(b) show the collective motion of a dense suspension of *Bacillus subtilis* bacteria. These are rod-shaped microorganisms of $5\mu\text{m}$ in length and $0.8\mu\text{m}$ width that move by means of multiple flagella. The emergent behavior of a dense suspension is rather surprising, and difficult to predict from the features of an individual. As Fig. 1.1(a)-(b) show, a pattern resembling classical turbulence in a fluid

is apparent. Although the Reynolds numbers associated to bacterial turbulence are much lower than in the classical one, a simple picture of fluctuating vortical motion of stochastic intensity can be recognized in Fig. 1.1(a)-(b). Another example of an interesting, structural collective effect is shown in Fig. 1.1(c) where cells of the social bacteria *Myxococcus xanthus* exhibit ripple-like, multicellular structures as they penetrate and prey on an *Escherichia coli* colony.

A different type of microorganism that is important for life on Earth are microalgae. They are responsible for the production of about half of our atmospheric oxygen by processing the greenhouse gas carbon dioxide. Additionally, they can show interesting collective effect such as the suspension of *Euglena gracilis* depicted in Fig. 1.1(d). The structure that is collectively formed by the algae resembles the plumes of Rayleigh-Bénard-convection and accordingly the effect was termed “bioconvection”. However, microalgae can also organize on much larger scales and form structures such as the alga bloom shown in Fig. 1.2(a). Although these algal blooms are stunningly beautiful, they can be harmful, as they lower the oxygen concentration in water or secrete toxic substances, killing marine life either way.

Both bacteria and microalgae can be found in the motile planktonic state, as it is shown in Fig.1.1-1.2, but when the conditions are feasible they can adhere to surfaces, colonize them, and collectively form a biofilm. Figure 1.2(b) shows a striking example of a biofilm growing in a hot spring. Biofilms can form on a vast amount of surfaces, and are often found in hospitals, where they constitute a health hazard. In fact, they can grow in infected human tissue, they can infect the mucus membrane in the respiratory tract of patients with cystic fibrosis. Medical devices such as catheters, prosthetic heart valves, cardiac pacemakers, and orthopedic devices can harbor pathogens, and because of their intimate contact biofilms can grow in the human body and trigger virulent infections [19]. Due to their physical and chemical properties, once formed biofilms are difficult to extinguish as antibiotics are usually ineffective, making the surgical removal of tissue the only method for treatment.

Even within a biofilm, many microorganisms can exhibit active motion. In physics, active particles are defined as synthetic or natural entities that are able to convert mechanical, chemical or biological energy into some form of persistent motion. The energy sources can be stored within the active particle, or they can be extracted from the environment, for example with stored sugars within a cell, or by means of photosynthesis.

Active motion is a general archetype in physics that can be employed to investigate the dynamics of both isolated particles and the collective behavior of large numbers thereof. In fact, the concept of active motion is not restricted to particles at the colloidal scale (such as microorganisms), but has been successfully employed to study a myriad of systems besides microswimmers such as sheep herds [20, 21], bird flocks [22–25], or schools of fish [26].

In addition to the microswimmer’s intrinsic activity, the interactions between swimmers or between swimmers and their physical boundaries play an important role

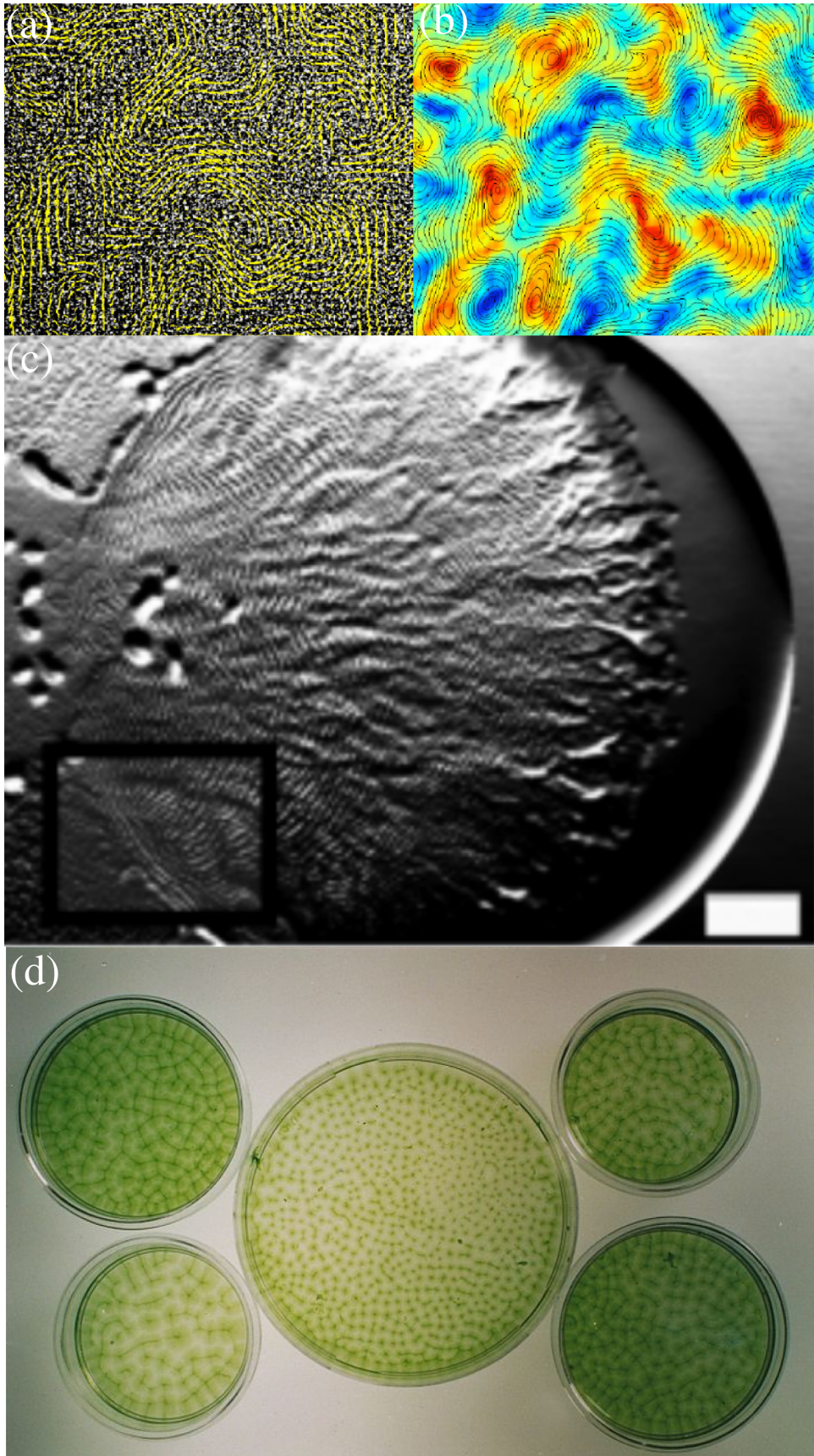


FIGURE 1.1: (a) Dense suspension of *Bacillus subtilis* showing bacterial turbulence; yellow lines show the flow field of bacteria. Reprinted from [1]. (b) Turbulent vorticity field obtained from the flow field in (a). Reprinted from [1]. (c) Rippling structure of *Myxococcus xanthus* preying on an *Escherichia coli* colony. Reprinted from [2] Copyright 2008 National Academy of Sciences. (d) Example of a bioconvection pattern of *Euglena gracilis*. Reprinted from [3].

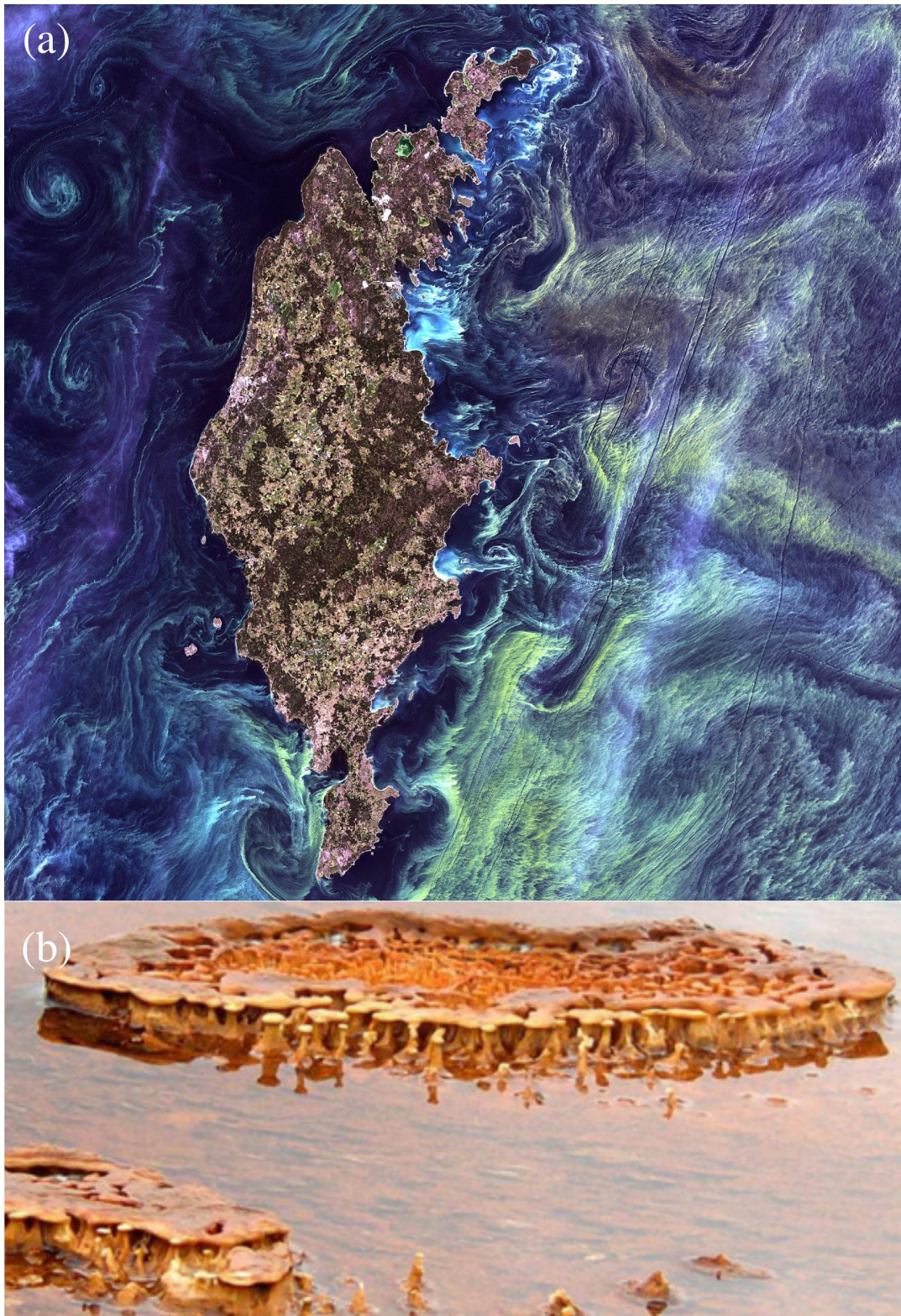


FIGURE 1.2: (a) Algal bloom of phytoplankton, around the Swedish island Gotland in the Baltic Sea. [4] (b) Biofilm in a hydrothermal hot spring. (Biscuit Basin, Yellowstone National Park, USA) Reprinted by permission from Springer Nature, *Nature Reviews Microbiology*, [5], Copyright 2004, Springer Nature.

in the swimmer's dynamics. Steric interactions between active particles can already lead to a fascinating clustering effect called motility induced phase separation [11, 27–31]. Confining a self-propelled particle into a narrow channel shows an interesting nonequilibrium effect, as the probability to find the particle close to the confining wall increases with self propulsion velocity [32–40]. This is especially interesting for the motility of soil dwelling microalgae that regularly encounter solid surfaces such as *Chlamydomonas reinhardtii*.

However, microswimmers are typically immersed in aqueous solutions and thus subject to the corresponding hydrodynamic flow field. As the swimmers active motion imposes hydrodynamic flows, collective effects due to the hydrodynamic coupling between swimmers or walls can arise. An example for the influence of hydrodynamic interactions is the circular motion of *Escherichia coli* cells close to flat surfaces [41–43]. Theoretical considerations also suggest self-concentration effects due to hydrodynamic interactions [44–48].

Another important aspect of microswimmer interactions are their chemical signaling mechanisms. The simplest is the chemotaxis, i.e., a bacterium can follow a gradient of a nutrient chemical [15]. To follow the gradient, the organisms need a way of steering, often referred to as swimming strategy. It has been found that multiflagellated microswimmers usually follow a run-and-tumble mechanism [15], which consists of two phases of motility: the run phase in which they move on straight paths, and the tumble phase in which they reorient. Monoflagellated bacteria such as *Vibrio alginolyticus* have a different swimming strategy, that is, they follow a run-reverse-flick pattern [16]. In the run phase they simply propel forward, then in the reserve phase swim backwards, and finally reorient by a flick of their flagellum [49].

1.2 Swimming at low Reynolds number

The Reynolds number is a dimensionless number used in hydrodynamics that compares the inertial forces to the viscous forces in a fluid flow. For a microswimmer, like algae or bacteria, that swims in water the Reynolds number is typically around $\mathcal{R} = \mathcal{O}(10^{-5})$, meaning that inertial effects are negligible for microswimmers and viscous friction dominates. This manifests itself in the motion of microswimmers, if for example a bacterium would suddenly stop moving, it would only coast for 0.1 \AA [50]. Another essential consequence is that reciprocal motions do not lead to a net propulsion. For example, a scallop, which moves by opening and shutting its shell, would not have a net displacement at a low Reynolds number, as its motion is time reversible. An analogy that is often used is that for a human to experience similar conditions, they would have to swim in a pool of honey, which exerts considerable viscous forces.

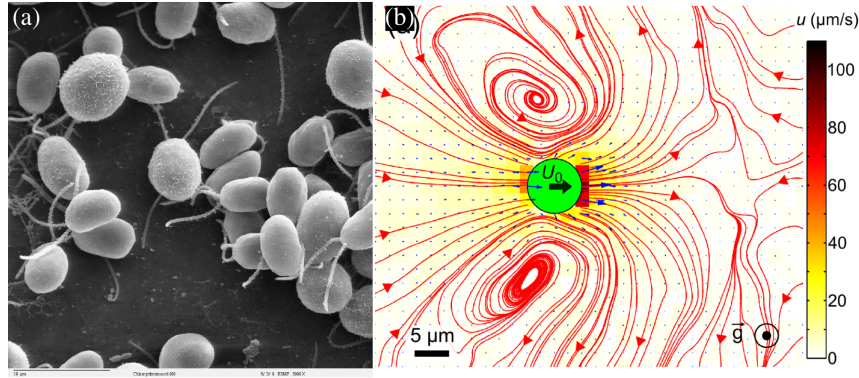


FIGURE 1.3: (a) Scanning electron microscopy image of *Chlamydomonas reinhardtii* algae. [6] (b) Hydrodynamic flow field around a *Chlamydomonas reinhardtii* alga. Reprinted with permission from [7] Copyright 2010 by the American Physical Society.

1.2.1 Examples of biological microswimmers

There is a myriad of biological microswimmers that can be found in nature, but in the biological sciences a few organisms have been selected by the scientific community because of their ease of cultivation, whose genomes have been fully mapped, and a lot is known about their biomolecular machinery. Such organisms are referred to as “model organisms”. Here, we will shortly present two multiflagellated organisms: the bacterium *Escherichia coli*, and the alga *Chlamydomonas reinhardtii*. The hydrodynamic flow field that these two organisms produce as they swim in the surrounding fluid is inherently different, since *Escherichia coli* is a pusher-type swimmer and *Chlamydomonas reinhardtii* a puller-type. Additionally, we will describe the organism *Vibrio alginolyticus*, which is a mono-flagellated bacterium. In contrast to *Escherichia coli* and *Chlamydomonas reinhardtii*, it does not follow the run-and-tumble swimming strategy but uses the run-reverse-flick strategy.

Puller-type swimmer

Chlamydomonas reinhardtii is a green alga that is typically found in wet soil, and is distributed worldwide. It is widely used as a model organism in biology, not only because the genome has been fully sequenced, but it also has an easy culturing procedure, and a great potential for genetic manipulation. Commercially, it is used for the production of biofuel and biopharmaceuticals.

An electron microscopy image of a few *Chlamydomonas reinhardtii* cells can be seen in Fig. 1.3(a). It can be seen that the cell has a pear shaped body and two flagella that beat in a breaststroke-like motion, by which the organism propels itself forward. The body is approximately $10\mu\text{m}$ in diameter and the flagella are about $10\mu\text{m}$ long. Furthermore, *Chlamydomonas reinhardtii* uses an analog of the run and tumble swimming strategy. In the run phase the two flagella beat in synchrony, and the cell swims on a straight path. When the organism decides to turn, the flagella

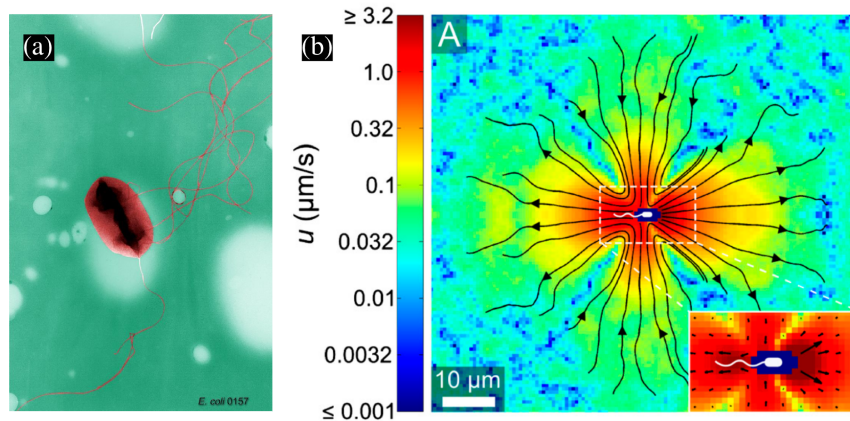


FIGURE 1.4: (a) Transmission electron microscopy image of an *Escherichia coli* bacterium. [8] (b) Hydrodynamic flow field around an *Escherichia coli* bacterium. Reprinted from [9].

desynchronize, the cell starts tumbling [51], and it can reorient towards gradients of nutrient or light.

As the organism propels itself forward, it produces the flow field in the surrounding fluid as shown in Fig. 1.3(b). It can be seen that the fluid is pulled towards the swimmer in its front and rear, hence it is called puller. However, on the sides of the swimmer the fluid is pushed away.

Pusher-type swimmer

Escherichia coli is a Gram-negative bacterium that is typically found in the intestine of humans and animals. In biology it is used as a model organism since its culturing procedure is rather simple, it is suitable for genetic manipulation and the genome has been sequenced.

A transmission electron microscopy image of an *Escherichia coli* is displayed in Fig. 1.4(a). It can be seen that it is rod-shaped and has a number of flagella emerging from different points in its body. The body is approximately $4\mu\text{m}$ in length and its flagella are about twice as long. *Escherichia coli* uses the run and tumble swimming strategy [15]. In the run state the flagella all rotate in the same direction, form a bundle, and the cell swims on a straight path. As the cell decides to turn, some (but not all) of the flagella start rotating in the opposite direction, the flagella bundle dissolves, and thus the cell tumbles and reorients.

When *Escherichia coli* propels forward it produces the hydrodynamic flow field shown in Fig. 1.4(b). Here, it can be seen that the fluid is pushed away from the organism in its front and its back, and thus it is termed a pusher. However, on the sides the fluid is pulled towards the swimmer.

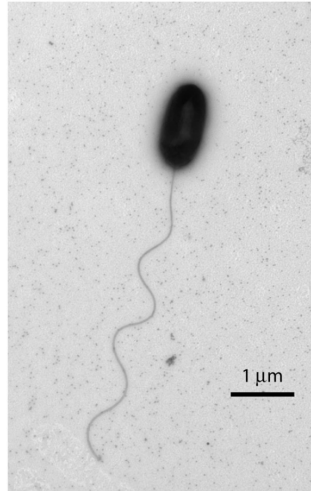


FIGURE 1.5: Transmission electron microscopy image of a *Vibrio alginolyticus* cell. Reprinted from [10].

Mono-flagellated swimmer

Vibrio alginolyticus is a Gram-negative marine bacterium, that can cause wound infection [52] and otitis. A transmission electron microscopy image of a *Vibrio alginolyticus* cell is depicted in Fig. 1.5, where it can be seen that it is rod-shaped and has a single flagellum. Its body is approximately 1 μm in length and its flagellum is about three times larger.

Since *Vibrio alginolyticus* is single-flagellated it cannot use the run and tumble swimming strategy to find nutrient gradients. In fact, it was found that they use the run-reverse-flick strategy [16]. Here, the organism runs forward, by propelling its flagellum in a counterclock-wise manner (run), then it reverses the direction of rotation and swims backward (reverse). Finally, it reorients (flick) due to a buckling instability in the flagellum [49].

From a theoretical point of view the statistics of a single run-reverse-flick swimmer was studied by [53]. It was found that the velocity correlation function and the mean-square-displacement (MSD) of the run-reverse-flick motility pattern differs vastly from the run and tumble pattern.

1.3 Literature review

In this section we give a short review of the relevant literature for this thesis. As the microswimmer and active matter fields are vastly growing it is not possible to cover all aspects within this section, nor in this thesis but the reader is referred to the reviews that are given in the following.

The swimming behavior inside a confinement is an interesting question as biological microswimmers such as bacteria or algae encounter this situation frequently in

their natural environment. Kantsler *et al.* [54] measured the interaction of a *Chlamydomonas reinhardtii* cell approaching and scattering at a wall using high-speed microscopic imaging. They found that the interaction of the cell with the wall is dominated by the ciliary contact and extracted a scattering angle of 16° . Furthermore, the corresponding micrographs show evidence that the short ranged contact dominates over long ranged hydrodynamic interactions with the wall. Lushi *et al.* [55] study this scenario in more detail by considering a simulation using a three-bead-spring model including hydrodynamic interactions in combination with experiments. They show that a shape asymmetric model is essential to capture the dynamics of a *Chlamydomonas reinhardtii* cell scattering off a wall, but also hydrodynamic interactions should not be neglected.

For the pusher-type swimmer *Escherichia coli* approaching a wall the hydrodynamic interactions are more important. In one of the most studied, surprising phenomena of active swimmers Berg and Turner [41] (see also the work of DiLuzio *et al.* [56]) showed that the motion of an *Escherichia coli* cell is influenced by the proximity to a flat solid surface. Later, Lauga *et al.* [42] and Berke *et al.* [43] showed that this is a hydrodynamic interaction with the solid surface. For a review on the hydrodynamics of swimming microorganisms see [57–59].

Another interesting model of a shaped asymmetric dumbbell swimmer has been put forward by Wysocki *et al.* [33]. They study the dynamics of a dumbbell swimmer inside a channel, a spherical cavity, and on a convex boundary and find a relation between the shape asymmetry of the dumbbell swimmer and the wall curvature. However, Wysocki *et al.* [33] also find that in a confining channel the swimmer shows an increased probability to stay close to the walls. This is a consequence of the nonequilibrium nature of the system and has also been found for simpler active particle systems [34–40] (see also [12]).

Collections of active particles with only steric interactions can show a clustering effect that was termed motility-induced phase separation (MIPS)[11, 27–31], which has been shown to correspond to a liquid-gas phase separation [11, 28, 29, 60, 61] (for a review see [62]). Including fixed objects into such a system of active particles influences the collective dynamics vastly. One finds for example an active depletion when two plates are included [63] or collective rotations around circular obstacles [64]. Models that extend the active particle to an asymmetric shape such as self propelled hard rods have an even richer phase diagram. Here, one can find a swarming, laning, jammed and a turbulent state [65–68]. The turbulent state was also found experimentally by Wensink *et al.* [69]. An essential question for biological systems is whether MIPS is influenced by the hydrodynamic interactions between the swimmers [70, 71]. Matas-Navarro *et al.* [72] and Theers *et al.* [73] both studied the collective dynamics of squirmers, which are spherical particles with a prescribed surface flow field and thus interact not only steric but also via hydrodynamics. They showed that the hydrodynamic interactions are suppressing the effect of MIPS. Here, the hydrodynamic interactions give torques that increase the reorientation of particles,

which hinders MIPS.

The simulation of single squirmers was studied intensely by Downton and Stark [74] and by Götze *et al.* [75] using a mesoscale simulation technique for the fluid called multiparticle collision dynamics (MPCD) (for a review on squirmer simulations see [76]). The MPCD technique was originally developed by Malevanets and Kapral [77] and reproduces the hydrodynamic modes up to the Navier-Stokes level (an extensive review can be found in [78]).

As mentioned above the hydrodynamic flow field of microswimmers can have important influences on the swimmer's collective behavior. Theoretical studies suggest that the hydrodynamic interactions between swimmers lead to self-concentration effects [44–48] (for a review see also [79]). In [44] a theoretical model that takes into account the hydrodynamic interactions between microswimmers using the Stokes equation is proposed. The resulting continuum model shows an instability of the homogeneous state of both puller and pusher-type swimmers which implies a self-concentration effect.

Since the hydrodynamic interactions usually have a polar or nematic nature a myriad of self propelled particle models that take into account angular interactions have been proposed [80–86] (for a review see also [87]). These models also apply to another class of active system, so called dry active matter. Examples for experimental systems that are classified as dry active matter are melanocytes [88], vibrated granular rods [89] or particles [90], migrating animal herds [91], and migrating cell layers [92] (for a review see also [93]).

It is often useful to eliminate the complexity of biological interactions and effects by investigating well controlled artificial microswimmers; this choice allows one to isolate specific physical effects and study the resulting active dynamics. Examples of artificial microswimmers are the catalytic Janus colloids [94, 95], or oil droplets in an aqueous solution [96–101] (a comprehensive list of artificial swimmers can be found in [12]). Kurzthaler *et al.* [102] used differential dynamic microscopy and particle tracking to study the behavior of an active Janus colloid. They compare the measured intermediate scattering function (ISF) to the analytical solution of the ISF of an active Brownian particle in 2d. Similar solutions for the ISF, which are also in 3d can be found in [103–105].

1.4 Scope and main results of the thesis

This thesis deals with the collective microswimmer motility in complex environments. It is organized as follows: in Chapter 2 we will review the theoretical background. Starting from the Stokes flow, we will point out the relevant hydrodynamics for the dynamics of microswimmers. We will then introduce the overdamped limit and discuss the concept of active Brownian particles. In Chapter 3 molecular dynamics and Brownian dynamics simulations are reviewed. Additionally, the multiparticle collision dynamics technique is introduced, which is used to simulate hydrodynamic flows.

Chapter 4 deals with the dynamics of a single microswimmer in complex geometries. We will first give a brief review of the literature on nonequilibrium wall accumulation, and then present our results on the near-wall swimming behavior of *Chlamydomonas reinhardtii*. Our main discovery is that the motility of *Chlamydomonas reinhardtii* in confinement is dominated by the curvature of the confining walls. In Chapter 5 we aim towards understanding the influence of hydrodynamic interactions between microswimmers. We first briefly review the relevant literature, and then present our study which predicts an optimal filling fraction for the self-concentration of biological microswimmers. In Chapter 6 we describe mathematically the swimming strategies of microorganisms, which are the run-and-tumble and the run-reverse-flick strategy. We present our study on the collective effects that are induced by the run-reverse-flick strategy, where we find an optimum in collective diffusion. In Chapter 7 we aim towards understanding the statistics of active particles with two motility stages. We provide a toy model that is exactly solvable and point out non-ergodic effects that can be relevant in the adhesion statistics of active particles. Finally, in the Appendix we give the CUDA kernel code snippets for integrating force poles next to microswimmers in an MPCD simulation. We would like to emphasize that the CUDA algorithms used for all MPCD and MD-MPCD hybrid simulations are in-house codes that were developed as part of this thesis work.

1.4.1 Main results

In Chapter 4, we study the motility of *Chlamydomonas reinhardtii* inside a confinement. We use an experimental setup in which we capture the statistical mechanics of a single cell in a controlled environment and compare to Brownian dynamics simulations of an asymmetric dumbbell. We show that the motility of *Chlamydomonas reinhardtii* is governed by the local wall curvature of the confining chamber. Using our simulations we find an excellent agreement to our experiments, without any fitting parameters. Additionally, we show that a dumbbell is the minimal model to explain the curvature guidance, where the corresponding torque that acts at the wall is the crucial ingredient. However, it is noteworthy that we did not need to include any hydrodynamic interactions into our model.

In Chapter 5 we study the influence of hydrodynamic interactions on the collective behavior of biological microswimmers from a theoretical point of view. We propose a new model for biological microswimmers, which accounts for asymmetric shape and the hydrodynamic flow fields that were measured experimentally. Here, we employ the multiparticle-collision-dynamics technique (MPCD) to capture the hydrodynamic interactions. We study the nonequilibrium phase diagram as Péclet number and filling fraction are varied and find heterogeneities in the swimmer's density. Furthermore, we find that there is a maximum in the density heterogeneities for an intermediate filling fraction, which is supported by an analytical theory that we propose. For both simulations and analytical calculations we show that this maximum results from a

competition of hydrodynamic and steric interactions. Ecologically, this maximum represents an optimum for the microswimmers' colonization of their environment.

The influence of the run-reverse-flick swimming strategy on the collective behavior of microswimmers is studied in Chapter 6. We use Brownian dynamics and squirmer simulations, as well as an analytical theory based on a probabilistic approach to study the collective diffusion behavior of interacting run-reverse-flick swimmers. Here, both our simulations and analytical theory predict a maximum in the collective diffusion coefficient at a forward- to backward-runtime ratio of ~ 1.3 . This coincides with the runtime ratio that was measured for *Vibrio alginolyticus* bacteria, which brings us to the hypothesis that these bacteria fine-tuned the intracellular molecular signaling to this runtime ratio.

In Chapter 7 we study the statistics of an active particle that has two motility stages. We explicitly solve the underlying Fokker-Planck equations for the intermediate scattering function (ISF), and validate these results using Brownian dynamics simulations. The ISF that we find shows an interesting behavior which resembles the properties of a supercooled liquid. We also study the MSD of the system and find a subdiffusive regime, for which we point out the implications on experimental measurements of adhesion statistics.

Chapter 2

Theoretical background

In this chapter we will review the theoretical background of the motility of microorganisms. In Sec. 2.1 we will describe the Stokes equation, which governs flows at low Reynolds numbers, and point out implications for the motion of microorganisms, as well as solutions of model flow fields. In Sec. 2.2 we will discuss the limit of overdamped dynamics, show the classical example of a Brownian particle, and introduce the active Brownian particle model. We will also address the theory of motility induced phase separation.

2.1 Stokes equation

The hydrodynamics of an incompressible viscous fluid are governed by the Navier-Stokes equations

$$\rho \left(\frac{\partial \mathbf{v}}{\partial t} + \mathbf{v} \cdot \nabla \mathbf{v} \right) = -\nabla p + \eta \nabla^2 \mathbf{v}, \quad (2.1)$$

$$\nabla \cdot \mathbf{v} = 0, \quad (2.2)$$

where ρ is the fluid's density, \mathbf{v} its velocity, p the pressure, η the dynamic viscosity and t the time. Physically, Eq. (2.1) arises from applying Newton's second law to fluid motion, and Eq. (2.2) represents the incompressibility condition for the fluid. When a body is immersed in a fluid, additional boundary conditions need to be applied to Eqs. (2.1)-(2.2). Usually, the no-slip boundary condition is applied, meaning that the

velocity $\mathbf{v}(S)$ at the surface S of an embedded object vanishes. This is motivated by the fact that adhesive forces at a boundary are greater than the cohesive forces. The resulting force imbalance gives the condition that the flow decays to zero at the boundary.

Given the solution of the Navier-Stokes equations (2.1)-(2.2) for a Newtonian fluid, the stress tensor can be calculated as

$$\boldsymbol{\sigma} = -p\mathbf{I} + \eta [\nabla\mathbf{v} + \nabla\mathbf{v}^T], \quad (2.3)$$

where \mathbf{I} is the unit tensor and the superscript T denotes the matrix transposition. The stress tensor has two characteristic terms; the first term $-p\mathbf{I}$ represents the hydrostatic pressure and produces isotropic stresses; the second term $\eta [\nabla\mathbf{v} + \nabla\mathbf{v}^T]$, called the *deviatoric* stress tensor, produces the viscous stresses. From the stress tensor the force \mathbf{F} and torque $\boldsymbol{\tau}$ acting on a body inside the fluid can be calculated as

$$\mathbf{F} = \int_S \boldsymbol{\sigma} \cdot \mathbf{n} dS, \quad (2.4)$$

$$\boldsymbol{\tau} = \int_S \mathbf{r} \times \boldsymbol{\sigma} \cdot \mathbf{n} dS, \quad (2.5)$$

where \mathbf{n} is the outward normal vector to the surface S of the body.

The Navier-Stokes equations (2.1)-(2.2), can be seen as a balance of inertial forces, which are on the left hand side of the equation, and viscous forces on the right hand side of the equation. The Reynolds number compares the inertial F_{inertial} and viscous F_{viscous} forces and is given by

$$\mathcal{R} = \frac{F_{\text{inertial}}}{F_{\text{viscous}}} = \frac{\rho UL}{\eta}, \quad (2.6)$$

where U is a characteristic velocity and L a characteristic length scale of the system. The density of water is $\rho \approx 10^3 \text{kg m}^{-3}$ and its viscosity is $\eta \approx 10^{-3} \text{Pa s}$. Considering the organism *Escherichia coli* with a typical length of $L \approx 2 \mu\text{m}$ and typical velocity of $U \approx 20 \mu\text{m s}^{-1}$, we arrive at $\mathcal{R} \approx 10^{-5}$. Similarly for *Chlamydomonas reinhardtii* we have $L \approx 10 \mu\text{m}$ and $U \approx 100 \mu\text{m s}^{-1}$ and arrive at $\mathcal{R} \approx 10^{-3}$. In both cases we have a very low Reynolds number, thus viscous forces dominate and inertial effects can be neglected. This allows for a great simplification of the Navier-Stokes equations, since the non-linear inertial terms on the left hand term of Eq. (2.1) can be neglected. The resulting equations are called the Stokes equations

$$\nabla p = \eta \nabla^2 \mathbf{v}, \quad (2.7)$$

$$\nabla \cdot \mathbf{v} = 0. \quad (2.8)$$

We note in passing that Stokes flow is relevant also in lubrication theory, rheology, flow of biological fluids, and in geophysical settings.

2.1.1 Swimming at low Reynolds numbers

The Stokes equations (2.7)-(2.8) are linear, which implies that the relation between kinetics and kinematics is linear. Thus, the force and torque acting on a body immersed in a Stokesian fluid can be written as

$$\mathbf{F} = -\eta (\mathbf{A} \cdot \mathbf{V} + \mathbf{B} \cdot \boldsymbol{\Omega}), \quad (2.9)$$

$$\boldsymbol{\tau} = -\eta (\mathbf{C} \cdot \mathbf{V} + \mathbf{D} \cdot \boldsymbol{\Omega}), \quad (2.10)$$

where \mathbf{V} is the translational and $\boldsymbol{\Omega}$ the rotational velocity of the body. The matrices $\mathbf{A}, \mathbf{B}, \mathbf{C}, \mathbf{D}$ are the resistance matrices of the body, which obey the relations [106]

$$\mathbf{A} = \mathbf{A}^T, \quad \mathbf{D} = \mathbf{D}^T, \quad \mathbf{B} = \mathbf{C}^T. \quad (2.11)$$

For a solid sphere of radius R one can find that

$$\mathbf{A} = 6\pi\eta R\mathbf{I}, \quad \mathbf{D} = 8\pi\eta R^3\mathbf{I}, \quad \mathbf{B} = \mathbf{C}^T = 0, \quad (2.12)$$

but in general these matrices are not of diagonal form. In fact, if \mathbf{A} is not diagonal then there will be an anisotropic drag, which means that force and velocity are not parallel. Furthermore, when $\mathbf{F} \cdot \mathbf{V} < 0$ the motion results in a loss of energy due to viscous dissipation. An example to illustrate this fact is a prolate ellipsoid with a major axis l_1 and minor axis l_2 , for which $l_1 \gg l_2$. Given its orientation \mathbf{e} the resistance matrix is $\mathbf{A} = A_{\parallel}\mathbf{e} \otimes \mathbf{e} + A_{\perp}(\mathbf{I} - \mathbf{e} \otimes \mathbf{e})$, where \otimes is the tensor production and $A_{\perp} \approx 2A_{\parallel}$. The result of the anisotropic form of \mathbf{A} is that the force perpendicular to the orientation is twice as large as in the parallel direction.

An important consequence of drag anisotropy is the possibility of locomotion at low Reynolds numbers. Most biological microswimmers propel by means of a flagellum, which is a slender appendage that moves in a periodic wave-like manner. In the following we assume that the microswimmer moves in x direction and that the flagellum beats normal to the x axis. A small segment of the flagellum can be approximated as a straight, thin rod, with a viscous drag force $\mathbf{f} = \xi_{\parallel}\mathbf{v}_{\parallel} + \xi_{\perp}\mathbf{v}_{\perp}$, and where $\xi_{\perp} = 2\xi_{\parallel}$, \mathbf{v}_{\parallel} is the velocity parallel to the segment's tangent and \mathbf{v}_{\perp} is the velocity perpendicular to the segment's tangent. Using $|\mathbf{v}_{\parallel}| = v \cos \theta$ and $|\mathbf{v}_{\perp}| = v \sin \theta$, the total force in the x direction, i.e. the propulsion force, is given by $f_{\text{prop}} = (\xi_{\parallel} - \xi_{\perp})v \sin \theta \cos \theta$. Therefore, a periodic change in shape can give a net propulsion force, which results in locomotion.

Going back to the Stokes equation (2.7), it is important to realize that it is time independent. A direct consequence of the time independence is that a periodic time reversible motion of an object inside the fluid does not lead to net motion. This is also known as the Purcell's *scallop theorem* [50]. A scallop moving at low Reynolds number will not have any net displacement, since its motion is completely time reversible.

2.1.2 Stokeslet solution and multipole expansion

The Stokes equation with an external force \mathbf{f}_{ext} is given by

$$\nabla p = \eta \nabla^2 \mathbf{v} + \mathbf{f}_{\text{ext}}, \quad (2.13)$$

$$\nabla \cdot \mathbf{v} = 0. \quad (2.14)$$

In free, three dimensional space the solution for the velocity field can formally be written as a convolution of the external force with the Green's function

$$\mathbf{v}(\mathbf{r}, t) = \int \mathbf{O}(\mathbf{r} - \mathbf{r}') \cdot \mathbf{f}^{\text{ext}}(\mathbf{r}', t) d\mathbf{r}'. \quad (2.15)$$

The Green's function is called the Oseen tensor and is given by

$$\mathbf{O}(\mathbf{r}) \equiv \frac{1}{8\pi\eta r} (\mathbf{I} + \hat{\mathbf{r}} \otimes \hat{\mathbf{r}}), \quad (2.16)$$

where $r = |\mathbf{r}|$ and $\hat{\mathbf{r}} = \mathbf{r}/r$. Considering a point force $\mathbf{f}_{\text{ext}} = f\mathbf{e}\delta(\mathbf{r})$, at position \mathbf{r} with the direction \mathbf{e} and strength f , where $\delta(\mathbf{r})$ is the Dirac distribution, the velocity field can be found explicitly as

$$\mathbf{v}(\mathbf{r}) = f\mathbf{O}(\mathbf{r}) \cdot \mathbf{e} = \frac{f}{8\pi\eta r} [\mathbf{e} + (\hat{\mathbf{r}} \cdot \mathbf{e})\hat{\mathbf{r}}], \quad (2.17)$$

which has been known as a 'Stokeslet' since the work of Hancock [107]. Useful model flow fields for microswimmers can be constructed from Eq. (2.17) as explained in the next section.

In most cases external forces are placed at a position \mathbf{x} , while one is interested in the flow field at position \mathbf{r} , as for example

$$\mathbf{v}(\mathbf{r}) = f\mathbf{O}(\mathbf{r} + \mathbf{x}) \cdot \mathbf{e}. \quad (2.18)$$

For analytical treatability it is then very useful to consider the multipole expansion of the Oseen tensor, which in components $i, j \in \{x, y, z\}$ is given by [108]

$$O_{ij}(\mathbf{r} + \mathbf{x}) = \sum_{n=0}^{\infty} \frac{1}{n!} (\mathbf{x} \cdot \nabla)^n O_{ij}(\mathbf{r}). \quad (2.19)$$

In the expansion Eq.(2.19), derivatives of the Oseen tensor are needed, here we give the first and second

$$\begin{aligned} \frac{\partial}{\partial r_k} O_{ij} &= \frac{1}{8\pi\eta} \left[\frac{1}{r^3} (-\delta_{ij}r_k + \delta_{jk}r_i + \delta_{ik}r_j) - \frac{3}{r^5} r_i r_j r_k \right], \quad (2.20) \\ \frac{\partial}{\partial r_m} \frac{\partial}{\partial r_k} O_{ij} &= \frac{1}{8\pi\eta} \left[\frac{1}{r^3} (-\delta_{ij}\delta_{km} + \delta_{jk}\delta_{im} + \delta_{ik}\delta_{jm}) \right. \\ &\quad - \frac{3}{r^5} (-\delta_{ij}r_m r_k + \delta_{jk}r_m r_i + \delta_{ik}r_m r_j \\ &\quad \left. + \delta_{mi}r_j r_k + \delta_{jm}r_i r_k + \delta_{mk}r_i r_j) + \frac{15}{r^7} r_i r_j r_k r_m \right]. \quad (2.21) \end{aligned}$$

We will use this multipole expansion to treat microswimmers, including hydrodynamic interactions, analytically in Sec. 5.1-5.2.

The velocity field induced by a force monopole, that is the Stokeslet solution [Eq.(2.17)], scales as $1/r$. It shows an anisotropy, as the flow in the direction parallel to the force v_{\parallel} is twice as large as in the perpendicular direction $v_{\perp} = v_{\parallel}/2$. This has important consequences for the locomotion of swimming microorganisms as already stated in Sec 2.1.1.

The Stokes equation [Eq. (2.7)] has some interesting mathematical properties: (i) it is linear, and (ii) contains no homogeneous (space independent) fields. It follows immediately from these two properties that if (\mathbf{v}, p) is a solution of the Stokes equation, then the pair $(\mathbf{v}_n \equiv \nabla^n \mathbf{v}, p_n \equiv \nabla^n p)$ of arbitrarily-high order derivatives is also a solution, where the external forcing \mathbf{f}_{ext} is replaced by the corresponding derivative [109]. These higher order derivatives are already included in the Taylor expansion in Eq. (2.19). We have then the interesting situation where the formal multipole expansion of the fundamental solution produces all solutions based on a distribution of singularities in the flow. The first derivative [Eq. (2.20)] gives a flow singularity corresponding to a force dipole, whose resulting velocity field scales as $1/r^2$ (see also Sec. 2.1.3). The second derivative [Eq. (2.21)] is a force quadrupole and its velocity field scales as $1/r^3$. Combinations of these solutions (and higher order derivatives) can be used to construct solutions in a variety of geometries such as the flow past a sphere [110].

In the presence of confining walls the flow fields are modified. Because of the mathematical analogy with the equations of electrostatics the solution (\mathbf{v}, p) can be found using the method of images. Here, an image of the flow singularity is placed behind the corresponding wall such that the correct boundary conditions are imposed at the wall.

2.1.3 Model flow fields

The dynamics in the Stokes regime are overdamped, which means that all inertial effects in the locomotion of a microorganism are negligible. This means that the forces in the system, microorganism together with fluid, have to add up to zero, i.e., the system has to be *force free*. Therefore, the simplest configuration of forces that can

model the effect of a swimming microorganism on the fluid is given by a force dipole. The Stokes equation for a force dipole can be solved exactly using two Stokeslets [Eq. (2.17)], with the following result for the flow velocity

$$\mathbf{v}(\mathbf{r}) = \frac{lf}{8\pi\eta r^2} \left[3 \left(\frac{\mathbf{r}}{r} \cdot \mathbf{e} \right)^2 - 1 \right]. \quad (2.22)$$

Here, l is the distance between the force poles i.e. the dipole length, f the applied force, \mathbf{e} the unit vector connecting the poles, and $r = |\mathbf{r}|$. If the force is positive, the swimmer is called a pusher like *Escherichia coli*, whereas a negative force corresponds to a puller like *Chlamydomonas reinhardtii*. A sketch of the characteristic flow field for pushers is shown in Fig. 2.1(a). It can be seen that the fluid is pushed away in the front and back of the swimmer, and pulled in on the sides. The sketch for pullers is shown in Fig. 2.1(b), where the fluid is pulled towards the swimmer in the front and the back and pushed away on the sides. In fact, it has been shown experimentally that the force dipole model [Eq. (2.22)] reproduces the fluid flow around an *Escherichia coli* cell very accurately [9]. For the puller-type swimmer *Chlamydomonas reinhardtii*

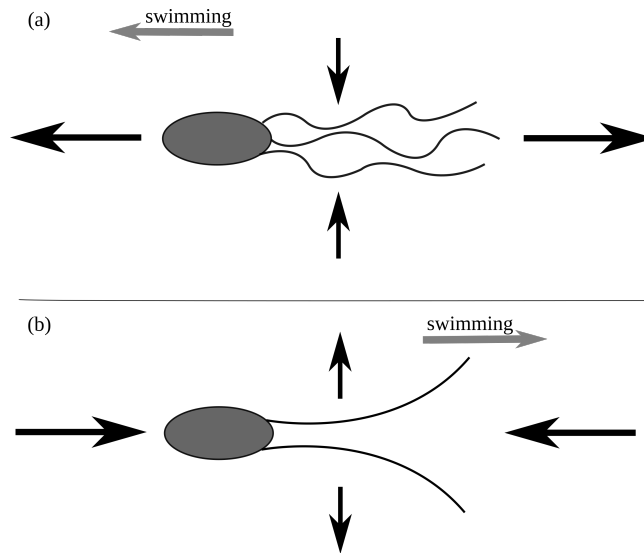


FIGURE 2.1: Sketch of the flow fields produced by (a) a pusher-type swimmer and (b) a puller-type swimmer. Black arrows are a sketch of the fluid velocity around the swimmers and gray arrows show the direction of motion.

it is more accurate to use a force-free configuration of three Stokeslets, as it was shown in [7].

In general, it is useful to have simple models for the flow field around microswimmers, since the role of hydrodynamic interactions between microswimmers is still a matter of debate in the literature. In fact, both publications presented in this thesis (see Sec. 4.1 and Sec. 5.1) address this matter.

2.2 Overdamped dynamics

The dynamics of a Brownian particle immersed in a fluid can be described by the Langevin equation [111]

$$m \frac{d\mathbf{u}(t)}{dt} = -\gamma \mathbf{u}(t) + \mathbf{F}(\mathbf{r}, t) + \mathbf{\Gamma}(t), \quad (2.23)$$

where m is the mass of the particle, γ is the friction coefficient, \mathbf{r} its position, $\mathbf{u}(t)$ its velocity and $\mathbf{F}(\mathbf{r}, t)$ is an external force. The term $\mathbf{\Gamma}(t)$ is a fluctuating and random force, which represents the force stemming from the collisions with the surrounding fluid molecules, that are subject to thermal motion. Typically, it is assumed to have zero mean $\langle \mathbf{\Gamma}(t) \rangle = 0$ and the correlation function $\langle \mathbf{\Gamma}(t) \otimes \mathbf{\Gamma}(t + \Delta t) \rangle = 2D_T \gamma^2 \delta(\Delta t) \mathbf{I}$, where $\delta(\cdot)$ is the Dirac distribution, and D_T is the translational diffusion coefficient. For micron-sized objects, such as colloids, bacteria or microalgae, the Reynolds number, which compares inertial and viscous effects, is low (see also Sec. 2.1). Therefore, we can neglect the inertial terms in Eq. (2.23), namely the left hand side and write

$$\mathbf{u}(t) = -\frac{1}{\gamma} [\mathbf{F}(\mathbf{r}, t) + \mathbf{\Gamma}(t)], \quad (2.24)$$

which is called the overdamped Langevin equation.

2.2.1 Brownian particle

For a single particle immersed in a fluid without an external force Eq. (2.24) reads

$$\frac{d\mathbf{r}(t)}{dt} = -\frac{1}{\gamma} \mathbf{\Gamma}(t). \quad (2.25)$$

This stochastic ordinary differential equation was found and solved by Einstein and Smoluchowski [112–114] to explain the motion of a particle immersed in a resting fluid. Because of the random force $\mathbf{\Gamma}(t)$, Eq. (2.25) cannot be solved explicitly for $\mathbf{r}(t)$, but there are various methods to derive a deterministic equation [111] for the probability distribution $P(\mathbf{r}, t)$ to find the particle at position \mathbf{r} at time t . For Eq. (2.24) one finds

$$\frac{\partial P(\mathbf{r}, t)}{\partial t} = D_T \nabla^2 P(\mathbf{r}, t), \quad (2.26)$$

which is the diffusion equation with translational diffusion coefficient D_T . The solution of this equation is

$$P(\mathbf{r}, t) = \left(\frac{1}{4\pi D_T t} \right)^{3/2} e^{-\frac{\mathbf{r}^2}{4D_T t}}. \quad (2.27)$$

Equation (2.26) is the simplest case of a class of partial differential equations (PDE's) called ‘‘Fokker-Planck equation’’. The MSD, which is the square of the particles distance traveled during a time t , is defined as

$$\langle (\mathbf{r}(t) - \mathbf{r}(0))^2 \rangle. \quad (2.28)$$

Without loss of generality we can assume that $\mathbf{r}(0) = 0$, using the definition of the average we have

$$\langle (\mathbf{r}(t) - \mathbf{r}(0))^2 \rangle = \int P(\mathbf{r}, t) \mathbf{r}^2 d\mathbf{r} = \int \left(\frac{1}{4\pi D_T t} \right)^{3/2} e^{-\frac{\mathbf{r}^2}{4D_T t}} \mathbf{r}^2 d\mathbf{r}. \quad (2.29)$$

Introducing polar coordinates, yields

$$4\pi \left(\frac{1}{4\pi D_T t} \right)^{3/2} \int_0^\infty r^4 e^{-\frac{r^2}{4D_T t}} dr, \quad (2.30)$$

where we already performed the angular integration. The integral in Eq. (2.30) can be solved with the following result for the MSD

$$\langle (\mathbf{r}(t) - \mathbf{r}(0))^2 \rangle = 6D_T t, \quad (2.31)$$

which is linear in time. This linear growth in time of the MSD characterizes diffusive transport.

2.2.2 Active Brownian particle

The key difference between a simple particle immersed in a fluid and a bacterium or microalgae is that the last two propel themselves forward inside the fluid. This can be modeled by including an active force $\mathbf{F}_{\text{active}} = \gamma v_0 \mathbf{e}(t)$ in Eq. (2.24), giving

$$\frac{d\mathbf{r}(t)}{dt} = -v_0 \mathbf{e} - \frac{1}{\gamma} \boldsymbol{\Gamma}(t), \quad (2.32)$$

where v_0 is the self-propulsion velocity and \mathbf{e} is the orientation of the particle. The orientation is also a dynamical variable which (in 3d) obeys the equation

$$\frac{d\mathbf{e}(t)}{dt} = \boldsymbol{\eta}(t) \times \mathbf{e}(t), \quad (2.33)$$

where $\boldsymbol{\eta}(t)$ is a Gaussian white noise with zero mean $\langle \boldsymbol{\eta}(t) \rangle = 0$ and correlator $\langle \boldsymbol{\eta}(t) \otimes \boldsymbol{\eta}(t + \Delta t) \rangle = 2D_R \delta(\Delta t) \mathbf{I}$, where D_R is the rotational diffusion coefficient. When modeling biological organisms, the thermal diffusion is usually small compared to the fluctuations that are caused by the biological nature of the organisms. Hence, it is useful to reinterpret the translational and rotational diffusion in terms of biological fluctuations.

Similarly to the Brownian particle, a Fokker-Planck equation for the probability $P(\mathbf{r}, \mathbf{e}, t)$ of finding the particle at position \mathbf{r} with orientation \mathbf{e} at time t can be computed, and reads

$$\frac{\partial P(\mathbf{r}, \mathbf{e}, t)}{\partial t} = -v_0 \mathbf{e} \cdot \nabla P(\mathbf{r}, \mathbf{e}, t) + D_R \left(\mathbf{e} \times \frac{\partial}{\partial \mathbf{e}} \right)^2 P(\mathbf{r}, \mathbf{e}, t) + D_T \nabla^2 P(\mathbf{r}, \mathbf{e}, t). \quad (2.34)$$

On the right-hand side of this equation we can recognize three characteristic terms; the first term stems from the self-propulsion of the active particle; the second term comes from the rotational diffusion of the particle; and the last term is due to translational diffusion. An interesting property that can be calculated is the MSD of an active particle. One possibility to compute this is to formally solve Eq. (2.32), which reads

$$\mathbf{r}(t) - \mathbf{r}(0) = - \int v_0 \mathbf{e}(t) + \frac{1}{\gamma} \mathbf{\Gamma}(t) dt. \quad (2.35)$$

From Eq. (2.35) we proceed by taking the square and averaging, giving

$$\langle [\mathbf{r}(t) - \mathbf{r}(0)]^2 \rangle = \int v_0^2 \langle \mathbf{e}(t) \cdot \mathbf{e}(t') \rangle dt dt' + \int \frac{1}{\gamma^2} \langle \mathbf{\Gamma}(t) \cdot \mathbf{\Gamma}(t') \rangle dt dt'. \quad (2.36)$$

For the second term in the sum in Eq. (2.36) we can use the correlator $\langle \mathbf{\Gamma}(t) \otimes \mathbf{\Gamma}(t') \rangle = 2D_T \gamma^2 \delta(t - t') \mathbf{I}$ that was prescribed before. The correlator of the orientation can be calculated in a similar manner to Eq. (2.36) by using the formal solution of Eq. (2.33). The final result of the MSD from Eq. (2.36) then reads

$$\langle [\mathbf{r}(t) - \mathbf{r}(0)]^2 \rangle = \frac{v_0^2}{2D_R^2} (e^{-2D_R t} + 2D_R t - 1) + 6D_T t. \quad (2.37)$$

A different method to compute the MSD in Eq. (2.37) is to consider the second moment of the probability $\int P(\mathbf{r}, \mathbf{e}, t) \mathbf{r}^2 d\mathbf{r} d\varphi$, which can be determined by solving Eq. (2.34)¹. The MSD in Eq. (2.37) is shown in Fig. 2.2 for different self-propulsion velocities. One can recognize three characteristic regimes: (i) at very small time scales the translational diffusion dominates and the motility is diffusive; (ii) on intermediate time scales the ballistic regime is dominant, where particles move on straight lines; (iii) on long time scales a second diffusive regime, which stems from the rotational diffusion can be found. Note that the situation is very different for the Brownian particle [see Eq. (2.31)], which only shows a diffusive regime stemming from the translational diffusion, whereas the two additional regimes of the active Brownian particle are activity induced. From the MSD in Eq. (2.37) the effective diffusion coefficient can be calculated as

$$D_{\text{eff}} = D_T + \frac{v_0^2}{6D_R}, \quad (2.38)$$

¹In practice only approximate solutions or solutions in Fourier space of Eq. (2.34) can be found (see also Sec. 2.2.3 and Sec. 7.1).

which involves both translational diffusion and a term stemming from the combination of self-propulsion and rotational diffusion. For bacteria or microalgae the latter is usually dominant, because of their large self-propulsion velocity.

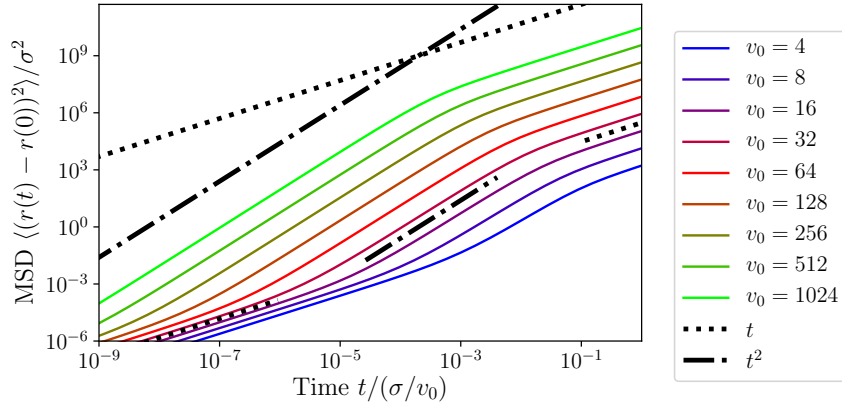


FIGURE 2.2: The solid lines show the MSD [Eq. (2.37)] of an active Brownian particle. The dotted line shows a linear scaling, and the dashed-dotted line a quadratic scaling.

The importance of the self-propulsion over the diffusion can be measured in terms of the Péclet number \mathcal{P} , which is typically defined as the ratio of advective to diffusive transport

$$\mathcal{P} = \frac{v_0 \sigma}{D}, \quad (2.39)$$

where σ is the typical size of the particle and D is a diffusion coefficient. Different choices for the diffusion coefficient have been proposed in the literature, as we can choose the rotational, translational or effective [Eq.(2.38)] diffusion coefficient. For microswimmers the Péclet number is typically large, at least of $\mathcal{O}(10)$.

2.2.3 Motility-induced phase separation

A simple toy model to study the collective effects of active swimmers is given by a collection of active Brownian particles [Eq.(2.32)], where particles are assumed to be spherical and the interactions are assumed to be purely repulsive. The equations of motion in 3d for particle i are then given by

$$\frac{d\mathbf{r}_i}{dt} = v_0 \mathbf{e}_i + \mathbf{F}_i / \gamma + \mathbf{\Gamma}_i, \quad (2.40)$$

$$\frac{d\mathbf{e}_i}{dt} = \boldsymbol{\eta}_i \times \mathbf{e}_i, \quad (2.41)$$

where one typically uses a Weeks-Chandler-Anderson potential to calculate the steric, repulsive forces between particles

$$\Phi(r_{ij}) = 4\epsilon \left[\left(\frac{\sigma}{r_{ij}} \right)^{12} - \left(\frac{\sigma}{r_{ij}} \right)^6 \right] + \epsilon, \quad (2.42)$$

if $r_{ij} < 2^{1/6}\sigma$, and 0 otherwise and with ϵ the energy scale and $r_{ij} \equiv |\mathbf{r}_i - \mathbf{r}_j|$ the distance between two particles. The system can be characterized by two dimensionless numbers, the filling fraction ϕ and the Péclet number \mathcal{P} . These span the nonequilibrium phase space, which was studied extensively in the recent years [11, 27–31]. It was found that above a typical filling fraction and Péclet number (see [11, 27–31]), the system phase separates into a gas and a dense phase. A typical snapshot of a simulation can be seen in Fig. 2.3, where a clear separation between large, solid-like clusters with little to no active motion within them and a gas phase can be seen. This state was termed motility-induced phase separation (MIPS). An intuitive explanation

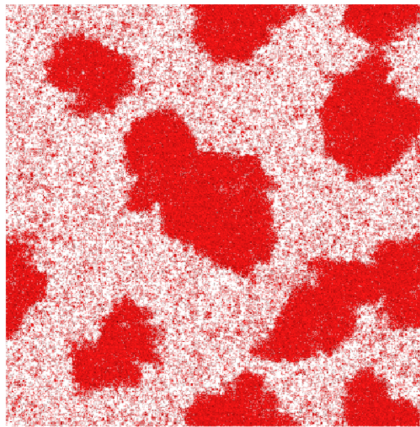


FIGURE 2.3: Representative snapshot of a simulation of active Brownian particles (reprinted with permission from [11] Copyright 2010 by the American Physical Society.) showing motility-induced phase separation. A clear separation between dense and gas phases can be seen.

for MIPS is the following: in a typical implementation of this model, the time for reorientation of a particle due to rotational diffusion is rather large, so on a small to intermediate time scales the particles all move on straight lines. If the filling fraction is sufficiently high, enough particles will encounter each other, effectively blocking each other. Since the reorientation time is rather large, the particles are likely to stay in this configuration and form a solid phase. A simple analytical model by [29] can also explain this effect.

An active Brownian particle [Eq. (2.34)] performs a persistent random walk with a step length of $l_0 = v_0/D_R$. Within this distance, particles can encounter each other, effectively reducing the persistence length l_0 . The particle is then stalled for a time τ_c by each collision, and encounters an average number of particles n_c . Therefore, the effective persistence length is $l = v_0(1/D_R - n_c\tau_c)$, which translates into the effective velocity

$$v = lD_R = v_0(1 - n_c\tau_cD_R). \quad (2.43)$$

Using the mean free time between collisions $\tau_{MF} = (v_0\rho\sigma_s)^{-1}$ with density ρ and cross section σ_s , the average number of collisions is $n_c = 1/[D_R(\tau_{MF} + \tau_c)]$. Inserting into

Eq. (2.43) and assuming $\tau_{MF} \ll \tau_c$ gives the density dependent velocity

$$v(\rho) = v_0 - \rho\zeta, \quad (2.44)$$

where $\zeta = v_0^2 \sigma_s \tau_c$ quantifies how much particles are slowed down by an interaction event (see also [29, 30]).

For the ease of analytical treatment we consider now a 2d case of Eq. (2.34). Taking particle interactions into account, Eq. (2.34) in two dimensions becomes

$$\frac{\partial P(\mathbf{r}, \varphi, t)}{\partial t} = -\mathbf{e}(\varphi) \cdot \nabla [v(\rho)P(\mathbf{r}, \varphi, t)] + D_R \frac{\partial P(\mathbf{r}, \varphi, t)}{\partial \varphi} + D_T \nabla^2 P(\mathbf{r}, \varphi, t), \quad (2.45)$$

where we used the orientation angle φ for the orientation $\mathbf{e} = (\cos \varphi, \sin \varphi)^T$. We now expand $P(\mathbf{r}, \varphi, t)$ in multipoles

$$\rho(\mathbf{r}, t) = \int_0^{2\pi} P(\mathbf{r}, \varphi, t) d\varphi, \quad (2.46)$$

$$\mathbf{p}(\mathbf{r}, t) = \int_0^{2\pi} \cos \varphi P(\mathbf{r}, \varphi, t) d\varphi, \quad (2.47)$$

where we only consider the first two fields in the expansion, which are the density $\rho(\mathbf{r}, t)$ and polarization $\mathbf{p}(\mathbf{r}, t)$. The resulting equations for density and polarization (neglecting higher-order terms such as the nematic tensor) are given by

$$\frac{\partial \rho}{\partial t} = -\nabla \cdot [v(\rho)\mathbf{p} - D_T \nabla \rho], \quad (2.48)$$

$$\frac{\partial \mathbf{p}}{\partial t} = -\frac{1}{2} \nabla [v(\rho)\rho] + D_T \nabla^2 \mathbf{p} - D_R \mathbf{p}. \quad (2.49)$$

In a long time scale and large length scale limit, Eq. (2.49) can be approximated as

$$\mathbf{p} \approx -\frac{1}{2D_R} \nabla [v(\rho)\rho]. \quad (2.50)$$

Plugging Eq. (2.44) and Eq. (2.50) into Eq. (2.48) gives

$$\frac{\partial \rho}{\partial t} = \nabla \cdot \left\{ \left[D_T + \frac{(v_0 - \rho\zeta)(v_0 - 2\rho\zeta)}{2D_R} \right] \nabla \rho \right\} = \nabla \cdot \mathcal{D} \nabla \rho, \quad (2.51)$$

where we defined a collective diffusion coefficient \mathcal{D} . The homogeneous state of the system becomes unstable when $\mathcal{D} < 0$, which results in the criterion that $\zeta_- \leq \zeta \leq \zeta_+$ with

$$\frac{\rho_0 \zeta_{\pm}}{v_*} = \frac{3v_0}{4v_*} \pm \frac{1}{4} \sqrt{\left(\frac{v_0}{v_*} \right)^2 - 1}, \quad (2.52)$$

where $v_* = 4\sqrt{D_T D_R}$ and a mean density ρ_0 . Equation (2.52) predicts an instability of the homogeneous state, i.e., the emergence of clustering similarly to the simulations shown in Fig.2.3.

Similar models including rods have also shown this effect [65]. In general, these models are very interesting from a theoretical perspective, as they show a nonequilibrium phase transition. Their biological relevance will be further discussed in Sec. 5.

Chapter 3

Computational methods

In this chapter we will discuss the basic computational concepts that are used in this thesis. Starting from the simplest example of a molecular dynamics (MD) simulation [Sec. 3.1], we will explain the concept of a neighbor list [Sec. 3.1.1] and then turn to Brownian dynamics [Sec. 3.1.2] and quaternion dynamics simulations [Sec. 3.1.3]. In Sec. 3.2 the multiparticle collision dynamics (MPCD) technique to simulate a fluid will be introduced and we will show how to introduce confining walls and how to couple solid objects to the surrounding fluid.

3.1 Molecular dynamics simulations

Molecular dynamics (MD) simulations are used to numerically integrate Newton's equations of motion, and therefore to study the movement of collections of atoms or molecules, when classical mechanics applies. Newton's equations for particles i with mass m , position \mathbf{r}_i , momentum \mathbf{p}_i are given by

$$\begin{aligned}\frac{d\mathbf{r}_i}{dt} &= \mathbf{p}_i/m, \\ \frac{d\mathbf{p}_i}{dt} &= \mathbf{f}_i,\end{aligned}\tag{3.1}$$

for each $i = 1, \dots, N$ in the system, where the forces between particles i and j are typically given by a pair potential $\mathbf{f}_i = -\nabla\phi(\mathbf{r}_i - \mathbf{r}_j)$. To discretize and integrate Eq. (3.1) a myriad of methods have been proposed [115]. The simplest discretization

method is the Euler algorithm, which is given by a simple Taylor expansion of the positions and velocities at the new time step

$$\begin{aligned}\mathbf{r}_i(t + \delta t) &= \mathbf{r}_i(t) + \delta t \mathbf{v}_i(t) + \frac{1}{2} \delta t^2 \mathbf{a}_i(t), \\ \mathbf{v}_i(t + \delta t) &= \mathbf{v}_i(t) + \delta t \mathbf{a}_i(t),\end{aligned}\tag{3.2}$$

where $\mathbf{v}_i(t)$ is the particle's velocity, $\mathbf{a}_i(t)$ is its acceleration and δt is the discretization time step. The MD algorithm then typically works as follows: first the accelerations $\mathbf{a}_i(t)$ are computed by using the position and velocity values at time t . Second, the positions and velocities are updated to time $t + \delta t$ according to the rule in Eq. (3.2). Afterwards, the boundary conditions are applied and finally, the list of neighbors for each particle (see also Sec. 3.1.1) is updated.

We will now first discuss the neighbor list, which is relevant for all MD simulations that have local interactions, then the case of Brownian dynamics simulations and quaternion dynamics simulations.

3.1.1 Neighbor list

An important ingredient for any MD simulation is the neighbor list, which contains information about the neighbors of a particle. The simplest way of finding all neighbors is of course to compute the distance between each particle, but this is computationally very inefficient as it scales with $\mathcal{O}(N^2)$, where N is the number of particles in the system. There are more efficient methods for computing the neighbors that scale with $\mathcal{O}(N)$. We use a cell linked-list, as it is convenient for the parallelization of an MD algorithm on a Graphics Processing Unit (GPU). For the cell linked-list, the system at hand is first divided into a regular grid which has a lattice constant $L \geq r_c$, where r_c is the cutoff radius of the potential that is used to compute forces between particles. As the forces are local, it is then sufficient to compute the forces between particles that are in the same cell, or in neighboring cells. This reduces the computational cost tremendously and enables us to integrate a system of $\mathcal{O}(10^5)$ particles or larger with local interactions on a modern computer within a reasonable computational time.

3.1.2 Brownian dynamics

Although the equations of motion we are concerned with are different from the classical Newton's equations of motion, the methods developed for classical MD simulations such as the neighbor list [Sec. 3.1.1] also apply to the stochastic differential equations that were presented in Sec. 2.2.

The equations of motion for N spherical active Brownian particles with position \mathbf{r}_i and orientation \mathbf{e}_i are given by (see also Sec. 2.2.3)

$$\frac{d\mathbf{r}_i}{dt} = v_0\mathbf{e}_i + \mathbf{F}_i/\gamma + \mathbf{\Gamma}_i, \quad (3.3)$$

$$\frac{d\mathbf{e}_i}{dt} = \boldsymbol{\eta}_i \times \mathbf{e}_i, \quad (3.4)$$

where we use a Weeks-Chandler-Anderson potential [Eq.(2.42)] to calculate the repulsive, hard-core forces \mathbf{F}_i among particles. Here, γ is the friction coefficient, $\mathbf{\Gamma}_i$ is a Gaussian white noise with zero mean and $\boldsymbol{\eta}_i$ are random vectors uniformly distributed on the unit sphere. The equation for the position \mathbf{r}_i [Eq. (3.3)] can be discretized using a second order stochastic Runge-Kutta algorithm [116]

$$\mathbf{r}_i(t + \delta t) = \mathbf{r}_i(t) + v_0\mathbf{e}_i\delta t + \frac{1}{\gamma} (\mathbf{F}_i(\mathbf{r}_i) + \mathbf{F}_i(\mathbf{R}_i)) \delta t + \mathbf{\Gamma}_i\sqrt{\delta t}, \quad (3.5)$$

where $\mathbf{R}_i = \mathbf{r}_i + v_0\mathbf{e}_i\delta t + \frac{1}{\gamma}\mathbf{F}_i(\mathbf{r}_i)\delta t + \mathbf{\Gamma}_i\sqrt{\delta t}$, such that the force is calculated at two stages. The second order stochastic Runge-Kutta method is useful, since it computes the forces between the particles more accurately than a simple Euler scheme; this choice effectively allows for a larger time step δt and thus a reduction in computational time.

For the orientation equation (3.4) a simple stochastic Euler algorithm is sufficient

$$\mathbf{e}_i(t + \delta t) = \mathbf{e}_i + \boldsymbol{\eta}_i \times \mathbf{e}_i\sqrt{\delta t} + \lambda\mathbf{e}_i, \quad (3.6)$$

where λ is a Lagrange multiplier used to impose the constraints $\mathbf{e}_i \cdot \mathbf{e}_i = 1$. A straightforward calculation starting from this normalization condition gives

$$\lambda = -1 + \sqrt{1 - \delta t (\boldsymbol{\eta}_i \times \mathbf{e}_i)^2}. \quad (3.7)$$

The simulation is then carried out in the following way: first, the forces $\mathbf{F}_i(\mathbf{r}_i) + \mathbf{F}_i(\mathbf{R}_i)$ are calculated; second, these forces are used to update the position Eq. (3.5) and the orientation Eq.(3.6); third, the boundary conditions are applied; and finally the neighbor list is updated.

Using this integration scheme one can study MIPS, as presented in Sec. 2.2.3. We are going to use these simulation methods in Sec. 4.1, Sec. 5.1 and Sec. 6.3.

3.1.3 Quaternion dynamics

The equations of motion for non-deformable, shape anisotropic objects, are usually formulated in terms of the Euler angles [117]. Attempting to discretize the Euler angles runs into a number of problems; first, trigonometric functions produce large rounding-off errors which accumulate over time and produce unphysical results; second, and most importantly, the Euler angles have discontinuous jumps and thus are

not a covering map of the rotation group $\text{SO}(3)$. However, the group $\text{SO}(3)$ is diffeomorphic to the real projective space $\mathbb{P}_3(\mathbb{R})$, which is represented by the quaternions $\mathbf{q} = (q_0, q_1, q_2, q_3)^T$, where $q_i \in \mathbb{R}$. This means that we can use the quaternions to formulate our equations of motion [115]

$$m\ddot{\mathbf{R}} = \mathbf{F}, \quad (3.8)$$

$$\ddot{\mathbf{q}} = \frac{1}{2} \left[\mathbf{W}(\dot{\mathbf{q}}) \begin{pmatrix} 0 \\ \boldsymbol{\Omega}^b \end{pmatrix} + \mathbf{W}(\mathbf{q}) \begin{pmatrix} 0 \\ \dot{\boldsymbol{\Omega}}^b \end{pmatrix} \right], \quad (3.9)$$

$$\dot{\mathbf{q}} = \frac{1}{2} \mathbf{W}(\mathbf{q}) \begin{pmatrix} 0 \\ \boldsymbol{\Omega}^b \end{pmatrix}, \quad (3.10)$$

$$\dot{\boldsymbol{\Omega}}_\alpha^b = (I_m^b)_\alpha^{-1} \left(T_\alpha^b + \left((I_m^b)_\beta - (I_m^b)_\gamma \right) \Omega_\beta^b \Omega_\gamma^b \right), \quad (3.11)$$

where \mathbf{R} is the center of mass position, $\boldsymbol{\Omega}$ the angular velocity, \mathbf{I}_m^b the moment of inertia tensor, m the mass, \mathbf{F} the force, T_α^b the torque in the body frame, and (α, β, γ) are cyclic permutations of the indices (x, y, z) . The matrix \mathbf{W} is constructed from the quaternions (see also [115])

$$\mathbf{W}(\mathbf{q}) = \begin{pmatrix} q_0 & -q_1 & -q_2 & -q_3 \\ q_1 & q_0 & -q_3 & q_2 \\ q_2 & q_3 & q_0 & -q_1 \\ q_3 & -q_2 & q_1 & q_0 \end{pmatrix}. \quad (3.12)$$

As for Euler angles, the quaternions can be used to switch between the laboratory frame and the body frame of an object. The superscript b denotes that the variable is computed in the body frame of the object. Switching between a vector in the body frame \mathbf{f}^b and the laboratory frame \mathbf{f} is done using the quaternion rotation

$$\mathbf{f}^b = \mathbf{D}(\mathbf{q})\mathbf{f}, \quad (3.13)$$

where the matrix $\mathbf{D}(\mathbf{q})$ is [115]

$$\mathbf{D} = \begin{pmatrix} q_0^2 + q_1^2 - q_2^2 - q_3^2 & 2(q_1q_2 + q_0q_3) & 2(q_1q_2 - q_0q_2) \\ 2(q_2q_1 - q_0q_3) & q_0^2 - q_1^2 + q_2^2 - q_3^2 & 2(q_2q_3 + q_0q_1) \\ 2(2q_3q_1 + q_0q_2) & 2(q_3q_2 - q_0q_1) & q_0^2 - q_1^2 - q_2^2 + q_3^2 \end{pmatrix}. \quad (3.14)$$

The equations (3.8)-(3.11) can be discretized and integrated using a Verlet algorithm [118]. The integration step starts by first updating the center of mass position and the quaternions according to

$$\mathbf{R}(t + \delta t) = \mathbf{R}(t) + \mathbf{U}(t)\delta t + \frac{\delta t^2}{2M}\mathbf{F}(t), \quad (3.15)$$

$$\mathbf{q}(t + \delta t) = (1 - \tilde{\lambda})\mathbf{q}(t) + \dot{\mathbf{q}}\delta t + \frac{\delta t^2}{2}\ddot{\mathbf{q}}, \quad (3.16)$$

$$\tilde{\lambda} = 1 - \dot{\mathbf{q}}^2\delta t^2/2 - \sqrt{1 - \dot{\mathbf{q}}^2 - \dot{\mathbf{q}} \cdot \ddot{\mathbf{q}}\delta t^3 - (\ddot{\mathbf{q}}^2 - \dot{\mathbf{q}}^4)\delta t^4/4}, \quad (3.17)$$

where $\tilde{\lambda}$ is used to keep the quaternion normalized: $\mathbf{q}^2 = 1$. Second, the boundary conditions are applied and right after, the neighbor list is updated. After this, the force $\mathbf{F}(t + \delta t)$ and torque $\mathbf{T}(t + \delta t)$ at time $t + \delta t$ are computed, and the velocity and angular velocity are updated according to

$$\mathbf{U}(t + \delta t) = \mathbf{U}(t) + \frac{\delta t}{2M} [\mathbf{F}(t) + \mathbf{F}(t + \delta t)], \quad (3.18)$$

$$\mathbf{\Omega}(t + \delta t) = \mathbf{\Omega}(t) + \frac{\delta t}{2} \mathbf{D}^T (\mathbf{I}^b)^{-1} \mathbf{D} \cdot [\mathbf{T}(t) + \mathbf{T}(t + \delta t)]. \quad (3.19)$$

By using this algorithm we can integrate the equations of motion of shape anisotropic objects such as dumbbells, which are used in Sec.5.1. Additionally, this algorithm is convenient to couple the dynamics of a solid object to a fluid simulation technique such as multiparticle collision dynamics (MPCD), which is discussed in the next section.

3.2 Multiparticle collision dynamics

Hydrodynamic interactions between microswimmers are a matter of discussion in the literature, and we will address this topic in both Sec. 4.1 and Sec. 5.1. Simulating the hydrodynamic interactions of microswimmers or even colloids is a daunting task, because the interactions are not local. Therefore, the hydrodynamic forces between particles cannot simply be computed as the local two-body forces that were treated in the last section. In fact, one should consider the full dynamics of the Navier-Stokes equations (2.1)-(2.2), including correlations between multiple particles. Direct discretization and integration of the Navier-Stokes equations (2.1)-(2.2), including the proper boundary conditions for microswimmers, is computationally unfeasible. Luckily, Malevanets and Kapral proposed the multiparticle collision dynamics (MPCD) method, which is a particles based, mesoscale method, that reproduces the hydrodynamic modes up to the Navier-Stokes level. In fact, this technique and lattice Boltzmann simulations have been the most prominent computational frameworks for simulating the fluid surrounding microswimmers. MPCD, however, is a particle based method, which is easy to couple to an MD simulation and it can resolve the entire hydrodynamics including lubrication forces, and thus proves to be ideal for our applications. There are various forms of the MPCD technique; here we present a version which includes an Andersen thermostat, denoted by MPCD-AT and then show an extension including angular momentum conservation denoted by MPCD-AT+a [78, 119, 120] in Sec. 3.2.1.

The MPCD fluid is modeled by N_{fl} point particles with mass m moving in a continuous two or three-dimensional domain (as opposed to lattice Boltzmann where only lattice position are allowed). The basic algorithm consists of two steps: the streaming step and the collision step. In the streaming step the positions are changed according to a simple ballistic evolution

$$\mathbf{r}_i(t + \delta t) = \mathbf{r}_i(t) + \mathbf{v}_i(t)\delta t, \quad (3.20)$$

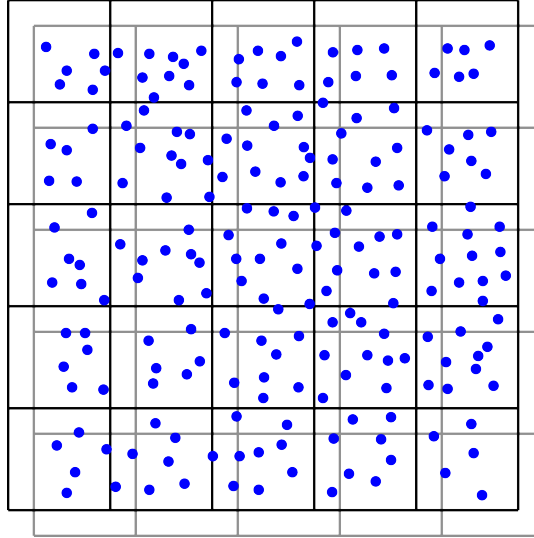


FIGURE 3.1: Sketch of MPCD particles inside cells. The gray and black grids represent the position of the grid used in the collision step before and after the grid shift.

where \mathbf{r}_i are the particles positions, $\mathbf{v}_i(t)$ are their velocities and δt is the MPCD time step.

In the collision step the system is divided into collision cells with lattice constant a (see also Fig. 3.1). In each collision cell $C(i)$ the center of mass velocity is kept constant and the fluctuating part of the velocity of particle i is randomized. This effectively models the randomization of the velocities due to thermal motion. The velocity of particle i is updated according to

$$\mathbf{v}'_i = \frac{1}{N_{C(i)}} \sum_{j \in C(i)} \mathbf{v}_j + \mathbf{v}_i^{\text{ran}} - \frac{1}{N_{C(i)}} \sum_{j \in C(i)} \mathbf{v}_j^{\text{ran}} \quad (3.21)$$

where $N_{C(i)}$ is the current number of particles in cell $C(i)$ (to which i belongs), and $\mathbf{v}_i^{\text{ran}}$ is a random velocity, whose components are Gaussian distributed with zero mean and variance $\sqrt{k_B T/m}$. Here, k_B is the Boltzmann constant and T is the fluid's temperature. Finally, the grid is shifted by a random vector at every time step, to ensure Galilean invariance and prevent the build-up of spurious correlations (see also Fig. 3.1). The components of the shifting vector are uniformly distributed on the interval $[-a/2, a/2]$.

3.2.1 Conservation laws

The number of particles in an MPCD simulation and their mass is fixed, thus mass is conserved by construction.

The conservation of momentum is valid within each cell $C(i)$. Starting from the updated center of mass velocity at time $t + \delta t$ within the cell, we calculate

$$\begin{aligned}
\frac{1}{N_{C(i)}} \sum_{k \in C(i)} \mathbf{v}'_k &= \frac{1}{N_{C(i)}} \sum_{k \in C(i)} \left(\frac{1}{N_{C(i)}} \sum_{j \in C(i)} \mathbf{v}_j + \mathbf{v}_k^{\text{ran}} - \frac{1}{N_{C(i)}} \sum_{j \in C(i)} \mathbf{v}_j^{\text{ran}} \right) \\
&= \frac{1}{N_{C(i)}} \sum_{j \in C(i)} \mathbf{v}_j + \frac{1}{N_{C(i)}} \sum_{k \in C(i)} \mathbf{v}_k^{\text{ran}} - \frac{1}{N_{C(i)}} \sum_{j \in C(i)} \mathbf{v}_j^{\text{ran}} \\
&= \frac{1}{N_{C(i)}} \sum_{j \in C(i)} \mathbf{v}_j,
\end{aligned} \tag{3.22}$$

where the final result is the center of mass velocity at time t . This calculation shows that the center of mass velocity in one collision cell is conserved and therefore also the momentum in that cell is conserved.

Additionally, the temperature is conserved in an MPCD fluid, which can be shown by considering the local temperature in the cell $C(i)$ after collision, that is

$$\begin{aligned}
N_{C(i)} T_{C(i)} &= \sum_{k \in C(i)} \mathbf{v}_k'^2 - \frac{1}{N_{C(i)}} \left(\sum_{k \in C(i)} \mathbf{v}'_k \right)^2 \\
&= \sum_{k \in C(i)} \left(\frac{1}{N_{C(i)}} \sum_{j \in C(i)} \mathbf{v}_j + \mathbf{v}_k^{\text{ran}} - \frac{1}{N_{C(i)}} \sum_{j \in C(i)} \mathbf{v}_j^{\text{ran}} \right)^2 - \frac{1}{N_{C(i)}} \left(\sum_{k \in C(i)} \mathbf{v}_k \right)^2 \\
&= \sum_{k \in C(i)} \left[\left(\frac{1}{N_{C(i)}} \sum_{j \in C(i)} \mathbf{v}_j \right)^2 + (\mathbf{v}_k^{\text{ran}})^2 + \left(\frac{1}{N_{C(i)}} \sum_{j \in C(i)} \mathbf{v}_j^{\text{ran}} \right)^2 \right. \\
&\quad \left. + \frac{2}{N_{C(i)}} \mathbf{v}_k^{\text{ran}} \cdot \sum_{j \in C(i)} \mathbf{v}_j - \frac{2}{N_{C(i)}} \mathbf{v}_k^{\text{ran}} \cdot \sum_{j \in C(i)} \mathbf{v}_j^{\text{ran}} - \frac{2}{N_{C(i)}^2} \sum_{j \in C(i)} \mathbf{v}_j \cdot \sum_{j \in C(i)} \mathbf{v}_j^{\text{ran}} \right] \\
&\quad - \frac{1}{N_{C(i)}} \left(\sum_{k \in C(i)} \mathbf{v}_k \right)^2,
\end{aligned} \tag{3.23}$$

collecting similar terms gives

$$\begin{aligned}
&= \frac{1}{N_{C(i)}} \left(\sum_{j \in C(i)} \mathbf{v}_j \right)^2 + \sum_{k \in C(i)} (\mathbf{v}_k^{\text{ran}})^2 + \frac{1}{N_{C(i)}} \left(\sum_{j \in C(i)} \mathbf{v}_j^{\text{ran}} \right)^2 \\
&\quad + \frac{2}{N_{C(i)}} \sum_{k \in C(i)} \mathbf{v}_k^{\text{ran}} \cdot \sum_{j \in C(i)} \mathbf{v}_j - \frac{2}{N_{C(i)}} \sum_{k \in C(i)} \mathbf{v}_k^{\text{ran}} \cdot \sum_{j \in C(i)} \mathbf{v}_j^{\text{ran}} \\
&\quad - \frac{2}{N_{C(i)}} \sum_{j \in C(i)} \mathbf{v}_j \cdot \sum_{j \in C(i)} \mathbf{v}_j^{\text{ran}} - \frac{1}{N_{C(i)}} \left(\sum_{k \in C(i)} \mathbf{v}_k \right)^2 \\
&= \sum_{k \in C(i)} (\mathbf{v}_k^{\text{ran}})^2 - \frac{1}{N_{C(i)}} \left(\sum_{j \in C(i)} \mathbf{v}_j^{\text{ran}} \right)^2,
\end{aligned} \tag{3.24}$$

where we used the momentum conservation in the first step. The result of Eq. (3.23)-(3.24) is the temperature of the random velocities $\mathbf{v}_j^{\text{ran}}$, which is by definition the temperature of the fluid. Thus, the derivation in Eq. (3.23)-(3.24) proves the conservation of temperature within a cell.

Multiparticle collision dynamics with angular momentum conservation

The MPCD-AT algorithm is momentum and temperature conserving, as we have shown in the last section, but it is not angular momentum conserving. However, the conservation of angular momentum is important for the dynamics of a fluid, especially when we consider objects like microswimmers immersed in a fluid.

During each collision step there will be a change in angular momentum $\Delta\mathbf{L}$. This can be accounted for in the collision step by subtracting the angular velocity $\boldsymbol{\omega}$, which is found by solving the equation $-\Delta\mathbf{L} = \boldsymbol{\Pi} \cdot \boldsymbol{\omega}$. Here, $\boldsymbol{\Pi}$ is the moment of inertia tensor given by

$$\boldsymbol{\Pi} \equiv \sum_{j \in \mathcal{C}(i)} m [(\mathbf{r}_j \cdot \mathbf{r}_j) \mathbf{I} - \mathbf{r}_j \otimes \mathbf{r}_j], \quad (3.25)$$

where the sum extends also to particle $i \in \mathcal{C}(i)$. The new collision rule of the MPCD-AT+a algorithm then reads

$$\begin{aligned} \mathbf{v}'_i = & \frac{1}{N_{\mathcal{C}(i)}} \sum_{j \in \mathcal{C}(i)} \mathbf{v}_j + \mathbf{v}_i^{\text{ran}} - \frac{1}{N_{\mathcal{C}(i)}} \sum_{j \in \mathcal{C}(i)} \mathbf{v}_j^{\text{ran}} \\ & + m \left\{ \boldsymbol{\Pi}^{-1} \sum_{j \in \mathcal{C}(i)} [\mathbf{r}_{j,c} \times (\mathbf{v}_i - \mathbf{v}_i^{\text{ran}})] \right\} \times \mathbf{r}_{i,c}, \end{aligned} \quad (3.26)$$

where $\mathbf{r}_{j,c}$ is the position of particle j with respect to the center of mass of the cell. Note that the moment of inertia tensor of the cell has to be updated at every time step.

3.2.2 Boundaries in MPCD

On the surface of a confining wall or a solid object immersed in a fluid, the no-slip boundary condition is usually imposed (see also Sec. 2.1). For the MPCD fluid this can be done using the bounce-back rule: when a particle collides with a wall within the streaming step its velocity \mathbf{v} is reversed at the point of collision to $-\mathbf{v}$. If the collision happens at a fraction λ of the time step, the particle then travels the remainder $(1-\lambda)$ of the time step into the direction $-\mathbf{v}$. Since there is a grid shift at each time step, there can be partially filled collision cells when a wall is introduced. These lead to the generation of a slip velocity at the wall. An effective way to prevent this is to introduce ghost particles that fill up the cells. These are virtual particles behind the wall that fill up the partially filled cells to the average number of particles per cell. The velocities of the ghost particles are Maxwell-Boltzmann distributed and the

temperature matches the fluid's. The collision step is then carried out for all particles including the ghost particles.

3.2.3 Forced flow

The no-slip condition can be tested simulating a Poiseuille flow. A direct way to create a Poiseuille flow is to use a forced flow, where a constant force acts on each particle in the system. Because the driving force injects energy into the system, in order to maintain a stationary state, dissipation must be also included. This is typically achieved by introducing two parallel walls confining the fluid and inducing viscous dissipation at the solid-liquid interface. Here, it is assumed that the force is in the x direction and the gap between the walls is in the z direction of a Cartesian coordinate system. The resulting flow profile can be predicted analytically and shows a parabolic profile in the direction of the force given by

$$v_x = \frac{|\mathbf{f}|\rho z(L_z - z)}{2\eta}, \quad (3.27)$$

where L_z is the extend of the channel in the z direction, ρ is the fluid's density and η is the viscosity. The viscosity of the MPCD-AT+a fluid can be computed analytically [78, 120, 121] and reads

$$\eta = \rho \left(\frac{k_B T \delta t}{m} \left[\frac{N_C}{N_C - 5/4} - \frac{1}{2} \right] + \frac{a^2}{24\delta t} \left[\frac{N_C - 7/5}{N_C} \right] \right), \quad (3.28)$$

where $N_C = \langle N_{C(i)} \rangle$ is the average number of MPCD particles in a collision cell. The viscosity has two contributions: the first part of the right-hand side of Eq. (3.28) is the kinetic contribution and the second part is the collisional contribution. As the time step is usually small $\delta t \ll 1$ the collisional contribution is dominant.

For the MPCD simulation, the walls are implemented using the bounce-back rule described in the Sec. 3.2.2 and the force on the particles is implemented by modifying the streaming step to [122]

$$\begin{aligned} \mathbf{r}_i(t + \delta t) &= \mathbf{r}_i(t) + \mathbf{v}_i(t)\delta t + \mathbf{f}\delta t^2/2, \\ \mathbf{v}_i(t + \delta t) &= \mathbf{v}_i(t) + \mathbf{f}\delta t, \end{aligned} \quad (3.29)$$

where \mathbf{f} is the force that acts on every fluid particle.

In Fig. 3.2 our simulated profile and the analytical prediction can be seen. In the simulation we used a system size of $50a \times 50a \times 48a$, with an average number of $N_C = 20$ particles per cell, a time step of $0.01\sqrt{ma^2/(k_B T)}$ and the force was set to $\mathbf{f} = 0.005k_B T/a \mathbf{e}_x$, where \mathbf{e}_x is the unit vector in the x direction. It can be seen that the simulations and theoretical prediction match well and that the slip at the wall is very small.

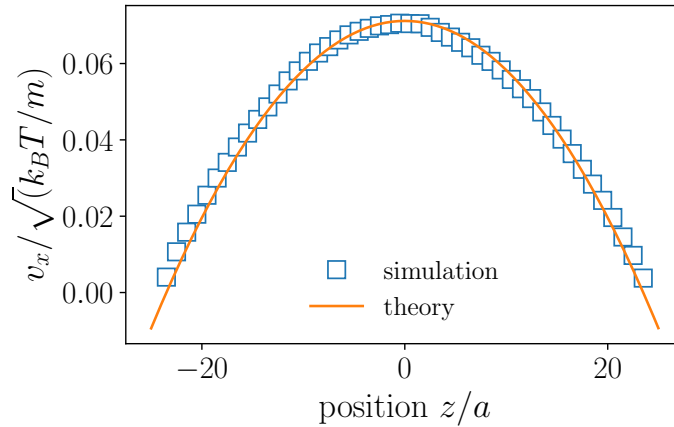


FIGURE 3.2: Parabolic flow profile from a forced flow simulation (squares) and theoretical prediction (line) between two walls.

3.2.4 Rigid objects immersed in an MPCD fluid

When a colloid or model microswimmer is immersed in the MPCD fluid the situation is slightly more complex, as momentum between the fluid and the object immersed in the fluid needs to be exchanged. Given a rigid object inside the fluid, the total change in momentum due to a bounce-back collision with an MPCD particle is

$$\mathbf{J}_i = 2m [\mathbf{v}_i - \mathbf{U} - \boldsymbol{\Omega} \times (\tilde{\mathbf{r}}_i - \mathbf{R})], \quad (3.30)$$

where \mathbf{U} is the object's velocity, $\boldsymbol{\Omega}$ its angular velocity, \mathbf{R} its center of mass position, and $\tilde{\mathbf{r}}_i$ is the position of the MPCD particle upon collision with the object. The updated velocity of the MPCD particle is then given by

$$\mathbf{v}'_i = \mathbf{v}_i - \mathbf{J}_i/m. \quad (3.31)$$

After the collision the MPCD particle then travels for the remainder of the time step with velocity \mathbf{v}'_i away from the object. Note that for multiple immersed objects the MPCD particle can collide multiple times within one time step. The linear and angular momentum of the immersed object are also updated according to

$$\mathbf{U}' = \mathbf{U} + \sum_i \mathbf{J}_i/M, \quad (3.32)$$

$$\boldsymbol{\Omega}' = \boldsymbol{\Omega} + \mathbf{I}_m^{-1} \sum_i (\mathbf{r}_i - \mathbf{R}) \times \mathbf{J}_i, \quad (3.33)$$

where M is the object's mass and \mathbf{I} its moment of inertia tensor. Note that these rules conserve both linear and angular momentum of the full system, that is, fluid and immersed object.

As mentioned above, there are MPCD collision cells which are cut off by the surface of the embedded object, and thus contain fewer fluid particles than average.

Similarly to the case of confining walls, the object is filled up with ghost particles that are uniformly distributed within the object. The ghost particles velocities are updated before each collision step according to

$$\mathbf{v}_i^g = \mathbf{U} + \boldsymbol{\Omega} \times (\mathbf{r}_i^g - \mathbf{R}) + \mathbf{v}_i^{\text{ran}}, \quad (3.34)$$

where the components of $\mathbf{v}_i^{\text{ran}}$ are Gaussian random numbers with zero mean and variance $\sqrt{k_B T/m}$. The ghost particles then take part in the usual collision step [Eq.(3.26)], and their updated velocities are $\mathbf{v}_i^{g'}$. The change in linear $\mathbf{J}_i^g = m(\mathbf{v}_i^{g'} - \mathbf{v}_i^g)$ and angular $\mathbf{L}_i^g = (\mathbf{r}_i^g - \mathbf{R}) \times \mathbf{J}_i^g$ momentum are then transferred to the swimmer

$$\mathbf{U}' = \mathbf{U} + \sum_i \mathbf{J}_i^g / M, \quad (3.35)$$

$$\boldsymbol{\Omega}' = \boldsymbol{\Omega} + \mathbf{I}_m^{-1} \sum_i \mathbf{L}_i^g. \quad (3.36)$$

Together with the quaternion dynamics presented in Sec. 3.1.3 we are able to simulate a collection of shape anisotropic objects immersed in a fluid while taking into account the full hydrodynamic interactions. This method is used in Sec. 5.1 to simulate microswimmers and their motion.

Simulation details

In the simulations that are described in the following section unless otherwise specified, we use an average number of particles $N_C = 20$ per cell and a time step of $\delta t = 0.01 \sqrt{ma^2/(k_B T)}$. The resulting viscosity of the MPCD fluid is $\nu = 3.88a \sqrt{k_B T/m}$ and we use a system size of $30a \times 30a \times 30a$.

Laminar flow around sphere and dumbbell

To test our implementation of the MPCD fluid, we simulate a laminar flow regime around a sphere and a dumbbell. We use periodic boundary conditions in all directions, which effectively gives a plug flow around the sphere, where the strength of the force on every MPCD particle is $\mathbf{f} = 0.05k_B T/a \mathbf{e}_x$.

The resulting flow profile around a sphere with diameter $d = 6a$ can be seen in Fig. 3.3. It can be seen that the no-slip boundary condition on the surface of the sphere is achieved. A similar picture can be seen in Fig. 3.4, where the flow around a dumbbell with diameters $d_1 = 7a$ and $d_2 = 3a$ is shown.

Equipartition theorem

The equipartition theorem is a simple direct test of the correct implementation of the dynamics of an object inside the MPCD fluid. For each component of the object's

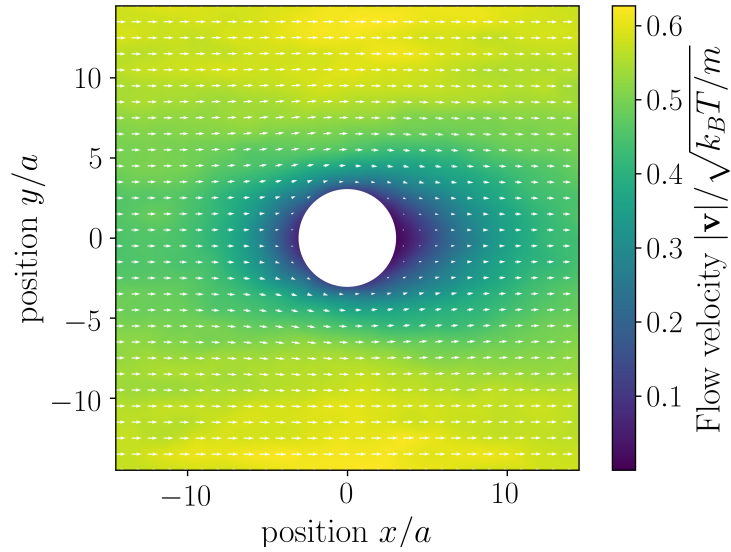


FIGURE 3.3: Two-dimensional cross section in the $z = 0$ plane of a sphere inside a 3d plug flow. The white arrows show the flow direction and the color code shows the magnitude of the flow velocity. It can be seen that the no-slip boundary condition on the sphere is well achieved.

velocity U_α with $\alpha \in \{x, y, z\}$ the following relation has to hold

$$\langle U_\alpha^2 \rangle = k_B T / M, \quad (3.37)$$

where M is the object's mass. Additionally, we can test the rotational motion by computing the following average for the angular velocity Ω_α^b , which reads

$$\langle (\Omega_\alpha^b)^2 \rangle = k_B T / I_{m\alpha}, \quad (3.38)$$

where $I_{m\alpha}$ is the moment of inertia tensor of the object.

For a sphere of diameter $d = 6a$ we find the theoretical value for the velocity square as $\langle U_{\text{theory}}^2 \rangle = 4.4 \times 10^{-4} k_B T / m$ and the simulations yield $\langle U_x^2 \rangle = \langle U_y^2 \rangle = \langle U_z^2 \rangle = 3.9 \times 10^{-4} k_B T / m$. The theoretical value for the angular velocity is $\langle (\Omega_{\text{theory}}^b)^2 \rangle = 3.1 \times 10^{-3} k_B T / ma^2$ and our simulations give $\langle (\Omega_x^b)^2 \rangle = \langle (\Omega_y^b)^2 \rangle = \langle (\Omega_z^b)^2 \rangle = 2.6 \times 10^{-3} k_B T / ma^2$.

Additionally, we performed the simulations with an asymmetric dumbbell with diameters $d_1 = 7a$ and $d_2 = 3a$. Here, the value of the theoretical prediction for the translational motion is $\langle U_{\text{theory}}^2 \rangle = 2.7 \times 10^{-4} k_B T / m$ and the simulations yield $\langle U_x^2 \rangle = \langle U_y^2 \rangle = \langle U_z^2 \rangle = 2.3 \times 10^{-4} k_B T / m$. For the angular velocity the theoretical prediction in x and y direction gives $\langle (\Omega_{x,y}^b)^2 \rangle = 1.3 \times 10^{-3} k_B T / ma^2$ and our simulations yield $\langle (\Omega_x^b)^2 \rangle = \langle (\Omega_y^b)^2 \rangle = 1.1 \times 10^{-3} k_B T / ma^2$. For the z direction, the theoretical prediction is $\langle (\Omega_z^b)^2 \rangle = 1.4 \times 10^{-3} k_B T / ma^2$ while the simulations yield $\langle (\Omega_z^b)^2 \rangle = 1.2 \times 10^{-3} k_B T / ma^2$.

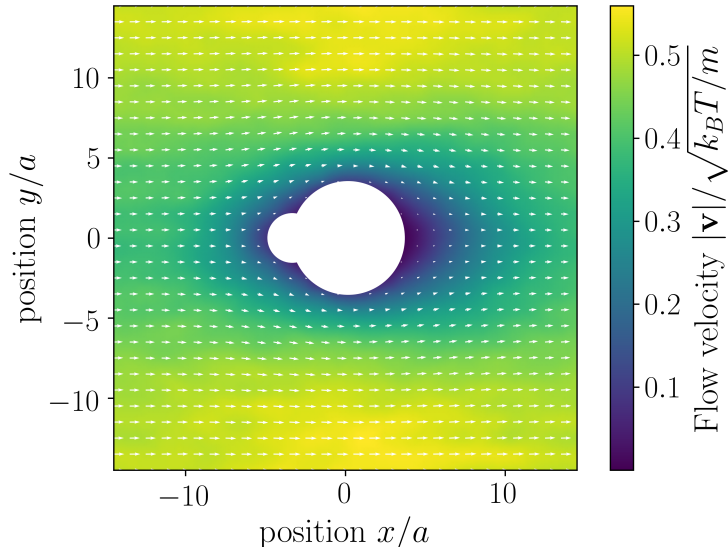


FIGURE 3.4: Two-dimensional cross section in the $z = 0$ plane of a dumbbell inside a 3d plug flow. The white arrows show the flow direction and the color code shows the magnitude of the flow velocity. It can be seen that the no-slip boundary condition on the dumbbells surface is well achieved.

Stokes drag of a sphere

The drag force that acts on a slowly moving, spherical particle in a viscous fluid is given by the Stokes' drag, which reads

$$\mathbf{F}_d = -6\pi\eta R\mathbf{U}, \quad (3.39)$$

where R is the particle's radius, \mathbf{U} its velocity and η the fluid's viscosity. Neglecting all other forces (for example diffusion), the equation of motion for the particle is given by

$$M\frac{d\mathbf{U}}{dt} = -6\pi\eta R\mathbf{U}, \quad (3.40)$$

which has the solution

$$\mathbf{U} = \mathbf{U}_0 e^{-\frac{6\pi\eta R}{M}t}, \quad (3.41)$$

where \mathbf{U}_0 is the velocity at time $t = 0$.

We simulate the Stokes' drag by giving an initial velocity of $\mathbf{U}_0 = 0.5\sqrt{k_B T/m} \mathbf{e}_y$ to a spherical particle. In Fig. 3.5 the theoretical prediction Eq. (3.41) and our simulation of the Stokes' drag can be seen. The prediction and our simulation match quite well, given that we are neglecting all contributions from the intrinsic noise of the MPCD fluid.

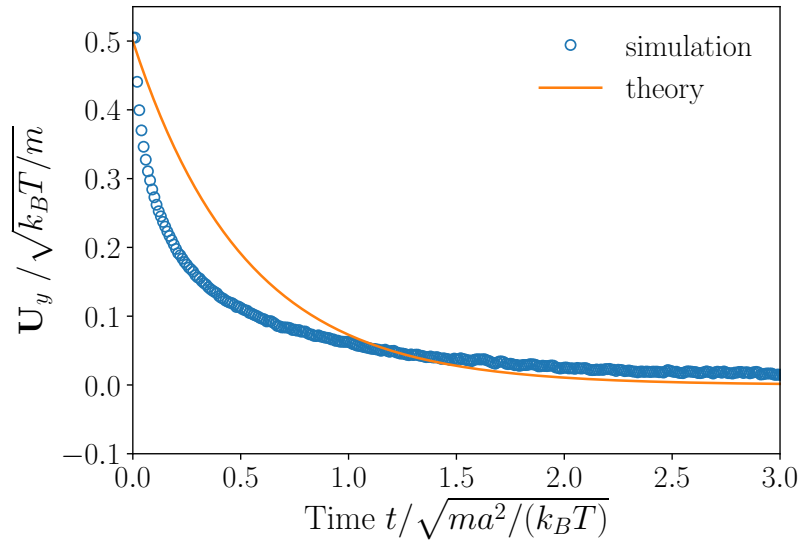


FIGURE 3.5: Velocity of a spherical particle slowing down due to Stokes' drag. Circles represent MPCD simulations and line show the theoretical prediction from Eq. (3.41).

Diffusion of a sphere

The translational diffusion coefficient of a spherical particle with radius R immersed in a fluid is given by

$$D_T = \frac{k_B T}{6\pi\eta R}, \quad (3.42)$$

where T is the fluid's temperature, k_B is the Boltzmann constant, and η is the fluid's viscosity. In Fig. 3.6 the MSD resulting from a simulation of a single spherical particle inside the MPCD fluid can be seen. It matches the theoretical prediction that $\langle(\mathbf{r}(t) - \mathbf{r}(0))^2\rangle = 6D_T t$ where we use D_T from Eq. (3.42).

3.2.5 Computational complexity of MPCD

A major advantage of the MPCD technique is the small computational cost. In MD simulations we always need to search for neighbors in the system and compute forces between them, which is not necessary in MPCD. Here, the particles only need to be sorted into boxes and the interactions between particles are mediated by the collision step, which does not need nearest-neighbor information or direct force computations. The resulting computational cost is of order $\mathcal{O}(N)$.

Another advantage of MPCD is that it is an ideal example of a parallel algorithm. Therefore, we implemented our code on graphical computational units (GPU). This enables us to integrate a system with a number of MPCD particles of order $\mathcal{O}(10^7)$.

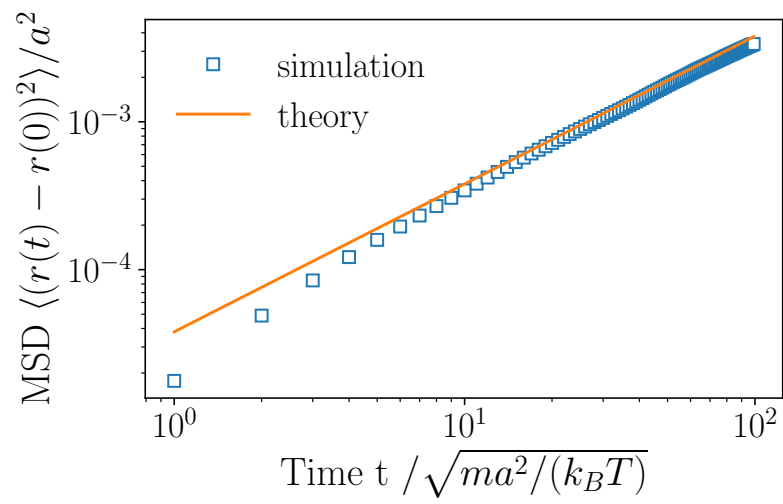


FIGURE 3.6: MSD of a spherical particle inside an MPCD fluid. Squares show the results of the MPCD simulations and the line shows the theoretical prediction from Eq. (3.42).

Chapter 4

Microswimmer motility in complex environments

The swimming behavior of microswimmers in complex environments can trigger fascinating phenomena, such as bioconvection [123], spiral vortices [124] or directed motion [125]. The natural habitat of microbes such as *Chlamydomonas reinhardtii* is in soil [126], porous media [127] or microdroplets [128], such that these complex environments are ubiquitous in the microbes' life. An important ingredient to understand these complex phenomena is understanding the motility of a single cell.

For the pusher-type swimmer *Escherichia coli* it was found that cells approaching a flat surface tend to swim in circles [41], and get trapped close to the surface. The reason for the circular motion are the hydrodynamic interactions with the boundary [42, 43]. For puller-type swimmers like *Chlamydomonas reinhardtii* this behavior is not expected, as their hydrodynamic flow field differs strongly from the pusher-type. In fact, it was found that *Chlamydomonas reinhardtii* tends to scatter off flat surfaces with an average angle of 16° [54]. This numerical value can be explained by the model we present in Sec. 4.2. The study we present in Sec. 4.1-4.2, concerns *Chlamydomonas reinhardtii* in a circular quasi 2d confinement.

From a theoretical point of view the motion in a circular 2d confinement shows interesting nonequilibrium phenomena. Consider an active Brownian particle [Eq.(2.32)-(2.33)] in a circular confinement. Figure 4.1 shows the simulated trajectories of such a particle and the corresponding probability distributions along the diameter can be

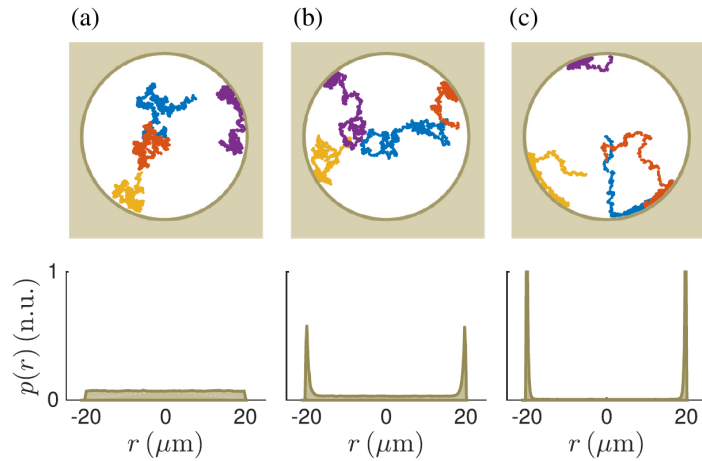


FIGURE 4.1: Simulated trajectories (top) and probability distributions (bottom) of an active Brownian particle. The radius of the particle is $1\mu\text{m}$ and the circular confinement $20\mu\text{m}$. The self-propulsion speed is (a) $v_0 = 0\mu\text{ms}^{-1}$, (b) $v_0 = 5\mu\text{ms}^{-1}$ and (c) $v_0 = 10\mu\text{ms}^{-1}$. Reprinted with permission from [12] Copyright 2010 by the American Physical Society.

seen. Figure 4.1(a) shows the limit of zero propulsion speed, which is the equilibrium case. In fact, for the equilibrium case the Boltzmann relation $p(r) \sim e^{-U(r)/k_B T}$, with an external potential $U(r)$ is valid. As we have a simple circular confinement, the expectation of a homogeneous distribution is confirmed in Fig. 4.1(a). Increasing to propulsion speed [Fig. 4.1(b)-4.1(c)], the probability to stay at the wall increases. This is a result of the nonequilibrium nature of the active Brownian particle: as the particle encounters the wall it will stay oriented towards the wall until the rotational diffusion changes its direction. Therefore, it will slide along the wall as seen in Fig. 4.1(c), and the probability to stay at the wall increases. In experiments this accumulation has been seen in [32], or also in Sec. 4.1. Furthermore, it has been shown that for specific classes of active particles a Boltzmann solution can be found [34–40]. However, in Sec. 4.1-4.2 we consider numerical solutions of the underlying Langevin equation, and analytical approximations for the corresponding Fokker-Planck equation.

An interesting modification of the active Brownian swimmer [Eq.(2.32)-(2.33)] with a dumbbell shape has been proposed by [33]. In Sec. 4.1-4.2 we use a modification of this model to explain the motion of a single *Chlamydomonas reinhardtii* cell in a circular quasi 2d confinement. An important point here is that we do not need to include hydrodynamic interactions into the model. As mentioned before, the situation is very different for a pusher-type swimmer such as *Escherichia coli*, since its dynamics are strongly influenced by the hydrodynamic interactions with walls. Importantly, the model we put forward in Sec. 4.1 also predicts that the motility of a *Chlamydomonas reinhardtii* cell is governed by the curvature of the confining walls, which is confirmed by the experiments also shown in Sec. 4.1. Furthermore, the curvature guidance is a direct consequence of the torque that the particle experiences due to its shape

anisotropy.

Finally, we would like to address the question of novelty for the publication in Sec. 4.1. First, many researchers have reported on the entrapment of pusher-type swimmers close to wall, whereas ours is the first experiment showing the near-wall swimming of a puller-type swimmer. Second, until now, it was assumed that pullers “scatter off” interfaces, however, we show that the interactions are rather different, as they are dominated by the curvature of the confining walls. Third, we were the first to be able to capture, both experimentally and theoretically, the statistics of a single *Chlamydomonas reinhardtii* cell, which enables us to obtain the essential physics underlying the near-wall swimming. Forth, we demonstrate that an active Brownian particle approach is not sufficient to explain the curvature guidance of the wall, but rather a shape anisotropic dumbbell is needed. Fifth, we do not need to incorporate hydrodynamic interactions into the theory, which is quite the opposite when comparing to pusher-type swimmers.

4.1 *Publication:* Curvature-Guided Motility of Microalgae in Geometric Confinement

Reprinted article with permission from:

Tanya Ostapenko, Fabian Jan Schwarzendahl, Thomas J. Bøddeker, Christian Titus Kreis, Jan Cammann, Marco G. Mazza, and Oliver Bäumchen,
Physical Review Letters **120**, 068002 (2018).

<https://doi.org/10.1103/PhysRevLett.120.068002>

Copyright (2018) by the American Physical Society.

Individual contribution: I theoretically investigated the model and implemented the numerical scheme. The simulations in Fig. 3 were performed by me and all other simulations were performed using codes developed on my own. Here, Jan Cammann modified the code to an elliptical geometry and performed simulations with my help. In the Supplemental Material, the theoretical considerations and analytical model were developed by me. Tanya Ostapenko and I contributed equally to the work.

Curvature-Guided Motility of Microalgae in Geometric ConfinementTanya Ostapenko,¹ Fabian Jan Schwarzendahl,^{1,2} Thomas J. Bøddeker,¹ Christian Titus Kreis,^{1,2}Jan Cammann,¹ Marco G. Mazza,¹ and Oliver Bäumchen^{1*}¹Max Planck Institute for Dynamics and Self-Organization (MPIDS), Am Faßberg 17, D-37077 Göttingen, Germany²Georg-August-Universität Göttingen, Friedrich-Hund-Platz 1, D-37077 Göttingen, Germany

(Received 8 May 2017; published 7 February 2018)

Microorganisms, such as bacteria and microalgae, often live in habitats consisting of a liquid phase and a plethora of interfaces. The precise ways in which these motile microbes behave in their confined environment remain unclear. Using experiments and Brownian dynamics simulations, we study the motility of a single *Chlamydomonas* microalga in an isolated microhabitat with controlled geometric properties. We demonstrate how the geometry of the habitat controls the cell's navigation in confinement. The probability of finding the cell swimming near the boundary increases with the wall curvature, as seen for both circular and elliptical chambers. The theory, utilizing an asymmetric dumbbell model of the cell and steric wall interactions, captures this curvature-guided navigation quantitatively with no free parameters.

DOI: 10.1103/PhysRevLett.120.068002

Life in complex geometries can manifest itself at the microscopic level through the myriad of ways in which microorganisms interact with their environment. This entails a broad spectrum of microbiological phenomena, ranging from amoebic crawling [1,2] and fibroblast migration [3], the directional migration of epithelial cells on curved surfaces [4], and microbial proliferation in space-limited environments [5] to the motility of biological microswimmers in confinement [6,7]. In fact, the natural habitats for microbial life are often nonbulk situations, including aqueous microdroplets [8] and the interstitial space of porous media, such as rocks [9,10] and soil [11]. The study of how self-propelled microorganisms in a liquid medium interact with their confining boundaries finds application in physiology with regards to spermatozoa motility in the reproductive tract [12–15], the motion of parasites in the vertebrate bloodstream [16], and in microbiology in the context of biofilm formation [17–20].

Upon interaction with a boundary, these microswimmers might undergo long-range hydrodynamic interactions, in addition to contact interactions [21,22]. For the description of their motility near interfaces, a distinction between “puller”- and “pusher”-type swimmers is required [23], since the flow fields around the two classes entail fundamental differences [24–28]. At flat interfaces, the contact of a spermatozoon's flagellum with a surface tends to rotate it towards a boundary, thus preventing these pusher-type swimmers from escaping flat or weakly-curved surfaces [29]. However, for the puller-type microswimmer, *Chlamydomonas*, a soil-dwelling microalga with two anterior flagella, steric interactions were found responsible for its microscopic scattering off of a flat interface [29]. Single scattering events of *Chlamydomonas* cells were also reported at convex interfaces, where two regimes emerge as

the cell scatters off: an initial, contact force regime and a second, hydrodynamics-dominated regime [30]. Beyond these details of the microscopic interactions at interfaces, the way in which the motility of a single cell is affected by the geometry of a confining domain remains elusive.

In this Letter, we report on the motility of a single *Chlamydomonas* cell in tailor-made microhabitats to elucidate the effects of geometric confinement. We find that the dominant attributes of the swimming statistics are the alga's spatial confinement, which limits its motion to its swimming plane, and the compartment's curved boundary in this plane. Our experiments are in quantitative agreement with Brownian dynamics simulations, whose main ingredients are steric wall interactions and the alga's torque at the compartment interface during a finite interaction time. While a conclusive description of the microscopic details of wall interactions might remain debated today, our results illuminate how a single puller-type cell's navigation in confinement is primarily dominated by the details of the environment's geometric constraints.

We employed optical microscopy techniques and particle tracking to study the motility of a single wild-type *Chlamydomonas reinhardtii* cell (SAG 11-32b) contained within an isolated quasi-two-dimensional microfluidic compartment (see the Supplemental Material [31], Sec. S1 for details). We study precisely a single isolated cell in order to exclude any cell-cell interactions or collective effects. Experiments were performed in circular compartments with radii $r_c = 25\text{--}500\ \mu\text{m}$, and elliptical chambers with comparable semiaxes dimensions. The height of all compartments was approximately $20\ \mu\text{m}$, about one cell diameter (body and flagella); thus, out-of-plane reorientations of the cell are inhibited. Each single-cell experiment was repeated up to 10 times using different

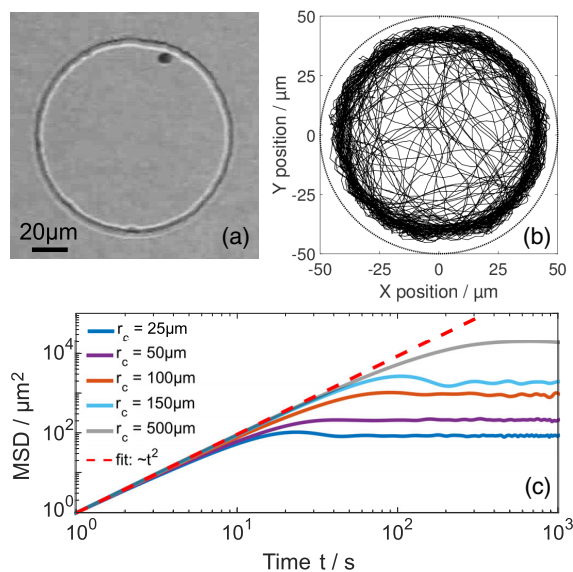


FIG. 1. Experimental design and trajectory analysis. (a) Optical micrograph of a single alga contained in a quasi-two-dimensional (2D) circular compartment. (b) Exemplar single-cell trajectory for $r_c = 50 \mu\text{m}$. (c) Mean-squared displacements (solid lines) for different compartment radii. The dashed line is a best fit to the short-time ballistic behavior ($\sim t^2$).

cells each time. Figure 1(a) displays an image from an experiment (Movie 1 in Ref. [31]) for $r_c = 50 \mu\text{m}$ from which the trajectory of the alga's body center was extracted [Fig. 1(b)]. The alga's trajectory shows a higher density of trajectory points closer to the concave interface, as compared to the compartment's center, which we study in greater detail in this work.

We use the mean-squared displacement (MSD) to characterize the alga's swimming behavior. Here, the MSD for the observation time t was extracted from a single alga's experimental trajectory for each compartment size; see Fig. 1(c). We find that the MSD curves show no clear transition between ballistic behavior, i.e., $\text{MSD} \sim t^2$ on short time scales to diffusive, i.e., $\text{MSD} \sim t$ on long time scales, as reported in previous studies on *Chlamydomonas* swimming in unconfined 2D environments (transition time from ballistic to diffusive ~ 2 s) [29]. A linear fit to the

initial regime of the experimental data yields an exponent of 1.90 ± 0.03 , in approximate agreement with a regime of ballistic swimming. On long time scales, the MSD reaches a plateau corresponding to the explorable area of its confined environment. Hence, we find that the alga's run-and-tumble-like motion in environments unconfined in the swimming plane [35] becomes predominantly ballistic swimming in confinement.

The experimental cell trajectories were statistically averaged and converted into relative probability density maps. Figure 2 displays a series of 2D heat maps of the relative probability density of the cell's positions for different compartment sizes. Our experimental data provide evidence for a pronounced near-wall swimming effect inside the compartment, whose significance decreases for increasing compartment size. This near-wall swimming effect is further quantified by azimuthally collapsing the heat maps into radial probability densities, $P(r)$, as depicted in Fig. 3(a). We define $P(r)$ as:

$$P(r) = \frac{h(r)/(2\pi r \Delta r)}{\int_0^{r_c} \frac{h(r)}{2\pi r \Delta r} dr}, \quad (1)$$

where r is the distance from the center of the compartment, and $h(r)$ is the count of all the alga's positions in a circular shell at distance r with thickness Δr . In order to compare data from different compartment sizes, we normalize $P(r)$ such that $\int_0^{r_c} P(r) dr = 1$. Note that a homogeneous distribution of trajectory points would result in $P(r) = 1/r_c = \text{const}$ by this definition. We observe that $P(r)$ starts from a plateau in proximity of the compartment's center and increases significantly close to the wall. The lateral extent (full-width-half-maximum) of the peak of $P(r)$ ranges from $3\text{--}5 \mu\text{m}$, about half a cell body diameter; the peak position is consistently $9\text{--}11 \mu\text{m}$ away from the wall. At the compartment wall, $P(r)$ drops off, representing a possible zone of flagella-wall contact interactions. As shown in Fig. 3(a), the maximum of $P(r)$ decreases for increasing compartment size, while the overall shape of $P(r)$ described above is preserved.

We compared these experimental results to Brownian dynamics simulations, where the *Chlamydomonas* cell is

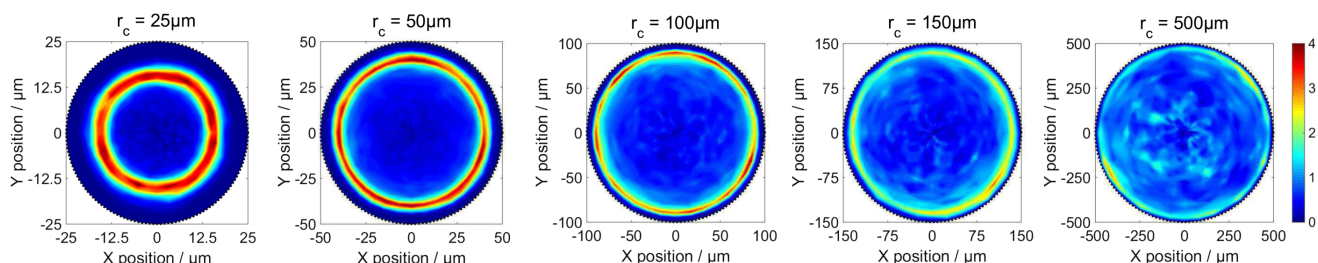


FIG. 2. Relative probability density for a single cell in circular confinement. Heat maps represent the alga's position obtained from experimental data for different compartment sizes: (L-R) $r_c = 25 \mu\text{m}$, $50 \mu\text{m}$, $100 \mu\text{m}$, $150 \mu\text{m}$, $500 \mu\text{m}$. Each map contains statistically averaged data from a minimum of 2–5 independent experiments.

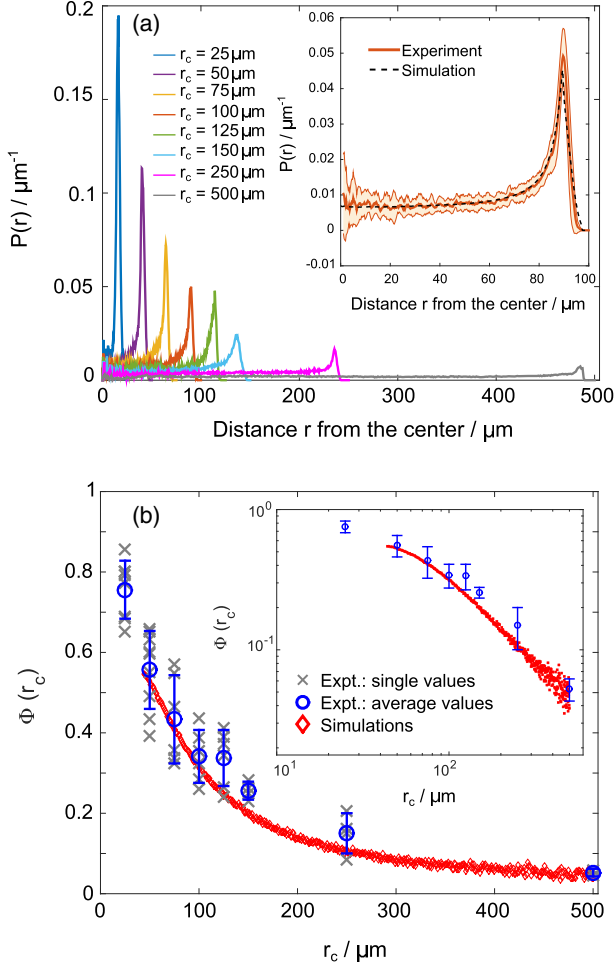


FIG. 3. (a) Radial probability densities $P(r)$ for compartment sizes, r_c , each from 2–10 independent experiments. (Inset) Close-up of the experimental data (average: solid line, standard deviation: background) and Brownian dynamics simulations (dashed line) for $r_c = 100 \mu\text{m}$. (b) Near-wall swimming probability $\Phi(r_c)$: experimental data (circles) denote mean values averaged over independent experiments (crosses) and Brownian dynamics simulations (diamonds). (Inset) Log-log representation of the same data.

modeled as an active asymmetric dumbbell (Sec. S2, Ref. [31]) consisting of two rigid spheres [36]. The smaller sphere represents the cell's body, and the larger sphere mimics the stroke-averaged area covered by the beating of the two anterior flagella. The Langevin equation represents a balance of forces, both deterministic and stochastic ones, experienced by the microswimmer [23]. The position \vec{r} of the dumbbell's center of mass is described by the equation of motion

$$\frac{d\vec{r}}{dt} = v_0 \vec{e} + \mu_w \vec{F}_w + \vec{\eta}. \quad (2)$$

Here, v_0 is the propulsion speed, $k_B T \mu_w$ denotes the diffusivity, μ_w is the mobility (ratio of velocity to an applied force), \vec{F}_w is the force associated with the steric wall interaction

(Weeks-Chandler-Andersen potential [37]) and $\vec{\eta}$ is a Gaussian white noise. The unit vector \vec{e} represents the direction of the propulsion velocity pointing from the small to the large sphere. The orientational equation of motion is

$$\frac{d\vec{e}}{dt} = (\vec{T}_w / \tau_w + \vec{\xi}) \times \vec{e}, \quad (3)$$

where \vec{T}_w is the torque acting at the wall, τ_w is the rotational drag coefficient, and $\vec{\xi}$ is a Gaussian white noise. The torque is a major ingredient in the simulations, since it may reorient the alga away from the interface. We also explicitly account for the alga's run-and-tumble swimming behavior [35].

Note that all geometric and dynamic parameters that entered the simulations were either measured directly from our experiments or extracted from the literature, including a microscopic interaction time ($\tau_w / k_B T$) at the interface [29]. We take the center of the segment connecting the centers of the small and large spheres as the dumbbell's axis of rotation. Hydrodynamic interactions are absent in this model and the dynamics are determined by steric interactions at the confining wall, where only the normal component of \vec{F}_w is considered. The radial probability densities $P(r)$ were extracted from both simulations and also an analytical approach; we refer the reader to the Supplemental Material for the details of the analytics (Sec. S3, Ref. [31]). An exemplar simulation curve is presented in the inset of Fig. 3(a), and we find excellent quantitative agreement of these data with the experiments.

In order to quantify the near-wall swimming statistics, we define the near-wall swimming probability, $\Phi(r_c)$, as the relative probability of finding the alga or dumbbell towards the wall as compared to the center. In our notation, this is written as:

$$\Phi(r_c) = 1 - \frac{r_c}{r_c - b} \int_0^{r_c - b} P(r) dr, \quad (4)$$

where b is the extent of wall influence, measured from high-resolution optical micrographs of wall interaction events (see [29]) as approximately $15 \mu\text{m}$. This corresponds to approximately the length of the flagella plus one cell radius (independent of compartment size). Figure 3(b) presents $\Phi(r_c)$ for experiments and Brownian dynamics simulations, which all agree quantitatively and show a monotonic decrease for increasing compartment radius r_c .

Analysis of the temporal swimming statistics (Sec. S4, Ref. [31]) reveals that the alga spends up to several seconds within the near-wall swimming zone for the smaller compartments. For large compartments, this time becomes comparable to the characteristic wall interaction time of about 0.15 s for a single wall interaction event [29]. Note that the alga swims with a typical velocity of $100 \pm 10 \mu\text{m/s}$, in agreement with swimming velocities reported in bulk [35]. The angular swimming statistics are based on the local swimming angle, measured relative to

the local wall tangent. Within the near-wall swimming zone, this angle features a maximum around zero degrees, indicating that the wall induces a preferred swimming direction parallel to the concave interface. Note that these angular statistics represent all navigational movement of the alga near the wall, which may include any microscopic interactions the alga might have with the boundaries.

Upon interaction with an interface, the alga reorients due to its characteristic torque with the wall and scatters off at some shallow angle (see also [29]). If the compartment is sufficiently curved, the alga will encounter another section of the interface in a short time, interact, scatter off, and continue swimming. This process will repeat itself such that, for small compartments (high curvature), it appears that the alga swims nonstop parallel to the interface in a clockwise or counterclockwise direction, since the alga will encounter another interface during its characteristic persistent swimming time. In contrast, for large compartments (low curvature), the alga will travel farther before meeting another interface. Thus, it is more likely that the alga's reorientation will direct it towards the compartment center. Nonetheless, due to the confinement the alga will encounter an interface before undergoing a run-and-tumble-like motion. The simulations and analytics capture this process: using an asymmetric dumbbell model, the alga will naturally experience a torque at the interface and reorient with a finite interaction time, subsequently encountering another interface before it can "tumble." This description is confirmed by a simultaneous comparison of concave and convex interfaces by adding a central pillar to the circular chambers. The analysis of experimental and simulated trajectories show that the alga scatters off at the pillar and escapes the convex wall (Sec. S5, Ref. [31]), consistent with studies on single microscopic scattering events [29,30].

To uncouple the effects of curvature from size-dependent geometric factors, we consider elliptical chambers. Experiments [Fig. 4(a)] and Brownian dynamics

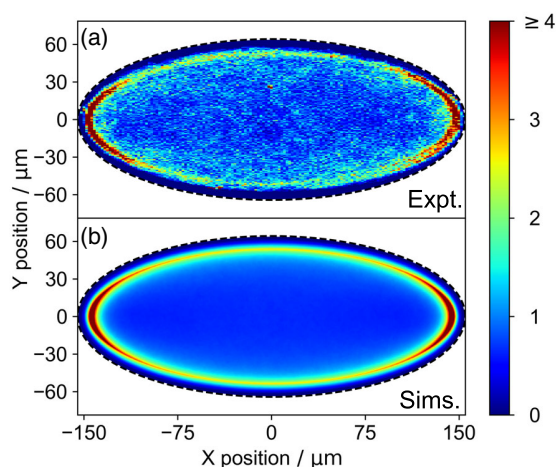


FIG. 4. Relative probability density for elliptical compartments (eccentricity = 0.91): (a) experiments and (b) simulations.

simulations [Fig. 4(b)] show a higher likelihood of finding the alga swimming in one of the apex regions of the compartments. We find in both experiments and simulations that the near-wall swimming probability density in elliptical chambers increases monotonically with the corresponding wall curvature, in line with the results obtained for circular compartments [Fig. 3(b)]. Hence, we have established unambiguous evidence that the (local) wall curvature controls the near-wall swimming effect in confinement. Note that the curvature scaling found in [38] is a consequence of assuming sliding motion along the confining surface, whereas our results derive from the dynamic action of the cell's characteristic torque at the wall due to steric wall interactions of its flagella. In contrast to the active dumbbell model, we find that a torque-free, spherical active Brownian particle cannot reproduce the experimental data. In fact, a simple active Brownian particle (e.g. [39]) strongly overestimates the magnitude of wall influence, nor does it capture the scaling with the wall curvature (Sec. S2, Ref. [31]).

In the absence of external flow, cell-cell interactions, photo- and chemotaxes, we isolated a curvature-guided motility mechanism for a single microalga in a confined microfluidic habitat with controlled geometric properties. The concave nature of the confining walls leads to an enhanced probability of near-wall swimming for puller-type microswimmers, as quantified by a statistical analysis of experimental cell trajectories. Brownian dynamics simulations based on an active asymmetric dumbbell model quantitatively capture the experiments and validate a characteristic curvature scaling of the near-wall swimming probability. The main ingredients of this curvature guidance are the torque that the alga experiences during an interaction event with the wall, the compartment's wall curvature, and the suppression of the alga's diffusive swimming regime in confinement. Hydrodynamics are not explicitly necessary to understand this swimming behavior, yet they might be required to capture the microscopic details of flagellar interactions with interfaces [29,30]. These findings provide evidence that enhanced near-wall swimming in confinement is not exclusive to microorganisms propelling themselves by rear-mounted appendages. The fact that we track the motility of a single cell allows for dissecting the fundamental physics of a puller-type microswimmer in confinement, whereas earlier studies focused on the collective behavior of bacterial suspensions in confinement, which is governed by cell-cell interactions and excluded volume effects [40–42].

These results may pave the way towards a fundamental understanding of the motility of microorganisms in their natural habitats. A consequence of enhanced detention times at a highly curved wall is a greater likelihood for the surface-association of planktonic cells at walls, which can trigger the formation of biofilms in liquid-immersed porous media. Thus, we expect that these insights are highly relevant in environmental applications, water filtration

systems, and photobioreactors [43]. We also anticipate that these insights may inspire new design principles for the guidance of cellular motion [44–47], complementary to existing rectification approaches [29].

The authors acknowledge M. Lorenz and the Algae Culture Collection (SAG) in Göttingen, Germany. We also thank S. Herminghaus for discussions, and A. Schella and D. Lavrentovich for technical assistance. F.J.S. and M.G.M. acknowledge financial support from the DFG Collaborative Research Center SFB 937 (Project A20). O.B. acknowledges support from the Joliot ESPCI Paris Chair and the Total-ESPCI Paris Chair.

T. O. and F. J. S. contributed equally to this work.

*To whom correspondence should be addressed.
oliver.baeumchen@ds.mpg.de

- [1] X. Sun, M. K. Driscoll, C. Guven, S. Das, C. A. Parent, J. T. Fourkas, and W. Losert, *Proc. Natl. Acad. Sci. U.S.A.* **112**, 12557 (2015).
- [2] H. Wu, M. Thiébaud, W.-F. Hu, A. Farutin, S. Rafai, M. C. Lai, P. Peyla, and C. Misbah, *Phys. Rev. E* **92**, 050701 (2015).
- [3] H. Jeon, S. Koo, W.M. Reese, P. Loskill, C.P. Grigoropoulos, and K.E. Healy, *Nat. Mater.* **14**, 918 (2015).
- [4] H. G. Yevick, G. Duclos, I. Bonnet, and P. Silberzan, *Proc. Natl. Acad. Sci. U.S.A.* **112**, 5944 (2015).
- [5] M. Delarue, J. Hartung, C. Schreck, P. Gniewek, L. Hu, S. Herminghaus, and O. Hallatschek, *Nat. Phys.* **12**, 762 (2016).
- [6] H. C. Berg and L. Turner, *Biophys. J.* **58**, 919 (1990).
- [7] W. Yan and J. F. Brady, *J. Fluid Mech.* **785**, R1 (2015).
- [8] R. U. Meckenstock *et al.*, *Science* **345**, 673 (2014).
- [9] J. Wierzbos, A. de los Ríos, and C. Ascaso, *Int. Microbiol.* **15**, 171 (2012).
- [10] C. K. Robinson *et al.*, *Environ. Microbiol.* **17**, 299 (2015).
- [11] L. Ranjard and A. Richaume, *Res. Microbiol.* **152**, 707 (2001).
- [12] M. Eisenbach and L. C. Giojalas, *Nat. Rev. Mol. Cell Biol.* **7**, 276 (2006).
- [13] P. Denissenko, V. Kantsler, D. J. Smith, and J. Kirkman-Brown, *Proc. Natl. Acad. Sci. U.S.A.* **109**, 8007 (2012).
- [14] V. Kantsler, J. Dunkel, M. Blayney, and R. E. Goldstein, *eLife* **3**, e02403 (2014).
- [15] R. Nosrati, A. Driouchi, C. M. Yip, and D. Sinton, *Nat. Commun.* **6**, 8703 (2015).
- [16] N. Heddergott, T. Krüger, S. B. Babu, A. Wei, E. Stellamanns, S. Uppaluri, T. Pföhl, H. Stark, M. Engstler, and S. M. Beverley, *PLoS Pathogens* **8**, e1003023 (2012).
- [17] P. Watnick and R. Kolter, *J. Bacteriol.* **182**, 2675 (2000).
- [18] L. Hall-Stoodley, J. W. Costerton, and P. Stoodley, *Nat. Rev. Microbiol.* **2**, 95 (2004).
- [19] H.-C. Flemming and J. Wingender, *Nat. Rev. Microbiol.* **8**, 623 (2010).
- [20] M. G. Mazza, *J. Phys. D* **49**, 203001 (2016).
- [21] E. Lauga and T. R. Powers, *Rep. Prog. Phys.* **72**, 096601 (2009).
- [22] T. Brotto, J.-B. Caussin, E. Lauga, and D. Bartolo, *Phys. Rev. Lett.* **110**, 038101 (2013).
- [23] J. Elgeti, R. G. Winkler, and G. Gompper, *Rep. Prog. Phys.* **78**, 056601 (2015).
- [24] K. Drescher, J. Dunkel, L. H. Cisneros, S. Ganguly, and R. E. Goldstein, *Proc. Natl. Acad. Sci. U.S.A.* **108**, 10940 (2011).
- [25] K. Drescher, R. E. Goldstein, N. Michel, M. Polin, and I. Tuval, *Phys. Rev. Lett.* **105**, 168101 (2010).
- [26] J. S. Guasto, K. A. Johnson, and J. P. Gollub, *Phys. Rev. Lett.* **105**, 168102 (2010).
- [27] K. C. Leptos, J. S. Guasto, J. P. Gollub, A. I. Pesci, and R. E. Goldstein, *Phys. Rev. Lett.* **103**, 198103 (2009).
- [28] E. Lushi, V. Kantsler, and R. E. Goldstein, *Phys. Rev. E* **96**, 023102 (2017).
- [29] V. Kantsler, J. Dunkel, M. Polin, and R. E. Goldstein, *Proc. Natl. Acad. Sci. U.S.A.* **110**, 1187 (2013).
- [30] M. Contino, E. Lushi, I. Tuval, V. Kantsler, and M. Polin, *Phys. Rev. Lett.* **115**, 258102 (2015).
- [31] See Supplemental Material at <http://link.aps.org/supplemental/10.1103/PhysRevLett.120.068002> for further details on the experimental methods and Brownian dynamics simulations, including the temporal and angular statistics of near-wall swimming and motility in compartments exhibiting concave and convex interfaces. The Supplemental Material also contains the derivation and details of an analytical model, a movie of a typical experiment, as well as Refs. [32–34].
- [32] J. C. Crocker and D. G. Grier, *J. Colloid Interface Sci.* **179**, 298 (1996).
- [33] S. E. Spagnolie, G. R. Moreno-Flores, D. Bartolo, and E. Lauga, *Soft Matter* **11**, 3396 (2015).
- [34] D. Takagi, J. Palacci, A. B. Braunschweig, M. J. Shelley, and J. Zhang, *Soft Matter* **10**, 1784 (2014).
- [35] M. Polin, I. Tuval, K. Drescher, J. P. Gollub, and R. E. Goldstein, *Science* **325**, 487 (2009).
- [36] A. Wysocki, J. Elgeti, and G. Gompper, *Phys. Rev. E* **91**, 050302(R) (2015).
- [37] J. D. Weeks, D. Chandler, and H. C. Andersen, *J. Chem. Phys.* **54**, 5237 (1971).
- [38] Y. Fily, A. Baskaran, and M. F. Hagan, *Soft Matter* **10**, 5609 (2014).
- [39] S. E. Spagnolie, C. Wahl, J. Lukasiak, and J.-L. Thiffeault, *Physica (Amsterdam)* **341D**, 33 (2017).
- [40] H. Wioland, F. G. Woodhouse, J. Dunkel, J. O. Kessler, and R. E. Goldstein, *Phys. Rev. Lett.* **110**, 268102 (2013).
- [41] I. D. Vladescu, E. J. Marsden, J. Schwarz-Linek, V. A. Martinez, J. Arlt, A. N. Morozov, D. Marenduzzo, M. E. Cates, and W. C. K. Poon, *Phys. Rev. Lett.* **113**, 268101 (2014).
- [42] E. Lushi, H. Wioland, and R. E. Goldstein, *Proc. Natl. Acad. Sci. U.S.A.* **111**, 9733 (2014).
- [43] P. M. Schenk, S. R. Thomas-Hall, E. Stephens, U. C. Marx, J. H. Mussnug, C. Posten, O. Kruse, and B. Hankamer, *Bioenergy Res.* **1**, 20 (2008).

- [44] D. B. Weibel, P. Garstecki, D. Ryan, W. R. DiLuzio, M. Mayer, J. E. Seto, and G. M. Whitesides, *Proc. Natl. Acad. Sci. U.S.A.* **102**, 11963 (2005).
- [45] X. Ai, Q. Liang, M. Luo, K. Zhang, J. Pan, and G. Luo, *Lab Chip* **12**, 4516 (2012).
- [46] S. K. Min, G. H. Yoon, J. H. Joo, S. J. Sim, and H. S. Shin, *Sci. Rep.* **4**, 4675 (2014).
- [47] S. Das, A. Garg, A. I. Campbell, J. Howse, A. Sen, D. Velegol, R. Golestanian, and S. J. Ebbens, *Nat. Commun.* **6**, 8999 (2015).

4.2 *Supplemental Material to Publication: Curvature-Guided Motility of Microalgae in Geometric Confinement*

Supplemental Material:

Curvature-guided motility of microalgae in geometric confinement

Tanya Ostapenko,¹ Fabian Jan Schwarzendahl,^{1,2} Thomas J. Bøddeker,¹
Christian Titus Kreis,^{1,2} Jan Cammann,¹ Marco G. Mazza,¹ and Oliver Bäumchen^{a1}

¹*Max Planck Institute for Dynamics and Self-Organization (MPIDS),*

Am Faßberg 17, D-37077 Göttingen, Germany.

²*Georg-August-Universität Göttingen, Friedrich-Hund-Platz 1, D-37077 Göttingen, Germany.*

^a oliver.baumchen@ds.mpg.de

S1. EXPERIMENTAL METHODS

Cell Cultivation

Cultures of wild-type *Chlamydomonas reinhardtii* (SAG 11-32b) were cultivated axenically in Tris-Acetate-Phosphate (TAP) medium on a 12 h–12 h day-night cycle, with daytime temperature of 24 °C and nighttime temperature of 22 °C in a Memmert IPP 100Plus incubator. The daytime light intensity was held at 1000–2000 Lux, and reduced to 0% during the night. All experiments were performed at the same time in the cell’s life cycle in order to ensure consistency in the cell’s size and behavior. In preparation for experiments, 15 mL of cell suspension were centrifuged for 10 minutes at 100 *g* at room temperature; 10–13 mL of solution were subsequently removed and the remaining 2–5 mL suspension was allowed to relax for 60–90 minutes. This suspension was diluted with room temperature TAP to enhance the likelihood for capturing precisely one cell in an isolated microcompartment.

Microfluidics

Arrays of stand-alone (i.e. no inlet or outlet) circular microfluidic compartments with a height of 20 μm were created using standard PDMS-based soft lithography techniques in a cleanroom. Additional experiments were conducted with circular compartments containing a pillar located at the center of the compartment, as well as elliptical chambers. Prior to experiments, both the PDMS device and a glass microscope slide were cleaned using air plasma (Electronic Diener Pico plasma system, 100% exposure, 30 seconds). After plasma cleaning, a small amount of 8wt% polyethelyne glycol was gently rinsed over both surfaces to prevent adhesion of the alga to the surfaces. After placing a droplet of the diluted algal suspension onto the feature side of the PDMS, the glass slide was placed on top and gently pressed to seal the compartment. Only compartments containing precisely one cell were used for experiments.

Microscopy

Cell imaging was conducted using an Olympus IX-81 inverted microscope contained in a closed box on a passive anti-vibration table with an interference bandpass filter ($\lambda \geq$

671 nm, full-width-half-maximum of 10 nm) in order to avoid any photoactive response of the cell. Videos ranging from 5-30 minutes were recorded using a Canon 600D camera at a frame rate of 24 frames per second at full resolution (1920 px \times 1080 px). This corresponds to approximately 7×10^3 – 40×10^3 total trajectory points for a single experiment. The single-cell experiments were repeated 2–10 times for each compartment size, corresponding to 35×10^3 – 120×10^3 total trajectory points.

Image Processing and Particle Tracking

The videos were sequenced into 8-bit grayscale images with improved contrast using custom-made MATLAB algorithms. The compartment boundaries were manually defined in order to denote the region of interest, as well as the compartment's center, for particle tracking. Two-dimensional particle detection was performed using algorithms written for colloidal systems; particle tracking was subsequently done in MATLAB based on tracking algorithms developed by Crocker and Grier [1].

Data Analysis

Mean-squared displacements (MSD) were extracted using a custom-made MATLAB script, based on trajectories containing a minimum of 7×10^3 – 14×10^3 data points for the $r_c = 25 - 250 \mu\text{m}$ and at least 40×10^3 data points for the $r_c = 500 \mu\text{m}$. This corresponds to MSD curves containing 2×10^3 – 10×10^3 points each.

A custom-made MATLAB algorithm based on a pixel grouping method for the data binning was applied to the trajectory data to compute the relative probability density heat maps by $c(x, y) = n_{\text{bin}} / (A_{\text{frac}} \sum n_{\text{bin}})$, where n_{bin} is the number of trajectory points within bin area A_{bin} , and $A_{\text{frac}} = A_{\text{bin}} / A_{\text{chamber}}$ is a geometric normalization factor. The radial probability densities $P(r)$ of the alga's distance r from the center of the compartment were calculated using Eq. 1 (main text) such that $\int_0^{r_c} P(r) dr = 1$. We define the near-wall swimming probability as in Eq. 2 (main text).

S2. STOCHASTIC BROWNIAN DYNAMICS SIMULATIONS

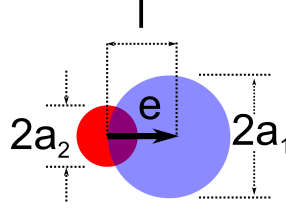


FIG. S1. Asymmetric dumbbell model representing the *Chlamydomonas* alga. The smaller sphere (radius a_2) represents the cell's body, and the larger sphere (radius a_1) mimics the stroke-averaged area covered by the beating flagella.

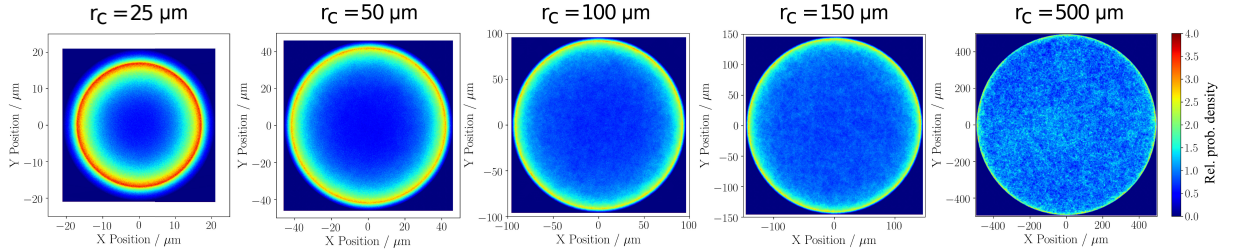


FIG. S2. (Color online) Relative probability density in confinement from Brownian dynamics simulations. The heat maps indicate the cell position for the same circular compartment sizes as in experiments: (L–R) $r_c = 25 \mu\text{m}$, $r_c = 50 \mu\text{m}$, $r_c = 100 \mu\text{m}$, $r_c = 150 \mu\text{m}$, $r_c = 500 \mu\text{m}$.

The force acting on the dumbbell at the wall is given by $\vec{F}_w = \vec{F}_1 + \vec{F}_2$ with $\vec{F}_\alpha = -\vec{\nabla}U_\alpha(r)$, $\alpha = 1, 2$. We use the Weeks–Chandler–Anderson repulsive potential $U_\alpha(d)/(k_B T) = 4\epsilon \left[\left(\frac{a_\alpha}{d}\right)^{12} - \left(\frac{a_\alpha}{d}\right)^6 \right] + \epsilon$, if $d < 2^{1/6}a_\alpha$, and 0 otherwise, where d is the distance of the sphere $\alpha \in \{1, 2\}$ to the wall of the compartment, $a_1 = 5 \mu\text{m}$, $a_2 = 2.5 \mu\text{m}$ are the radii of the spheres (see Fig. S1) and $\epsilon = 10$ is chosen to achieve a strong screening. The values for a_1 and a_2 were extracted from high-speed, high-resolution optical micrographs of *Chlamydomonas*.

The torque is given by $\vec{T}_w = \vec{T}_1 + \vec{T}_2$ where $\vec{T}_1 = (\vec{r}_1 - \vec{r}) \times \vec{F}_1 = l(\vec{e} \times \vec{F}_1)/2$, $\vec{T}_2 = -l(\vec{e} \times \vec{F}_2)/2$, and $l = 5 \mu\text{m}$. The position \vec{r} of the dumbbell's center of mass has the following equation of motion $\frac{d\vec{r}}{dt} = v_0\vec{e} + \mu_w\vec{F}_w + \vec{\eta}$. Here, \vec{F}_w is the steric wall interaction and $\vec{\eta}$ is a Gaussian white noise with zero mean and $\langle \vec{\eta}(t)\vec{\eta}(t') \rangle = 2k_B T \mu_w \mathbf{1}\delta(t - t')$. We use $v_0 = 100 \mu\text{m/s}$ and $k_B T \mu_w = 250 \mu\text{m}^2/\text{s}$, both based on experimental measurements.

Furthermore, the cell swims in the direction \vec{e} represented by a versor (a unit vector) pointing from the second to the first sphere (see Fig. S1). The orientational equation of motion is $\frac{d\vec{e}}{dt} = (\vec{T}_w/\tau_w + \vec{\xi}) \times \vec{e}$, where \vec{T}_w is the torque acting at the wall and $\vec{\xi}$ is a Gaussian white noise with $\langle \vec{\xi}(t)\vec{\xi}(t') \rangle = \frac{2k_B T}{\tau_p} \mathbf{1}\delta(t-t')$. Note that the shear time at the wall $\frac{\tau_w}{k_B T} = 0.15$ s (extracted from [2]) and the persistence time $\frac{\tau_p}{k_B T} = 2$ s (also taken from [2]) of synchronous flagella beating are not connected *via* the fluctuation-dissipation theorem. This is motivated by the fact that the tumble time is associated with the active motion of the cell, whereas the shear time is connected to the interactions between wall and cell.

The tumbling motion is explicitly included as follows: the cell is instantaneously reoriented with a relative angle ϕ_{tumble} , where ϕ_{tumble} is selected from a Gaussian distribution with a mean of $\frac{\pi}{2}$ and standard deviation of 0.1. The time between tumbling events, t_{tumble} , is sampled from an exponential distribution, with mean $\frac{\tau_p}{k_B T}$.

Figure S2 presents the relative probability density from our simulations of the model alga's position for different compartments.

Microscopic Scattering Angle Distribution in Simulations

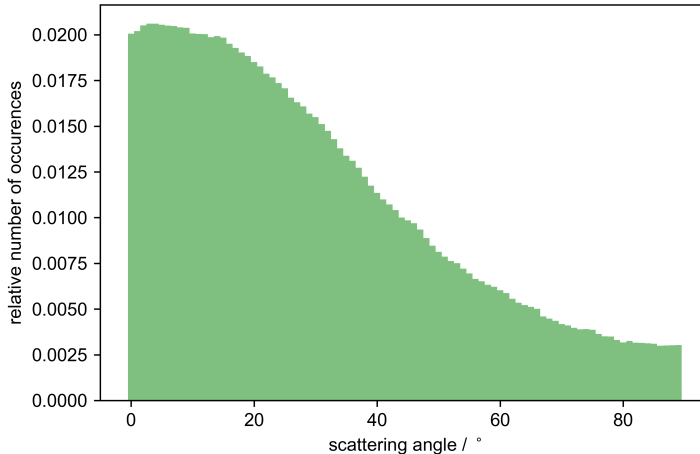


FIG. S3. Distribution of scattering angles from the dumbbell model. Values were taken at a distance of (20 ± 2.5) μm away from the wall, after the dumbbell scattered off to ensure that the dumbbell is no longer in contact with the wall and has completed the turning process.

Our simulated system quantitatively reproduces the maximum of the microscopic scat-

tering angle distribution, found experimentally in [2] (Fig. S3). To measure the scattering angle in the simulations, the active dumbbell was confined within a straight channel, with solid walls in the y -direction and periodic boundary conditions in the x -direction. After each scattering event off the wall, the angle spanned by the x -axis and the swimming direction was recorded. This was done for a channel of width $300 \mu\text{m}$. The scattering angle was recorded when the cell was separated by a distance of $(20 \pm 2.5) \mu\text{m}$ from the wall. This distance was chosen to directly compare with experimental values from [2], where the authors considered a distance of $20 \mu\text{m}$ from the wall, and also to make sure the dumbbell scattered off the wall and swam freely. These measurements yield the angle distribution shown in Fig. S3, with a maximum for the scattering angle of $\sim 18^\circ$, which is in agreement with the experimental value reported in [2].

Torque-Free Active Brownian Particle in Simulations

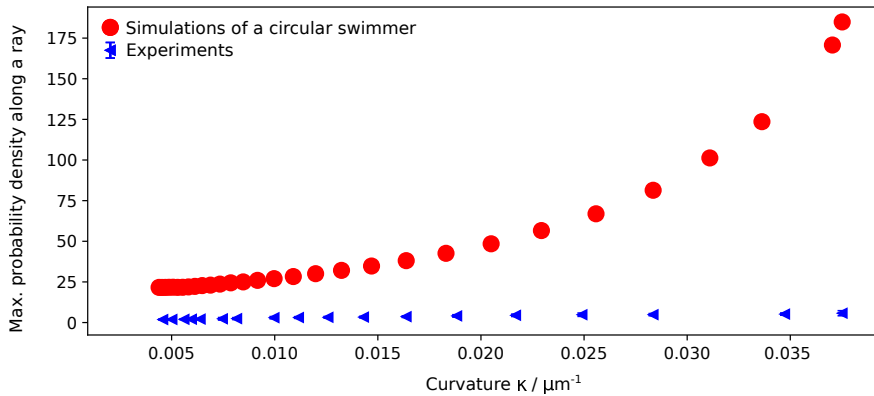


FIG. S4. (Color online) Probability density of a torque-free active Brownian particle in an elliptical compartment. Simulations were performed for a circular active Brownian particle, for which torque is absent during interaction with the compartment wall. The elliptical compartment has an eccentricity = 0.91 and a total area of $A_{tot} = 31316.7 \mu\text{m}^2$ (see also Fig. 4). The figure displays the maximum probability density close to the wall as a function of the local wall curvature. Compared to the experiments and the dumbbell model, a circular swimmer exhibits a much larger probability to be located near the wall, and a non-linear dependence on curvature. The torque that the active dumbbell model experiences during wall interactions is an essential ingredient in order to capture the experimental data (see Fig. 4 in main text).

S3. ANALYTICAL MODEL

The equations of motion for the analytical model are the same as for the Brownian dynamics simulations

$$\frac{d\vec{r}}{dt} = v_0\vec{e} + \mu_w\vec{F}_w + \vec{\eta}, \quad (\text{S1})$$

$$\frac{d\vec{e}}{dt} = (\vec{T}_w/\tau_w + \vec{\xi}) \times \vec{e}. \quad (\text{S2})$$

First, we assume that the total force \vec{F}_w is now in \hat{r} direction, with

$$\vec{F}_w = -(f_1(r) + f_2(r))\hat{r},$$

where $f_1(r)$ and $f_2(r)$ are the absolute values of the forces of first and second sphere respectively. We now change to polar coordinates (r, φ) , where r is the distance of the cell from the center of the compartment and φ the polar angle of its position vector. Furthermore, the unit vector \vec{e} is represented by the angle θ . Equation (S1) becomes

$$\frac{dr}{dt} = v_0\cos(\theta - \varphi) - \mu_w(f_1(r) + f_2(r)) + \eta_r.$$

The torque is defined as in the simulation as $\vec{T}_w = \vec{T}_1 + \vec{T}_2$, where $\vec{T}_1 = (\vec{r}_1 - \vec{r}) \times \vec{F}_1 = l(\vec{e} \times \vec{F}_1)/2$ and $\vec{T}_2 = -l(\vec{e} \times \vec{F}_2)/2$. Using the relation $(\vec{e} \times \hat{r}) \times \hat{r} = \sin(\theta - \varphi)\hat{r}$, equation (S2) becomes

$$\frac{d\theta}{dt} = \frac{l}{2\tau_w}(f_2(r) - f_1(r))\sin(\theta + \varphi) + \xi.$$

Since the system is symmetric in φ , we neglect the dependence on φ and choose $\varphi = 0$. We obtain the following equations

$$\begin{aligned} \frac{dr}{dt} &= v_0\cos(\theta) - \mu_w(f_1(r) + f_2(r)) + \eta_r, \\ \frac{d\theta}{dt} &= \frac{l}{2\tau_w}(f_2(r) - f_1(r))\sin(\theta) + \xi. \end{aligned}$$

The Fokker-Planck equation of this system reads

$$\begin{aligned} \partial_t p(t, r, \theta) &= -\frac{1}{r}\partial_r [r(v_0\cos\theta - \mu_w(f_1(r) + f_2(r)) - \mu_w\partial_r)p(t, r, \theta)] \\ &\quad - \partial_\theta \left[\left(\frac{l}{2\tau_w}(f_2(r) - f_1(r))\sin(\theta) - \frac{1}{\tau_p}\partial_\theta \right) p(t, r, \theta) \right]. \end{aligned}$$

From this, we compute effective hydrodynamic equations by taking the following averages

$$\begin{aligned}\rho_r(t, r) &= \int_0^{2\pi} p(t, r, \theta) d\theta, \\ \rho_\theta(t, r) &= \int_0^{2\pi} \cos(\theta) p(t, r, \theta) d\theta,\end{aligned}$$

neglecting higher order contributions, this approach gives the following two equations

$$\begin{aligned}\partial_t \rho_r &= -\frac{1}{r} \partial_r [r (v_0 \rho_\theta - \mu_w (f_1(r) + f_2(r)) \rho_r - \mu_w \partial_r \rho_r)], \\ \partial_t \rho_\theta &= \frac{1}{r} \partial_r \left[r \left(\mu_w (f_1(r) + f_2(r)) \rho_\theta - \frac{v_0}{2} \rho_r + \mu_w \partial_r \rho_\theta \right) \right] - \frac{1}{\tau_p} \rho_\theta \\ &\quad + \left[\frac{l}{2\tau_w} (f_2(r) - f_1(r)) \right] \rho_r.\end{aligned}$$

Here, ρ_r corresponds to the density and ρ_θ to the polarization of the particle. We now try to find stationary solutions of these

$$\begin{aligned}0 &= -\frac{1}{r} \partial_r [r (v_0 \rho_\theta - \mu_w (f_1(r) + f_2(r)) \rho_r - \mu_w \partial_r \rho_r)], \\ 0 &= \frac{1}{r} \partial_r \left[r \left(\mu_w (f_1(r) + f_2(r)) \rho_\theta - \frac{v_0}{2} \rho_r + \mu_w \partial_r \rho_\theta \right) \right] - \frac{1}{\tau_p} \rho_\theta \\ &\quad + \left[\frac{l}{2\tau_w} (f_2(r) - f_1(r)) \right] \rho_r.\end{aligned}$$

The first equation can be solved for ρ_θ :

$$\rho_\theta = \frac{\mu_w}{v_0} [(f_1(r) + f_2(r)) + \partial_r] \rho_r + \frac{C_1}{r}.$$

The constant C_1 is determined by the boundary condition. To find the correct boundary condition we consider the probability flux of the original Fokker-Planck equation:

$$\vec{J} = \begin{pmatrix} -(v_0 \cos \theta - \mu_w (f_1(r) + f_2(r)) - \mu_w \partial_r) p(t, r, \theta) \\ - \left(\frac{l}{2\tau_w} (f_2(r) - f_1(r)) \sin(\theta) - \frac{1}{\tau_p} \partial_\theta \right) p(t, r, \theta) \end{pmatrix}$$

The radial part of the flux for ρ_θ , is then given by:

$$\begin{aligned}J_{r, \rho_\theta} &= - \int_0^{2\pi} \cos \theta (v_0 \cos \theta - \mu_w (f_1(r) + f_2(r)) - \mu_w \partial_r) p(t, r, \theta) \\ &= \mu_w (f_1(r) + f_2(r)) \rho_\theta - \frac{v_0}{2} \rho_r + \mu_w \partial_r \rho_\theta\end{aligned}$$

The flux should vanish at the boundary $\vec{J} \cdot \vec{n} = 0$, such that C_1 is determined by:

$$\left[\mu_w (f_1(r) + f_2(r)) \rho_\theta - \frac{v_0}{2} \rho_r + \mu_w \partial_r \rho_\theta \right]_{r=r_c} = 0.$$

In the following we will neglect diffusion, which is justified by Fig. 1(c) in the main text. Hence we continue to treat the following equations:

$$\begin{aligned} 0 &= \frac{1}{r} \partial_r \left[r \left(\mu_w (f_1(r) + f_2(r)) \rho_\theta - \frac{v_0}{2} \rho_r \right) \right] + \left[\frac{l}{2\tau_w} (f_2(r) - f_1(r)) \right] \rho_r, \\ \rho_\theta &= \frac{\mu_w}{v_0} [(f_1(r) + f_2(r))] \rho_r + \frac{C_1}{r}, \\ \left[\mu_w (f_1(r) + f_2(r)) \rho_\theta - \frac{v_0}{2} \rho_r \right]_{r=r_c} &= 0. \end{aligned} \quad (\text{S3})$$

To solve the equations (S3) we need to specify a model for the cell-wall interaction. For the sake of analytical treatability, we choose exponential repulsive forces

$$f_i(r) = \frac{U_0}{\lambda} \exp \left[\frac{r - (r_c - a_i)}{\lambda} \right],$$

where a_i , $i = 1, 2$, are the sizes of the spheres, r_c is the size of the compartment, U_0 is the strength of the interaction potential, and λ is the associated interaction length scale. Furthermore, we define $A_+ = \frac{U_0}{\lambda} [e^{-\frac{(r_c - a_1)}{\lambda}} + e^{-\frac{(r_c - a_2)}{\lambda}}]$ and $A_- = \frac{U_0}{\lambda} [e^{-\frac{(r_c - a_2)}{\lambda}} - e^{-\frac{(r_c - a_1)}{\lambda}}]$. Combining the first two equations (S3) and performing a coordinate transformation $z = e^{-\frac{r}{\lambda}}$ yields:

$$\left(1 - \frac{v_0^2}{2\mu_w^2 A_+^2} z^2 \right) \partial_z \rho_r(z) + \left(\frac{1}{z \ln(z)} - \frac{1}{z} - \frac{v_0 \lambda A_- l}{2\tau_w \mu_w^2 A_+^2} - \frac{z}{\ln(z)} \frac{v_0^2}{\mu_w^2 A_+^2} \right) \rho_r + \frac{1}{\ln(z)} \frac{C_1 v_0}{\mu_w A_+} = 0.$$

The terms $-\frac{v_0^2}{2\mu_w^2 A_+^2} z^2$ and $\frac{z}{\ln(z)} \frac{v_0^2}{\mu_w^2 A_+^2}$ are of higher order in z and only give a contribution for $r \ll 1$. Therefore these can safely be neglected and we have to solve the equation:

$$\partial_z \rho_r(z) + \left(\frac{1}{z \ln(z)} - \frac{1}{z} - \frac{v_0 \lambda A_- l}{2\tau_w \mu_w^2 A_+^2} \right) \rho_r + \frac{1}{\ln(z)} \frac{C_1 v_0}{\mu_w A_+} = 0.$$

The solution of this equation is

$$\rho_r(z) = \frac{e^{\alpha z} z^2}{\ln(z)} \left(C_2 + \frac{C_1 v_0}{\mu_w A_+} \left[\frac{e^{-\alpha z}}{z} + \alpha \text{Ei}(-\alpha z) \right] \right)$$

where $\alpha = \frac{v_0 \lambda A_-}{2\tau_w \mu_w^2 A_+^2}$ and Ei is the exponential integral, defined by:

$$\text{Ei}(z) = \int_{-z}^{\infty} \frac{e^t}{t} dt.$$

C_1 and C_2 are determined from the following boundary conditions:

$$\begin{aligned} \left[\mu_w (f_1(r) + f_2(r)) \rho_\theta - \frac{v_0}{2} \rho_r \right]_{r=r_c} &= 0, \\ \int_0^{r_c} r \rho_r(r) &= 1, \end{aligned}$$

which are in terms of z :

$$\left[\frac{\mu_w^2 A_+^2}{v_0} \frac{1}{z^2} \rho_r - \frac{\mu_w A_+ C_1}{\lambda} \frac{1}{z \ln(z)} - \frac{v_0}{2} \rho_r \right]_{z=z(r_c)} = 0,$$

$$\int_1^{z(r_c)} \lambda^2 \frac{\ln(z)}{z} \rho_r(z) dz = 1.$$

Furthermore the following indefinite integral is needed:

$$\int \lambda^2 \frac{\ln(z)}{z} \rho_r(z) dz = \lambda^2 \left[C_2 e^{\alpha z} \left(-\frac{1}{a^2} + \frac{z}{a} \right) + \frac{C_1 v_0}{\mu_w A_+ a} (\ln(z) + (\alpha z - 1) e^{\alpha z} \text{Ei}(-\alpha z)) \right].$$

The radial probability density is then given by $P(r) = r \rho_r(z(r))$ and is shown below in Fig. S5. For both plots, we used $U_0 = 0.12 k_b T$ and $\lambda = 3.75 \mu\text{m}$ as best fits for the strength of the interaction potential and the interaction length, respectively.

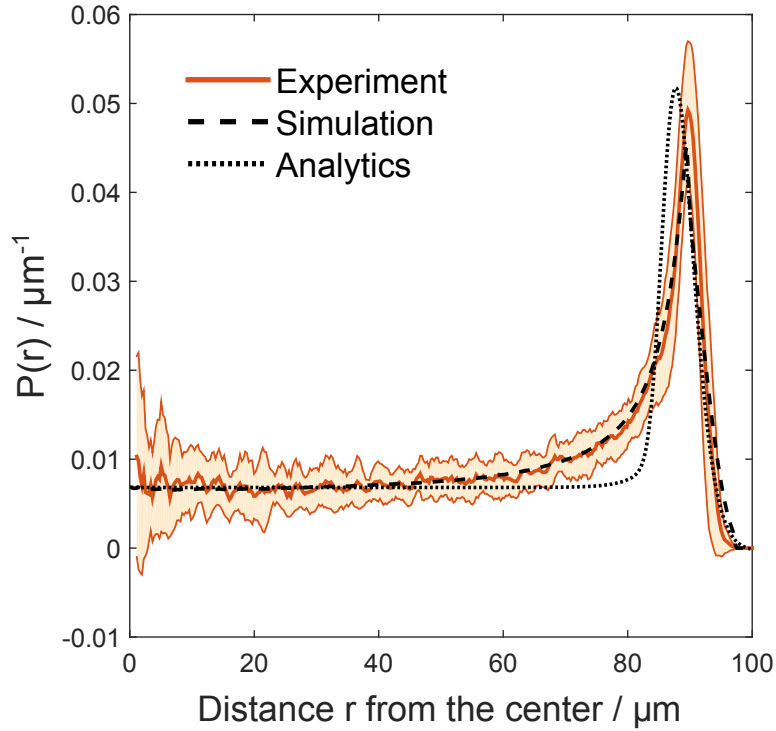


FIG. S5. (Color online) Comparison of experiment, simulation, and analytics for a compartment radius r_c of $100 \mu\text{m}$.

S4. TEMPORAL AND ANGULAR STATISTICS OF NEAR-WALL SWIMMING

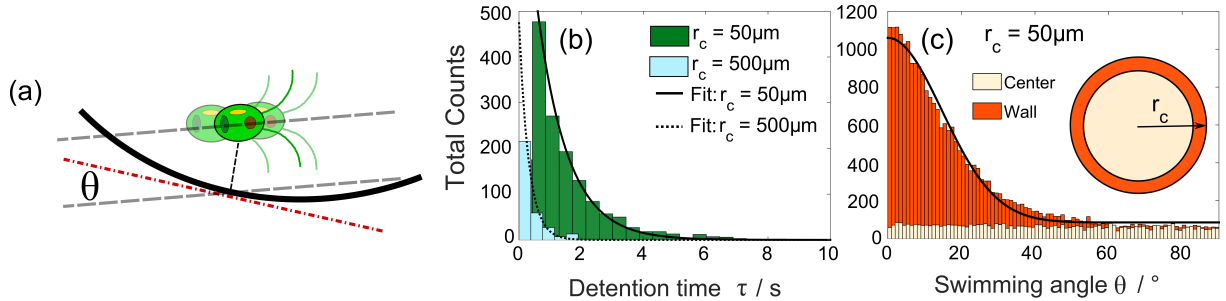


FIG. S6. (Color online) Statistics of near-wall swimming. (a) Schematic illustration of the swimming angle with respect to the wall tangent. (b) Detention time distributions for swimming near the concave interface for $r_c = 50 \mu\text{m}$ and $r_c = 500 \mu\text{m}$. (c) Experimental swimming angle distributions for $r_c = 50 \mu\text{m}$ near and far (“center”) from the wall of the compartment. The inset illustrates the definition of “wall” and “center” for the purposes of the distributions.

We define the wall detention time τ as the time that the alga spends within the near-wall swimming zone (distance b from the wall). As depicted in Fig. S6(b), the distribution of experimental detention times exhibits a maximum at approximately $\tau_{\text{max}} = 0.5 \text{ s}$ for $r_c = 50 \mu\text{m}$, featuring an exponential decay e^{-t/τ^*} towards longer detention times with a decay time of $\tau^* = 1 \text{ s}$. For larger compartments, the maxima of the detention time distributions are shifted to shorter times and the decay times are also significantly reduced (see Fig. S6(b)): $\tau_{\text{max}} < 0.2 \text{ s}$ and $\tau^* = 0.3 \text{ s}$ are found for $r_c = 500 \mu\text{m}$, indicating that the wall detention time becomes comparable to the typical interaction time reported for flat interfaces [2].

Since the cell has a non-zero velocity at all times during experiments, these results imply that the alga tends to spend more time swimming near the interface in smaller compartments than for larger ones. However, the alga’s detention time at the interface does not yield any information about the directionality of the alga’s swimming. It also does not allow us to distinguish between two possible extreme cases: (i) the alga probes the wall repeatedly at the same location, eventually escaping the interface after some time, and (ii) the alga swims non-stop either clock- or counterclockwise along the curved interface.

In order to characterize the swimming direction, we analyzed the local swimming angle θ (see Fig. S6(a)), which is measured relative to the local wall tangent. We consider two

regions in the compartment: “wall” and “center” (see Fig. S6(c) inset). As discussed above, the near-wall region is defined from a distance b from the interface for all compartment sizes. All trajectories outside this region contribute to the swimming angle distribution towards the center of the compartment. As shown in Fig. S6(c), we find that θ displays an isotropic distribution towards the center of the compartment. However, within the near-wall swimming zone, θ shows a maximum around zero swimming angle, indicating that the wall induces a preferred swimming direction parallel to the concave interface. The distribution decays towards larger angles in line with Gaussian statistics (standard deviation 12° , solid line in Fig. S6(c)). Note that these experimental distributions represent all navigational movement of the alga, which may include any microscopic interactions the alga might have with the compartment boundaries.

S5. MOTILITY IN COMPARTMENTS EXHIBITING CONCAVE AND CONVEX INTERFACES

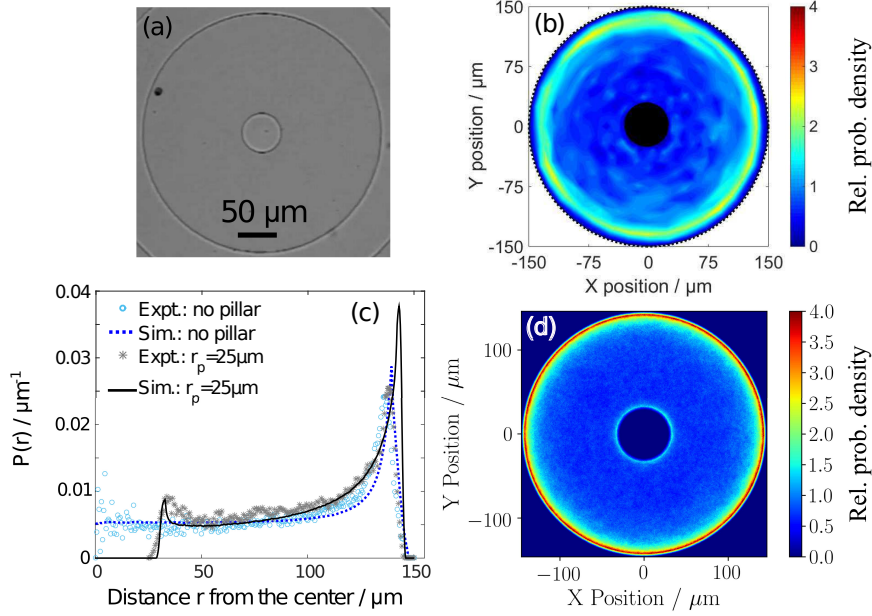


FIG. S7. (Color online) Motility in circular compartments containing a central pillar. (a) An exemplar image from an experiment for compartment radius $r_c = 150 \mu\text{m}$ and pillar radius $r_p = 25 \mu\text{m}$. The relative probability density heat maps for experiment (b) and simulations (d) show an increased relative probability at the concave interface, as compared to the rest of the compartment, consistent with what we observed for circular compartments without a central pillar. (c) The radial probability density $P(r)$ for experiments (symbols) and simulations (lines) with and without a central pillar. In the presence of a pillar, $P(r)$ slightly increases at the convex wall. This effect can be attributed to a finite interaction time of the alga at the pillar, in accordance with the previously reported transition between an incoming flagellar contact regime and an outgoing hydrodynamic regime [6].

The results described in the main text suggest that the alga may not remain swimming near the convex interface of a cylindrical obstacle, in contrast to pusher-type swimmers, e.g. bacteria [4] and spermatozoa [5]. An alga contained in a circular compartment including a central pillar establishes a simultaneous comparison between the behavior at concave and convex interfaces within the same compartment. The analysis of experimental and simulated trajectories (see Fig. S7) show that the alga scatters off at the pillar and escapes the convex

wall. This observation is consistent with studies on single microscopic scattering events at flat [2] and convex [6] interfaces. We also note that $P(r)$ in the vicinity of the convex pillar interface is slightly increased as compared to the value of $P(r)$ away from any walls (see Fig. S7), which can be attributed to the alga's finite interaction time at the interface.

REFERENCES: SUPPLEMENTAL MATERIAL

- [1] J. C. Crocker, D. G. Grier, *J. Colloid Interface Sci.* **179**, 298–310 (1996).
- [2] V. Kantsler, J. Dunkel, M. Polin, R. E. Goldstein, *Proc. Natl Acad. Sci. USA* **110**, 1187–1192 (2013).
- [3] M. Polin, I. Tuval, K. Drescher, J. P. Gollub, R. E. Goldstein, *Science* **325**, 487–490 (2009).
- [4] S. E. Spagnolie, G. R. Moreno-Flores, D. Bartolo, E. Lauga, *Soft Matter* **11**, 3396–3411 (2015).
- [5] D. Takagi, J. Palacci, A. B. Braunschweig, M. J. Shelley, J. Zhang, *Soft Matter* **10**, 1784–1789 (2014).
- [6] M. Contino, E. Lushi, I. Tuval, V. Kantsler, M. Polin, *Phys. Rev. Lett.* **115**, 258102 (2015).

Chapter 5

Implications of hydrodynamics on microswimmer dynamics

The scientific literature of active swimmers reflects the young age of the field with its explosive growth and fierce debates. Interestingly, and sometimes maddeningly, opposing claims are made on the relevance of hydrodynamic interactions in very similar setups. Thus, to understand these phenomena it is important to disentangle effects due the different interactions, such as hydrodynamics and steric effects between microswimmers.

To tackle this task from a theoretical point of view it is essential to have a model microswimmer that includes all relevant degrees of freedom. In the recent years a number of models have been proposed like the shape-anisotropic raspberry swimmer [129–131], the force-counterforce model [14, 132–134], the catalytic dimers [135], the squirmer model [70–72, 74, 75, 136–149], or other hydrodynamic models [14, 150–152, 152, 153]. We will now discuss the squirmer and force-counterforce model, as they are the most prominent in the literature.

The squirmer model, first introduced by [136], imposes a velocity field on the surface of the swimmer given by

$$\mathbf{v}_s = \frac{3}{2}v_0(1 + \beta\mathbf{e} \cdot \hat{\mathbf{r}}_s)[(\mathbf{e} \cdot \hat{\mathbf{r}}_s)\hat{\mathbf{r}}_s - \mathbf{e}], \quad (5.1)$$

where \mathbf{e} is the squirmer's orientation, $\hat{\mathbf{r}}_s$ is the unit vector connecting the center of the

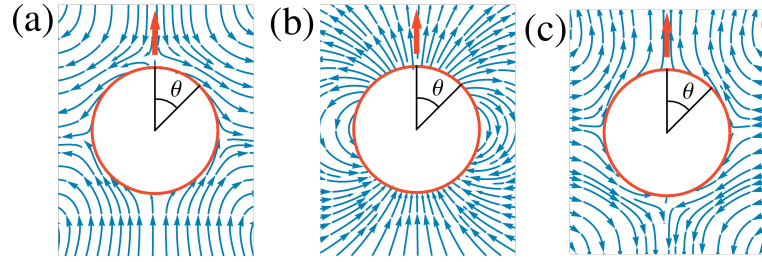


FIGURE 5.1: (a) Puller-type squirmer with $\beta = 5$, (b) neutral squirmer, (c) pusher-type squirmer with $\beta = -5$ [13].

squirmer to the surface, v_0 is the self-propulsion velocity and β is a tunable parameter used to switch between a neutral, pusher, or puller-type squirmer. Figure 5.1 shows the resulting flow fields in the lab frame of a puller [Fig. 5.1(a)], neutral [Fig. 5.1(b)], or pusher-type squirmer [Fig. 5.1(c)]. This model has also been extended to a spheroidal shape, but constructing more general shapes is not straightforward.

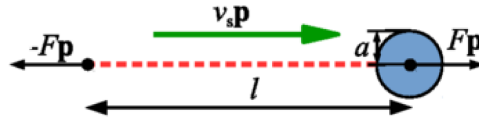


FIGURE 5.2: The force-counterforce model: one force acts on the spherical body, the second force on the fluid. Reprinted with permission from [14] Copyright 2010 by the American Physical Society.

The force-counterforce model [14, 132–134] is motivated by the dipolar flow field of an *Escherichia coli* cell (see also Sec. 2.1.3). Figure 5.2 shows the setup of the force-counterforce model. One force pole is placed on the spherical swimmer body and the other force pole is acting on the fluid. Usually only hydrodynamic interactions are considered here and no excluded volume effects are resolved.

In Sec. 5.1 we propose a novel model, that takes into account the polar nature of the flow fields and the shape anisotropy of microswimmers. As we have shown in Sec.4.1 the anisotropic shape has vast implications on the motility of *Chlamydomonas reinhardtii*. Having this in mind, we continue using the stroke-averaged model and add the force pole structure that was measured experimentally (see also Sec.2.1.3). Using this model, we study the nonequilibrium phase behavior of microswimmers.

The effect of steric interactions can give rise to motility-induced phase separation (see also Sec 2.2.3), which is a self-concentration effect that is possible at high filling fractions ($\phi \gtrsim 0.4$). Although it is a fascinating theoretical result, its biological relevance is questionable because this kind of high filling fraction is very rare in biological systems. Furthermore, hydrodynamic interactions suppress motility-induced phase separation, as they enhance the reorientation of swimmers [72, 73]. It is thus unlikely to see it in experimental systems [72, 73].

However, hydrodynamic interactions can also lead to self-concentration effects. Using coarse-grained analytical models, it was found that a homogeneous state in the configuration of microswimmers is destabilized by hydrodynamic interactions among

the microswimmers [44–48]. In Sec. 5.1 we report on density heterogeneities due to hydrodynamic interactions using our model and find a maximum of density heterogeneities with respect to the filling fraction in the system. This maximum is also recovered by the analytical model we propose. Both theory and simulations show that this maximum results from a competition between hydrodynamic and steric interactions between the microswimmers. Importantly, the maximum in density heterogeneities that we find occurs at much lower filling fraction as opposed to motility-induced phase separation, and can therefore have an ecological effect. Finally we would like to stress that for both our theory and simulations in Sec. 5.1, the self-concentration effect is very different from motility-induced phase separation, as it is induced by the hydrodynamic interactions.

5.1 *Publication:* Maximum in density heterogeneities of active swimmers

Reprinted article with permission from:

Fabian Jan Schwarzendahl and Marco G. Mazza,

Soft Matter **14**, 4666-4678 (2018).

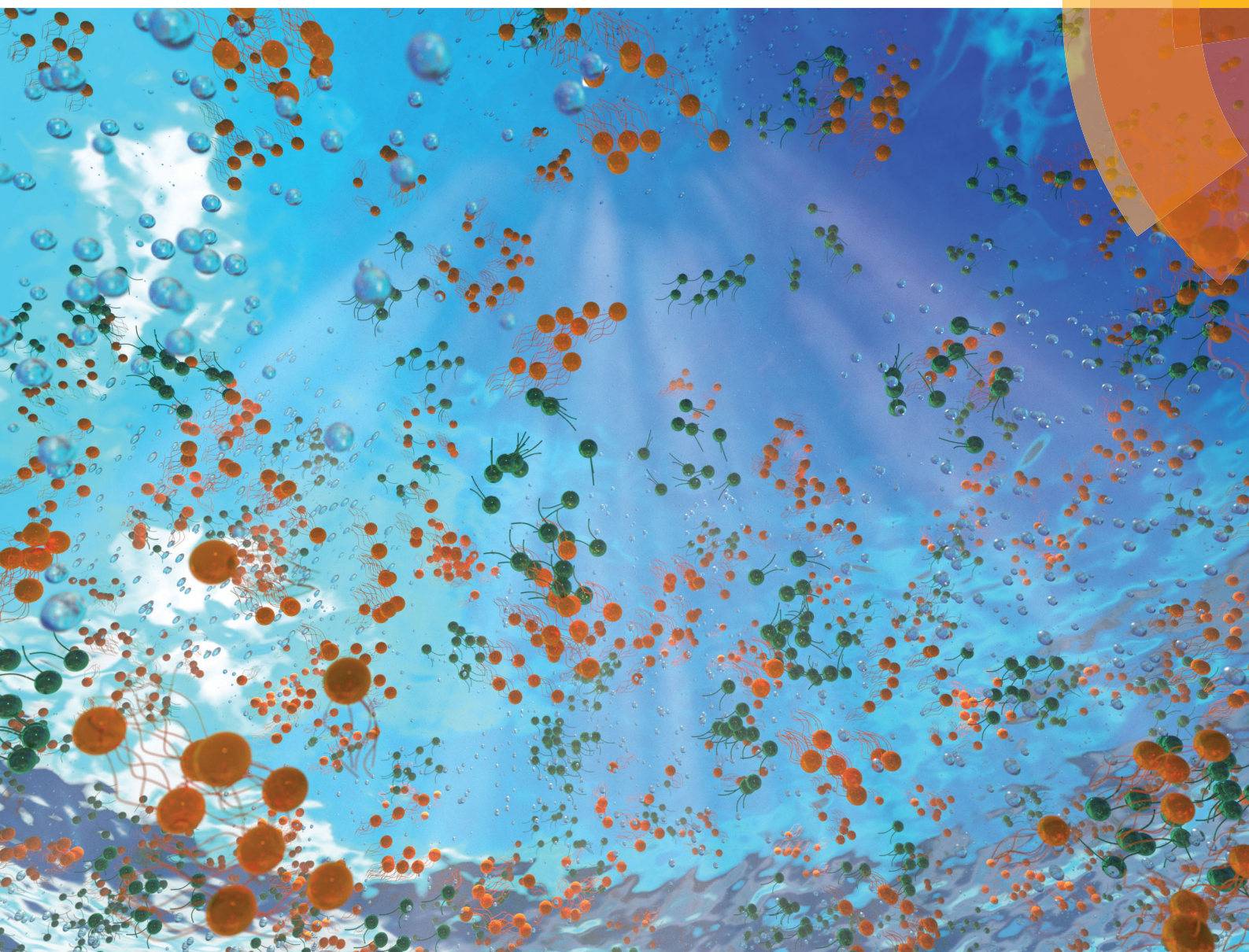
<https://doi.org/10.1039/C7SM02301D>

Licensed under a Creative Commons Attribution 3.0 Unported Licence, Published by The Royal Society of Chemistry.

Individual contribution: I developed the model and wrote the manuscript in close collaboration with M. G. Mazza. I implemented the numerical code and performed all simulations of all data shown in the publication. The theoretical model was developed by me in close collaboration with M. G. Mazza.

Soft Matter

rsc.li/soft-matter-journal



ISSN 1744-6848



ROYAL SOCIETY
OF CHEMISTRY

PAPER

Fabian Jan Schwarzendahl and Marco G. Mazza
Maximum in density heterogeneities of active swimmers



Cite this: *Soft Matter*, 2018, 14, 4666

Maximum in density heterogeneities of active swimmers†

Fabian Jan Schwarzendahl^{ab} and Marco G. Mazza^{ib} *^a

Suspensions of unicellular microswimmers such as flagellated bacteria or motile algae can exhibit spontaneous density heterogeneities at large enough concentrations. We introduce a novel model for biological microswimmers that creates the flow field of the corresponding microswimmers, and takes into account the shape anisotropy of the swimmer's body and stroke-averaged flagella. By employing multiparticle collision dynamics, we directly couple the swimmer's dynamics to the fluid's. We characterize the nonequilibrium phase diagram, as the filling fraction and Péclet number are varied, and find density heterogeneities in the distribution of both pullers and pushers, due to hydrodynamic instabilities. We find a maximum degree of clustering at intermediate filling fractions and at large Péclet numbers resulting from a competition of hydrodynamic and steric interactions between the swimmers. We develop an analytical theory that supports these results. This maximum might represent an optimum for the microorganisms' colonization of their environment.

Received 22nd November 2017,
Accepted 15th April 2018

DOI: 10.1039/c7sm02301d

rsc.li/soft-matter-journal

1. Introduction

Physical interactions in suspensions of microswimmers consisting of bacteria or algae have been recognized to play an important role in the swimmers' collective behavior.^{1–3} The nonequilibrium character of active suspensions, where the energy injection takes place at the scale of the microorganisms, produces myriad mesmerizing phenomena, such as complex interaction with solid surfaces,^{4–6} the spontaneous formation of spiral vortices,⁷ directed motion,⁸ swarming,⁹ bacterial turbulence,¹⁰ and self-concentration.¹¹

Almost invariably, motile microorganisms move in an aqueous environment, where, because of their size, viscous forces dominate, and inertial forces are completely negligible. In fact, consideration of the Navier–Stokes equations identifies that the nature of the dynamics is dictated by the ratio of viscous to inertial forces, known as the Reynolds number $\mathcal{R} = \sigma v \rho / \eta$, where σ is the typical size of the microorganism, v its mean velocity, and ρ , η are the fluid's density and viscosity, respectively. For *Escherichia coli*, e.g., $\sigma \approx 10 \mu\text{m}$, $v \approx 30 \mu\text{m s}^{-1}$, and for water $\rho \approx 10^3 \text{ kg m}^{-3}$, $\eta \approx 10^{-3} \text{ Pa s}$, which result in $\mathcal{R} \approx 10^{-5}$. As noted by Purcell,¹² this means that if the propulsion of a swimmer were to suddenly disappear, it would only coast for 0.1 Å.

Thus, the state of motion is only determined by the forces acting at that very moment, and inertia is negligible.

Due to the microswimmers' low Reynolds numbers, the sum of viscous drag and thrust balances out to zero, in most situations. A direct consequence of force-free motion is that the leading term of the solution of the Stokes equation for a microswimmer is a symmetric force dipole (or stresslet).

Biological microswimmers are complex systems because of the combination of biological, biochemical and physical processes all taking place at the same time. It is thus of great scientific value to develop theoretical models that isolate the relevant degrees of freedom and interactions. Considerable work has been done in recent years, and various models have been introduced, like the squirmer model,^{13–31} the shape anisotropic raspberry swimmer,^{32–34} the force-counterforce model,^{35–38} the catalytic dimers,³⁹ or other hydrodynamic models.^{40–43} Experiments have confirmed that the flow field of flagellated bacteria like *E. coli* is to very good approximation modeled by a simple force dipole,⁴⁴ whereas *Chlamydomonas reinhardtii* are modeled by three Stokeslets.⁴⁵ Furthermore, as cell shapes vary greatly in the natural world, and realistic steric interactions are important in dense suspensions, a model that allows for flexibility in the shape of a microswimmer is a highly desirable feature. In this article we fill this lacuna. We derive a model for a flexible-shape microswimmer that produces self-propulsion by means of a force dipole for pusher-like microswimmers, or three Stokeslets for puller-like microswimmers.

An efficient method to simulate fluids at mesoscopic scales, and their hydrodynamics is the multiparticle collision dynamics (MPCD) technique.⁴⁶ MPCD is a particle-based simulation method

^a Max-Planck-Institute for Dynamics and Self-Organization, Am Fassberg 17, 37077 Göttingen, Germany. E-mail: marco.mazza@ds.mpg.de

^b Georg-August-Universität Göttingen, Friedrich-Hund-Platz 1, 37077 Göttingen, Germany

† Electronic supplementary information (ESI) available. See DOI: 10.1039/c7sm02301d



that correctly produces hydrodynamic modes. Due to its particle nature MPCD naturally includes thermal fluctuations, and can be easily coupled to molecular dynamics methods of solutes, colloids,⁴⁷ and active swimmers.^{20,24,26} The MPCD technique in fact proves to be ideal for our purposes.

The nonequilibrium phase diagram of microswimmers has been subject to considerable interest, especially with regard to the emergence of density heterogeneities in the swimmers' distribution.² We explore the phase diagram of active swimmers and describe the presence of heterogeneities in the spatial distribution of both pushers and pullers. These heterogeneities arise due to the hydrodynamic interactions between the swimmers and relate to existing hydrodynamic theories.^{2,48–50} Interestingly, we find a maximum in the heterogeneities as filling fraction and Péclet number are varied. By using both computer simulations and analytical theory, we demonstrate that this maximum results from a competition between hydrodynamic and steric interactions, where the latter temper the hydrodynamic instability at higher filling fractions. This optimum might have important biological implications on the ability of motile bacteria and algae to form colonies or biofilms.

The remainder of this article is organized as follows. In Section II we introduce the model for the microswimmer. Section III describes the physical properties of the fluid and the microswimmer's flow field. In Section IV we present the non-equilibrium phase diagram of our model microswimmers, and specifically we characterize the density heterogeneities emerging from their hydrodynamic interactions and show that these are tempered by steric interactions at higher filling fractions. In Section V we present an analytical theory and show that we also find a maximum in heterogeneity, which is mediated by the interplay of hydrodynamic and steric interactions. Finally, in Section VI we discuss our main results and summarize our conclusions.

II. Model

We employ a stroke-averaged model of biological microswimmers, similarly to,^{1,10,51} taking into account the asymmetric shape of biological microswimmers due to the cell's body and the flagella. The swimmer is thus modeled as an asymmetric dumbbell, as depicted in Fig. 1, that mimics a *C. reinhardtii* or an *E. coli* cell. The smaller sphere models the swimmer's body and the larger sphere is a stroke average of the region spanned by flagellar motion. The rigid body dynamics of the dumbbells is simulated using Newton's equations and quaternion dynamics (for details see Appendix A1 and A2).

In addition to the rigid body dynamics, we simulate the fluid surrounding the swimmers using MPCD (see Appendix A3), which is a mesoscopic, particle based method, that reproduces hydrodynamics at the Navier–Stokes level.⁴⁷ Precise measurements⁴⁴ show that the flow field of pusher-type microswimmers is well modeled by a force dipole. The pullers flow field, on the other hand, is well represented by a three-Stokeslet solution of the Stokes equation.⁴⁵ These two flow-field models are included in our simulations by adding force regions to the fluid, as

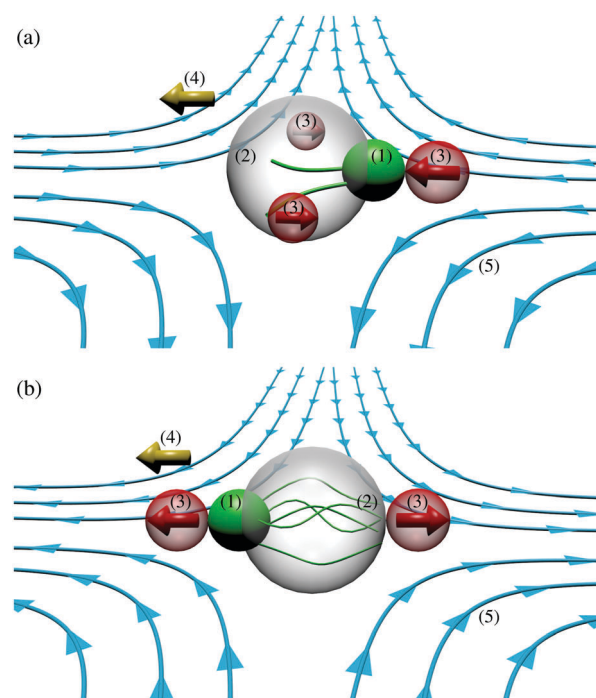


Fig. 1 Schematic representation in a perspective view of the active swimmer model for (a) a puller-type, and (b) a pusher-type microswimmer. In both panels, the small green spheres (1) represent the swimmer's body, and the larger transparent spheres (2) represent the stroke-averaged space spanned by the flagella. The red spheres (3) with embedded arrows represent the regions where the forces are applied. The golden arrows (4) represent the swimming direction. The lines with arrows (5) are a sketch of the hydrodynamic streamlines generated by the swimmers.

depicted by the red regions (3) in Fig. 1. Furthermore, we couple the fluid and swimmers' dynamics by imposing a no-slip boundary condition on the swimmers' surface (for details see Appendix A4).

It should be noted that the dumbbell model introduced here has an anisotropic rigid shape that can be easily modified to more complex shapes. Squirmer models have so far been described for spherical or ellipsoidal shapes.²⁵ Our hydrodynamic flow field is very similar to the three-bead-spring model.⁵² However, the rigid body dynamics differ in the fact that in the three-bead-spring model the beads are connected by springs, whereas ours is a rigid model.

In the following, we express all physical quantities in terms of the MPCD particle mass m , the size of an MPCD grid cell a , and the temperature T of the fluid. We simulate (see Section IV) $N = 300$ – 1560 active swimmers in a cubic domain with side length of $100a$, which is approximately 20 times the size of an individual swimmer, and with periodic boundary conditions. The resulting filling fraction ranges between $\phi = 0.05$ and $\phi = 0.29$. The average number of MPCD particles per cell is $\langle N_C \rangle = 20$ such that the total number of MPCD particles in a simulation is 2×10^7 . The Reynolds number considered here ranges from $\mathcal{R} \sim 0.01$ to $\mathcal{R} \sim 0.1$ and the Péclet number reaches from 2.2×10^2 to 2.6×10^3 .

The full details of our numerical implementation are given in Appendix A.



III. Characterization of the fluid and active hydrodynamics

In the following we describe calculations aimed at characterizing the thermal (equilibrium) properties of our model in the passive case, and also the flow field generated by the active motion.

We first consider a passive colloid (with the same geometry described above, and in Fig. 1) immersed in the MPCD fluid, that is, we carried out equilibrium simulations without activity. The equipartition theorem applied to the passive colloid for the translational motion predicts that the average of each velocity component squared is $\langle U_\alpha^2 \rangle = k_B T / M$, where M is the colloid's mass, k_B is the Boltzmann constant, and $\alpha = x, y, z$. For our system, we find a theoretical value of the translational motion $\langle U_{\text{theory}}^2 \rangle = 2.7 \times 10^{-4} k_B T / m$ and the simulations give $\langle U_x^2 \rangle = \langle U_y^2 \rangle = \langle U_z^2 \rangle = 2.3 \times 10^{-4} k_B T / m$. In case of the rotational motion, the equipartition theorem predicts for the angular velocity $\langle (\Omega_\alpha^b)^2 \rangle = k_B T / I_{\text{mxx}}$, where I_{mxx} is the moment of inertia tensor. Considering our swimmer, whose long axis is aligned with the z axis of a Cartesian reference frame, the theoretical prediction for the angular motion in x and y direction yields $\langle (\Omega_{xy}^b)^2 \rangle = 1.3 \times 10^{-3} k_B T / ma^2$ while the simulations yield $\langle (\Omega_x^b)^2 \rangle = \langle (\Omega_y^b)^2 \rangle = 1.1 \times 10^{-3} k_B T / ma^2$. In the z direction, the theory predicts $\langle (\Omega_z^b)^2 \rangle = 1.4 \times 10^{-3} k_B T / ma^2$ and the simulations give $\langle (\Omega_z^b)^2 \rangle = 1.2 \times 10^{-3} k_B T / ma^2$.

We now consider the active motion at $\mathcal{R} \ll 1$. Hydrodynamics at low Reynolds numbers (relevant for micron-sized objects) allow a great simplification of the Navier–Stokes equations: the nonlinear, inertial effects can be neglected, and the governing equations are the Stokes equations

$$\eta \nabla^2 \mathbf{u} = \nabla p - \mathbf{f}^{\text{ext}}, \quad \nabla \cdot \mathbf{u} = 0, \quad (1)$$

where $\mathbf{u}(\mathbf{r})$ is the fluid velocity, $p(\mathbf{r})$ the pressure, $\mathbf{f}^{\text{ext}}(\mathbf{r})$ is a body force acting on the fluid at position \mathbf{r} , and η is the viscosity of the fluid. Solving the Stokes equations means obtaining expressions for \mathbf{u} and p that satisfy eqn (1) and the boundary conditions. From this knowledge, the stress tensor $\boldsymbol{\sigma}$ can be calculated. For a Newtonian fluid, $\boldsymbol{\sigma}$ depends linearly on the instantaneous values of the velocity gradient, so that one can write $\boldsymbol{\sigma} = -p\mathbf{I} + \eta[\nabla \otimes \mathbf{u} + (\nabla \otimes \mathbf{u})^T]$, where \otimes indicates the

tensor product, and \mathbf{I} the identity tensor. Because the Stokes equations are linear, their solution can be formally written in terms of the convolution of a Green's function with the inhomogeneous term $\mathbf{f}^{\text{ext}53,54}$

$$\mathbf{u}(\mathbf{r}, t) = \int \mathbf{O}(\mathbf{r} - \mathbf{r}') \cdot \mathbf{f}^{\text{ext}}(\mathbf{r}', t) d\mathbf{r}'. \quad (2)$$

In free, three-dimensional space, the Green's function is found by considering a point force $\mathbf{f}^{\text{ext}} = f\mathbf{e}\delta(\mathbf{r})$ acting on an infinite, quiescent fluid, where \mathbf{e} is the unit vector representing the direction of the force, and $\delta(\mathbf{r})$ is the Dirac distribution.

A straightforward calculation⁵⁵ gives the Oseen tensor $\mathbf{O}(\mathbf{r}) \equiv \frac{1}{8\pi\eta r}(\mathbf{I} + \hat{\mathbf{r}} \otimes \hat{\mathbf{r}})$ where $\hat{\mathbf{r}} \equiv \mathbf{r}/r$, $r = |\mathbf{r}|$, and the resulting flow field $\mathbf{u}(\mathbf{r}) = \frac{f}{8\pi\eta r}[e + (\hat{\mathbf{r}} \cdot e)\hat{\mathbf{r}}]$, which is termed a 'Stokeslet' and decays with distance as r^{-1} .

A theoretical prediction for the puller flow field is constructed from three Stokeslets, and for the pusher we use two Stokeslets. The Stokeslets positions are placed at the midpoints of the respective force regions in the swimmer model (see Fig. 1).

We now consider the flow field generated by the active motion of our model microswimmer. We switch on the active motion with a force $f_0 = 50k_B T/a$ and carry out the full dynamics as described in Section II (see also Appendix A for a full definition of f_0). Fig. 2 shows the flow fields of a pusher and a puller in the lab frame. As expected, the flow field of the puller is contractile, as fluid is drawn in from the front and the back, while fluid is pushed away normal to the swimming direction [Fig. 2(a)]. The situation is reversed in the pusher case [Fig. 2(c)] where fluid is pushed out at the front and back of the swimmer. The theoretical predictions for both the puller [Fig. 2(b)] and the pusher [Fig. 2(d)] show a good quantitative agreement with the simulated flow fields. For the Stokesian algebraic decay of $\mathbf{u}(\mathbf{r})$, the reader is referred to Section I in the ESI.†

The effective velocity $v_{\text{eff}} \equiv |\langle \mathbf{e} \cdot \mathbf{U} \rangle|$ of an isolated swimmer in the steady state depends linearly on the active force f_0 .¹ Here, \mathbf{e} is the swimmer's orientation and \mathbf{U} is the swimmer's velocity. From our simulations, we calculate v_{eff} for a pusher [see Fig. 3].

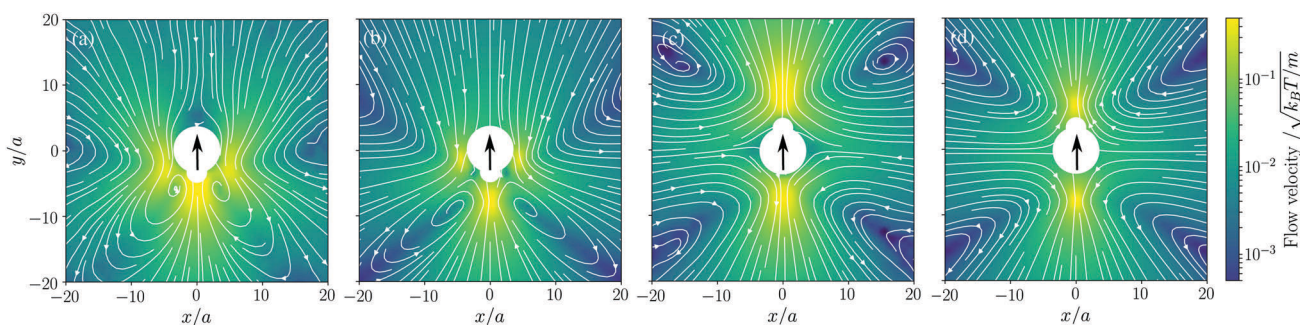


Fig. 2 Time-averaged flow field generated by (a) our model puller, (b) theoretical puller, (c) our model pusher, and (d) theoretical pusher. We show cross-sections on the x – y plane at $z = 0$. The force strength is $f_0 = 50k_B T/a$. The large central white regions show the hard cores of the active swimmers. The thin lines with arrows mark the streamlines, while the color code shows the magnitude of the flow velocity normalized to the thermal velocity. The large black arrows indicate the direction of motion.



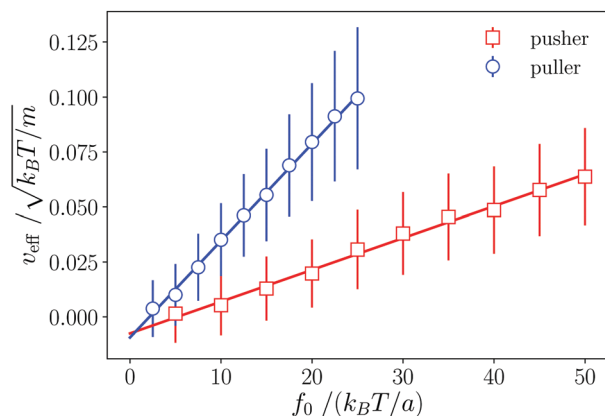


Fig. 3 Dependence of the pusher and puller velocity v_{eff} on the active force f_0 . Lines are linear fits to the simulated data. The observed linear dependence is evidence of the Stokes flow regime.

The linear fit has a slope of $\alpha = (1.45 \pm 5 \times 10^{-2}) \times 10^{-3} \sqrt{\frac{ma^2}{k_B T}}$.

The analogous results for pullers are also shown in Fig. 3, where

the slope of the linear fit is $\alpha = (4.4 \pm 7 \times 10^{-2}) \times 10^{-3} \sqrt{\frac{ma^2}{k_B T}}$.

The linear dependence of v_{eff} on f_0 shows that our simulations correspond to the Stokes flow regime.

Further simulations on the two particle interaction statistics and two particle flow fields can be found in Section I (ESI†).

IV. Density heterogeneities

In the following we will study the nonequilibrium phase behavior of our active swimmer model. The filling fraction we employ here is computed using the volume of the swimmer's body V_B , as well as the volume that is spanned by the flagella sphere V_F , while taking into account their overlap volume V_{O1}

$$\phi = \frac{(V_B + V_F - V_{O1})N}{V}, \quad (3)$$

where V is the volume of the simulated system. Note, that in an experiment only the body of the cell would be taken into account, thus the filling fraction should then be rescaled by $V_B/(V_B + V_F - V_{O1}) = 7.5 \times 10^{-2}$. Furthermore, we vary the strength of the active force f_0 , which changes the propulsion speed v_{eff} as well as the strength of the hydrodynamic interactions between the swimmers. The Péclet number captures the ratio of advection to diffusion, and can be computed using

$$\mathcal{P} = \frac{v_{\text{eff}}\sigma}{D}, \quad (4)$$

where we used the linear relation (fitted slope) between active velocity and force dipole strength from Section III. Furthermore, $\sigma = 5a$ is the typical length of the swimmer and for the diffusion constant we assume $D = \frac{k_B T}{6\pi\eta\sigma}$.

We analyze the system's density using a Voronoi tessellation⁵⁶ and compute the local volume for each swimmer.

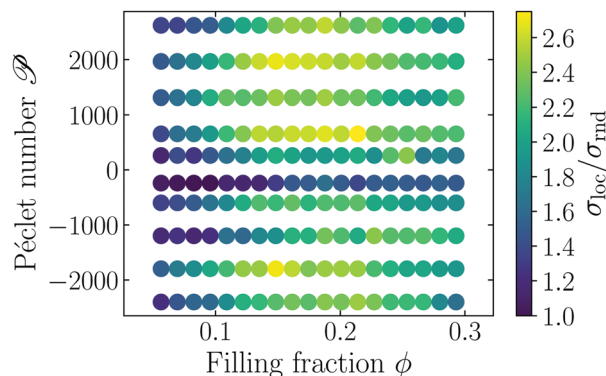


Fig. 4 Standard deviation of local Voronoi volume σ_{loc} compared to standard deviation σ_{rnd} of a homogeneous configuration. The Péclet number \mathcal{P} as well as the global filling fraction ϕ are varied. Positive Péclet numbers correspond to pusher-type and negative to puller-type swimmers.

A global measure for the heterogeneity of a configuration of swimmers is given by the standard deviation of the distribution of local Voronoi volumes σ_{loc} . In order to remove trivial scaling factors, we compare σ_{loc} to the standard deviation σ_{rnd} of local Voronoi volumes for random homogeneous configurations of nonoverlapping, passive dumbbells (as in Fig. 1) with the same filling fraction. Fig. 4 shows the resulting phase diagram, with the dependence of $\sigma_{\text{loc}}/\sigma_{\text{rnd}}$ on Péclet number and filling fraction. Here, positive values of \mathcal{P} correspond to pusher-type swimmers, whereas negative values are puller-type swimmers.

The phase diagram shows that for both pullers and pushers, initially $\sigma_{\text{loc}}/\sigma_{\text{rnd}}$ grows with \mathcal{P} and filling fraction, then it reaches a maximum and drops to lower values. The initial increase is related to an instability that is mediated by the hydrodynamic interactions of the microswimmers which has also been found in ref. 1, 2 and 48–50. Intuitively this can be understood in the following way: the hydrodynamic flow field from the swimmers creates heterogeneities in the fluid's velocity, which couple back to the swimmers and produce heterogeneities in the density. It should be noted that the Péclet number of the system has to be rather large, such that the hydrodynamic interaction between the swimmers is strong enough to produce heterogeneous structures. As the filling fraction increases, steric interactions grow in importance and compete with the hydrodynamic instability. Thus, we ascribe the presence of the maximum in $\sigma_{\text{loc}}/\sigma_{\text{rnd}}$ to a tapering effect of the steric interactions on the hydrodynamic instability. This tapering effect becomes visible only when steric interactions are fully accounted for.

To test the hypothesis that steric interactions stabilize the hydrodynamic instability, we carry out two more types of simulations: first, we exclude the steric effects by setting the hard-core repulsion [eqn (A6)] to zero, thus only hydrodynamic effects are included. Second, we carry out Brownian dynamics simulations, which completely neglect hydrodynamic interactions. More details about the Brownian dynamics simulations are given in Section III of the ESI†

In Fig. 5 we show our original simulations that fully account for hydrodynamic and steric interactions, the simulations



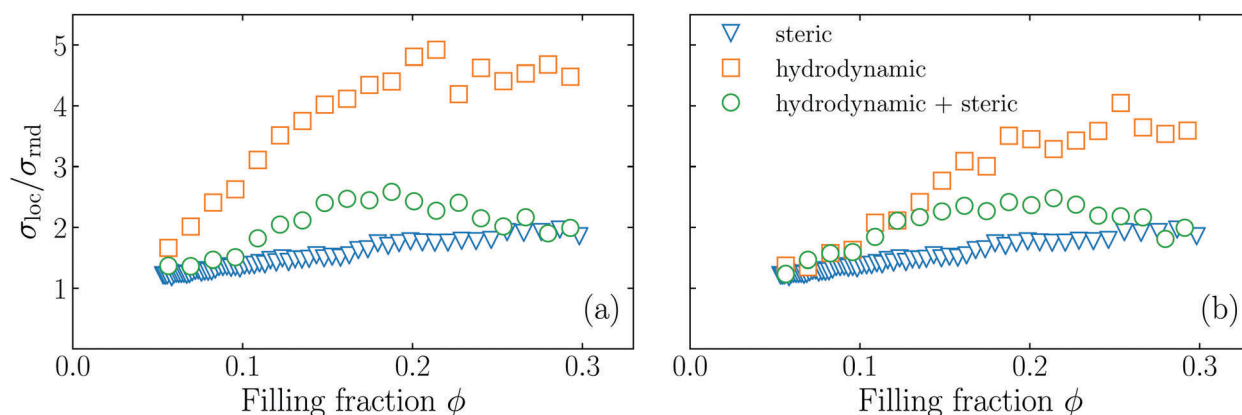


Fig. 5 Dependence on the filling fraction of the standard deviation of local Voronoi volumes σ_{loc} compared to the standard deviation σ_{rnd} of a homogeneous configuration for pushers (a), and pullers (b). The Péclet number is fixed to $\mathcal{P} = 2.6 \times 10^3$ for pushers and $\mathcal{P} = 2.4 \times 10^3$ for pullers. The circles are the results for simulations with both hydrodynamic and steric interactions; the squares are the results for simulations including only hydrodynamic interactions; and the triangles are simulations including only steric interactions.

without steric interactions, and the active Brownian simulations. The simulations with hydrodynamics alone give rise to a strong increase of $\sigma_{\text{loc}}/\sigma_{\text{rnd}}$, but no maximum occurs, while the active Brownian simulations show a monotonic increase of $\sigma_{\text{loc}}/\sigma_{\text{rnd}}$, which is much less pronounced. Our original simulations (with both hydrodynamics and steric effects) exhibit intermediate values of $\sigma_{\text{loc}}/\sigma_{\text{rnd}}$. Thus, we conclude that the maximum which we see is mediated by an interplay of the hydrodynamic interactions and the steric interactions, confirming our hypothesis.

V. Theoretical analysis

To bolster our numerical results, we develop an analytical theory of microswimmers that explicitly includes hydrodynamic and steric interactions. As in our numerical model (see Section II), we consider the dynamics of an asymmetric dumbbell, which is described by the following effective Langevin equations

$$\frac{d\mathbf{r}_{Li}}{dt} = \mathbf{u}(\mathbf{r}_{Li}), \quad (5)$$

$$\frac{d\mathbf{r}_{Si}}{dt} = \mathbf{u}(\mathbf{r}_{Si}), \quad (6)$$

where \mathbf{r}_{Li} is the position of the front sphere of the swimmer i with radius a_L and \mathbf{r}_{Si} the position of the respective back sphere with radius a_S . The front and back spheres of each swimmer are connected by an infinitely thin rigid rod of length l . The swimmer is coupled to the fluid velocity \mathbf{u} , which is determined by the Stokes equation including a stochastic and an active force term

$$\eta \nabla^2 \mathbf{u} = \nabla p - \mathbf{f}^{\text{active}} + \mathbf{f}^{\text{noise}}. \quad (7)$$

Here, the active force is given by a force dipole

$$\mathbf{f}^{\text{active}} = \sum_i f \mathbf{e}_i [\delta(\mathbf{r} - \mathbf{r}_{Li}) - \delta(\mathbf{r} - \mathbf{r}_{Si})], \quad (8)$$

which points along the orientation of the swimmer \mathbf{e}_i and has a force strength f . The orientation is defined as $\mathbf{e}_i = (\mathbf{r}_{Li} - \mathbf{r}_{Si})/l$, *i.e.*, the unit vector connecting the back to the front sphere.

Furthermore, fluctuations in the swimmers motion are added to the fluid *via*

$$\mathbf{f}^{\text{noise}} = \sum_i \xi_i^L(t) \delta(\mathbf{r} - \mathbf{r}_{Li}) - \xi_i^S(t) \delta(\mathbf{r} - \mathbf{r}_{Si}), \quad (9)$$

where $\xi_i^{L,S}(t)$ are noise terms with $\langle \xi_i^{L,S}(t) \xi_j^{L,S}(t') \rangle = 2\Gamma_{L,S} \mathbf{I} \delta_{ij} \delta(t - t')$, and $\Gamma_{L,S} = 6\pi\eta a_{L,S}$ are the friction coefficients of the front and back sphere. Considering only the active term eqn (7) can be solved

$$\mathbf{u} = f \sum_i [\mathbf{O}(\mathbf{r} - \mathbf{r}_{Li}) - \mathbf{O}(\mathbf{r} - \mathbf{r}_{Si})] \cdot \mathbf{e}_i, \quad (10)$$

with the Oseen tensor $\mathbf{O}(\mathbf{r}) \equiv \frac{1}{8\pi\eta r} (\mathbf{I} + \hat{\mathbf{r}} \otimes \hat{\mathbf{r}})$, which is regularized by using $\mathbf{O}(|\mathbf{r}| \leq a_{L,S}) \equiv \mathbf{I}/\Gamma_{L,S}$. Given the solution (10), the flow velocity can be eliminated from eqn (5) and (6). Using the hydrodynamic center $\mathbf{r}^C = \frac{\Gamma_L \mathbf{r}_L + \Gamma_S \mathbf{r}_S}{\Gamma_L + \Gamma_S}$, we can simplify eqn (5) and (6) to

$$\frac{d\mathbf{r}_i^C}{dt} = v_0 \mathbf{e}_i + \frac{1}{\zeta_{\text{hy}}} \sum_{j \neq i} \mathbf{F}_{ij} + \xi_i, \quad (11)$$

$$\frac{d\mathbf{e}_i}{dt} = \left[\frac{1}{l^2 \zeta_{\text{hy}}} \sum_{j \neq i} \boldsymbol{\tau}_{ij} + \xi_i^R \right] \times \mathbf{e}_i, \quad (12)$$

where v_0 is the propulsion speed and $\zeta_{\text{hy}} = 3\pi\eta(a_S + a_L)$ is the hydrodynamic friction coefficient. The leading order of the multipole expansion of the hydrodynamic force \mathbf{F}_{ij} and torque $\boldsymbol{\tau}_{ij}$ between swimmers i and j are given in Section IV (ESI[†]). The random forces ξ_i and ξ_i^R are Gaussian white noises with

$$\langle \xi_{i,\alpha}(t) \xi_{j,\beta}(t') \rangle = 2D \delta_{ij} \delta_{\alpha\beta} \delta(t - t'), \quad (13)$$

$$\langle \xi_{i,\alpha}^R(t) \xi_{j,\beta}^R(t') \rangle = 2D_R \delta_{ij} \delta_{\alpha\beta} \delta(t - t'), \quad (14)$$

where D is the translational and D_R the rotational diffusion coefficient.

Following,¹ we derive the one-body Smoluchowski equation from eqn (11) and (12). As we have seen in Section IV steric interactions among swimmers may play a crucial role in their dynamics.



Thus, we explicitly include the effect of steric interactions by means of the Ansatz^{57,58}

$$v(c) = v_0 - c\zeta. \quad (15)$$

Here, c is the concentration and the constant ζ quantifies how much the swimmers are slowed down by the steric interactions (for more details see ref. 57 and 58). The Smoluchowski equation then reads

$$\begin{aligned} \partial_t p = & -\nabla \cdot [v(c)ep] - \frac{1}{\zeta_{\text{hy}}} \nabla \cdot (\mathbf{F}_{\text{hy}} p) \\ & - \frac{1}{\zeta_{\text{hy}}^2} \left(\mathbf{e} \times \frac{\partial}{\partial \mathbf{e}} \right) \cdot \boldsymbol{\tau}_{\text{hy}} p \\ & + D\Delta p + D_{\text{R}} \left(\mathbf{e} \times \frac{\partial}{\partial \mathbf{e}} \right)^2 p, \end{aligned} \quad (16)$$

where $p(\mathbf{r}, \mathbf{e}, t)$ is the one-particle probability distribution function of finding a swimmer at position \mathbf{r} , with orientation \mathbf{e} at time t . The first term on the right hand side of eqn (16) takes into account the active motion with a density dependent velocity, due to steric interactions; the second term accounts for the hydrodynamic forces and the third term for the hydrodynamic torques; the last two terms are responsible for translational and rotational diffusivity respectively. Here, \mathbf{F}_{hy} are the hydrodynamic two-body forces, and $\boldsymbol{\tau}_{\text{hy}}$ is the hydrodynamic torque between two particles (see also ESI,† Section V). To make progress with this equation, we follow the standard path: we consider a multipole expansion and compute moment equations for the concentration c , the polarization \mathbf{P} and the nematic order tensor \mathbf{Q}

$$c(\mathbf{r}, t) = \int d\mathbf{e} p(\mathbf{r}, \mathbf{e}, t), \quad (17)$$

$$\mathbf{P}(\mathbf{r}, t) = \frac{1}{c(\mathbf{r}, t)} \int d\mathbf{e} \mathbf{e} p(\mathbf{r}, \mathbf{e}, t), \quad (18)$$

$$\mathbf{Q}(\mathbf{r}, t) = \frac{1}{c(\mathbf{r}, t)} \int d\mathbf{e} \left(\mathbf{e} \otimes \mathbf{e} - \frac{1}{3} \mathbf{I} \right) p(\mathbf{r}, \mathbf{e}, t). \quad (19)$$

The full equations for c , \mathbf{P} and \mathbf{Q} are given in Section V (ESI†). We linearize these moment equations around the isotropic state, described by $c = c_0 + \delta c$, $\mathbf{P} = \delta \mathbf{P}$ and $\mathbf{Q} = \delta \mathbf{Q}$ and turn to Fourier space, with wave vector \mathbf{k} , where the fields are denoted by $\delta \tilde{c}(\mathbf{k})$, $\delta \tilde{\mathbf{P}}(\mathbf{k})$, and $\delta \tilde{\mathbf{Q}}(\mathbf{k})$. To first order in the fluctuations the equations governing the temporal evolution read

$$\partial_t \delta \tilde{c} = - \left[ik_i \left(v_0 c_0 - \zeta c_0^2 + c_0^2 \frac{\Delta a l^2 f}{30 \eta \bar{a}} \right) \delta \tilde{P}_i + D k_i k_i \delta \tilde{c} \right], \quad (20)$$

$$\begin{aligned} \partial_t \delta \tilde{P}_i = & - \left[ik_j (v_0 - \zeta c_0) \delta \tilde{Q}_{ij} + ik_i \frac{1}{3} \left(\frac{v_0}{c_0} - 2\zeta \right) \delta \tilde{c} \right. \\ & \left. + (D k_j k_j + D_{\text{R}}) \delta \tilde{P}_i \right], \end{aligned} \quad (21)$$

$$\begin{aligned} \partial_t \delta \tilde{Q}_{ij} = & - \left[i \frac{2}{5} (v_0 - \zeta c_0) [k_i \delta \tilde{P}_j]^{\text{ST}} + \frac{3lf}{8\pi\eta} c_0 \mathcal{M}_{ij} (\delta \tilde{Q}_{ij}) \right. \\ & \left. + (4D_{\text{R}} + k_n k_n D) \delta \tilde{Q}_{ij} \right], \end{aligned} \quad (22)$$

where $k = |\mathbf{k}|$ is the absolute value of the wavevector,

$$(\mathcal{M}_{ij}) = \frac{4}{5} \pi \begin{pmatrix} -\frac{2}{3} (\delta \tilde{Q}_{2,2} + \delta \tilde{Q}_{3,3}) & \frac{2}{3} \delta \tilde{Q}_{2,1} & -\delta \tilde{Q}_{3,1} \\ \frac{2}{3} \delta \tilde{Q}_{2,1} & \frac{2}{3} \delta \tilde{Q}_{2,2} & -\delta \tilde{Q}_{3,2} \\ -\delta \tilde{Q}_{3,1} & -\delta \tilde{Q}_{3,2} & \frac{2}{3} \delta \tilde{Q}_{3,3} \end{pmatrix}, \quad (23)$$

$[\mathbf{A}_{ij}]^{\text{ST}}$ is the symmetric traceless form of the tensor \mathbf{A}_{ij} , and we now denote $i, j = x, y, z$. The terms involving the force dipole strength f stem from the hydrodynamic interactions and can cause instabilities in the system. To analyze the stability of the system we will first consider pullers ($f < 0$) and in the second step pushers ($f > 0$), where we systematically keep terms up to order k^2 .

For pullers ($f < 0$) the concentration fluctuations $\delta \tilde{c}$ are dominant. To analyze the fluctuations in the concentration we use a large length-scale and long time-scale ($D_{\text{R}} t \gg 1$) approximation for the longitudinal polarization $\delta \tilde{P}_{\parallel} = \hat{k}_i \delta \tilde{P}_i$, $\hat{k}_i \equiv k_i/k$, which reads

$$\delta \tilde{P}_{\parallel} \approx -\frac{ik}{3D_{\text{R}}} \left(\frac{v_0}{c_0} - 2\zeta \right) \delta \tilde{c}, \quad (24)$$

whereas the fluctuations $\delta \tilde{Q}_{ij}$ are of higher order in k , when terms of order k^2 in eqn (20) are kept. Inserting the quasi-stationary solution eqn (24) into the eqn (20) yields

$$\begin{aligned} \partial_t \delta \tilde{c} = & -\frac{k^2}{3D_{\text{R}}} \left[3DD_{\text{R}} + v_0^2 + c_0 \left(-3v_0\zeta + \frac{\delta a l^2 v_0 f}{30\eta \bar{a}} \right) \right. \\ & \left. + c_0^2 2\zeta \left(\zeta - \frac{\delta a l^2 f}{30\eta \bar{a}} \right) \right] \delta \tilde{c}. \end{aligned} \quad (25)$$

For pullers the term $c_0 \left(-3v_0\zeta + \frac{\delta a l^2 v_0 f}{30\eta \bar{a}} \right)$ introduces an instability at low concentrations c_0 , which are counteracted by the term $c_0^2 2\zeta \left(\zeta - \frac{\delta a l^2 f}{30\eta \bar{a}} \right)$, that stabilizes the system at higher concentrations. Since the first term is dominated by the hydrodynamic interactions and the second term by the steric interactions, we can draw the same conclusion as from the simulations: the hydrodynamic interactions cause heterogeneities in the system which are suppressed by the steric effects at larger c_0 . Moreover, inspection of the fastest-growing eigenvalue reveals a maximum of instability as a function of c_0 and, hence, a maximum degree of heterogeneity. The position of the maximum of the filling fraction can be estimated from microscopic information extracted from scattering events between two swimmers; we find $\phi^{\text{max}} = 0.12$, which is consistent with the simulation in Fig. 5(b) (for details see Appendix B).

We also find an instability in the splay fluctuations of the nematic tensor $\delta \tilde{Q}_{\parallel\parallel} = \hat{k} \cdot \tilde{\mathbf{Q}} \cdot \hat{k}$. Here, the approximation of the polarization fluctuations [eqn (21)] is different, since we need to consider eqn (22) for the counting of powers of k . In the large length and time scale limit we arrive at

$$\delta \tilde{P}_i = -ik_n \frac{1}{D_{\text{R}}} (v_0 - \zeta c_0) \delta \tilde{Q}_{in}. \quad (26)$$



Inserting eqn (26) into eqn (22) and projecting on the splay part yields

$$[k_i \delta \tilde{P}_j]^{ST} \frac{k_i k_j}{k^2} = -ik^2 \frac{1}{2D_R} (v_0 - \zeta c_0) \delta \tilde{Q}_{\parallel\parallel}. \quad (27)$$

Combining eqn (27) with eqn (22) gives

$$\begin{aligned} \partial_t \delta \tilde{Q}_{\parallel\parallel} = & - \left[k^2 \left(D + \frac{4v_0^2}{15D_R} \right) + 4D_R - c_0 \left(\frac{8\zeta v_0 k^2}{15D_R} + \frac{2lf}{25\eta} \right) \right. \\ & \left. + c_0^2 \frac{4k^2 \zeta^2}{15D_R} \right] \delta \tilde{Q}_{\parallel\parallel}. \end{aligned} \quad (28)$$

From this term we also find a maximum instability, but the resulting instability is sub-dominant compared to the instability in the concentration fluctuations.

For pushers ($f > 0$) the bend component of the nematic tensor fluctuations $\delta \tilde{Q}_{\perp\perp} = \hat{k} \delta \tilde{Q} (\mathbf{I} - \hat{k} \otimes \hat{k})$ become unstable, since here $k_i \mathcal{M}_{ij} (\delta_{jl} - k_j k_l) < 0, \forall l = x, y, z$. For the polarization we use the large length and time scale limit in eqn (26). Inserting eqn (26) into the term $[k_i \delta \tilde{P}_j]^{ST}$ of eqn (22), and projecting onto the bend part gives

$$[k_i \delta \tilde{P}_j]^{ST} \frac{k_i}{k} (\delta_{jl} - k_j k_l / k^2) = -ik^2 \frac{1}{2D_R} (v_0 - \zeta c_0) \delta \tilde{Q}_{\perp\perp}. \quad (29)$$

Therefore, we have a single equation for the bend nematic fluctuations $\delta \tilde{Q}_{\perp\perp}$, which is given by

$$\begin{aligned} \partial_t \delta \tilde{Q}_{\perp\perp} = & - \left[k^2 \left(D + \frac{v_0^2}{5D_R} \right) + 4D_R \right. \\ & \left. - c_0 \left(\frac{2\zeta v_0 k^2}{5D_R} + \frac{3lf}{25\eta} \right) + c_0^2 \frac{k^2 \zeta^2}{5D_R} \right] \delta \tilde{Q}_{\perp\perp}. \end{aligned} \quad (30)$$

Here, the term $-c_0 \left(\frac{2\zeta v_0 k^2}{5D_R} + \frac{3lf}{25\eta} \right)$ destabilizes the system at low concentrations c_0 through nematic fluctuations, which are counteracted by the term $c_0^2 \frac{k^2 \zeta^2}{5D_R}$, that stabilizes the system for higher concentrations. Again, the first term, which destabilizes the system, is dominated by the hydrodynamic interactions, whereas the second, stabilizing term comes from the steric interactions. Additionally from microscopic information extracted from scattering events between two swimmers we can estimate the filling fraction of the maximum heterogeneities, with the result $\phi^{\max} = 0.23$, which is in accordance with the simulation from Fig. 5(a) (for details see Appendix B).

VI. Conclusions

We have presented a new model for biological microswimmers that is based on Stokeslets and the stroke averaged motion of their flagella. The Stokeslets were distributed to model the flow fields of *C. reinhardtii* or *E. coli* cells. Furthermore, our model takes into account the anisotropic shape of a microswimmer. Typical for this is the shape of a *C. reinhardtii* cell, which is well modeled by an asymmetric dumbbell.¹⁰ Self-propulsion is generated through a symmetry breaking due to the asymmetric shape and force-free motion. The fluid and the hydrodynamic interactions are explicitly included with MPCD.

We show that the flow fields produced in our simulations can be predicted using simple formulae from the literature. These formulae also correspond to the experimentally measured flow fields.^{44,45} Additionally, we test the effective velocity of the microswimmer model, and find that it depends linearly on the applied force, in agreement with the Stokes flow regime.

We study the phase diagram in terms of filling fraction and Péclet number. We find that both pullers and pushers exhibit density heterogeneities. The density heterogeneities show a maximum at intermediate filling fractions and high Péclet number. To determine the mechanism underpinning this phenomenon, we perform additional simulations, in which either the steric interactions or the hydrodynamic interactions were switched off. Simulations with active Brownian particles showed a small linear increase in the density heterogeneities, while simulations without the steric interactions show strong density heterogeneities. This is an instability caused only by the hydrodynamic interactions, which is known from the literature.^{1,2,48-50} However, no maximum arises in the simulations with only hydrodynamic or only steric interactions, which shows that the maximum in the density heterogeneities is mediated by an interplay of the hydrodynamic and the steric interactions. The hydrodynamic interactions destabilize the system, whereas the steric interactions stabilize the system as the filling fraction grows and thus a maximum in density heterogeneity arises.

We have also developed an analytical theory based on a Smoluchowski equation which includes steric as well as hydrodynamic interactions. We computed the hydrodynamic moments of this equation and performed a linear stability analysis of the moment equations around the homogeneous state. For both puller and pusher-type swimmers, we found that at low concentration the system is destabilized by hydrodynamic interactions. At higher concentrations, however, the instabilities are counteracted by the steric interaction. This interplay gives rise to a maximum in the instability of the homogeneous state, and thus a maximum heterogeneity in the concentration of swimmers. The position of the maxima calculated from the analytics is in accordance with the simulations. Our continuum theory does not explicitly account for steric effects at the microscopic level, which induce short range correlations, and lubrication forces, and influence the short range hydrodynamics. These effects, however, are captured by the numerical simulations. The agreement between our theory and simulations gives us confidence that our assumptions effectively includes the dominant physical effects.

The physical pictures from both simulations and analytical theory fit together: both show that the homogeneous state is not stable and there is a maximum of instability. Also, both analyses show that the instability arises from hydrodynamic interactions and is suppressed by the steric interactions.

The maximum in the density heterogeneities might have important biological implications: it points to a possible, optimal filling fraction and Péclet number for the formation of heterogeneous distributions of motile microorganisms. Bacteria or microalgae exhibiting these optimal parameters are more likely to form colonies or biofilms.



Conflicts of interest

There are no conflicts of interest to declare.

Appendix A: model details

The microswimmer is characterized by its mass M , center of mass position \mathbf{R} and orientation \mathbf{q} . In the following we describe the equations governing the motion of the microswimmer, the fluid dynamics implemented through the MPCD, and their coupling.

1. Rigid body dynamics of swimmers

As we do not consider shape deformable swimmers, we are only concerned with rigid-body dynamics. The most general motion of a rigid body is the combination of a translation along an axis (the Mozzì axis) and a rotation around the same axis, as per the Mozzì–Chasles theorem.⁵⁹ Any orientation in space can be described using three numbers, that are commonly represented with the Euler angles, which correspond to three elementary rotations. However, there are a number of issues with the choice of the Euler angles. For instance, the composition of rotations with Euler angles or rotation matrices is rather complex, and involves trigonometric functions which lead to an accumulation of rounding-off errors. Eventually the matrices representing the rotations may become not orthogonal. Importantly, for some values of the Euler angles there are discontinuous jumps in the representation. More fundamentally, the Euler angles do not generate a covering map of the rotation group $SO(3)$, that is, the map from Euler angles to $SO(3)$ is not always a local homeomorphism. Fortunately, the topology of $SO(3)$ is diffeomorphic to the real projective space $\mathbb{P}_3(\mathbb{R})$ which admits a universal cover represented by the group of unit quaternions $\mathbf{q} = (q_0, q_1, q_2, q_3)^T$, where the superscript T indicates the matrix transposition.

The equations of motion for the rigid body dynamics in three dimensions and in terms of quaternions read⁶⁰

$$m\ddot{\mathbf{R}} = \mathbf{F}, \quad (\text{A1})$$

$$\ddot{\mathbf{q}} = \frac{1}{2} \left[\mathbf{W}(\dot{\mathbf{q}}) \begin{pmatrix} 0 \\ \boldsymbol{\Omega}^b \end{pmatrix} + \mathbf{W}(\mathbf{q}) \begin{pmatrix} 0 \\ \dot{\boldsymbol{\Omega}}^b \end{pmatrix} \right], \quad (\text{A2})$$

$$\dot{\mathbf{q}} = \frac{1}{2} \mathbf{W}(\mathbf{q}) \begin{pmatrix} 0 \\ \boldsymbol{\Omega}^b \end{pmatrix}, \quad (\text{A3})$$

$$\dot{\boldsymbol{\Omega}}_x^b = (I_m^b)_x^{-1} \left(T_x^b + \left((I_m^b)_\beta - (I_m^b)_\gamma \right) \Omega_\beta^b \Omega_\gamma^b \right), \quad (\text{A4})$$

where $\boldsymbol{\Omega}^b$ is the angular velocity of the swimmer, \mathbf{I}_m^b the moment of inertia tensor of the swimmer in the body frame, and the indices (x, β, γ) take on as values the cyclic permutations of (x, y, z) . In eqn (A1), $\mathbf{F} = -\nabla\Phi$ and $\mathbf{T} = \mathbf{R}_F \times \mathbf{F}$ are the force and torque, respectively, acting on the swimmer due to steric interactions with the neighbor, where \mathbf{R}_F is the vector connecting the center of mass of the swimmer to the point of contact with the neighbor, and the matrix \mathbf{W} is (see also ref. 61)

$$\mathbf{W}(\mathbf{q}) = \begin{pmatrix} q_0 & -q_1 & -q_2 & -q_3 \\ q_1 & q_0 & -q_3 & q_2 \\ q_2 & q_3 & q_0 & -q_1 \\ q_3 & -q_2 & q_1 & q_0 \end{pmatrix}. \quad (\text{A5})$$

The repulsive, steric interactions among swimmers are modeled using a Weeks–Chandler–Andersen potential⁶²

$$\Phi(r_{ij,ab}) = 4\varepsilon \left[\left(\frac{\sigma_{ab}}{r_{ij,ab}} \right)^{12} - \left(\frac{\sigma_{ab}}{r_{ij,ab}} \right)^6 \right] + \varepsilon \quad (\text{A6})$$

if $r_{ij,ab} < 2^{1/6}\sigma_{ab}$, and $\Phi(r_{ij,ab}) = 0$ otherwise, where $r_{ij,ab} \equiv |\mathbf{r}_{ia} - \mathbf{r}_{jb}|$ is the distance between sphere a of swimmer i and sphere b of swimmer j , ε is the energy scale and σ_{ab} is the sum of the radii of sphere a and sphere b . For the numerical integration we use the Verlet algorithm proposed in ref. 60, which was also used and discussed in detail in ref. 25.

Given a vector in the laboratory frame \mathbf{f} the transformation to the body frame vector \mathbf{f}^b is given by

$$\mathbf{f}^b = \mathbf{D}\mathbf{f}, \quad (\text{A7})$$

where the matrix $\mathbf{D}(\mathbf{q})$ is constructed from the quaternions.

Quaternions are represented as $\mathbf{q} = q_0 + q_1\mathbf{i} + q_2\mathbf{j} + q_3\mathbf{k}$, with $q_0, \dots, q_3 \in \mathbb{R}$, and $\mathbf{i}^2 = \mathbf{j}^2 = \mathbf{k}^2 = \mathbf{ijk} = -1$.

The unitary matrix \mathbf{D} that transforms vectors from the lab to the body frame is (see also ref. 61)

$$\mathbf{D} = \begin{pmatrix} q_0^2 + q_1^2 - q_2^2 - q_3^2 & 2(q_1q_2 + q_0q_3) & 2(q_1q_2 - q_0q_3) \\ 2(q_2q_1 - q_0q_3) & q_0^2 - q_1^2 + q_2^2 - q_3^2 & 2(q_2q_3 + q_0q_1) \\ 2(2q_3q_1 + q_0q_2) & 2(q_3q_2 - q_0q_1) & q_0^2 - q_1^2 - q_2^2 + q_3^2 \end{pmatrix}. \quad (\text{A8})$$

Thus, the orientation of the swimmer at any given time is found from $\mathbf{D}^{-1}(\mathbf{q}(t))(0,0,1)^T$.

Note that all quantities that do not carry an index b are calculated in the laboratory frame.

2. Center of mass and moment of inertia

Fig. 6 shows the detailed geometry and dimensions of our model microswimmers (both pullers and pushers). In the body frame, the swimmer is aligned with the z direction and the coordinates of the centers of the B and F spheres are z_1 and z_2 , respectively. Given a homogeneous mass distribution the center of mass of the swimmer is given by

$$z_{\text{CoM}} = \left\{ V_1 z_1 + V_2 z_2 - V_{\text{Sc}_1} \left[z_1 + \frac{3}{4} \frac{(d_f - h_1)^2}{3d_f/2 - h_1} \right] - V_{\text{Sc}_2} \left[z_2 + \frac{3}{4} \frac{(d_b - h_2)^2}{3d_b/2 - h_2} \right] \right\} (V_1 + V_2 - V_{\text{Sc}_1} - V_{\text{Sc}_2})^{-1}, \quad (\text{A9})$$

where V_i are the volumes of the spheres and V_{Sc_i} are the volumes of their spherical caps, which are cut by the other sphere⁶³

$$V_{\text{Sc}_i} = \frac{1}{3} \pi h_i^2 (3d_i/2 - h_i), \quad (\text{A10})$$



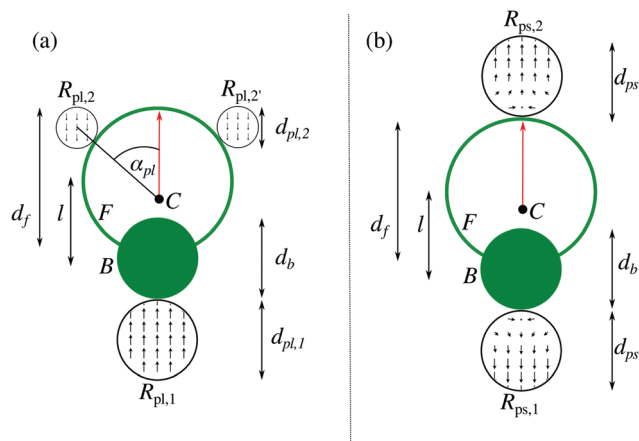


Fig. 6 Details of the geometry of our model puller-type swimmer (a) and pusher-type swimmer (b). Regions B (green) and F (empty circle) are the body with diameter d_b and stroke-averaged flagella with diameter d_f , respectively, and they are separated by a distance l . The red arrow denotes the swimmers orientation and C is the center of mass. Black circles are the force poles acting on the fluid. For pullers (a) the region $R_{pl,1}$ has the diameter $d_{pl,1}$ and the regions $R_{pl,2}$, $R_{pl,2'}$ have the diameter $d_{pl,2}$. For pushers (b) the regions $R_{ps,1}$ and $R_{ps,2}$ have the diameter d_{ps} .

and h_i are the heights of the spherical caps

$$h_1 = \frac{(d_b/2 - d_f/2 + l)(d_b/2 + d_f/2 - l)}{2l}, \quad (A11)$$

$$h_2 = \frac{(d_f/2 - d_b/2 + l)(d_f/2 + d_b/2 - l)}{2l}.$$

The moment of inertia for a spherical cap about the x - as well as y -direction is

$$I_{Sc_i,(x,y)} = \rho \int_V (x^2 + z^2) dV$$

$$= \rho \int_0^{2\pi} d\varphi \int_0^{a \cos(\frac{d_i/2 - h_i}{d_i/2})} d\theta \sin \theta$$

$$\times \int_{\frac{d_i/2 - h_i}{\cos \theta}}^{d_i/2} dr r^2 [(\cos \varphi \sin \theta r)^2 + (\cos \theta r)^2]$$

$$= \rho \pi \frac{1}{60} h_i^2 (-9h_i^3 + 45h_i^2 d_i/2 - 80h_i (d_i/2)^2 + 60(d_i/2)^3), \quad (A12)$$

and about the z -direction is

$$I_{Sc_i,z} = \rho \int_V (x^2 + y^2) dV$$

$$= \rho \int_0^{2\pi} d\varphi \int_0^{a \cos(\frac{d_i/2 - h_i}{d_i/2})} d\theta \sin \theta$$

$$\times \int_{\frac{d_i/2 - h_i}{\cos \theta}}^{d_i/2} dr r^2 [(\cos \varphi \sin \theta r)^2 + (\sin \varphi \sin \theta r)^2]$$

$$= \rho \pi \frac{1}{30} h_i^3 (3h_i^2 - 15h_i d_i/2 + 20(d_i/2)^2). \quad (A13)$$

By using the moment of inertia of a sphere $I_{Sp_i} = \frac{8}{15} \rho \pi (d_i/2)^5$ and with the use of the parallel axis theorem, we compute the moments of inertia of the swimmer as

$$I_{(x,y)} = I_{Sp_1,(x,y)} - I_{Sc_1,(x,y)} + \rho(V_1 - V_{Sc_1})x_1^2, \quad (A14)$$

$$I_z = I_{Sp_1,z} + I_{Sp_2,z} - I_{Sc_1,z} - I_{Sc_2,z}. \quad (A15)$$

3. Multiparticle collision dynamics

To simulate a fluid at fixed density ρ and temperature T surrounding the swimmers, we use the MPCD algorithm, which is a mesoscopic, particle based method⁴⁶ to simulate a fluid at the Navier–Stokes level of description. We include the Andersen thermostat and the conservation of angular momentum into the MPCD dynamics; the resulting algorithm is usually denoted as MPC-AT+a.^{47,64,65} The fluid is modeled using N_f point-like particles of mass m , whose dynamics are executed through two steps: the streaming step and the collision step. In the streaming step the fluid particles' positions \mathbf{r}_i , $i \in [1, N_f]$ are updated according to

$$\mathbf{r}_i(t + \delta t) = \mathbf{r}_i(t) + \mathbf{v}_i(t)\delta t, \quad (A16)$$

where $\mathbf{v}_i(t)$ is their velocity and δt is the MPCD timestep.

The collision step mediates the interactions between the particles. Here, the system is divided into N_c collision cells with a regular grid of lattice constant a . The center of mass velocity in each cell $\mathbf{C}(i)$ is calculated and remains constant during the collision step, whereas the fluctuating part of the velocity of every fluid particle i is randomized, which mimics the collision between particles. Hence, the velocity of particle i is updated as follows⁶⁴

$$\mathbf{v}'_i = \frac{1}{N_{C(i)}} \sum_{j \in C(i)} \mathbf{v}_j + \mathbf{v}_i^{\text{ran}} - \frac{1}{N_{C(i)}} \sum_{j \in C(i)} \mathbf{v}_j^{\text{ran}}$$

$$+ m \left\{ \mathbf{\Pi}^{-1} \sum_{j \in C(i)} [\mathbf{r}_{j,c} \times (\mathbf{v}_i - \mathbf{v}_i^{\text{ran}})] \right\} \times \mathbf{r}_{i,c}, \quad (A17)$$

where the random velocity $\mathbf{v}_i^{\text{ran}}$ has components sampled from a Gaussian distribution with zero mean and variance $\sqrt{k_B T/m}$, $N_{C(i)}$ is the number of fluid and ghost particles (see Section A4) in cell $\mathbf{C}(i)$. The vector $\mathbf{r}_{j,c}$ is the position of the neighboring particle j relative to the center of mass of the cell $\mathbf{C}(i)$. In eqn (A17), $\mathbf{\Pi}^{-1}$ is the inverse of the moment of inertia tensor $\mathbf{\Pi} \equiv \sum_{j \in C(i)} m[(\mathbf{r}_j \cdot \mathbf{r}_j)\mathbf{I} - \mathbf{r}_j \otimes \mathbf{r}_j]$ for the fluid particles in cell $\mathbf{C}(i)$. Note that $\mathbf{\Pi}^{-1}$ is a dynamical quantity that has to be updated at every timestep, and it also includes the ghost particles within the swimmer (see Section A4).

To ensure Galilean invariance and avoid the build-up of spurious correlations in the velocities,⁶⁶ the usual grid shift is performed at each timestep, that is, the grid is shifted by a random vector, whose components are uniformly distributed in the interval $[-a/2, a/2]$.



4. Coupling of the swimmer's and fluid's dynamics

No velocity field is prescribed in our model of microswimmers. Locomotion is achieved by obeying the conservation of momentum in the collisions between the fluid particles and the swimmers; the shape asymmetry then induces self-propulsion. Two physical effects need to be included: we impose no-slip boundary conditions on the model swimmer's surface, and the force poles are explicitly included (see Fig. 1). Both effects induce modifications of the streaming and collision steps of the MPCD algorithm that we explain in the following.

a. Streaming step. To ensure the no-slip boundary condition the bounce-back rule⁶⁷ is applied to the MPCD particles that hit the spheres during the streaming step. The velocity of the fluid particle is reversed and the change in momentum is given by

$$\mathbf{J}_i = 2m[\mathbf{v}_i - \mathbf{U} - \boldsymbol{\Omega} \times (\tilde{\mathbf{r}}_i - \mathbf{R})], \quad (\text{A18})$$

where \mathbf{R} is the center-of-mass position of the swimmer colliding with the fluid particle, \mathbf{U} and $\boldsymbol{\Omega}$ are the linear and angular velocity of the swimmer, $\tilde{\mathbf{r}}_i$ is the position of the fluid particle upon collision with the sphere. The updated fluid particle velocity reads

$$\mathbf{v}'_i = \mathbf{v}_i - \mathbf{J}_i/m. \quad (\text{A19})$$

In addition, the fluid particles are reflected back along the direction of their initial velocity. For this, we use an exact ray tracing method to detect the collision of the MPCD particle onto the swimmer's surface. If a collision is detected the MPCD particle is propagated back onto the swimmer's surface and then the bounce-back rule is applied. If the particle travels a fraction λ , $0 < \lambda < 1$ of the timestep towards the swimmer, then after the collision with the swimmer, it will travel for the time $(1 - \lambda)\delta t$ away from the swimmer's surface. Furthermore, we allow for multiple collisions within the same timestep; this has been shown to prevent spurious depletion forces among colloids.⁶⁸ The new linear and angular velocities of the swimmer after the collision with the fluid particles read

$$\mathbf{U}' = \mathbf{U} + \sum_i \mathbf{J}_i/M, \quad (\text{A20})$$

$$\boldsymbol{\Omega}' = \boldsymbol{\Omega} + \mathbf{I}_m^{-1} \sum_i (\mathbf{r}_i - \mathbf{R}) \times \mathbf{J}_i. \quad (\text{A21})$$

The force poles are added as external force regions⁶⁹ in the streaming step for each swimmer. This is done by modifying the streaming step inside the force regions to

$$\mathbf{r}_i(t + \delta t) = \mathbf{r}_i(t) + \mathbf{v}_i(t)\delta t + \mathbf{f}_{ac}^{lab} \frac{\delta t^2}{2}, \quad (\text{A22})$$

$$\mathbf{v}_i(t + \delta t) = \mathbf{v}_i(t) + \mathbf{f}_{ac}^{lab} \delta t, \quad (\text{A23})$$

where the force in the lab frame reads

$$\mathbf{f}_{ac}^{lab} \equiv \mathbf{f}_{ac} - [\mathbf{U} + \boldsymbol{\Omega} \times (\mathbf{r}_i - \mathbf{R})]/\delta t, \quad (\text{A24})$$

and \mathbf{f}_{ac} is the active force discussed in the following. The flow fields are modeled by force poles. While mathematically such force poles are point forces, any numerical implementation must mollify this requirement.

Pullers. The flow field is modeled by three Stokeslets, and the active force \mathbf{f}_{ac}^{lab} is applied to $R_{pl,1}$, $R_{pl,2}$ and $R_{pl,2'}$ [see Fig. 6(a)]. The region $R_{pl,1}$ with diameter $d_{pl,1}$ is located at the rear of the swimmer and its force points into the direction of the swimmer's orientation. The other two regions $R_{pl,2}$ and $R_{pl,2'}$ are placed on the side of the swimmer and have the opposite orientation. The angle α_{pl} between the orientation of the puller and the line connecting the center of mass C and the midpoint of the region $R_{pl,2}$ (or $R_{pl,2'}$) defines their position on the boundary of the swimmer. The diameter of both $R_{pl,2}$ and $R_{pl,2'}$ is $d_{pl,2} = d_{pl,1}/(2)^{1/3}$, such that they have half the volume of $R_{pl,1}$, making the fluid force free. The total force in the region $R_{pl,1}$ is $f = f_0 \frac{1}{6} \pi d_{pl,1}^3 \rho$ and in the regions $R_{pl,2}$, $R_{pl,2'}$ is $f = f_0 \frac{1}{6} \pi d_{pl,2}^3 \rho$.

Pushers. The flow field is modeled by a force dipole. We apply the force \mathbf{f}_{ac}^{lab} to all fluid particles located within spherical regions [see Fig. 6(b)]. The regions $R_{ps,1}$ and $R_{ps,2}$ where \mathbf{f}_{ac}^{lab} is applied are equally sized spheres with diameter d_{ps} and the two forces \mathbf{f}_{ac} are equal and opposite, to ensure that the fluid is overall force free. To generate a smooth flow on the boundary of the swimmer the direction of the applied force in regions $R_{ps,1}$ and $R_{ps,2}$ is modeled as follows. For fluid particles $\mathbf{r}_i \in R_{ps,1}$ or $R_{ps,2}$ we apply the force

$$\mathbf{f}_{ac}^b = \begin{cases} \begin{pmatrix} 0 \\ 0 \\ 1 \end{pmatrix} f_0, & \text{if } s_z^b > d_{ps}/2, \\ \begin{pmatrix} \frac{2s_z^b}{d_{ps}} s_x^b / |s^b| \\ \frac{2s_z^b}{d_{ps}} s_y^b / |s^b| \\ \left(\frac{2s_z^b}{d_{ps}} - 1 \right) s_z^b / |s^b| \end{pmatrix} f_0, & \text{if } s_z^b < d_{ps}/2. \end{cases} \quad (\text{A25})$$

Here, $\mathbf{s}^b = (s_x^b, s_y^b, s_z^b)^T$ is the distance between the MPCD particle and the center of the region $R_{ps,1}$ or $R_{ps,2}$. The small, black arrows in Fig. 6(b) give a schematic representation of the flow field arising from eqn (A25). As before the superscript b denotes the body frame, in which the swimmer's orientation is aligned with the z axis. The constant f_0 gives the strength of the force that is applied. The total force in one of the two regions can be estimated by integrating eqn (A25), which yields $f = f_0 \frac{5}{48} \pi d_{ps}^3 \rho$. This takes into account the redirection of the force on the boundary of the swimmer and the density ρ of the fluid.

b. Collision step. To guarantee the no-slip boundary conditions on the surface of the swimmers, it is necessary to fill each swimmer with ghost particles, such that the collision step can be properly executed.⁶⁵ The positions of the ghost particles \mathbf{r}_i^g are uniformly distributed within the swimmer,[‡] and are advected with the swimmer in each timestep. The ghost

[‡] We recommend to fill the swimmer with multiple ghost particles, rather than using a single ghost particle of large mass, as this would result in a wrong value of the torque.



particles density is matched to the fluid's density so as to make the swimmer neutrally buoyant. Before every collision step the ghost velocities \mathbf{v}_i^g are updated according to

$$\mathbf{v}_i^g = \mathbf{U} + \boldsymbol{\Omega} \times (\mathbf{r}_i^g - \mathbf{R}) + \mathbf{v}_i^{\text{ran}}, \quad (\text{A26})$$

where the components of $\mathbf{v}_i^{\text{ran}}$ are sampled from a Gaussian distribution. The ghost particles then (together with the fluid particles) take part in the collision step [see eqn (A17)], and their velocities are updated to $\mathbf{v}_i^{g'}$. The resulting change in linear momentum due to the ghost particles is $\mathbf{J}_i^g = m(\mathbf{v}_i^{g'} - \mathbf{v}_i^g)$ and the change in angular momentum is $\mathbf{L}_i^g = (\mathbf{r}_i^g - \mathbf{R}) \times \mathbf{J}_i^g$. These changes are then transferred to the swimmer¹⁷

$$\mathbf{U}' = \mathbf{U} + \sum_i \mathbf{J}_i^g / M, \quad (\text{A27})$$

$$\boldsymbol{\Omega}' = \boldsymbol{\Omega} + \mathbf{I}_m^{-1} \sum_i \mathbf{L}_i^g. \quad (\text{A28})$$

5. Algorithm implementation

In this section we explain how the present algorithm is implemented. First, note that the MPCD algorithm scales as $\mathcal{O}(N)$, and thus is particularly prone to an efficient implementation with parallel programming. We therefore implemented the entire dynamics (both swimmer and MPCD) on graphics processing unit (GPU) cards using the Nvidia CUDA language. Parallelization of the MPCD algorithm is rather straightforward. The streaming step is performed for each fluid particle independently in a separate CUDA kernel, whereas ghost particles are simply translated together with the corresponding swimmer. Then, a kernel for each particle is started to carry out the bounce-back rule and afterwards a kernel for each particle is started to apply the periodic boundary conditions. The collision step eqn (A17) is implemented with the following kernels:

1. the cell of each particle is found and the center of mass for each cell is found by starting a kernel for each particle;
2. the two sums over the velocities in eqn (A17) are computed, where a kernel for each velocity component of each particle is started;
3. a kernel for each particle is started to compute the number of particles in each cell;
4. a kernel for each cell is started to normalize the velocities and compute the center of mass;
5. a kernel for each particle is started to compute its position with respect to the center of mass;
6. a kernel for each particle is started to compute the cross product in eqn (A17) and the contributions in each cell are summed;
7. six kernels for each particle are started to compute the contribution to the six components of the inertia tensor in the corresponding cell;
8. a kernel for each cell is started to compute the inverse of the respective inertia tensors;
9. for each cell a kernel is started to compute the curly bracket in eqn (A17);

10. a kernel for each particle is started to add all contributions of eqn (A17) and finish the collision step, while considering the rule for ghost particles eqn (A26);

11. a kernel for each ghost particle is started, which computes the momentum and angular momentum transfer [eqn (A27) and (A28)] to the swimmers.

Some of these computations could be combined into single kernels, but it is computationally more efficient to start many kernels with small computations, which we have opted for in this algorithm. After the MPCD steps the rigid body dynamics part (see also Section A1) of the code is executed. It consists of the following kernels, one for each swimmer:

1. the velocity and angular velocity stemming from the fluid interaction are added to the swimmers;
2. the positions and quaternions are updated;
3. periodic boundary conditions are applied;
4. the neighbor list between swimmers is updated (here we use a linked list);
5. the steric forces and torques are computed;
6. the velocities and angular velocities are updated.

This concludes the algorithm, which now goes back to the streaming step of the MPCD part.

6. Computational details

We carried out three-dimensional simulations with an average of $\langle N_C \rangle = 20$ fluid particles per cell. The timestep of the MPCD algorithm is fixed to $\delta t = 10^{-2} \sqrt{ma^2/(k_B T)}$, whereas the MD timestep is $\delta t_{\text{MD}} = 5 \times 10^{-4} \sqrt{ma^2/(k_B T)}$. The resulting kinematic viscosity $\nu = \eta/\rho$ of the fluid for the MPC-AT+a algorithm (including both kinetic and collisional contribution) can be calculated exactly as $\nu = 3.88a\sqrt{k_B T/m}$.^{47,65,70} Simulations using a forced flow (for details see ref. 69) produced a viscosity of $\nu = 3.69a\sqrt{k_B T/m}$.

The large sphere F associated to the stroke-averaged flagella of the swimmer has a diameter of $d_f = 7a$, while the small sphere B associated to the body of the swimmer has $d_b = 3a$, and the distance between the spheres centers is $l = 7a$. The choice of the geometrical parameters is dictated by a combination of factors. First, it is computationally convenient to make the swimmers' linear size a few times the grid spacing a . Second, inspired by the geometric properties of *C. reinhardtii* a ratio $d_f/d_b \gtrsim 2$ is advisable.¹⁰ For the sake of clarity in the comparison of our results, we maintain the same geometry also for pushers. The energy scale of the steric interactions is set to $\varepsilon = 10k_B T$. For pushers we fix the diameter of the force dipole regions $R_{\text{ps},1}$ and $R_{\text{ps},2}$ to $d_{\text{ps}} = 3a$. The region $R_{\text{pl},1}$ of the pullers has the same diameter $d_{\text{pl},1} = 3a$ and accordingly the regions $R_{\text{pl},2}$ and $R_{\text{pl},2'}$ have the diameter $d_{\text{pl},2} = 3a/(2)^{1/3}$. The angle between the swimmers orientation and the line connecting the center of mass of the pullers C to the midpoint of the regions $R_{\text{pl},2}$ and $R_{\text{pl},2'}$ is $\alpha_{\text{pl}} = 107^\circ$.

To initialize the simulations, we distribute the swimmers homogeneously (and without overlaps) across a cubic box with periodic boundary conditions.



Appendix B: estimate of maximum from theoretical prediction

To estimate the maximum predicted from the analytical treatment, we computed the maximum of the eigenvalues in eqn (30) for pushers and eqn (25) for pullers. As a first step, we have to find estimates for both the wavenumber k and the constant quantifying the steric interactions ζ . Since we expect the hydrodynamic interactions to be relevant on the size of the swimmer, we chose the distance between the force poles l to determine the characteristic wavenumber $k = 2\pi/l$. The constant ζ quantifying the steric interactions can be estimated from ref. 58

$$\zeta = v_0^2 \sigma_s \tau_c \quad (\text{A29})$$

where v_0 is the propulsion speed, σ_s the geometrical cross section, and τ_c is the collision time. The collision time can be estimated from the center-of-mass distance of two colliding swimmers, where we considered collisions as shown in Fig. S5 and S6 (ESI[†]). The resulting collision time for pullers is $\tau_c = 9.5a/\sqrt{k_B T/m}$ and for pushers $\tau_c = 18.0a/\sqrt{k_B T/m}$. The propulsion speed is extracted from Fig. 3 and the geometrical cross section is $\sigma_s = 4\pi\sigma^2$. Here, $\sigma = l/2 = 7.5a$ is the effective steric radius of the swimmer also estimated from the distance of the force poles. To finally obtain a filling fraction we use $\phi = c_0(V_B + V_F - V_{O1})$ [see eqn (3)].

Acknowledgements

We gratefully acknowledge insightful conversations with Johannes Blaschke, Jens Elgeti, Stephan Herminghaus, Sebastian Mair, and Kuang-Wu Lee. We also gratefully acknowledge support from the Deutsche Forschungsgemeinschaft (SFB 937, project A20). Open Access funding provided by the Max Planck Society.

References

- 1 A. Baskaran and M. C. Marchetti, *Proc. Natl. Acad. Sci. U. S. A.*, 2009, **106**, 15567–15572.
- 2 B. Ezhilan, M. J. Shelley and D. Saintillan, *Phys. Fluids*, 2013, **25**, 070607.
- 3 J. Elgeti, R. G. Winkler and G. Gompper, *Rep. Prog. Phys.*, 2015, **78**, 056601.
- 4 E. Lauga, W. R. DiLuzio, G. M. Whitesides and H. A. Stone, *Biophys. J.*, 2006, **90**, 400–412.
- 5 A. P. Berke, L. Turner, H. C. Berg and E. Lauga, *Phys. Rev. Lett.*, 2008, **101**, 038102.
- 6 T. Ostapenko, F. J. Schwarzendahl, T. J. Böddeker, C. T. Kreis, J. Cammann, M. G. Mazza and O. Bäumchen, *Phys. Rev. Lett.*, 2018, **120**, 068002.
- 7 H. Wioland, F. G. Woodhouse, J. Dunkel, J. O. Kessler and R. E. Goldstein, *Phys. Rev. Lett.*, 2013, **110**, 268102.
- 8 H. Wioland, E. Lushi and R. E. Goldstein, *New J. Phys.*, 2016, **18**, 075002.
- 9 M. F. Copeland and D. B. Weibel, *Soft Matter*, 2009, **5**, 1174–1187.
- 10 H. H. Wensink, J. Dunkel, S. Heidenreich, K. Drescher, R. E. Goldstein, H. Löwen and J. M. Yeomans, *Proc. Natl. Acad. Sci. U. S. A.*, 2012, **109**, 14308–14313.
- 11 C. Dombrowski, L. Cisneros, S. Chatkaew, R. E. Goldstein and J. O. Kessler, *Phys. Rev. Lett.*, 2004, **93**, 098103.
- 12 E. M. Purcell, *Am. J. Phys.*, 1977, **45**, 3–11.
- 13 M. J. Lighthill, *Commun. Pure Appl. Math.*, 1952, **5**, 109–118.
- 14 J. R. Blake, *J. Fluid Mech.*, 1971, **46**, 199–208.
- 15 T. Ishikawa and T. J. Pedley, *Phys. Rev. Lett.*, 2008, **100**, 088103.
- 16 M. T. Downton and H. Stark, *J. Phys.: Condens. Matter*, 2009, **21**, 204101.
- 17 I. O. Götzke and G. Gompper, *Phys. Rev. E: Stat., Nonlinear, Soft Matter Phys.*, 2010, **82**, 041921.
- 18 I. Llopis and I. Pagonabarraga, *J. Non-Newtonian Fluid Mech.*, 2010, **165**, 946–952.
- 19 A. A. Evans, T. Ishikawa, T. Yamaguchi and E. Lauga, *Phys. Fluids*, 2011, **23**, 111702.
- 20 A. Zöttl and H. Stark, *Phys. Rev. Lett.*, 2012, **108**, 218104.
- 21 F. Alarcón and I. Pagonabarraga, *J. Mol. Liq.*, 2013, **185**, 56–61.
- 22 K. Ishimoto and E. A. Gaffney, *Phys. Rev. E*, 2013, **88**, 062702.
- 23 J. J. Molina, Y. Nakayama and R. Yamamoto, *Soft Matter*, 2013, **9**, 4923–4936.
- 24 A. Zöttl and H. Stark, *Phys. Rev. Lett.*, 2014, **112**, 118101.
- 25 M. Theers, E. Westphal, G. Gompper and R. G. Winkler, *Soft Matter*, 2016, **12**, 7372–7385.
- 26 J. Blaschke, M. Maurer, K. Menon, A. Zöttl and H. Stark, *Soft Matter*, 2016, **12**, 9821–9831.
- 27 F. Alarcon, C. Valeriani and I. Pagonabarraga, *Soft Matter*, 2017, **13**, 814–826.
- 28 T. Ishikawa, J. T. Locsei and T. J. Pedley, *Phys. Rev. E: Stat., Nonlinear, Soft Matter Phys.*, 2010, **82**, 021408.
- 29 G.-J. Li and A. M. Ardekani, *Phys. Rev. E: Stat., Nonlinear, Soft Matter Phys.*, 2014, **90**, 013010.
- 30 I. Pagonabarraga and I. Llopis, *Soft Matter*, 2013, **9**, 7174–7184.
- 31 R. Matas-Navarro, R. Golestanian, T. B. Liverpool and S. M. Fielding, *Phys. Rev. E: Stat., Nonlinear, Soft Matter Phys.*, 2014, **90**, 032304.
- 32 J. de Graaf, H. Menke, A. J. T. M. Mathijssen, M. Fabritius, C. Holm and T. N. Shendruk, *J. Chem. Phys.*, 2016, **144**, 134106.
- 33 L. P. Fischer, T. Peter, C. Holm and J. de Graaf, *J. Chem. Phys.*, 2015, **143**, 084107.
- 34 J. de Graaf, T. Peter, L. P. Fischer and C. Holm, *J. Chem. Phys.*, 2015, **143**, 084108.
- 35 R. W. Nash, R. Adhikari, J. Tailleur and M. E. Cates, *Phys. Rev. Lett.*, 2010, **104**, 258101.
- 36 R. W. Nash, R. Adhikari and M. E. Cates, *Phys. Rev. E: Stat., Nonlinear, Soft Matter Phys.*, 2008, **77**, 026709.
- 37 J. P. Hernandez-Ortiz, C. G. Stoltz and M. D. Graham, *Phys. Rev. Lett.*, 2005, **95**, 204501.
- 38 J. Stenhammar, C. Nardini, R. W. Nash, D. Marenduzzo and A. Morozov, *Phys. Rev. Lett.*, 2017, **119**, 028005.
- 39 L. F. Valadares, Y.-G. Tao, N. S. Zacharia, V. Kitaev, F. Galembeck, R. Kapral and G. A. Ozin, *Small*, 2010, **6**, 565–572.



- 40 D. Saintillan and M. J. Shelley, *Phys. Rev. Lett.*, 2007, **99**, 058102.
- 41 R. Singh, S. Ghose and R. Adhikari, *J. Stat. Mech.: Theory Exp.*, 2015, **2015**, P06017.
- 42 J. W. Swan, J. F. Brady, R. S. Moore and C. 174, *Phys. Fluids*, 2011, **23**, 071901.
- 43 D. Saintillan and M. J. Shelley, *J. R. Soc., Interface*, 2011, DOI: 10.1098/rsif.2011.0355.
- 44 K. Drescher, J. Dunkel, L. H. Cisneros, S. Ganguly and R. E. Goldstein, *Proc. Natl. Acad. Sci. U. S. A.*, 2011, **108**, 10940–10945.
- 45 K. Drescher, R. E. Goldstein, N. Michel, M. Polin and I. Tuval, *Phys. Rev. Lett.*, 2010, **105**, 168101.
- 46 A. Malevanets and R. Kapral, *J. Chem. Phys.*, 1999, **110**, 8605–8613.
- 47 G. Gompper, T. Ihle, D. M. Kroll and R. G. Winkler, *Multi-particle collision dynamics: a particle-based mesoscale simulation approach to the hydrodynamics of complex fluids*, Springer, 2009, vol. Advanced computer simulation approaches for soft matter sciences III, pp. 1–87.
- 48 T. Ishikawa, J. T. Locsei and T. J. Pedley, *J. Fluid Mech.*, 2008, **615**, 401–431.
- 49 D. Saintillan and M. J. Shelley, *Phys. Rev. Lett.*, 2008, **100**, 178103.
- 50 P. T. Underhill, J. P. Hernandez-Ortiz and M. D. Graham, *Phys. Rev. Lett.*, 2008, **100**, 248101.
- 51 A. Wysocki, J. Elgeti and G. Gompper, *Phys. Rev. E: Stat., Nonlinear, Soft Matter Phys.*, 2015, **91**, 050302.
- 52 E. Lushi, V. Kantsler and R. E. Goldstein, *Phys. Rev. E*, 2017, **96**, 023102.
- 53 S. E. Spagnolie and E. Lauga, *J. Fluid Mech.*, 2012, **700**, 105–147.
- 54 A. Zöttl and H. Stark, *J. Phys.: Condens. Matter*, 2016, **28**, 253001.
- 55 J. K. G. Dhont, *An introduction to dynamics of colloids*, Elsevier, 1996.
- 56 C. H. Rycroft, *Chaos*, 2009, **19**, 041111.
- 57 J. Bialké, H. Löwen and T. Speck, *EPL*, 2013, **103**, 30008.
- 58 J. Stenhammar, A. Tiribocchi, R. J. Allen, D. Marenduzzo and M. E. Cates, *Phys. Rev. Lett.*, 2013, **111**, 145702.
- 59 H. Goldstein, C. P. Poole and J. L. Safko, *Classical Mechanics*, Addison-Wesley, 3rd edn, 2001.
- 60 I. P. Omelyan, *Phys. Rev. E: Stat. Phys., Plasmas, Fluids, Relat. Interdiscip. Top.*, 1998, **58**, 1169–1172.
- 61 M. P. Allen and D. J. Tildesley, *Computer Simulation of Liquids*, Oxford University Press, 1989.
- 62 J. D. Weeks, D. Chandler and H. C. Andersen, *J. Chem. Phys.*, 1971, **54**, 5237–5247.
- 63 I. N. Bronstein and K. A. Semendjajew, *Taschenbuch der Mathematik*, BSB B. G. Teubner Verlagsgesellschaft, Nauka-Verlag, Leipzig, Moskau, 19th edn, 1979.
- 64 H. Noguchi, N. Kikuchi and G. Gompper, *Europhys. Lett.*, 2007, **78**, 10005.
- 65 I. O. Götzke, H. Noguchi and G. Gompper, *Phys. Rev. E: Stat., Nonlinear, Soft Matter Phys.*, 2007, **76**, 046705.
- 66 T. Ihle and D. M. Kroll, *Phys. Rev. E: Stat., Nonlinear, Soft Matter Phys.*, 2001, **63**, 020201.
- 67 A. Lamura, G. Gompper, T. Ihle and D. M. Kroll, *Europhys. Lett.*, 2001, **56**, 319.
- 68 J. T. Padding and A. A. Louis, *Phys. Rev. E: Stat., Nonlinear, Soft Matter Phys.*, 2006, **74**, 031402.
- 69 D. S. Bolintineanu, J. B. Lechman, S. J. Plimpton and G. S. Grest, *Phys. Rev. E: Stat., Nonlinear, Soft Matter Phys.*, 2012, **86**, 066703.
- 70 H. Noguchi and G. Gompper, *Phys. Rev. E: Stat., Nonlinear, Soft Matter Phys.*, 2008, **78**, 016706.



5.2 *Supplementary Information to Publication: Maximum in density heterogeneities of active swimmers*

Supplementary Information: Maximum in density heterogeneities of active swimmers

Fabian Jan Schwarzendahl^{1,2} and Marco G. Mazza¹

¹*Max-Planck-Institute for Dynamics and Self-Organization, Am Fassberg 17, 37077 Göttingen, Germany*

²*Georg-August-Universität Göttingen, Friedrich-Hund-Platz 1, 37077 Göttingen, Germany*

I. CHARACTERIZATION OF THE ACTIVE HYDRODYNAMICS

In the following we further characterize the fluid dynamics and the interactions mediated by the hydrodynamics in our microswimmer model.

A. Flow field scaling

In unbounded space, the fundamental solutions of the Stokes equation under point-like forcing has generally an algebraic decay with distance. It is therefore important to verify that our model reproduces such algebraic decay of the velocity over some interval of distances. Figure S1 shows the scaling behavior of the flow field behind both puller and pusher-type swimmers. In addition to the simulated data the theoretical prediction for a pusher (force dipole) and puller (three stokeslets), as well as the respective scalings are displayed. We find a good agreement with the theoretical prediction and the respective scaling laws.

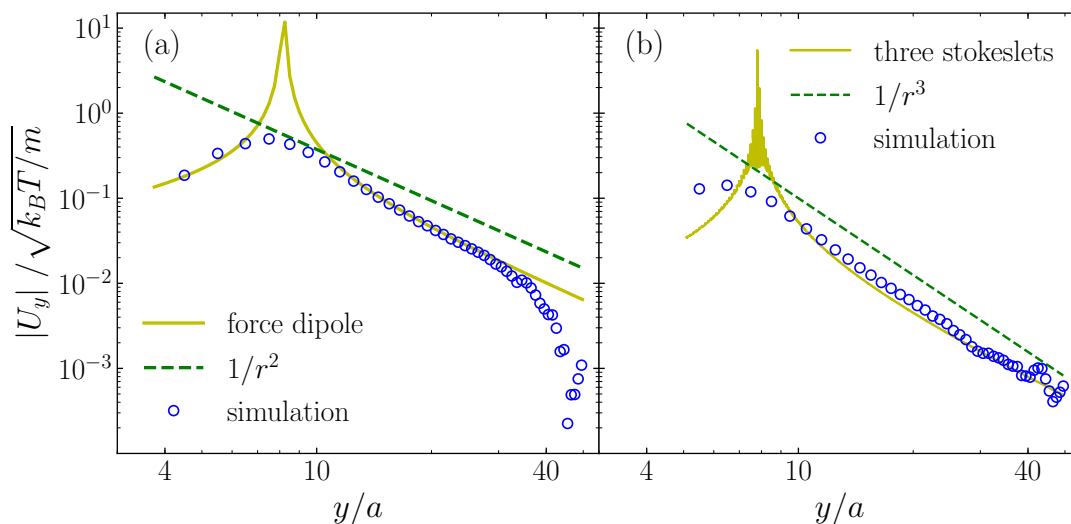


FIG. S1. Scaling behavior of the flow field behind (a) a pusher and (b) puller microswimmer. Blue circles show the numerical calculations, yellow continuous lines show the theoretical prediction of (a) a force dipole and (b) three Stokeslets, and green dashed lines show the expected power-law scaling for (a) $1/r^2$ and (b) $1/r^3$.

B. Two particle interactions

To characterize the two-particle interactions of our model, we first simulate two swimmers starting in a parallel configuration $e_1 \cdot e_2 = 1$, for initial center-of-mass (CoM) to center-of-mass distances $d_{\text{CoM}} = 7a$ and $d_{\text{CoM}} = 12a$. Second, we simulate two swimmers starting with a relative angle of $\pi/4$ and $\pi/2$, where the initial distance is $d_{\text{CoM}} = 12a$.

In the following, we will show the time evolution of d_{CoM} as well as the orientational correlation function $\langle \cos \theta \rangle = \langle \mathbf{e}_1 \cdot \mathbf{e}_2 \rangle$ for both pusher and puller type swimmers. Additionally, we provide videos of each simulation to help understand the dynamics of the collisions.

a. Parallel configuration with $d_{\text{CoM}} = 7a$. Figure S2(a) shows a scattering event between two pusher-type swimmers. The swimmers attract each other and stay in a parallel configuration until the steric interactions reorient them and they then start diverging from each other. Puller-type swimmers [Fig. S2(b)] immediately turn away from each other and perform a reorientation of an angle of π such that they are parallel again. Immediately after this, a secondary collision causes them to turn away from each other and start swimming into different directions. See also video `2_pusher_d7a.avi` for pushers, and video `2_puller_d7a.avi` for pullers.

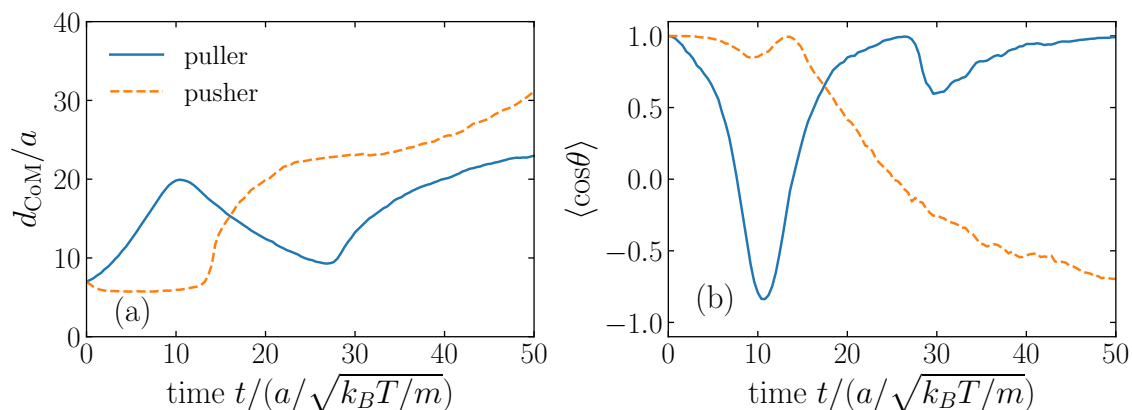


FIG. S2. Scattering event between two swimmers starting in a parallel configuration, with $d_{\text{CoM}} = 7a$. Solid lines show puller and dashed lines pusher-type swimmers. (a) Center-of-mass to center-of-mass distance of the two swimmers. (b) Orientational correlation of the swimmers.

b. Parallel configuration with $d_{\text{CoM}} = 12a$. Figure S3(a) shows a scattering event between two pusher-type swimmers. The pushers attract each other and stay in a parallel configuration until the steric interactions reorient them and they then start diverging from each other. Puller-type swimmers [Fig. S3(b)] quickly reorient away from each other and become parallel again, assuming a configuration in which one swimmer is behind the other.

For the same initial configuration we also computed the flow field, which can be seen in Fig. S4. The pusher-type swimmers have almost a stagnation point between them, which gives a relative attraction and corresponding flow lines favor a parallel configuration. This is in accordance with the behavior seen in Fig. S3(a) and the video `2_pusher_d12a.avi`. Puller-type swimmers exhibit a region with very high velocity between them, favoring a reorientation as seen by the orientational correlation function in Fig. S3. The configuration in which the swimmers are behind each other is assumed because of the very low flow velocity at the point $x = 0a$, $y = -10a$. See also video `2_pusher_d12a.avi` for pushers, and video `2_puller_d12a.avi` for pullers.

c. Relative angle $\pi/4$ with $d_{\text{CoM}} = 12a$. Figure S5(a) shows a scattering event between two pusher-type swimmers. The pushers collide and turn away from each other because of a complex interplay of hydrodynamic and steric interactions. Puller-type swimmers [Fig. S5(b)] collide, immediately turn away from each other and swim into different directions. See also video `2_pusher_d12a_45deg.avi` for pushers and video `2_puller_d12a_45deg.avi` for pullers.

d. Relative angle $\pi/2$ with $d_{\text{CoM}} = 12a$. Figure S6(a) shows a scattering event between two pusher-type swimmers. The pushers collide and turn away from each other because of a complex interplay of hydrodynamic and steric interactions. Puller-type swimmers [Fig. S6(b)] collide, immediately turn away from each other and swim into different directions. See also video `2_pusher_d12a_90deg.avi` for pushers and video `2_puller_d12a_90deg.avi` for pullers.

In summary, the behavior of pusher-type swimmers due to hydrodynamic interactions can be summarized by saying that they attract each other and align with each other. This behavior is expected, as it is shown experimentally by

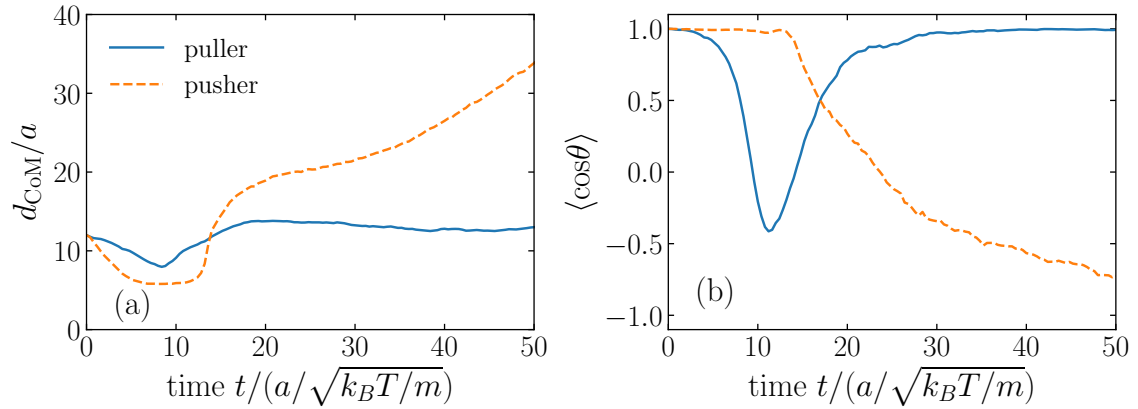


FIG. S3. Scattering event between two swimmers starting in parallel configuration, with $d_{\text{CoM}} = 12a$. Solid lines show puller and dashed lines pusher-type swimmers. (a) Center-of-mass to center-of-mass distance of the two swimmers. (b) Orientational correlation of the swimmers.

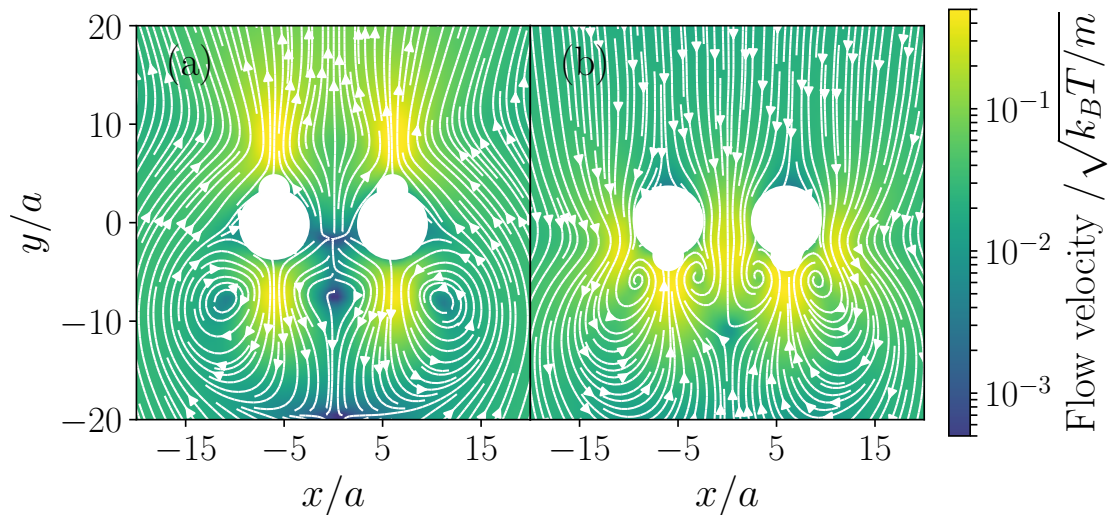


FIG. S4. Time-averaged flow field generated by (a) two model pushers (b) two model pullers. The swimmers are kept in a parallel configuration with $d_{\text{CoM}} = 12a$. We show cross-sections on the x - y plane at $z = 0$. The force strength is $f_0 = 50k_B T/a$. The large central white regions mark the hard cores of the active swimmers. The thin lines with arrows mark the streamlines, while the color code indicates the magnitude of the flow velocity normalized to the thermal velocity.

[1] and suggested by theoretical studies [2].

The behavior of puller-type swimmers due to their flow field can be summarized as generally dealigning. This behavior is also suggested by theoretical studies [2]. Interestingly, for an initially close-to-parallel alignment we observe a chain-like swimming behavior after the scattering event. This chain-like motion is mediated by the three-Stokeslet flow field.

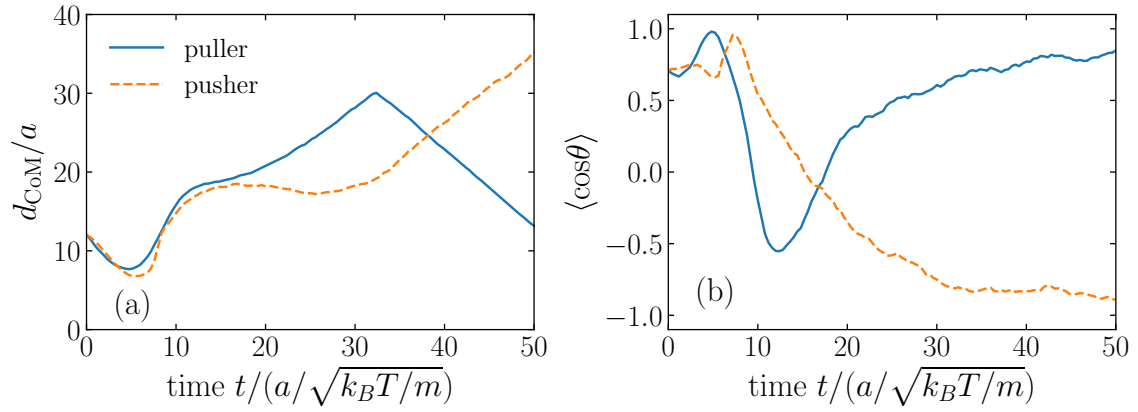


FIG. S5. Scattering event between two swimmers starting with a relative angle of $\pi/4$ and $d_{\text{CoM}} = 12a$. Solid lines show puller and dashed lines pusher-type swimmers. (a) Center-of-mass to center-of-mass distance of the two swimmers. (b) Orientational correlation of the swimmers.

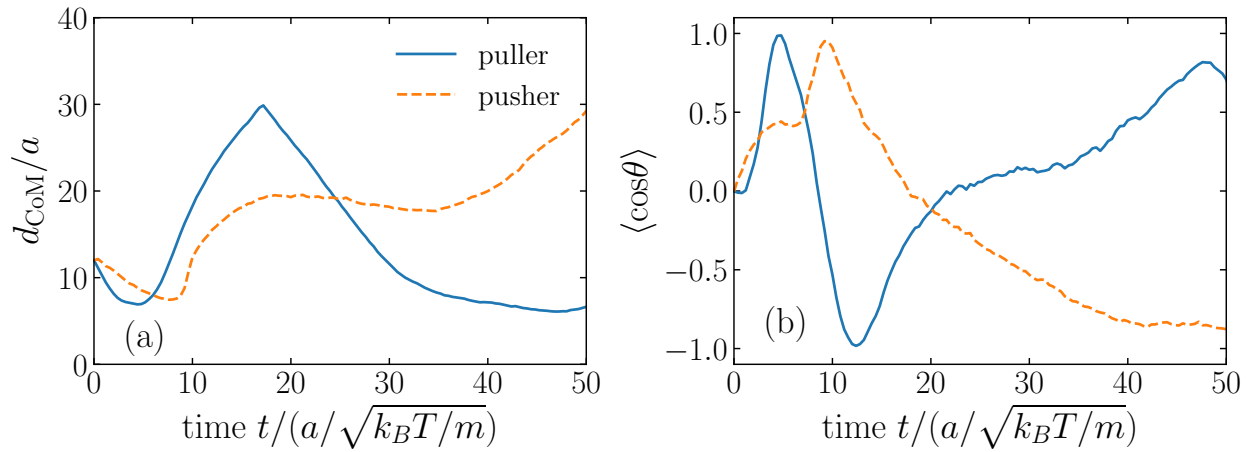


FIG. S6. Scattering event between two swimmers starting with a relative angle of $\pi/2$ and $d_{\text{CoM}} = 12a$. Solid lines show puller and dashed lines pusher type swimmers. (a) Center-of-mass to center-of-mass distance of the two swimmers. (b) Orientational correlation of the swimmers.

II. RESULTS AT LOWER REYNOLDS NUMBER

To test the relevance of the Reynolds number on our results, we perform additional simulations with $N = 300 - 1560$ swimmers. Here, we use a smaller MPCD timestep of $\delta t = 2 \times 10^{-3} \sqrt{ma^2/(k_B T)}$ and an average of $\langle N_C \rangle = 5$ MPCD particles per cell. We note that the small value of MPCD timestep ensures that the fluid remains incompressible. The resulting Reynolds number is $\mathcal{R} = 10^{-3}$, and the Peclet number is $\mathcal{P} = 220$. Figure S7 shows the resulting standard deviation of local Voronoi volume σ_{loc} compared to standard deviation σ_{rnd} of a homogeneous configuration for both pullers and pushers. For both puller and pusher-type swimmers we find a maximum. Thus, the qualitative behavior of Fig. 5 in the main text is recovered. We conclude that in the tested regime the Reynolds number has only minor effects.

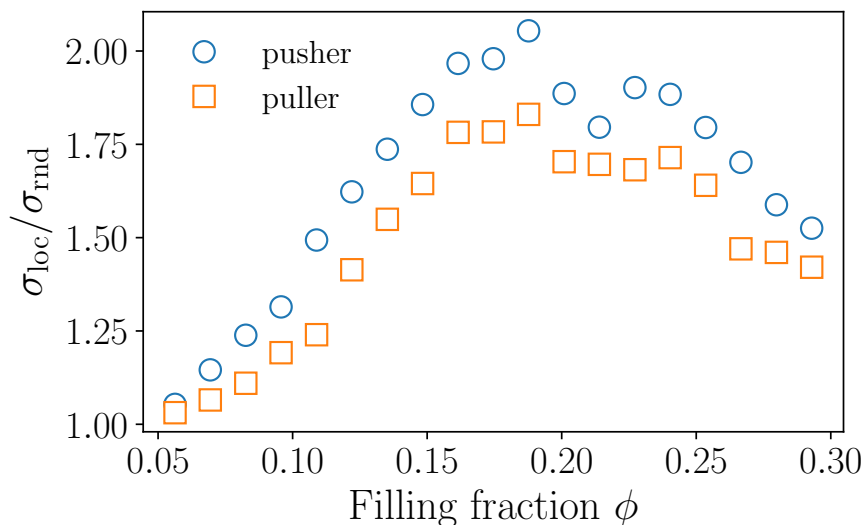


FIG. S7. Standard deviation of local Voronoi volume σ_{loc} compared to standard deviation σ_{rnd} of a homogeneous configuration. Global filling fraction is varied, the Péclet number is fixed to $\mathcal{P} = 220$ and the Reynolds number is $\mathcal{R} = 10^{-3}$. Circles are pusher and squares are puller-type swimmers.

III. BROWNIAN DYNAMICS SIMULATIONS

The Brownian dynamics simulations are carried out with hard spheres, that propel forward with a typical speed v_0 along their orientation \mathbf{e} [see also [3–6]]. The equation governing the translational motion for the position \mathbf{r} reads

$$\frac{d\mathbf{r}}{dt} = v_0 \mathbf{e} + \mathbf{F}/\gamma + \boldsymbol{\eta}, \quad (\text{S1})$$

where \mathbf{F} is the force between particles and $\boldsymbol{\eta}$ is a random white noise with zero mean and $\langle \boldsymbol{\eta}(t)\boldsymbol{\eta}(t') \rangle = 2D\mathbf{I}\delta(t-t')$. Here, $D = k_B T/\gamma$ is the translational diffusion constant, which is related to the friction coefficient γ . The potential between the particles is a Weeks–Chandler–Anderson potential [7]

$$\Phi(r_{ij}) = 4\tilde{\epsilon} \left[\left(\frac{\sigma}{r_{ij}} \right)^{12} - \left(\frac{\sigma}{r_{ij}} \right)^6 \right] + \tilde{\epsilon} \quad (\text{S2})$$

if $r_{ij} < 2^{1/6}\sigma$, and $\Phi(r_{ij}) = 0$ otherwise. Here $r_{ij} \equiv |\mathbf{r}_i - \mathbf{r}_j|$ is the distance between swimmer i and swimmer j and $\tilde{\epsilon} = 1000k_B T$ is the energy scale. Furthermore, we include orientational diffusion by using

$$\frac{d\mathbf{e}}{dt} = \boldsymbol{\zeta} \times \mathbf{e} \quad (\text{S3})$$

where ζ is a Gaussian white noise with $\langle \zeta(t)\zeta(t') \rangle = 2D_r \mathbf{I} \delta(t-t')$. Here, the rotational diffusion coefficient is related to the translational diffusion coefficient by $D_r = 3D/\sigma^2$. The Péclet number is defined by $\mathcal{P} = v_0\sigma/D$, equivalently to the definition in the main text.

IV. MULTIPOLE EXPANSION OF HYDRODYNAMIC FORCES AND TORQUES

The hydrodynamic forces and torques in the analytical theory are approximated with two point forces. In addition, the correlations between noise and hydrodynamic interactions are neglected. Using these approximations, the velocities induced by swimmer 2 at the position of the front \mathbf{r}_{L_1} and back \mathbf{r}_{S_1} sphere of swimmer 1 are found from Eq. (10) in the main text and read

$$u_i(\mathbf{r}_{L_1}) = f [O_{ij}(\mathbf{r}_{L_1} - \mathbf{r}_{L_2}) - O_{ij}(\mathbf{r}_{L_1} - \mathbf{r}_{S_2})] e_{2,j}, \quad (\text{S4})$$

$$u_i(\mathbf{r}_{S_1}) = f [O_{ij}(\mathbf{r}_{S_1} - \mathbf{r}_{L_2}) - O_{ij}(\mathbf{r}_{S_1} - \mathbf{r}_{S_2})] e_{2,j}, \quad (\text{S5})$$

where O_{ij} is the Oseen tensor and $e_{2,j}$ is the orientation of swimmer 2. We now change coordinates in terms of the hydrodynamic center of the swimmers

$$\mathbf{e}_\mu = (\mathbf{r}_{L_\mu} - \mathbf{r}_{S_\mu})/l, \quad (\text{S6})$$

$$\mathbf{r}_\mu^C = \frac{a_L \mathbf{r}_{L,\mu} + a_S \mathbf{r}_{S,\mu}}{a_L + a_S}, \quad (\text{S7})$$

where $\mu = 1, \dots, N$ are particle indices. Equation (S4)-(S5) become

$$u_i(\mathbf{r}_{L_1}) = f \left[O_{ij} \left(\mathbf{r}_{12}^C + \frac{a_S l}{2\bar{a}} (\mathbf{e}_1 - \mathbf{e}_2) \right) - O_{ij} \left(\mathbf{r}_{12}^C + \frac{l}{2\bar{a}} (a_S \mathbf{e}_1 + a_L \mathbf{e}_2) \right) \right] e_{2,j}, \quad (\text{S8})$$

$$u_i(\mathbf{r}_{S_1}) = f \left[O_{ij} \left(\mathbf{r}_{12}^C - \frac{l}{2\bar{a}} (a_L \mathbf{e}_1 + a_S \mathbf{e}_2) \right) - O_{ij} \left(\mathbf{r}_{12}^C - \frac{a_L l}{2\bar{a}} (\mathbf{e}_1 - \mathbf{e}_2) \right) \right] e_{2,j}, \quad (\text{S9})$$

where $\bar{a} = (a_S + a_L)/2$. Equations (S8) and (S9) are now used to compute forces and torques between the particles

$$\begin{aligned} \partial_t \mathbf{r}_\mu^C &= \frac{a_L \partial_t \mathbf{r}_{L\mu} + a_S \partial_t \mathbf{r}_{S\mu}}{a_L + a_S} \\ &= \frac{a_L \mathbf{u}(\mathbf{r}_{L\mu}) + a_S \mathbf{u}(\mathbf{r}_{S\mu})}{a_L + a_S} \\ &= \frac{1}{\zeta_{hy}} \sum_{\mu \neq \nu} \mathbf{F}_{\mu\nu}, \end{aligned} \quad (\text{S10})$$

$$\begin{aligned} \partial_t \mathbf{e}_\mu &= \left(\mathbf{e}_\mu \times \frac{\partial_t \mathbf{r}_{L\mu} + \partial_t \mathbf{r}_{S\mu}}{l} \right) \times \mathbf{e}_\mu \\ &= \left(\mathbf{e}_\mu \times \frac{\mathbf{u}(\mathbf{r}_{L\mu}) + \mathbf{u}(\mathbf{r}_{S\mu})}{l} \right) \times \mathbf{e}_\mu \\ &= \frac{1}{\zeta_{hy}} \sum_{\mu \neq \nu} \boldsymbol{\tau}_{\mu\nu} \times \mathbf{e}_\mu, \end{aligned} \quad (\text{S11})$$

where the last step in both Eq. (S10) and Eq. (S11) implicitly defines $\mathbf{F}_{\mu\nu}$ and $\boldsymbol{\tau}_{\mu\nu}$. In the orientational equation we projected on the perpendicular part of \mathbf{e}_μ because $|\mathbf{e}_\mu|^2 = 1$. Physically, this is related to the fact that the two spheres of one swimmer are connected by a stiff rod. The hydrodynamic friction coefficient is $\zeta_{hy} = \frac{1}{6\pi\eta\bar{a}}$. On account of the finite extension of our swimmers, we need to consider a multipole expansion of the force and torque defined in Eq.(S10)-(S11). The multipole expansion of the Oseen tensor is given by [8]

$$O_{ij}(\mathbf{r} + \mathbf{x}) = \sum_{n=0}^{\infty} \frac{1}{n!} (\mathbf{x} \cdot \nabla)^n O_{ij}(\mathbf{r}). \quad (\text{S12})$$

We expand Eq.(S10)-(S11) up to $n = 2$, which correspond to neglecting terms of order $\mathcal{O}(\frac{1}{r^4})$. Therefore, we need the first two derivatives of the Oseen tensor, which are given by

$$\partial_k O_{ij} = \frac{1}{8\pi\eta} \left[\frac{1}{r^3} (-\delta_{ij}r_k + \delta_{jk}r_i + \delta_{ik}r_j) - \frac{3}{r^5} r_i r_j r_k \right], \quad (\text{S13})$$

$$\begin{aligned} \partial_m \partial_k O_{ij} = \frac{1}{8\pi\eta} \left[\frac{1}{r^3} (-\delta_{ij}\delta_{km} + \delta_{jk}\delta_{im} + \delta_{ik}\delta_{jm}) \right. \\ \left. - \frac{3}{r^5} (-\delta_{ij}r_m r_k + \delta_{jk}r_m r_i + \delta_{ik}r_m r_j + \delta_{mi}r_j r_k + \delta_{jm}r_i r_k + \delta_{mk}r_i r_j) + \frac{15}{r^7} r_i r_j r_k r_m \right], \end{aligned} \quad (\text{S14})$$

where $\partial_i \equiv \frac{\partial}{\partial r_i}$. Collecting all terms from the multipole expansion up to $\mathcal{O}(\frac{1}{r^4})$, we arrive at the following two-body expressions for force and torque

$$\mathbf{F}_{12} = \frac{9}{4} f \bar{a} l \frac{\hat{\mathbf{r}}_{12}}{r_{12}^2} S_{ij}(\hat{\mathbf{r}}_{12}) e_{2i} e_{2j} - \frac{9}{16} f l^2 \Delta a \frac{1}{r_{12}^3} [\hat{\mathbf{r}}_{12} S_{ijk}(\hat{\mathbf{r}}_{12}) e_{2i} e_{2j} e_{2k} - \mathbf{e}_2 S_{ij}(\hat{\mathbf{r}}_{12}) e_{2i} e_{2j}], \quad (\text{S15})$$

$$\boldsymbol{\tau}_{12} = -\frac{9}{4} f \bar{a} l^3 (\mathbf{e}_1 \times \hat{\mathbf{r}}_{12}) \frac{1}{r_{12}^3} S_{ijk}(\hat{\mathbf{r}}_{12}) e_{2i} e_{2j} e_{2k}, \quad (\text{S16})$$

where we used the symmetric traceless tensors

$$S_{ij}(\hat{\mathbf{r}}) = \left[\hat{r}_i \hat{r}_j - \frac{1}{3} \delta_{ij} \right], \quad (\text{S17})$$

$$S_{ijk}(\hat{\mathbf{r}}) = 5\hat{r}_i \hat{r}_j \hat{r}_k - (\delta_{ik} \hat{r}_i + \delta_{ik} \hat{r}_j + \delta_{ij} \hat{r}_k), \quad (\text{S18})$$

and summation over repeated indices is employed.

V. LINEAR STABILITY ANALYSIS

The Smoluchowski equation of our analytical model reads

$$\partial_t p = -\nabla \cdot [v(c)\mathbf{e}p] - \frac{1}{\zeta_{hy}} \nabla \cdot (\mathbf{F}_{hy} p) - \frac{1}{\zeta_{hy} l^2} \left(\mathbf{e} \times \frac{\partial}{\partial \mathbf{e}} \right) \cdot \boldsymbol{\tau}_{hy} p + D\Delta p + D_R \left(\mathbf{e} \times \frac{\partial}{\partial \mathbf{e}} \right)^2 p, \quad (\text{S19})$$

where $p \equiv p(\mathbf{r}, \mathbf{e}, t)$, and the force and torque terms are computed using a mean field Ansatz

$$\langle X_{12} \rangle = \int d\mathbf{r}_2 \int d\mathbf{e}_2 X_{12} p(\mathbf{r}_2, \mathbf{e}_2, t). \quad (\text{S20})$$

Using the definitions of the moments for, respectively, the concentration, polarization, and nematicity

$$c(\mathbf{r}, t) = \int d\mathbf{e} p(\mathbf{r}, \mathbf{e}, t), \quad (\text{S21})$$

$$\mathbf{P}(\mathbf{r}, t) = \frac{1}{c(\mathbf{r}, t)} \int d\mathbf{e} \mathbf{e} p(\mathbf{r}, \mathbf{e}, t), \quad (\text{S22})$$

$$\mathbf{Q}(\mathbf{r}, t) = \frac{1}{c(\mathbf{r}, t)} \int d\mathbf{e} \left(\mathbf{e} \otimes \mathbf{e} - \frac{1}{3} \mathbf{I} \right) p(\mathbf{r}, \mathbf{e}, t), \quad (\text{S23})$$

we can find the following expressions for the hydrodynamic force and torque terms

$$F_{hy,i} = \frac{9}{4} f \bar{a} l K_i^{F1} + \frac{9}{16} f l^2 \Delta a K_i^{F2}, \quad (\text{S24})$$

$$\tau_{hy,i} = -\frac{9}{4} f \bar{a} l^3 \varepsilon_{imn} e_{1m} e_{1j} K_{nj}^\tau, \quad (\text{S25})$$

with

$$K_i^{F1} = \int d\mathbf{r}_2 \frac{\hat{r}_{12i}}{r_{12}^2} S_{ij}(\hat{\mathbf{r}}_{12}) c(\mathbf{r}_2, t) Q_{ij}(\mathbf{r}_2, t), \quad (\text{S26})$$

$$K_i^{F2} = \int d\mathbf{r}_2 \frac{1}{r_{12}^3} S_{ij}(\hat{\mathbf{r}}_{12}) c(\mathbf{r}_2, t) P_j(\mathbf{r}_2, t), \quad (\text{S27})$$

$$K_{nj}^\tau = \int d\mathbf{r}_2 \frac{\hat{r}_{12n}}{r_{12}^3} S_{ijk}(\hat{\mathbf{r}}_{12}) c(\mathbf{r}_2, t) Q_{lk}(\mathbf{r}_2, t). \quad (\text{S28})$$

We now compute moment equations using Eq. (S21)-(S23) for the Smoluchowski Eq. (S19)

$$\partial_t c = -\partial_i (v(c)cP_i) + D\Delta c - \frac{9f\bar{a}l}{4\zeta_{hy}} K_i^{F_1} c + \frac{9fl^2\Delta a}{16\zeta_{hy}} K_i^{F_2} c, \quad (\text{S29})$$

$$\partial_t cP_i = -\partial_j (v(c)cQ_{ij}) - \frac{1}{3}\partial_i (v(c)c) + D\Delta cP_i - D_{RC}cP_i - \frac{3lf}{40\pi\eta} (4K_{ij}^{\tau_1}(\mathbf{r}, t) - K_{ji}^{\tau_1}(\mathbf{r}, t) - \delta_{ij}K_{mm}^{\tau_1}(\mathbf{r}, t)) cP_j \quad (\text{S30})$$

$$\partial_t cQ_{ij} = -\frac{2}{5}(\partial_i v(c)cP_j)^{\text{ST}} + D\Delta cQ_{ij} - 4D_{RC}cQ_{ij} - \frac{3lf}{8\pi\eta} [K_{ij}^{\tau}]^{\text{ST}} c, \quad (\text{S31})$$

where we use the symmetric traceless part $[Y_{ij}]^{\text{ST}} = \frac{1}{2}(Y_{ij} + Y_{ji}) - \frac{1}{3}\delta_{ij}Y_{kk}$. Note that here we neglected terms of order $\mathcal{O}(\mathbf{Q}^2)$. We will now linearize these moment equations around the isotropic state

$$\begin{aligned} c &= c_0 + \delta c, \\ \mathbf{P} &= \delta \mathbf{P}, \\ \mathbf{Q} &= \delta \mathbf{Q}, \end{aligned} \quad (\text{S32})$$

and turn to Fourier space, where the fields are denoted by $\delta\tilde{c}$, $\delta\tilde{\mathbf{P}}$, and $\delta\tilde{\mathbf{Q}}$. First, note that all terms of order $\mathcal{O}(\mathbf{P}^2)$, $\mathcal{O}(\mathbf{Q}\mathbf{P})$, and $\mathcal{O}(\mathbf{Q}^2)$ will vanish at our level of approximation. Therefore, there is no contribution from hydrodynamic forces or torques in the polarization Eq. (S30). Second, the three terms proportional to $K_i^{F_1}c$ and $K_i^{F_2}c$, stemming from the concentration Eq. (S29), and the term proportional to $[K_{ij}^{\tau}]^{\text{ST}}c$ from the nematic stress tensor Eq. (S31) require special care in their evaluation. We will treat each of these three terms separately in the following.

A. $K_i^{F_1}c$ term

The linearized form of the $K_i^{F_1}c$ term is

$$\partial_i c_0^2 \int d\mathbf{r}_2 \frac{\hat{r}_{12i}}{r_{12}^2} S_{ij}(\hat{\mathbf{r}}_{12}) \delta Q_{ij}(\mathbf{r}_2, t) \quad (\text{S33})$$

and turning to Fourier space yields

$$ic_0^2 k_i \delta \tilde{Q}_{jk} \mathcal{F} \left[\frac{\hat{r}_i}{r^2} \left(\hat{r}_j \hat{r}_k - \frac{1}{3} \delta_{jk} \right) \right] (k), \quad (\text{S34})$$

where we used the convolution theorem, and $\mathcal{F}[h(\mathbf{r})](\mathbf{k}) = \int d\mathbf{r} h(\mathbf{r}) e^{-i\mathbf{k}\cdot\mathbf{r}}$ denotes the Fourier transform of the function $h(\mathbf{r})$. Without loss of generality we can set $\mathbf{k} = k\mathbf{e}_z$, and using spherical coordinates gives

$$ic_0^2 \delta \tilde{Q}_{jk} \int_0^\infty d\rho \int_0^{2\pi} d\varphi \int_0^\pi d\theta k \sin\theta \cos\theta \left(\hat{r}_j \hat{r}_k - \frac{1}{3} \delta_{jk} \right) e^{-ik\rho \cos\theta} = 0. \quad (\text{S35})$$

B. $K_i^{F_2}c$ term

The linearized form of the $K_i^{F_2}c$ term is

$$\partial_i c_0^2 \int d\mathbf{r}_2 \frac{1}{r_{12}^3} S_{ij}(\hat{\mathbf{r}}_{12}) \delta P_j(\mathbf{r}_2, t) \quad (\text{S36})$$

turning to Fourier space and using the convolution theorem yields

$$ic_0^2 k_i \delta \tilde{P}_j \mathcal{F} \left[\frac{1}{r_{12}^3} \left(\hat{r}_i \hat{r}_j - \frac{1}{3} \delta_{ij} \right) \right] (k). \quad (\text{S37})$$

We can again set $\mathbf{k} = k\mathbf{e}_z$, and by using spherical coordinates we find

$$ic_0^2 \delta \tilde{P}_j \int_0^\infty d\rho \int_0^{2\pi} d\varphi \int_0^\pi d\theta \frac{k}{\rho} \sin\theta \left(\hat{r}_j \cos\theta - \frac{1}{3} \delta_{j3} \right) e^{-ik\rho \cos\theta} = -\frac{8}{9} \pi c_0^2 k P_3. \quad (\text{S38})$$

The integrals were solved using Mathematica (see also the supplementary file `Integrals_hydroTerms.pdf`).

C. $[K_{ij}^T]^{ST}$ c term

The term $[K_{ij}^T]^{ST} c$ in its linearized form reads

$$c_0^2 \left[\int d\mathbf{r}_2 \frac{\hat{r}_{12i}}{r_{12}^3} S_{njm}(\hat{\mathbf{r}}_{12}) \delta Q_{nm}(\mathbf{r}_2, t) \right]^{ST}. \quad (\text{S39})$$

Turning to Fourier space and using the convolution theorem gives

$$c_0^2 \delta \tilde{Q}_{nm} \mathcal{F} \left[\frac{\hat{r}_i}{r^3} S_{njm} \right] (k). \quad (\text{S40})$$

This can be evaluated when we use $\mathbf{k} = k\mathbf{e}_z$ and spherical coordinates

$$c_0^2 \delta \tilde{Q}_{nm} \int_0^\infty d\rho \int_0^{2\pi} d\varphi \int_0^\pi d\theta \frac{1}{\rho} \sin\theta \hat{r}_i S_{njm} = c_0^2 \mathcal{M}_{ij}(\delta \tilde{Q}_{ij}), \quad (\text{S41})$$

where the matrix $\mathcal{M}_{ij}(\delta \tilde{Q}_{ij})$ was evaluated using Mathematica (see also the supplementary file `Integrals_hydroTerms.pdf`) to be

$$(\mathcal{M}_{ij}) = \frac{4}{5} \pi \begin{pmatrix} -\frac{2}{3}(\delta \tilde{Q}_{2,2} + \delta \tilde{Q}_{3,3}) & \frac{2}{3} \delta \tilde{Q}_{2,1} & -\delta \tilde{Q}_{3,1} \\ \frac{2}{3} \delta \tilde{Q}_{2,1} & \frac{2}{3} \delta \tilde{Q}_{2,2} & -\delta \tilde{Q}_{3,2} \\ -\delta \tilde{Q}_{3,1} & -\delta \tilde{Q}_{3,2} & \frac{2}{3} \delta \tilde{Q}_{3,3} \end{pmatrix}. \quad (\text{S42})$$

The linearized equations are then given by

$$\partial_t \delta \tilde{c} = - \left[ik_i \left(v_0 c_0 - \zeta c_0^2 + c_0^2 \frac{\Delta a l^2 f}{30 \eta \bar{a}} \right) \delta \tilde{P}_i + D k_i k_i \delta \tilde{c} \right], \quad (\text{S43})$$

$$\partial_t \delta \tilde{P}_i = - \left[ik_j (v_0 - \zeta c_0) \delta \tilde{Q}_{ij} + ik_i \frac{1}{3} \left(\frac{v_0}{c_0} - 2\zeta \right) \delta \tilde{c} + (D k_j k_j + D_R) \delta \tilde{P}_i \right], \quad (\text{S44})$$

$$\partial_t \delta \tilde{Q}_{ij} = - \left[i \frac{2}{5} (v_0 - \zeta c_0) [k_i \delta \tilde{P}_j]^{ST} + \frac{3lf}{8\pi\eta} c_0 \mathcal{M}_{ij}(\delta \tilde{Q}_{ij}) + (4D_R + k_n k_n D) \delta \tilde{Q}_{ij} \right]. \quad (\text{S45})$$

-
- [1] I. S. Aranson, A. Sokolov, J. O. Kessler and R. E. Goldstein, *Phys. Rev. E*, 2007, **75**, 040901.
[2] E. Lauga and T. R. Powers, *Reports on Progress in Physics*, 2009, **72**, 096601.
[3] A. Wysocki, R. G. Winkler and G. Gompper, *EPL (Europhysics Letters)*, 2014, **105**, 48004.
[4] Y. Fily and M. C. Marchetti, *Phys. Rev. Lett.*, 2012, **108**, 235702.
[5] G. S. Redner, M. F. Hagan and A. Baskaran, *Phys. Rev. Lett.*, 2013, **110**, 055701.
[6] J. Bialké, T. Speck and H. Löwen, *Phys. Rev. Lett.*, 2012, **108**, 168301.
[7] J. D. Weeks, D. Chandler and H. C. Andersen, *J. Chem. Phys.*, 1971, **54**, 5237–5247.
[8] S. Kim and S. Karrila, *Microhydrodynamics: Principles and Selected Applications*, Dover Publications, 2005.

Chapter 6

Swimming strategies of microorganisms

Bacteria and microalgae follow gradients of nutrient, chemicals, or light. *Chlamydomonas reinhardtii* for example are phototactic, i.e., they follow light gradients [154], while *Escherichia coli* are chemotactic, as they follow gradients of nutrients [15]. To follow nutrient gradients or simply find nutrients, microorganisms have evolved many different swimming strategies, that are suited to their morphology and their environment.

In this chapter we will first introduce one of the most studied motility modes: run and tumble. This swimming mechanism has received so much attention because it is associated with one of the most important model organisms in microbiology: *Escherichia coli*. We will then focus on a second swimming strategy: run-reverse-flick. We will show how run-reverse-flick can be investigated numerically and analytically, while including interactions between microswimmers. Finally we will present results concerning the collective behavior of run-reverse-flick swimmers.

6.1 Run and tumble strategy

Escherichia coli execute the run and tumble swimming strategy [15]. It consists of two motility states, the run and the tumble state. In the run state the flagella of the *Escherichia coli* all rotate counterclockwise (as observed from the body) and because



FIGURE 6.1: Run and tumble trajectory of an *Escherichia coli* bacterium. Reprinted by permission from Springer Nature, Springer eBook, [15], Copyright Springer-Verlag New York, Inc. 2004.

of mechanical and hydrodynamic interactions the flagella come together and form a bundle, that rotates coherently. The *Escherichia coli* then is able to swim on a straight path. If the cell now decides to change direction, it will change the direction of rotation of a number (not all) of its flagella. Thereby, the flagella bundle dissolves, the *Escherichia coli* cell starts tumbling and thus reorient. A typical trajectory can be seen in Fig. 6.1.

Chlamydomonas reinhardtii also follows a eukaryotic equivalent of run and tumble motion [51]. In its run mode, the two flagella beat in a breaststroke-like manner and the cell swims on a straight path. As it decides to change direction, the flagella desynchronize, the cell starts tumbling and changes its direction.

Statistically, the MSD of a run and tumble particle can be computed by using a continuous time random walk approach [53, 155]. A simple calculation gives

$$\langle (\mathbf{r}(t) - \mathbf{r}(0))^2 \rangle_{\text{rt}} = 2v_0^2 \tilde{\tau}^2 \left(e^{-t/\tilde{\tau}} + t/\tilde{\tau} - 1 \right), \quad (6.1)$$

where v_0 is the particle's self-propulsion velocity and $\tilde{\tau} = \frac{\tau_{\text{run}}}{1 - \cos \varphi_0}$ is the effective time scale. Here, τ_{run} is the mean time during which the particle is in the run state and φ_0 is the mean reorientation angle. Here, the tumble of the particle is assumed to be instantaneous, which is valid both for *Chlamydomonas reinhardtii* and *Escherichia coli*. The MSD in Eq. (6.1) has two characteristic regimes: on short time scales it shows

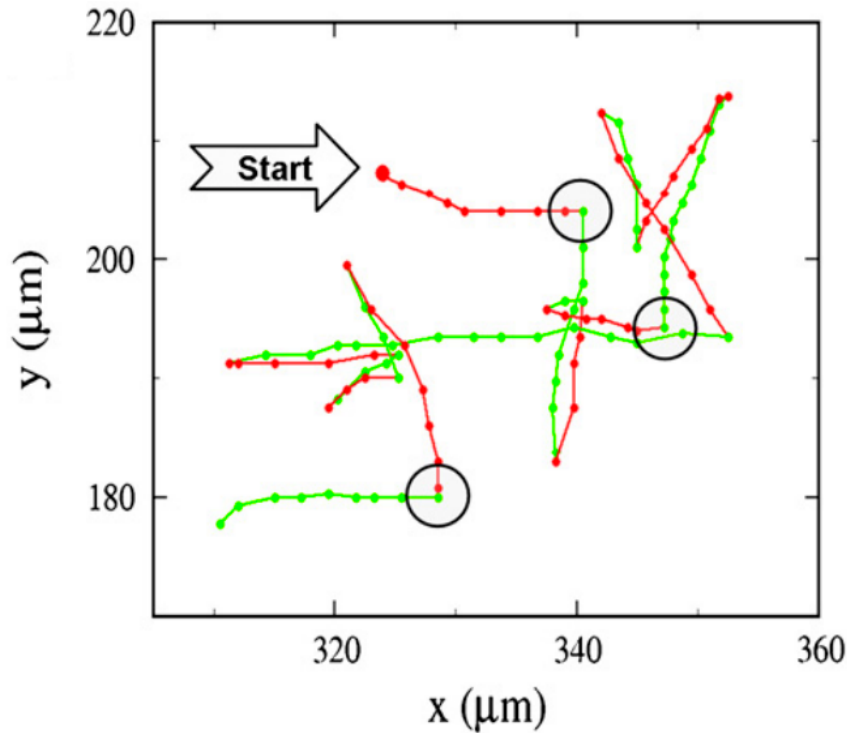


FIGURE 6.2: Experimental observation of the run-reverse-flick trajectory of a *Vibrio alginolyticus* bacterium. Green lines mark the forward running state, red lines mark the backward running state, and the black circles show a flick event. Reprinted from [16].

a ballistic behavior, resembling the run mode, and on large time scales it is diffusive with diffusion coefficient $D_{\text{rt}} = v_0^2 \bar{\tau} / 3$, which stems from the random reorientations in the tumble phase. Considering the MSD of the active Brownian particle in Eq. (2.37), the MSD of the run-and-tumble particle in Eq. (6.1) is recovered for $D_R = 1/(2\tau)$ and $D_T = 0$. In fact, for most situations the active Brownian particle and a run-and-tumble particle can be used equivalently (see also [156]).

6.2 Run-reverse-flick strategy

The bacterium *Vibrio alginolyticus* has only a single flagellum attached to its rear to propel itself forward. Therefore, it is unable to reorient itself using the run and tumble mechanism discussed in the last section. In fact, it was found that *Vibrio alginolyticus* has three motility phases: run, reverse and flick [16]. Starting in the run phase the bacterium propels forward by rotating its flagellum counterclockwise, it then switches the direction of rotation to clockwise. The bacterium then swims backwards, which is the reverse phase. This is followed by the flick, a sharp reorientation of the bacterium's swimming direction due to a buckling instability in the flagellum [49]. A typical trajectory of this process can be seen in Fig. 6.2.

Theoretically, the MSD of the run-reverse-flick strategy can be computed using a continuous time random walk approach and is given by [53]

$$\langle (\mathbf{r}(t) - \mathbf{r}(0))^2 \rangle_{\text{rrf}} = v_0^2 \tau t \left(1 - e^{-t/\tau} \right), \quad (6.2)$$

where the mean forward and backward run times are both taken equal to τ and the flick is assumed to be instantaneous. The MSD in Eq. (6.2) shows a ballistic regime at small time scales, which appears due to the run and reverse phases. Because of the flick the MSD in Eq. (6.2) has a diffusive regime at large time scales. Note that this diffusion process cannot be easily related to the active Brownian particle, as it was the case for the run-and-tumble motion.

In the following we will study the collective effects of the run-reverse-flick strategy. We will first introduce a scheme for the numerical implementation of run-reverse-flick which includes interactions between multiple particles, and then present an analytical approach based on probabilistic equations, which can also capture collective effects. Finally, we present an interesting result: run-reverse-flick particles have an optimum in their collective diffusion.

6.3 Numerical implementation of run-reverse-flick

Given the orientation \mathbf{e}_i of a run-reverse-flick particle, the swimming strategy is implemented as follows: We start with the forward running phase, and select a forward-run time t_f by drawing a random number from an exponential distribution e^{-t/τ_f} , where τ_f is the mean forward-run time. The particle will then stay in the forward running state with constant \mathbf{e}_i for the time t_f . Next, we have the reverse state: Here, the direction is reversed to $\mathbf{e}_i \rightarrow -\mathbf{e}_i$. Furthermore, a backward-run time t_b is drawn from another exponential distribution e^{-t/τ_b} , where τ_b is the backward-run time. At the end of the backward run phase the particle will perform the flick. Here, a new orientation \mathbf{e}'_i is assigned, which is characterized by $\mathbf{e}_i \cdot \mathbf{e}'_i = \alpha_i$, where α_i is drawn from a Gaussian distribution with mean $\mu_\alpha = 0$ and standard deviation $\sigma_\alpha = 0.1$. Afterwards the particle will instantaneously go back to the forward state. In the following we will use an overdamped Langevin model and also our implementation of the squirmer model.

Overdamped Langevin run-reverse-flick

The first model we use for the run-reverse-flick particles only includes steric interactions. We model the run-reverse-flick particles using overdamped Langevin equations [11, 28, 31, 157] (see also Sec. 2.2.3)

$$\frac{d\mathbf{r}_i}{dt} = v_0 \mathbf{e}_i + \mathbf{f}_s(\mathbf{r}_i, \mathbf{r}_j), \quad (6.3)$$

where v_0 is the propulsion speed of particle i and \mathbf{e}_i is its orientation. The steric interactions $\mathbf{f}_s(\mathbf{r}_i, \mathbf{r}_j) = -\nabla\Phi(r_{ij})$ are modeled using a Weeks-Chandler-Anderson (WCA) potential [158], which reads

$$\Phi(r_{ij}) = 4\tilde{\epsilon} \left[\left(\frac{\sigma}{r_{ij}} \right)^{12} - \left(\frac{\sigma}{r_{ij}} \right)^6 \right] + \tilde{\epsilon}, \quad (6.4)$$

if $r_{ij} < 2^{1/6}\sigma$, and $\Phi(r_{ij}) = 0$ otherwise. Here $r_{ij} \equiv |\mathbf{r}_i - \mathbf{r}_j|$ is the distance between swimmer i and swimmer j and $\tilde{\epsilon} = 10k_B T$ is the energy scale. For the numerical implementation we used the algorithm for Brownian dynamics simulations presented in Sec. 3.1.2.

Squirmer run-reverse-flick

We also consider a model that, in addition to steric effects, explicitly includes hydrodynamic interactions between the particles. Here, the swimmer's equations of motion are given by Eq. (3.8)-(3.11), where we use a WCA potential [Eq.(2.42)] to compute the steric forces between the spherical particles. Hydrodynamic interactions are implemented by using the MPCD technique presented in Sec. 3.2.1, and the swimmers by mean of the method of Sec. 3.2.4. As we are modeling microswimmers, the self-propulsion and flow field need to be included into our simulation. In the present context, it is easier to implement a squirmer model than the asymmetric dumbbell model for computational reasons. The squirmer model imposes the following velocity on the surface of the swimmer

$$\mathbf{v}_s = \frac{3}{2}v_0 (1 + \beta \mathbf{e} \cdot \hat{\mathbf{r}}_s) [(\mathbf{e} \cdot \hat{\mathbf{r}}_s)\hat{\mathbf{r}}_s - \mathbf{e}], \quad (6.5)$$

where \mathbf{e} is the squirmer's orientation, $\hat{\mathbf{r}}_s$ the unit vector pointing from the center of the squirmer to the surface, v_0 the self-propulsion velocity and β is a tunable parameter used to switch between a neutral, pusher, or puller type squirmer (see also Sec. 5). In the forward state the swimmer is considered to be a pusher, that is $\beta < 0$, and in the backward running state the flow field corresponds to a puller, such that $\beta > 0$.

6.3.1 Single particle statistics

In this section, the numerical implementation of the run-reverse-flick swimming strategy is tested using simulations of a single particle with the Langevin model [Sec. 6.3], meaning that $\mathbf{f}_s(\mathbf{r}_i, \mathbf{r}_j) = 0$ [see Eq. (6.3)].

First, we simulate the case where the forward and backward runtime are equal $\tau_f = \tau_b$. Figure 6.3(a) shows the MSD of our simulated data, as well as the theoretical prediction, Eq. (6.2). Furthermore, Fig. 6.3(b) shows the relative error between the simulation and analytics. The agreement between the simulated data and the theoretical prediction is good, as the relative error is between 10^{-2} to 10^{-5} for times larger than $10^{-2}\sigma/v_0$. Secondly, we compute the diffusion coefficient for varying runtime

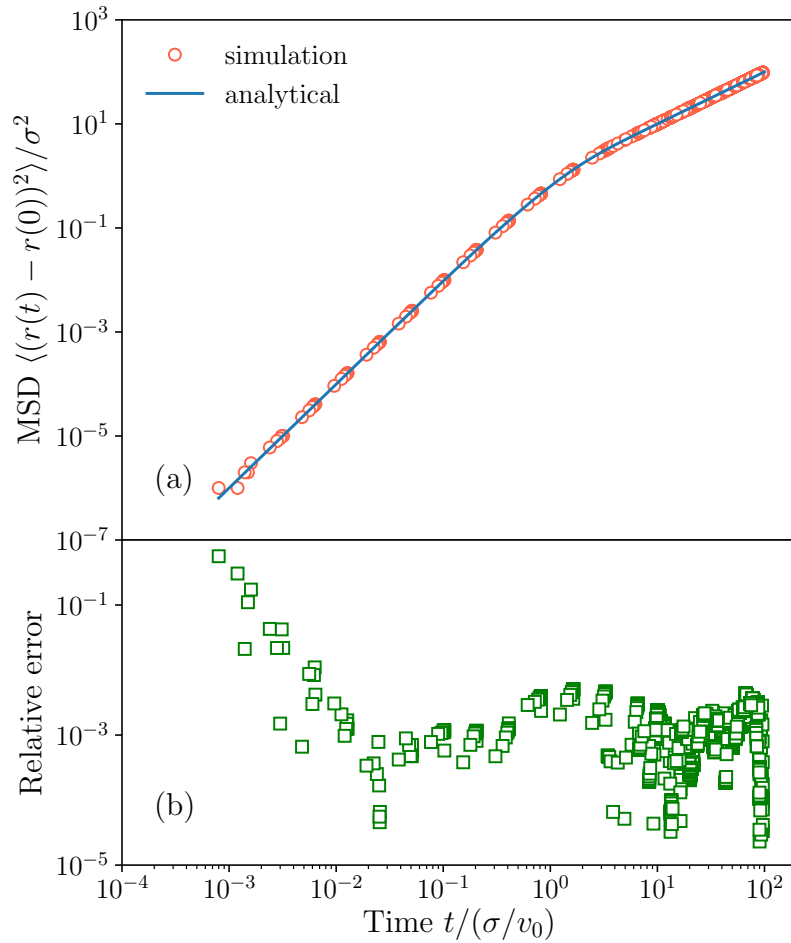


FIGURE 6.3: (a) Comparison of MSD from simulations (orange circles) to analytical prediction (blue line) [Eq. (6.2)]. (b) Relative error of simulation to theoretical prediction.

ratios τ_f/τ_b . The theoretical prediction is given by [53](Supplementary Information)

$$D_0 = \frac{v_0^2}{d} \frac{\tau_b^3 + \tau_f^3}{(\tau_b + \tau_f)^2}, \quad (6.6)$$

where d is the number of spacial dimensions. Figure 6.4 shows the comparison of the diffusion coefficient from our simulations to Eq. (6.6). It can be seen that both for two and three dimensions the agreement is excellent.

Thus, we can conclude that the present implementation of the run-reverse-flick strategy reproduces the behavior of the MSD and diffusion coefficient, as predicted by [53].

6.4 Analytical treatment of run-reverse-flick

To treat the run-reverse-flick swimmers analytically, we use an approach based on a master equation, where we consider one equation for the forward running state and

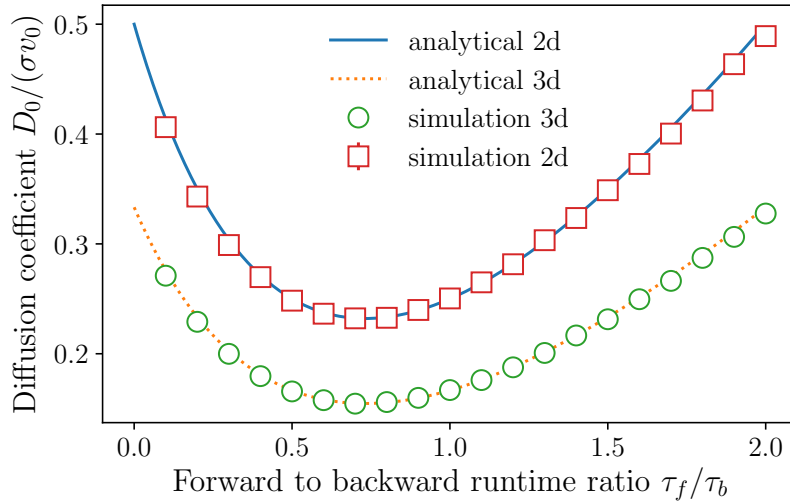


FIGURE 6.4: Comparison of the diffusion coefficient from simulations (squares for 2d, circles for 3d) to analytical prediction (line for 2d, dotted line for 3d) Eq. (6.6).

one for the backward running state. Note that Taktikos et al. [53] use a different approach based on continuous time random walks, which is not suitable for our case since it cannot capture interactions among particles. The equations we propose are for the probability of a particle to be in the forward running state $P_f(\mathbf{r}, \theta)$ or in the backward running state $P_b(\mathbf{r}, \theta)$, and read

$$\partial_t P_f(\mathbf{r}, \theta) = -\mathbf{e}(\theta) \cdot \nabla v(\rho) P_f(\mathbf{r}, \theta) - \frac{1}{\tau_f} P_f(\mathbf{r}, \theta) + \frac{1}{2\tau_b} \left[P_b(\mathbf{r}, \theta + \frac{\pi}{2}) + P_b(\mathbf{r}, \theta - \frac{\pi}{2}) \right], \quad (6.7)$$

$$\partial_t P_b(\mathbf{r}, \theta) = -\mathbf{e}(\theta) \cdot \nabla v(\rho) P_b(\mathbf{r}, \theta) - \frac{1}{\tau_b} P_b(\mathbf{r}, \theta) + \frac{1}{\tau_f} P_f(\mathbf{r}, \theta + \pi). \quad (6.8)$$

where \mathbf{r} is the particle's position, and $\mathbf{e}^T = (\cos\theta, \sin\theta)$ (T denotes the matrix transpose) is the particle's orientation, which is parametrized by the angle θ . The function $v(\rho)$ is the propulsion speed, which also takes into account the interactions between particles by having a dependence on the density ρ [30, 157] (see also Sec.2.2.3). Physically, the terms in Eq. (6.7)-(6.8) have the following meaning. The term $-\frac{1}{\tau_f} P_f(\mathbf{r}, \theta)$ in Eq. (6.7) gives the loss of probability from the forward to the backward state, with rate $\frac{1}{\tau_f}$. The corresponding gain in the backward state Eq. (6.8) is then given by $\frac{1}{\tau_f} P_f(\mathbf{r}, \theta + \pi)$, where the change π in the angle accounts for the reverse. Furthermore, the term $-\frac{1}{\tau_b} P_b(\mathbf{r}, \theta)$ in Eq. (6.8) for the backward state is a loss in probability to the forward state with rate $\frac{1}{\tau_b}$. The subsequent gain in the forward probability is given by $\frac{1}{2\tau_b} (P_b(\mathbf{r}, \theta + \frac{\pi}{2}) + P_b(\mathbf{r}, \theta - \frac{\pi}{2}))$, where the factor $\pm\pi/2$ takes into account the reorientation that is inherent to the flicking event. The probability of finding a

particle $P(\mathbf{r}, \theta)$, no matter if it is in the forward or backward state, is given by

$$P(\mathbf{r}, \theta) = P_f(\mathbf{r}, \theta) + P_b(\mathbf{r}, \theta). \quad (6.9)$$

Note that with this definition the total probability is conserved.

6.4.1 Moment expansion

To make progress with Eq.(6.7) and Eq.(6.8), we compute the moment equations for the forward and backward densities $\rho_{f,b}(\mathbf{r})$ and the respective polarizations $\mathbf{p}_{f,b}(\mathbf{r})$ by using

$$\rho_{f,b} \equiv \int_0^{2\pi} P_{f,b} d\theta, \quad (6.10)$$

$$\mathbf{p}_{f,b} \equiv \int_0^{2\pi} \mathbf{e} P_{f,b} d\theta. \quad (6.11)$$

Neglecting all higher moments, we obtain the equations

$$\partial_t \rho_f = -\nabla \cdot v(\rho) \mathbf{p}_f - \frac{1}{\tau_f} \rho_f + \frac{1}{\tau_b} \rho_b, \quad (6.12)$$

$$\partial_t \rho_b = -\nabla \cdot v(\rho) \mathbf{p}_b - \frac{1}{\tau_b} \rho_b + \frac{1}{\tau_f} \rho_f, \quad (6.13)$$

$$\partial_t \mathbf{p}_f = -\frac{1}{2} \nabla v(\rho) \rho_f - \frac{1}{\tau_f} \mathbf{p}_f, \quad (6.14)$$

$$\partial_t \mathbf{p}_b = -\frac{1}{2} \nabla v(\rho) \rho_b - \frac{1}{\tau_b} \mathbf{p}_b - \frac{1}{\tau_f} \mathbf{p}_f. \quad (6.15)$$

It is convenient to use the fields for the overall density ρ and the density difference ρ_- defined as

$$\rho \equiv \rho_f + \rho_b \quad (6.16)$$

$$\rho_- \equiv \rho_f - \rho_b \quad (6.17)$$

such that Eq.(6.12) and Eq.(6.13) become

$$\partial_t \rho = -\nabla \cdot (v(\rho) \mathbf{p}_f + v(\rho) \mathbf{p}_b), \quad (6.18)$$

$$\partial_t \rho_- = -\nabla \cdot (v(\rho) \mathbf{p}_f - v(\rho) \mathbf{p}_b) - \frac{1}{\tau_f} (\rho + \rho_-) + \frac{1}{\tau_b} (\rho - \rho_-). \quad (6.19)$$

We now linearize the Eqs.(6.14),(6.15),(6.18) and (6.19) around the homogeneous state represented by $\rho = \rho_0 + \delta\rho$, $\rho_- = \delta\rho_-$, $\mathbf{p}_f = \delta\mathbf{p}_f$ and $\mathbf{p}_b = \delta\mathbf{p}_b$. In addition, we transform the space components to Fourier space with wave vector \mathbf{k} , and the time component to Laplace space with frequency s . Furthermore, we effectively include the interactions by using $v(\rho) = v_0(1 - \zeta\rho)$, where v_0 is the self-propulsion speed and ζ quantifies how much the particles are slowed down by interactions (see also Sec. 2.2.3). The fields are then denoted by $\delta\tilde{\rho}$, $\delta\tilde{\rho}_-$, $\delta\tilde{\mathbf{p}}_f$, $\delta\tilde{\mathbf{p}}_b$, and the resulting linearized equations

are

$$s\delta\tilde{\rho} = -iv_0(1 - \zeta\rho_0)\mathbf{k} \cdot (\delta\tilde{\mathbf{p}}_f + \delta\tilde{\mathbf{p}}_b) + \rho_0, \quad (6.20)$$

$$s\delta\tilde{\rho}_- = -iv_0(1 - \zeta\rho_0)\mathbf{k} \cdot (\delta\tilde{\mathbf{p}}_f - \delta\tilde{\mathbf{p}}_b) - \frac{1}{\tau_f}(\rho_0 + \delta\tilde{\rho} + \delta\tilde{\rho}_-) + \frac{1}{\tau_b}(\rho_0 + \delta\tilde{\rho} - \delta\tilde{\rho}_-), \quad (6.21)$$

$$s\delta\tilde{\mathbf{p}}_f = -i\frac{1}{4}v_0\mathbf{k}(\delta\tilde{\rho}(1 - 2\zeta\rho_0) + \delta\tilde{\rho}_-(1 - \zeta\rho_0)) - \frac{1}{\tau_f}\delta\tilde{\mathbf{p}}_f, \quad (6.22)$$

$$s\delta\tilde{\mathbf{p}}_b = -i\frac{1}{4}v_0\mathbf{k}(\delta\tilde{\rho}(1 - 2\zeta\rho_0) - \delta\tilde{\rho}_-(1 - \zeta\rho_0)) - \frac{1}{\tau_b}\delta\tilde{\mathbf{p}}_b - \frac{1}{\tau_f}\delta\tilde{\mathbf{p}}_f, \quad (6.23)$$

where we assumed that $\rho(t=0) = \rho_0$ and all other fields vanish at $t=0$. This system of linear equations can be solved using a computer algebra system. From the resulting density fluctuations $\delta\tilde{\rho}$, the MSD can be calculated using

$$\langle[\mathbf{r}(t) - \mathbf{r}(0)]^2\rangle = \mathcal{L}^{-1}\left\{\frac{1}{2\pi}\int(\nabla_{\mathbf{k}}^2\delta\tilde{\rho}(\mathbf{k}, s))\delta(\mathbf{k})d\mathbf{k}\right\}(t), \quad (6.24)$$

where \mathcal{L}^{-1} is the inverse Laplace transformation and $\nabla_{\mathbf{k}}^2$ is the Laplace operator with respect to \mathbf{k} . For the case $\tau_f = \tau_b$ and in the limit $\tau_c \rightarrow 0$, the MSD Eq. (6.2) is recovered. The diffusion constant can be calculated by

$$\begin{aligned} D &= \lim_{t \rightarrow \infty} \frac{\langle[\mathbf{r}(t) - \mathbf{r}(0)]^2\rangle}{4t} \\ &= \frac{v_0^2(\rho_0\zeta - 1)}{4(\tau_b + \tau_f)} [2(\rho_0\zeta - 1)\tau_b^2 + (2 - \rho_0\zeta)\tau_b\tau_f + (-2 + 3\rho_0\zeta)\tau_f^2], \end{aligned} \quad (6.25)$$

which in the limit of $\zeta \rightarrow 0$ gives Eq.(6.6).

6.5 Maximum in collective diffusion of run-reverse-flick particles

To study the influence of the run-reverse-flick pattern on the collective behavior we use the diffusion coefficient D . However, as we vary the run time ratio τ_f/τ_b the bare diffusion coefficient D_0 of a single particle changes. Therefore, we normalize D/D_0 , to only observe the collective effects. In addition to the run-time ratio, we vary the filling fraction ϕ of the system.

The resulting nonequilibrium phase diagram for the two-dimensional simulations with only steric interactions and $N = 2 \times 10^5$ particles can be seen in Fig. 6.5. For a fixed filling fraction, the data consistently show a maximum at the runtime ratio of ~ 1.2 . From the theory (Sec. 6.4.1) we can expand the normalized diffusion constant to first order in $\rho_0\zeta$ and obtain

$$D/D_0 = 1 + \rho_0\zeta \frac{-\tau_b^2 + 3\tau_b\tau_f - 5\tau_f^2}{2(\tau_b^2 - \tau_b\tau_f + \tau_f^2)} + \mathcal{O}(\rho_0^2\zeta^2), \quad (6.26)$$

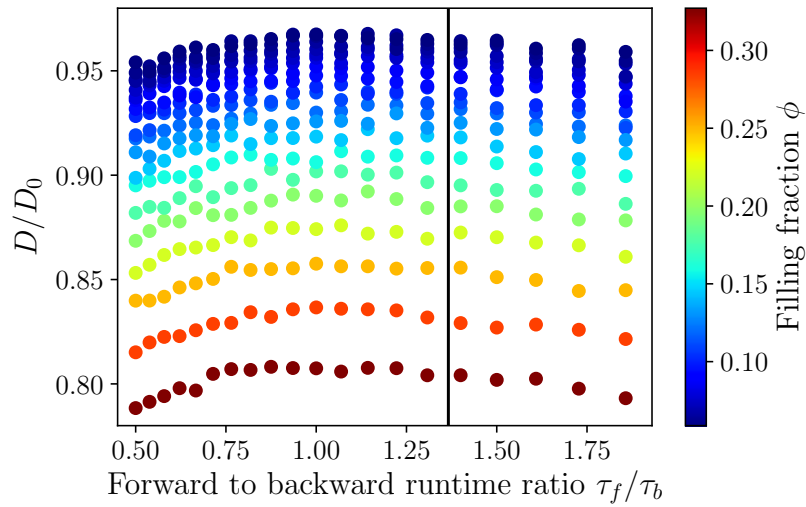


FIGURE 6.5: Nonequilibrium phase diagram for two dimensional interacting run-reverse-flick particles. The normalized diffusion constant D/D_0 is shown for different runtime ratios τ_f/τ_b and filling fractions ϕ (color code). For fixed filling fraction a maximum at $\tau_f/\tau_b \sim 1.2$ is found. The black line shows the theoretical prediction of the maximum from Eq. (6.26).

which has a maximum at the runtime ratio $\tau_f/\tau_b = (1 + \sqrt{3})/2 \approx 1.37$. This maximum approximately coincides with the maxima found in the simulations and is marked with a black line in Fig.6.5.

The maximum in diffusion found in Fig. 6.5 and Eq. (6.26) constitutes an optimum in the collective swimming behavior, that can be utilized by microorganisms using the run-reverse-flick swimming strategy. In fact, it was measured by [16] that *Vibrio alginolyticus* have a runtime ratio of $\tau_f/\tau_b \sim 1.3$. This brings us to the hypothesis that *Vibrio alginolyticus* bacteria optimized their run times to obtain a maximal collective diffusion coefficient. However, to demonstrate this hypothesis more experiments with different microorganisms that use the run-reverse-flick strategy would be needed.

Chapter 7

Motility states of active particles

In this chapter we will present a theoretical model to study the statistical mechanics of active particles exhibiting two motility states, which can be seen as a toy model for the adhesion of bacteria to solid interfaces. The experimental system we have in mind is a microswimmer in a quasi two dimensional confinement, that is initially in a highly motile state, and then after a characteristic time τ_{ad} it adheres to one of the confining surfaces and transitions to a low motility state. A realistic example for this is a *Chlamydomonas reinhardtii* cell, whose adhesion can be triggered by light [159]. Figure 7.1(a) shows a cell in the motile state performing its breaststroke motion; when the light is turned on, the cell adheres to a surface and it goes on to perform a gliding motion on one of the surfaces [Fig.7.1(b)]. In the following we assume that the transition to the gliding state is irreversible, that is, no transitions back to the high motility state is possible.

We will now first present the analytical treatment of this problem including an exact solution for the ISF, which we will support using active Brownian simulations and we will discuss the non-ergodic effects. Additionally, we will show the MSD of such a process, which shows an interesting subdiffusive regime.

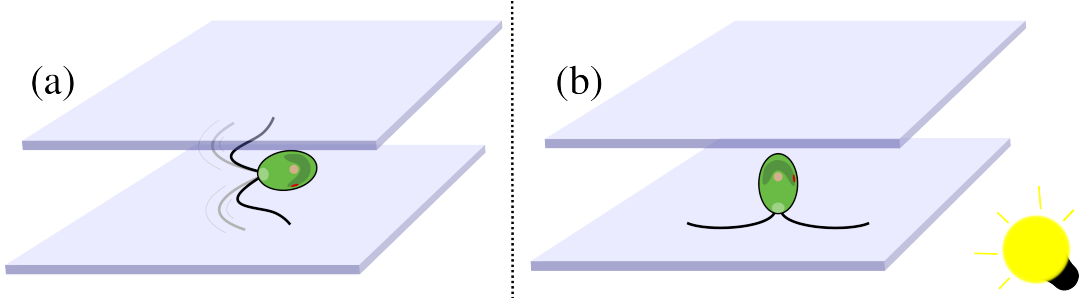


FIGURE 7.1: Schematic representation of a *Chlamydomonas reinhardtii* cell in a quasi two dimensional confinement with different motility stages: (a) performing the highly motile breaststroke motion; (b) the less motile gliding motion on the surface of a substrate.

7.1 Intermediate scattering function of two active motility states

To treat the problem of two active motility states we propose the following equations for the probability to be in the highly active state $P_h(\mathbf{r}, \mathbf{e}_h)$ with position \mathbf{r} and orientation $\mathbf{e}_h(\varphi_h)$ and the low active state with probability $P_l(\mathbf{r}, \mathbf{e}_l)$ with orientation $\mathbf{e}_l(\varphi_l)$, which are given by

$$\begin{aligned} \frac{\partial P_h(\mathbf{r}, \varphi_h, t)}{\partial t} = & -v_h \mathbf{e}(\varphi_h) \cdot \nabla P_h(\mathbf{r}, \varphi_h, t) \\ & + D_{R,h} \frac{\partial^2 P_h(\mathbf{r}, \varphi_h, t)}{\partial \varphi_h^2} + D_{T,h} \nabla^2 P_h(\mathbf{r}, \varphi_h, t) - \frac{1}{\tau} P_h(\mathbf{r}, \varphi_h, t), \end{aligned} \quad (7.1)$$

$$\begin{aligned} \frac{\partial P_l(\mathbf{r}, \varphi_l, t)}{\partial t} = & -v_l \mathbf{e}(\varphi_l) \cdot \nabla P_l(\mathbf{r}, \varphi_l, t) \\ & + D_{R,l} \frac{\partial^2 P_l(\mathbf{r}, \varphi_l, t)}{\partial \varphi_l^2} + D_{T,l} \nabla^2 P_l(\mathbf{r}, \varphi_l, t) + \frac{1}{\tau} P_h(\mathbf{r}, \varphi_h, t). \end{aligned} \quad (7.2)$$

For the sake of simplicity, we will consider here dynamics in 2d, strictly. Here, v_h and v_l are the self-propulsion velocities, $D_{T,h}$ and $D_{T,l}$ are the translational diffusion coefficients, $D_{R,h}$ and $D_{R,l}$ are the rotational diffusion coefficients associated to the high and low motility state respectively, and τ is the characteristic switching time after which the particle switches from the high to the low motility state. The total probability of finding a particle at position \mathbf{r} at time t is then given by

$$P(\mathbf{r}, t) = \int_0^{2\pi} P_h(\mathbf{r}, \varphi_h, t) d\varphi_h + \int_0^{2\pi} P_l(\mathbf{r}, \varphi_l, t) d\varphi_l. \quad (7.3)$$

The Fourier transform of the total probability [Eq.(7.3)] is related to the ISF which measures the density-density correlations in Fourier space and is given by

$$\mathcal{F}(\mathbf{k}, t) = \frac{1}{N} \langle \rho_{\mathbf{k}}(t) \rho_{-\mathbf{k}}(0) \rangle, \quad (7.4)$$

where N is the number of particles in the system, \mathbf{k} is the wave vector in Fourier space

and $\rho_{\mathbf{k}}$ is the density in Fourier space. Using Eq.(7.3) and the definition in Eq.(7.4) the ISF can be written as

$$\begin{aligned} \mathcal{F}(\mathbf{k}, t) &= \int_0^{2\pi} \tilde{P}_h(\mathbf{r}, \varphi_h, t) d\varphi_h \int_0^{2\pi} \tilde{P}_h(\mathbf{r}, \varphi_h, 0) d\varphi_h \\ &+ \int_0^{2\pi} \tilde{P}_l(\mathbf{r}, \varphi_l, t) d\varphi_l \int_0^{2\pi} \tilde{P}_l(\mathbf{r}, \varphi_l, 0) d\varphi_l, \end{aligned} \quad (7.5)$$

where $\tilde{f}(\mathbf{k})$ is the two-dimensional Fourier transform of the function f with wave vector \mathbf{k} .

To find an explicit expression for the ISF [Eq. (7.5)] we transform Eq. (7.1)-(7.2) into Fourier space; the equations then read

$$\begin{aligned} \frac{\partial \tilde{P}_h(\mathbf{k}, \varphi_h, t)}{\partial t} &= -iv_h \mathbf{e}(\varphi_h) \cdot \mathbf{k} \tilde{P}_h(\mathbf{k}, \varphi_h, t) \\ &+ D_{R,h} \frac{\partial^2 \tilde{P}_h(\mathbf{k}, \varphi_h, t)}{\partial \varphi_h^2} - D_{T,h} \mathbf{k}^2 \tilde{P}_h(\mathbf{k}, \varphi_h, t) - \frac{1}{\tau} \tilde{P}_h(\mathbf{k}, \varphi_h, t), \end{aligned} \quad (7.6)$$

$$\begin{aligned} \frac{\partial \tilde{P}_l(\mathbf{k}, \varphi_l, t)}{\partial t} &= -iv_l \mathbf{e}(\varphi_l) \cdot \mathbf{k} \tilde{P}_l(\mathbf{k}, \varphi_l, t) \\ &+ D_{R,l} \frac{\partial^2 \tilde{P}_l(\mathbf{k}, \varphi_l, t)}{\partial \varphi_l^2} - D_{T,l} \mathbf{k}^2 \tilde{P}_l(\mathbf{k}, \varphi_l, t) + \frac{1}{\tau} \tilde{P}_h(\mathbf{k}, \varphi_h, t). \end{aligned} \quad (7.7)$$

We will now first treat Eq. (7.6) as it can be solved alone, and then use the result to compute the solution of Eq. (7.7). Without loss of generality we can write the wave vector as

$$\mathbf{k} = k \begin{pmatrix} \cos \theta_k \\ \sin \theta_k \end{pmatrix}, \quad (7.8)$$

then the scalar product of the orientation and the wave vector in Eq.(7.6) is

$$\mathbf{e} \cdot \mathbf{k} = k \begin{pmatrix} \cos \varphi_h \\ \sin \varphi_h \end{pmatrix} \cdot \begin{pmatrix} \cos \theta_k \\ \sin \theta_k \end{pmatrix} = k \cos(\varphi_h - \theta_k). \quad (7.9)$$

Plugging Eq. (7.9) back into Eq. (7.6) gives

$$\begin{aligned} \frac{\partial \tilde{P}_h(\mathbf{k}, \varphi_h, t)}{\partial t} &= -iv_h k \cos(\varphi_h - \theta_k) \tilde{P}_h(\mathbf{k}, \varphi_h, t) \\ &+ D_{R,h} \frac{\partial^2 \tilde{P}_h(\mathbf{k}, \varphi_h, t)}{\partial \varphi_h^2} - D_{T,h} k^2 \tilde{P}_h(\mathbf{k}, \varphi_h, t) - \frac{1}{\tau} \tilde{P}_h(\mathbf{k}, \varphi_h, t), \end{aligned} \quad (7.10)$$

where $i = \sqrt{-1}$ is the imaginary unit. To make further progress we use a separation of variables Ansatz (neglecting \mathbf{k} as it can now be considered a parameter) given by

$$\tilde{P}_h(\mathbf{k}, \varphi_h, t) = A(t)\lambda(\varphi_h), \quad (7.11)$$

which gives the two ordinary differential equations

$$\frac{\partial A(t)}{\partial t} = \left[-D_{T,h}k^2 - \frac{1}{\tau} - \frac{D_{R,h}a_h}{4} \right] A(t), \quad (7.12)$$

$$\frac{\partial^2 \lambda(\varphi_h)}{\partial \varphi_h^2} = \left[-i \frac{v_h k}{D_{R,h}} \cos(\varphi_h - \theta_k) + \frac{a_h}{4} \right] \lambda(\varphi_h), \quad (7.13)$$

with separation constant a_h . Equation (7.12) is solved by a simple exponential, which is

$$A(t) = e^{\left[-D_{T,h}k^2 - \frac{1}{\tau} - \frac{D_{R,h}a_h}{4} \right] t}, \quad (7.14)$$

whereas Eq.(7.13) can be transformed into the Mathieu equation, that is

$$\frac{\partial^2 \lambda(\varphi)}{\partial \varphi^2} = [-2is \cos(2\varphi) + a_h] \lambda(\varphi), \quad (7.15)$$

where we used the variable transformation $\varphi = (\varphi_h - \theta_k)/2$ and replaced $s = 2v_h k/D_{R,h}$. The solution to the Mathieu equations [Eq. (7.15)] is given by the periodic Mathieu functions $ce_{2m}(\varphi, is)$ which can be expressed as a Fourier series [160]

$$ce_{2m}(\varphi, is) = \sum_{r=0}^{\infty} A_{h,2r}^{(2m)} \cos(2r\varphi), \quad (7.16)$$

where the Fourier coefficients are determined by the following eigenvalue problem [160]

$$\begin{pmatrix} 0 & \sqrt{2}is & & & & & & & \\ \sqrt{2}is & 4 & is & & & & & & \\ & is & 16 & is & & & & & \\ & & is & 36 & is & & & & \\ & & & \ddots & \ddots & \ddots & & & \\ & & & & is & 4r^2 & is & & \\ & & & & & & \ddots & & \end{pmatrix} \begin{pmatrix} \sqrt{2}A_{h,0}^{(2m)} \\ A_{h,2}^{(2m)} \\ A_{h,4}^{(2m)} \\ A_{h,6}^{(2m)} \\ \vdots \\ A_{h,2r}^{(2m)} \\ \vdots \end{pmatrix} = a_{h,2m} \begin{pmatrix} \sqrt{2}A_0^{(2m)} \\ A_{h,2}^{(2m)} \\ A_{h,4}^{(2m)} \\ A_{h,6}^{(2m)} \\ \vdots \\ A_{h,2r}^{(2m)} \\ \vdots \end{pmatrix}. \quad (7.17)$$

Here, the constant a_h that arises from the separation of variables takes on the eigenvalues $a_{h,2m}$. The solution of $\tilde{P}_h(\mathbf{k}, \varphi_h, t)$ then reads

$$\tilde{P}_h(\mathbf{k}, \varphi_h, t) = e^{\left[-D_{T,h}k^2 - \frac{1}{\tau} \right] t} \sum_{m=0}^{\infty} e^{-\frac{D_{R,h}a_{h,2m}}{4} t} ce_{2m}((\varphi_h - \theta_k)/2, i2v_h k/D_{R,h}), \quad (7.18)$$

and the orientation average is

$$\int_0^{2\pi} \tilde{P}_h(\mathbf{r}, \varphi_h, t) d\varphi_h = e^{\left[-D_{T,h}k^2 - \frac{1}{\tau} \right] t} \sum_{m=0}^{\infty} e^{-\frac{D_{R,h}a_{h,2m}}{4} t} A_{h,0}^{2m}, \quad (7.19)$$

which in the limit $\tau \rightarrow \infty$ was also reported in [102].

Furthermore, the limit $\tau \rightarrow \infty$ of Eq.(7.19) is also the homogeneous solution of Eq.(7.7) (with appropriate constants $D_{T,l}, D_{R,l}, v_l$) and the full solution of Eq.(7.7) can be found using the method of variation of parameters. It is important to note that we can only solve Eq.(7.7) because we assumed that the orientation variables \mathbf{e}_h and \mathbf{e}_l in high and low activity state [Eq.(7.1)-(7.2)] are different. The orientation average of the full solution of the low activity state [Eq.(7.7)] is given by

$$\int_0^{2\pi} \tilde{P}_l(\mathbf{r}, \varphi_l, t) d\varphi_l = \sum_{n=0}^{\infty} e^{-\omega_l^n t} A_{l,0}^{2n} \left(\frac{1}{\tau} \sum_{m=0}^{\infty} \frac{1}{\omega_h^m - \omega_l^n} A_{h,0}^{2m} e^{-(\omega_h^m - \omega_l^n)t} + C_l \right), \quad (7.20)$$

where we used $\omega_h^m = k^2 D_{T,h} + 1/\tau + D_{R,h} a_{h,2m}/4$ and $\omega_l^n = k^2 D_{T,l} + D_{R,l} a_{l,2n}/4$, and where $A_{l,0}^{2n}$ and $a_{l,2n}$ are determined with Eq.(7.17) and the appropriate constants $D_{T,l}, D_{R,l}$ and v_l .

Summing Eq.(7.19) and Eq.(7.20) gives the ISF of the full system [Eq.(7.5)], which will be further discussed in Sec.7.4.

7.2 Simulation of two active motility states

To simulate a system with two active motility states we use the following equations in the highly motile state

$$\frac{d\mathbf{r}(t)}{dt} = -v_h \mathbf{e}_h - \mathbf{\Gamma}_h(t), \quad (7.21)$$

$$\frac{d\mathbf{e}_h(t)}{dt} = \mathbf{\eta}_h(t) \times \mathbf{e}_h(t), \quad (7.22)$$

where \mathbf{r} is the position, \mathbf{e}_h the orientation, v_h is the self-propulsion velocity and $\mathbf{\Gamma}_h$ and $\mathbf{\eta}_h$ are fluctuating terms with correlation functions

$$\langle \mathbf{\Gamma}_h(t) \rangle = 0, \quad (7.23)$$

$$\langle \mathbf{\Gamma}_h(t) \otimes \mathbf{\Gamma}_h(t + \Delta t) \rangle = 2D_{T,h} \delta(\Delta t) \mathbf{I}, \quad (7.24)$$

$$\langle \mathbf{\eta}_h(t) \rangle = 0, \quad (7.25)$$

$$\langle \mathbf{\eta}_h(t) \otimes \mathbf{\eta}_h(t + \Delta t) \rangle = 2D_{R,h} \delta(\Delta t) \mathbf{I}, \quad (7.26)$$

where $D_{T,h}$ is the translational and $D_{R,h}$ the rotational diffusion coefficient in the high motility state. After a time t_{switch} which is a random number drawn from the exponential distribution $e^{-\frac{t_{\text{switch}}}{\tau}}$ with characteristic switching time τ , the system goes to the low motility state. The equations of motion in the low motility state are

$$\frac{d\mathbf{r}(t)}{dt} = -v_l \mathbf{e}_l - \mathbf{\Gamma}_l(t), \quad (7.27)$$

$$\frac{d\mathbf{e}_l(t)}{dt} = \mathbf{\eta}_l(t) \times \mathbf{e}_l(t), \quad (7.28)$$

where the position \mathbf{r} from Eq. (7.21) is kept, but the particle obtains a new random orientation \mathbf{e}_l . Also, the fluctuating terms change to $\mathbf{\Gamma}_l$ and $\mathbf{\eta}_l$ with correlation

functions

$$\langle \mathbf{\Gamma}_l(t) \rangle = 0 \quad (7.29)$$

$$\langle \mathbf{\Gamma}_l(t) \otimes \mathbf{\Gamma}_l(t + \Delta t) \rangle = 2D_{T,l}\delta(\Delta t)\mathbf{I} \quad (7.30)$$

$$\langle \boldsymbol{\eta}_l(t) \otimes \rangle = 0 \quad (7.31)$$

$$\langle \boldsymbol{\eta}_l(t)\boldsymbol{\eta}_l(t + \Delta t) \rangle = 2D_{R,l}\delta(\Delta t)\mathbf{I} \quad (7.32)$$

where $D_{T,l}$ and $D_{R,l}$ are the translational and rotational diffusion coefficients in the low motility state. To integrate Eq. (7.21)-(7.22) and Eq. (7.27)-(7.28) numerically we use the algorithm show in Sec. 3.1.2.

7.3 Mean square displacement of two active motility states

The MSD can be found using the ISF by means of the relation

$$\langle (\mathbf{r}(t) - \mathbf{r}(0))^2 \rangle = -6 \frac{\partial}{\partial (k^2)} \mathcal{F}(k, t) |_{k^2=0}. \quad (7.33)$$

Using the result for the ISF from Sec.7.1 we find the following expression for the MSD

$$\begin{aligned} \langle (\mathbf{r}(t) - \mathbf{r}(0))^2 \rangle = & 2 \left\{ \frac{v_h^2 \tau [1 - e^{-t/\tau}]}{D_{R,h}} - \frac{v_h^2 \tau (1 - e^{-t(D_{R,h}+1/\tau)})}{D_{R,h}(1 + D_{R,h}\tau)} \right. \\ & + 2D_{T,l} \left[t + \tau (e^{-t/\tau} - 1) \right] + \frac{e^{-t(D_{R,l}+1/\tau)}}{D_{R,l}^2(D_{R,l}\tau - 1)} \\ & \times \left[-v_l^2 e^{t/\tau} + e^{t(D_{R,l}+1/\tau)} (D_{R,l}\tau - 1) (2D_{R,l}^2 D_{T,h}\tau + v_l^2 (D_{R,l}t - 1 - D_{R,l}\tau)) \right. \\ & \left. \left. - D_{R,l}^2 \tau e^{D_{R,l}t} (-v_l^2 \tau + 2D_{T,h} (D_{R,l}\tau - 1)) \right] \right\}. \quad (7.34) \end{aligned}$$

In Fig. 7.2 we show the MSD from Eq. (7.34) as well as simulated MSDs [Eq. (7.21)-(7.22) and Eq. (7.27)-(7.28)] for different adhesion times τ . The parameters we used are summed up in Tab. 7.1.

$D_{T,h}$	$0.02v_h\sigma$
$D_{R,h}$	$3D_{T,h}/\sigma^2$
v_l	$0.1v_h$
$D_{T,l}$	$0.002v_h\sigma$
$D_{R,l}$	$3D_{T,l}/\sigma^2$

TABLE 7.1: Parameter values used for the MSD in Fig. 7.2 and the ISF in Fig. 7.3, where σ is the particle radius and v_h is the particle velocity in the high motility state.

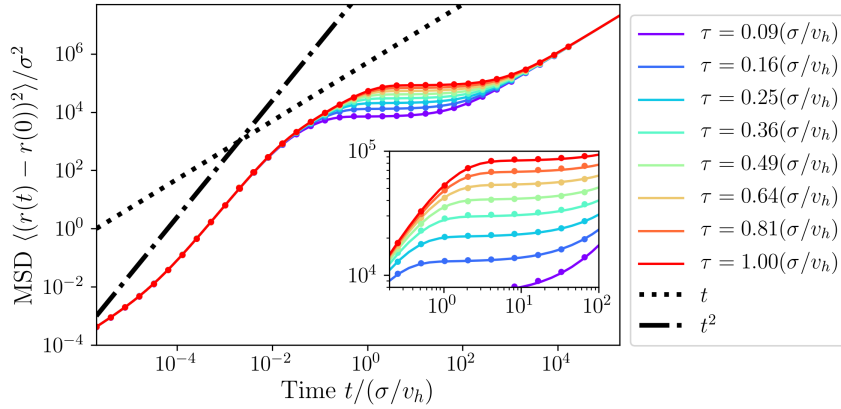


FIGURE 7.2: MSD of an active particle with two motility states. Data points show the simulations and lines show the analytical results Eq. (7.34). Different colors show the MSD with different switching times τ , the dotted line shows a linear and the dashed-dotted shows a quadratic scaling. The inset shows a zoom of the data, where a plateau of the MSD can be seen. This is related to the switching of the motility state.

The MSD in Fig. 7.2 shows up to five characteristic regimes: (i) for very small times the behavior is diffusive, due to simple translational diffusion; (ii) the second scaling is ballistic which is induced by the activity; (iii) next, there is another diffusive scaling which comes from the rotational diffusion; (iv) the following regime shows a plateau, which is related to the switching to a lower motility state; and (v) finally shows a diffusive regime.

Interestingly, the system has a non-ergodic behavior, as the MSD shows a leveling off, which is induced by the switching of motility states. This behavior has an important consequence for the statistical analysis of the MSD of active particles or microswimmers. Imagine an experimental situation where the data acquired stop somewhere during the plateau regime. The experimentalist might conclude that a subdiffusive regime is reached. Our results however show that this is only a transient state, and a true diffusive regime will be reached at much later times. Again, this is a consequence of the switching of motility states. While this is not so common for artificial swimmers, it is a regularly encountered situation in biological swimmers.

7.4 Intermediate scattering function of two motility states

The ISF measures the density-density correlations in Fourier space and thus holds the full information of a dynamical system. In general it is given by

$$\mathcal{F}(\mathbf{k}, t) = \frac{1}{N} \langle \rho_{\mathbf{k}}(t) \rho_{-\mathbf{k}}(0) \rangle, \quad (7.35)$$

where N is the number of particles in the system, \mathbf{k} is the wavevector in Fourier space, and $\rho_{\mathbf{k}}$ is the Fourier transform of the density. In Sec. 7.1 we derived the

ISF analytically and from particle based simulations it is easily computed using the definition of the Fourier transform.

In Fig. 7.3 the ISF of an active Brownian particle with two different motility states can be seen. We show different switching times, and a range of wavevectors for each switching time. The parameters we used are the same as in Sec. 7.3 and are displayed in Tab. 7.1.

It can be seen that the analytical calculation and the numerical results agree extremely well for several orders of magnitude in time, for all switching times and wave vectors. In the behavior of the ISF several regimes can be seen: for large wave vectors (Fig. 7.3 red and orange data) and small times the ISF oscillates, which corresponds to particles running on straight path, i.e. ballistic motion. On intermediate time scales and small wave vectors (Fig. 7.3 blue and purple data), the ISF first decays, corresponding to a diffusive motion and then becomes constant, which is induced by the switching to a lower motility state. Finally, the ISF decays to zero due to the diffusive motion in the lower motility state. Interestingly this resembles the behavior of a supercooled liquid, as it is known from glass physics [161]. In case of a supercooled liquid the ISF levels off due to a caging effect: the particles are very closely packed such that they can barely move. However, the caging effect can be seen as a lower motility state, since it effectively reduces the diffusion coefficient. This is very similar to our two motility stage model as the activity is reduced here, which effectively results in a lower diffusion coefficient.

Our calculations (both analytical and simulational) were restricted to 2d. It is interesting to extend these calculations to 3d, and verify which conclusions still hold. We leave this task to future work.

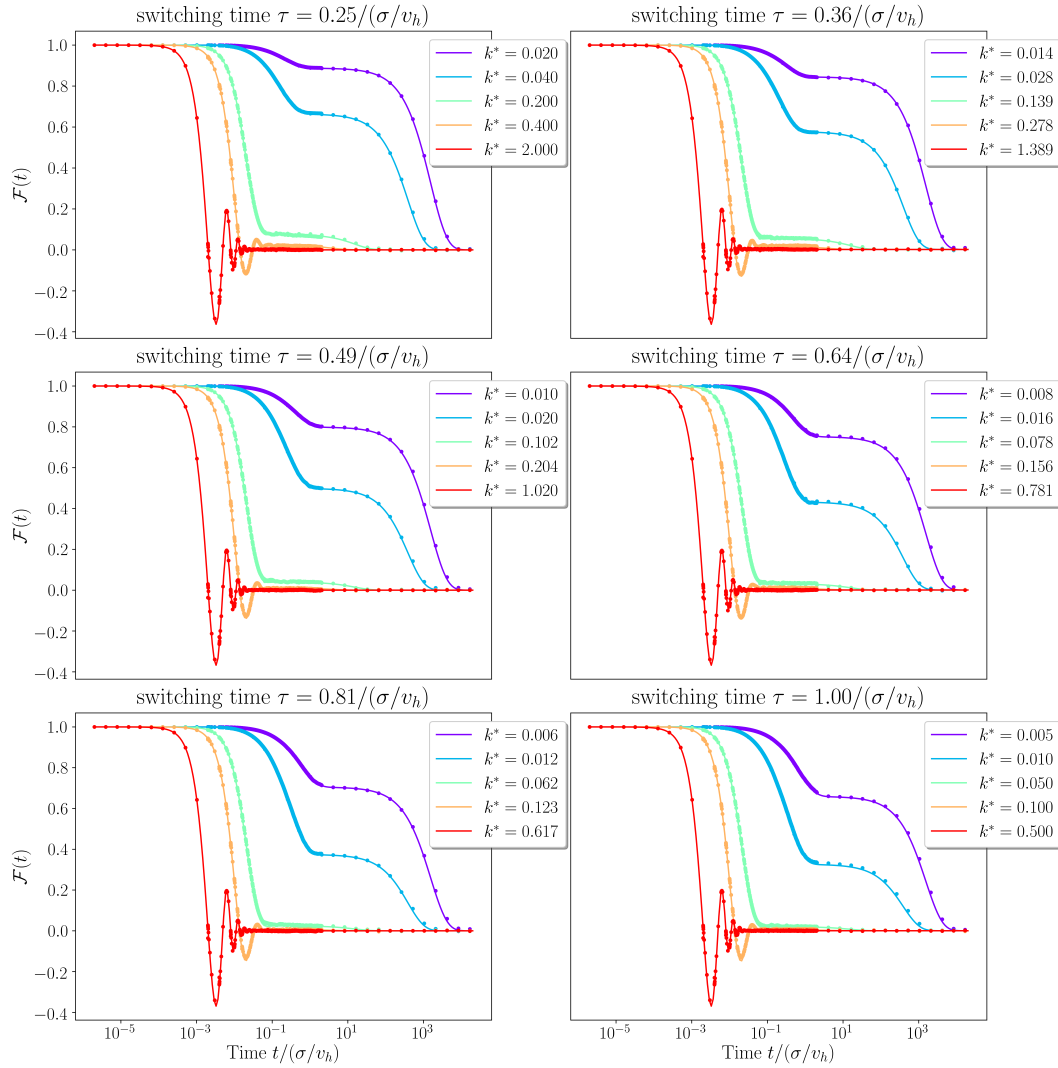


FIGURE 7.3: Intermediate scattering function (ISF) for different switching times τ . For each switching time a range of wavevectors $k^* = kv_h/\tau$ is shown (color code). The data points show simulations and the lines show the analytical calculation from Sec. 7.1. The leveling off in the ISF is induced by the switching of motility states.

Chapter 8

Conclusions and outlook

8.1 Conclusions

In this thesis we have studied the collective effects of microswimmers in complex environments. We investigated the effects of confinement on the alga *Chlamydomonas reinhardtii*, the influence of hydrodynamic interactions between microswimmers, the implications on collective motion of the run-reverse-flick swimming strategy and statistical effects of an active Brownian particle with two motility stages.

In Chapter 4 we studied the swimming behavior of a single *Chlamydomonas reinhardtii* cell in a quasi two-dimensional circular and elliptical confinement. We showed that the *Chlamydomonas reinhardtii* cell has an increased probability to swim close to a wall, and discovered that the probability of being close to the wall scales with the wall curvature. In fact, we found that this curvature guidance is a direct consequence of the shape anisotropy of the cell and its flagella. From a theoretical point of view, the key ingredient in our model is the torque that is associated with the shape anisotropy. However, it is noteworthy that we did not need to include any hydrodynamic interactions into the model to explain the swimming behavior.

Chapter 5 deals with the consequences of hydrodynamics on microswimmers. Here, we first presented a new model that has an anisotropic swimmer shape similar to the *Chlamydomonas reinhardtii* model in Chapter 4, but also takes into account the hydrodynamic flow fields that were experimentally measured for puller- and pusher-type

swimmers. To capture the entire hydrodynamic interactions we employed the multiparticle collision dynamics technique that was presented in Sec. 3.2. We studied the nonequilibrium phase diagram of a collection of swimmers and found that they exhibit density heterogeneities. In fact, we discovered a maximum in the density heterogeneities at an intermediate filling fraction, which represents an optimum for a self-concentration of the microswimmers. Importantly, this effect is induced by a competition between hydrodynamic and steric interactions between the microswimmers. Here, the hydrodynamic interactions destabilize the system leading in principle, to divergent density fluctuations. This instability however is tempered by the steric interactions between the swimmers. This competition of hydrodynamic and steric forces is recovered by the analytical theory that we present. It is worth pointing out that the density heterogeneities that we found have nothing to do with the so-called motility induced phase separation. This latter is a clustering effect that appears only due to a very slow reorientation dynamics (i.e. very low rotational diffusivity) of the particles. To date, no experiment has observed the dramatic condensation of active particles predicted by motility induced phase separation. Additionally, the maximum in density heterogeneities described in this thesis appears at a much lower filling fraction than motility induced phase separation, which makes it relevant for biological microswimmers.

The effect of the run-reverse-flick swimming strategy on the collective behavior of microswimmers was studied in Chapter 6. Here, we first presented methods for how to include the run-reverse-flick swimming strategy into Brownian dynamics and squirmer simulations. We also show an approach to include steric interactions into an analytical theory that includes the run-reverse-flick swimming strategy. Using these computational and analytical methods, we studied the behavior of collective diffusion of run-reverse-flick microswimmers. We find a maximum in the dependence of the collective diffusion coefficient on the forward to backward runtime ratio for a rather broad range of filling fractions. This maximum consistently occurs at a runtime ratio of 1.2. Physically, this maximum represents an optimum in the diffusivity of large numbers of microswimmers. Intriguingly, this is the same ratio that was found experimentally for the bacterium *Vibrio alginolyticus* [16], which brings us to the hypothesis that the organism tuned its runtime ratio to match the optimal collective diffusion. If these results were to be confirmed for multiple organisms, they would point to the tantalizing conclusion that specific physical forces applied an evolutionary pressure that shaped a very delicate balance of biomolecular processes internal to the cell. This is, of course, an ambitious research project left for the future.

Chapter 7 deals with the statistical effects of microswimmers with two motility stages. We present a toy model, which has two motility stages and find an exact analytical expression for the ISF of the system. We study the MSD of the system and find a subdiffusive regime, which is induced by the switching of motility states. Furthermore, we investigate the ISF and find a non-ergodic behavior for which we draw a comparison to a supercooled liquid.

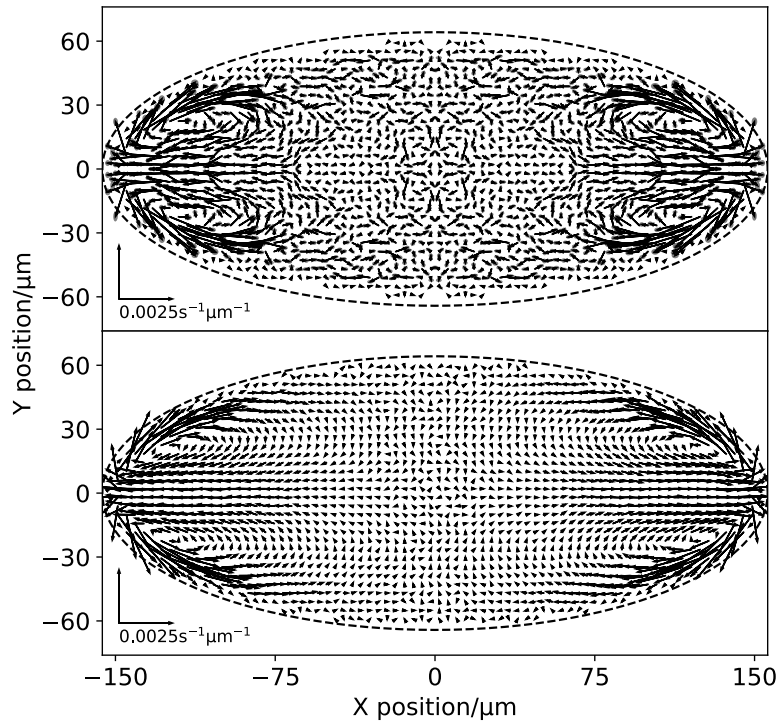


FIGURE 8.1: Probability flux of a *Chlamydomonas reinhardtii* cell inside a quasi two dimensional elliptical confinement. Top panel shows the experimental data and bottom panel the simulations (see also Chapter 4). The apparent loops in the probability flux are a hallmark of nonequilibrium behavior. The figure was kindly provided by Jan Cammann.

8.2 Outlook

The topic of this thesis “collective effects of microswimmers in “complex environments” is rather general, hence there is a plethora of future work. We will present possibilities and some preliminary results for each chapter from 4 to 7 in the following.

In Chapter 4 we showed that the motility of a *Chlamydomonas reinhardtii* is guided by the confining walls. However, the confining geometries we studied were limited to a number of circular and elliptical confining chambers. Since *Chlamydomonas reinhardtii* is a soil-dwelling alga, it frequently encounters more complex confinements. Therefore, we aim to analyze the behavior inside different elliptical chambers in more detail. In Fig. 8.1 we show the probability flux inside an ellipse, where one can identify loops in the probability flux. As pointed out by [162] this is a hallmark of the nonequilibrium character of the system, which we will try to characterize further in the future. We hope that this will enable us to also understand the dynamics inside more complex geometries, which can also include convex curvatures that are more common in natural environments.

The density heterogeneities due to the hydrodynamic interactions between microswimmers that we find in Chapter 5, are rather loose, dynamic structures. Further analysis of these structures including a comparison to experiments would help to elucidate how relevant the hydrodynamic interactions are for collective motion of microswimmers. Another interesting question is whether the system shows bacterial turbulence of the type depicted in Fig. 1.1(b). Our simulations could give a more detailed insight into the nature of this phenomenon as we have direct access to the hydrodynamic flows and the microswimmer flows. However, studying the influence of confining walls on the collective behavior is another interesting question. So far, the effect of flat, planar walls has been studied, but in the natural environment the confining surfaces of, for example, a *Chlamydomonas reinhardtii* cell in soil are very rough. We think that a roughness of the confining walls will tremendously effect the corresponding fluid flows, as well as the microswimmer surface interaction and hence the collective behavior.

Concerning the run-reverse-flick strategy an interesting question is to see if a similar effect as motility induced phase separation can be found. A preliminary nonequilibrium phase diagram on this matter can be seen in Fig. 8.2. Here, we do not find any large scale clusters, as for the motility induced phase separation, but we rather find small dynamic clusters. Also, these dynamic clusters are in a very different region in phase space as compared to motility induced phase separation, hence we conclude that the origin is different. However, further analysis including a comparison with our analytical theory (Sec. 6.4) is needed here. Nonetheless, motility induced phase separation seems to be suppressed because of the backward run phase, which prevents the particles from blocking each other.

Another interesting question concerns the adhesion of particles to surfaces in combination with the influence of collective effects. In Chapter 7 we presented a toy model to study the effect of different motility stages. It would be interesting to further develop this model in three dimensions and introduce a probabilistic mechanism for adhesion. Collective effects will then certainly play a more important role, since particles should be able to adhere to one another. Importantly, electrostatic interactions are often considered to play a crucial role in the bacterial adhesion process. Therefore, we would suggest to include into our simulations a DLVO-type (Derjaguin, Landau, Verwey, Overbeek) potential (between particles and with the confining surfaces), which describes the electrostatic interactions between charged surfaces immersed in a liquid medium.

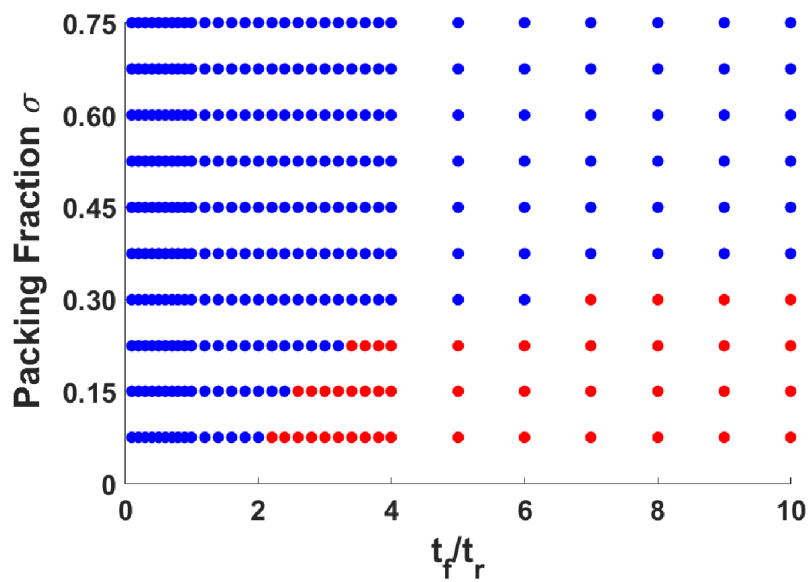


FIGURE 8.2: Phase diagram of run-reverse-flick model of active particles in two dimensions. The abscissa shows the runtime ratio and the ordinate shows the packing fraction. Blue symbols indicate a homogeneous particle configuration, red symbols show dynamic clusters. No large scale clusters as in motility induced phase separation are found. The figure was kindly provided by Arghadwip Paul.

Appendix

The hybrid MD-MPCD code that was used in Sec. 5.1 was developed by us. No simulation package was used. Since the implementation of the force poles is the computationally novel part of the simulation, we give the corresponding CUDA kernels here. MPCD simulation of Sec. 5.1. The code snippet for our puller-type swimmers is:

```

__global__ void SRD_add_force_swimmers_GPU(
    int *gost_list,
    FLOATTYPE *molecule_x, FLOATTYPE *molecule_y, FLOATTYPE *molecule_z,
    FLOATTYPE *molecule_velocity_x,
    FLOATTYPE *molecule_velocity_y,
    FLOATTYPE *molecule_velocity_z,
    FLOATTYPE *molecule_q0,
    FLOATTYPE *molecule_q1,
    FLOATTYPE *molecule_q2,
    FLOATTYPE *molecule_q3,
    FLOATTYPE *molecule_0_x,
    FLOATTYPE *molecule_0_y,
    FLOATTYPE *molecule_0_z,
    FLOATTYPE *molecule_e_x,
    FLOATTYPE *molecule_e_y,
    FLOATTYPE *molecule_e_z,
    FLOATTYPE *molecule_force_direction_front_1_x,
    FLOATTYPE *molecule_force_direction_front_1_y,
    FLOATTYPE *molecule_force_direction_front_1_z,
    FLOATTYPE *molecule_force_direction_front_2_x,
    FLOATTYPE *molecule_force_direction_front_2_y,
    FLOATTYPE *molecule_force_direction_front_2_z,
    FLOATTYPE *molecule_force_direction_back_x,
    FLOATTYPE *molecule_force_direction_back_y,
    FLOATTYPE *molecule_force_direction_back_z,
    FLOATTYPE *molecule_ux, FLOATTYPE *molecule_uy, FLOATTYPE *molecule_uz,

```

```

FLOATYPE *molecule_umass ,
FLOATYPE *SRD_ptls_x ,FLOATYPE *SRD_ptls_y ,FLOATYPE *SRD_ptls_z ,
FLOATYPE *SRD_ptls_vx ,FLOATYPE *SRD_ptls_vy ,FLOATYPE *SRD_ptls_vz ,
int *molecule_flick_key ,
FLOATYPE *Upx , FLOATYPE *Upy , FLOATYPE *Upz ,
FLOATYPE *Mxyz ,
FLOATYPE X0 ,FLOATYPE Y0 ,FLOATYPE Z0 ,
int *Unorm , int *Ulist ,
int *lockSRD ,int *lockMD)
{

int n ;
int l_srd_work_particle ;

FLOATYPE v_add_x=0 ,v_add_y=0 ,v_add_z=0 ;

FLOATYPE l_dx , l_dy , l_dz ;
FLOATYPE l_dx_2 , l_dy_2 , l_dz_2 ;
FLOATYPE l_dist ;
FLOATYPE l_dist_1 ;
FLOATYPE l_dist_2 ;
FLOATYPE s_x ,s_y ,s_z ;
FLOATYPE s_x1 ,s_y1 ,s_z1 ;
FLOATYPE s_x2 ,s_y2 ,s_z2 ;
FLOATYPE ix ,iy ,iz ;

int is_sphere=0 ;

int molecule_SRD_x ,molecule_SRD_y ,molecule_SRD_z ;
FLOATYPE l_SRD_ptls_x ,l_SRD_ptls_y ,l_SRD_ptls_z ;

int l_swimmer_cells = (int)((FLOATYPE)Nx*O_SIDEEX) + EXTRABOX_FD/2 ;
FLOATYPE l_molecule_x ,l_molecule_y ,l_molecule_z ;

int i1 = blockIdx.x*blockDim.x + threadIdx.x ;
int i2 = i1 % ( (int)((Nx*2*O_SIDEEX+EXTRABOX_FD)*
                (Ny*2*O_SIDEY+EXTRABOX_FD)*(Nz*2*O_SIDEZ+EXTRABOX_FD))) ;
int i = (i1-i2)/((int)((Nx*2*O_SIDEEX+EXTRABOX_FD)*
                (Ny*2*O_SIDEY+EXTRABOX_FD)*(Nz*2*O_SIDEZ+EXTRABOX_FD))) ;

if(i1<(N_PARTICLE* (int)((Nx*2*O_SIDEEX+EXTRABOX_FD)*
                (Ny*2*O_SIDEY+EXTRABOX_FD)*(Nz*2*O_SIDEZ+EXTRABOX_FD))) )
    && i < N_PARTICLE && i >=0)
{
    int index ;

    l_molecule_x =molecule_x[i] ;
    l_molecule_y =molecule_y[i] ;
    l_molecule_z =molecule_z[i] ;

    SRD_find_index(l_molecule_x ,l_molecule_y ,l_molecule_z ,&index ,
                  &molecule_SRD_x ,&molecule_SRD_y ,&molecule_SRD_z ,
                  0.0 , 0.0 , 0.0) ;

    int k1 = i2 % ( (int)((Ny*2*O_SIDEY+EXTRABOX_FD)
                    *(Nz*2*O_SIDEZ+EXTRABOX_FD))) ;
    int k = molecule_SRD_x - l_swimmer_cells
            + (i2-k1) / ( (int)((Ny*2*O_SIDEY+EXTRABOX_FD)*

```



```

(Nz*2*O_SIDEZ+EXTRABOX_FD));

int m = k1 % ((int)((Nz*2*O_SIDEZ+EXTRABOX_FD))) ;
int l= molecule_SRD_y - l_swimmer_cells
      + (k1 - m) / ( (int)((Nz*2*O_SIDEZ+EXTRABOX_FD)));

m= molecule_SRD_z - l_swimmer_cells + m;

if(k>=Nx) k -= Nx;
if(k<0) k+=Nx;
if(l>=Ny) l -= Ny;
if(l<0) l+=Ny;
if(m>=Nz) m -= Nz;
if(m<0) m+=Nz;

//two forces on front sphere:
FLOATTYPE lab_direction_force_1_x=DIRECTION_FORCE_1_X;
FLOATTYPE lab_direction_force_1_y=DIRECTION_FORCE_1_Y;
FLOATTYPE lab_direction_force_1_z=DIRECTION_FORCE_1_Z;

FLOATTYPE lab_direction_force_2_x=DIRECTION_FORCE_2_X;
FLOATTYPE lab_direction_force_2_y=DIRECTION_FORCE_2_Y;
FLOATTYPE lab_direction_force_2_z=DIRECTION_FORCE_2_Z;

rotate_frame(&lab_direction_force_1_x,
             &lab_direction_force_1_y,
             &lab_direction_force_1_z,
             molecule_q0[i],molecule_q1[i],
             molecule_q2[i],molecule_q3[i],1);
rotate_frame(&lab_direction_force_2_x,
             &lab_direction_force_2_y,
             &lab_direction_force_2_z,
             molecule_q0[i],molecule_q1[i],
             molecule_q2[i],molecule_q3[i],1);

molecule_shift(&s_x, &s_y,&s_z,
               l_molecule_x,l_molecule_y,l_molecule_z,
               lab_direction_force_1_x,
               lab_direction_force_1_y,
               lab_direction_force_1_z,F_DIST_FRONT_1);
molecule_shift(&s_x1, &s_y1,&s_z1,
               l_molecule_x,l_molecule_y,l_molecule_z,
               lab_direction_force_2_x,
               lab_direction_force_2_y,
               lab_direction_force_2_z,F_DIST_FRONT_2);

index_to_position(&ix,&iy,&iz, k, l, m, 0.0, 0.0, 0.0);

distanceSRD( s_x,s_y,s_z,ix,iy,iz,&l_dx,&l_dy,&l_dz,&l_dist);
distanceSRD( s_x1,s_y1,s_z1,ix,iy,iz,&l_dx,&l_dy,&l_dz,&l_dist_1);

molecule_shift(&s_x2, &s_y2,&s_z2,
               l_molecule_x,l_molecule_y,l_molecule_z,
               molecule_e_x[i], molecule_e_y[i], molecule_e_z[i],
               -F_DIST_BACK);

distanceSRD( s_x2,s_y2,s_z2,ix,iy,iz,&l_dx,&l_dy,&l_dz,&l_dist_2);
if( l_dist < FORCE_SHELL_F )
{

```

```

        is_sphere =0;
    }
    if( l_dist_1 < FORCE_SHELL_F )
    {
        is_sphere =1;
    }
    if( l_dist_2 < FORCE_SHELL_B )
    {
        is_sphere =2;
    }

    if(is_sphere ==0 || is_sphere ==1 || is_sphere ==2 )
    {
        for(n=0; n<Unorm[k + NO*1+ N1*m];n++)
        {
            l_srd_work_particle= Ulist[ (k + NO*1+ N1*m ) * N3 + n];

            if(gost_list[l_srd_work_particle] ==-1
                || gost_list[l_srd_work_particle] ==-2 )
            {

                l_SRD_ptls_x= SRD_ptls_x[l_srd_work_particle] ;
                l_SRD_ptls_y= SRD_ptls_y[l_srd_work_particle] ;
                l_SRD_ptls_z= SRD_ptls_z[l_srd_work_particle] ;

                FLOATTYPE f_dir_x;
                FLOATTYPE f_dir_y;
                FLOATTYPE f_dir_z;

                if( is_sphere ==0 )
                {
                    distanceSRD(l_SRD_ptls_x,
                                l_SRD_ptls_y,
                                l_SRD_ptls_z,
                                s_x,s_y,s_z,
                                &l_dx,&l_dy,&l_dz,&l_dist);
                    f_dir_x=molecule_force_direction_front_1_x[i];
                    f_dir_y=molecule_force_direction_front_1_y[i];
                    f_dir_z=molecule_force_direction_front_1_z[i];

                }

                if( is_sphere ==1 )
                {
                    distanceSRD(l_SRD_ptls_x,
                                l_SRD_ptls_y,
                                l_SRD_ptls_z,
                                s_x1,s_y1,s_z1,
                                &l_dx,&l_dy,&l_dz,&l_dist);
                    f_dir_x=molecule_force_direction_front_2_x[i];
                    f_dir_y=molecule_force_direction_front_2_y[i];
                    f_dir_z=molecule_force_direction_front_2_z[i];

                }
                else if( is_sphere ==2 )
                {
                    distanceSRD(l_SRD_ptls_x,
                                l_SRD_ptls_y,
                                l_SRD_ptls_z,

```

```
        s_x2,s_y2,s_z2,
        &l_dx,&l_dy,&l_dz,&l_dist);
    f_dir_x=molecule_force_direction_back_x[i];
    f_dir_y=molecule_force_direction_back_y[i];
    f_dir_z=molecule_force_direction_back_z[i];
}

if( (l_dist < FORCE_RADIUS_F_SQ && is_sphere==0 )
|| (l_dist < FORCE_RADIUS_F_SQ && is_sphere==1 )
|| (l_dist < FORCE_RADIUS_B_SQ && is_sphere==2 ) )
{
    distanceSRD(l_SRD_ptls_x,
                l_SRD_ptls_y,
                l_SRD_ptls_z,
                l_molecule_x,l_molecule_y,l_molecule_z,
                &l_dx_2,&l_dy_2,&l_dz_2,&l_dist_2);

    v_add_x = MDforce * f_dir_x-molecule_velocity_x[i]
              - molecule_0_y[i]* l_dz_2
              + molecule_0_z[i]* l_dy_2;
    v_add_y = MDforce * f_dir_y-molecule_velocity_y[i]
              - molecule_0_z[i]* l_dx_2
              + molecule_0_x[i]* l_dz_2;
    v_add_z = MDforce * f_dir_z-molecule_velocity_z[i]
              - molecule_0_x[i]* l_dy_2
              + molecule_0_y[i]* l_dx_2;
    SRD_ptls_vx[l_srd_work_particle]+=v_add_x;
    SRD_ptls_vy[l_srd_work_particle]+=v_add_y;
    SRD_ptls_vz[l_srd_work_particle]+=v_add_z;

    SRD_ptls_x[l_srd_work_particle]+=
        v_add_x*0_SIDEY*DTSRD*0.5;
    SRD_ptls_y[l_srd_work_particle]+=
        v_add_y*0_SIDEY*DTSRD*0.5;
    SRD_ptls_z[l_srd_work_particle]+=
        v_add_z*0_SIDEZ*DTSRD*0.5;
}
}
}
}
}
```

For the pusher-type swimmers the code snippet is:

```
__global__ void SRD_add_force_swimmers_GPU(
    int *gost_list,
    FLOATTYPE *molecule_x,FLOATTYPE *molecule_y, FLOATTYPE *molecule_z,
    FLOATTYPE *molecule_velocity_x,
    FLOATTYPE *molecule_velocity_y,
    FLOATTYPE *molecule_velocity_z,
    FLOATTYPE *molecule_0_x,
    FLOATTYPE *molecule_0_y,
    FLOATTYPE *molecule_0_z,
    FLOATTYPE *molecule_e_x,
    FLOATTYPE *molecule_e_y,
    FLOATTYPE *molecule_e_z,
    FLOATTYPE *molecule_ux,FLOATTYPE *molecule_uy,
    FLOATTYPE *molecule_uz,FLOATTYPE *molecule_umass,
```

```

FLOATYPE *SRD_ptls_x, FLOATYPE *SRD_ptls_y, FLOATYPE *SRD_ptls_z,
FLOATYPE *SRD_ptls_vx, FLOATYPE *SRD_ptls_vy, FLOATYPE *SRD_ptls_vz,
FLOATYPE *molecule_q0, FLOATYPE *molecule_q1,
FLOATYPE *molecule_q2, FLOATYPE *molecule_q3,
int *molecule_flick_key,
FLOATYPE *Upx, FLOATYPE *Upy, FLOATYPE *Upz,
FLOATYPE *Mxyz,
FLOATYPE X0, FLOATYPE Y0, FLOATYPE Z0,
int *Unorm, int *Ulist,
int *lockSRD, int *lockMD)
{

int n;
int l_srd_work_particle;

FLOATYPE v_add_x=0, v_add_y=0, v_add_z=0;

FLOATYPE l_dx, l_dy, l_dz;
FLOATYPE l_dx_2, l_dy_2, l_dz_2;
FLOATYPE l_dist;
FLOATYPE l_dist_2;
FLOATYPE s_x, s_y, s_z;
FLOATYPE s_x2, s_y2, s_z2;
FLOATYPE ix, iy, iz;

int is_sphere=0;

int molecule_SRD_x, molecule_SRD_y, molecule_SRD_z;
FLOATYPE l_SRD_ptls_x, l_SRD_ptls_y, l_SRD_ptls_z;

int l_swimmer_cells = (int)((FLOATYPE)Nx*O_SIDEY) + EXTRABOX_FD/2;
FLOATYPE l_molecule_x, l_molecule_y, l_molecule_z;

int i1 = blockIdx.x*blockDim.x + threadIdx.x;
int i2 = i1 % ( (int)((Nx*2*O_SIDEY+EXTRABOX_FD)*
                (Ny*2*O_SIDEY+EXTRABOX_FD)*(Nz*2*O_SIDEZ+EXTRABOX_FD)));
int i = (i1-i2)/( (int)((Nx*2*O_SIDEY+EXTRABOX_FD)*
                (Ny*2*O_SIDEY+EXTRABOX_FD)*(Nz*2*O_SIDEZ+EXTRABOX_FD)));

if(i1<(N_PARTICLE* (int)((Nx*2*O_SIDEY+EXTRABOX_FD)*
                (Ny*2*O_SIDEY+EXTRABOX_FD)*(Nz*2*O_SIDEZ+EXTRABOX_FD)) )
    && i < N_PARTICLE && i >=0)
{
    int index;

    l_molecule_x =molecule_x[i];
    l_molecule_y =molecule_y[i];
    l_molecule_z =molecule_z[i];

    SRD_find_index(l_molecule_x, l_molecule_y, l_molecule_z, &index,
                  &molecule_SRD_x, &molecule_SRD_y, &molecule_SRD_z,
                  0.0, 0.0, 0.0);

    int k1 = i2 % ( (int)((Ny*2*O_SIDEY+EXTRABOX_FD)
                    *(Nz*2*O_SIDEZ+EXTRABOX_FD)) ) ;
    int k = molecule_SRD_x - l_swimmer_cells
            + (i2-k1) / ( (int)((Ny*2*O_SIDEY+EXTRABOX_FD)
                    *(Nz*2*O_SIDEZ+EXTRABOX_FD)) );

```

```

int m = k1 % ((int)((Nz*2*O_SIDEZ+EXTRABOX_FD)) ) ;
int l= molecule_SRD_y - l_swimmer_cells
      + (k1 - m) / ( (int)((Nz*2*O_SIDEZ+EXTRABOX_FD)));

m= molecule_SRD_z - l_swimmer_cells + m;

if(k>=Nx) k -= Nx;
if(k<0) k+=Nx;
if(l>=Ny) l -= Ny;
if(l<0) l+=Ny;
if(m>=Nz) m -= Nz;
if(m<0) m+=Nz;

molecule_shift(&s_x, &s_y,&s_z,
                l_molecule_x,l_molecule_y,l_molecule_z,
                molecule_e_x[i], molecule_e_y[i], molecule_e_z[i],
                F_DIST_FRONT);

index_to_position(&ix,&iy,&iz, k, l, m , 0.0, 0.0, 0.0);

distanceSRD( s_x,s_y,s_z,ix,iy,iz,&l_dx,&l_dy,&l_dz,&l_dist);

molecule_shift(&s_x2, &s_y2,&s_z2,
                l_molecule_x,l_molecule_y,l_molecule_z,
                molecule_e_x[i], molecule_e_y[i], molecule_e_z[i],
                -F_DIST_BACK);

distanceSRD( s_x2,s_y2,s_z2,ix,iy,iz,&l_dx,&l_dy,&l_dz,&l_dist_2);
if( l_dist < FORCE_SHELL_F )
{
    is_sphere =1;
}

if( l_dist_2 < FORCE_SHELL_B )
{
    is_sphere =2;
}

if(is_sphere ==1 || is_sphere ==2 )
{
    for(n=0; n<Unorm[k + N0*l+ N1*m];n++)
    {
        l_srd_work_particle= Ulist[ (k + N0*l+ N1*m )* N3 + n];

        if(gost_list[l_srd_work_particle] ==-1 ||
           gost_list[l_srd_work_particle] ==-2 )
        {

            l_SRD_ptls_x= SRD_ptls_x[l_srd_work_particle] ;
            l_SRD_ptls_y= SRD_ptls_y[l_srd_work_particle] ;
            l_SRD_ptls_z= SRD_ptls_z[l_srd_work_particle] ;

            FLOATTYPE fdx=0.0,fdy=0.0,fdz=0.0;
            FLOATTYPE rx,ry,rz;

            if( is_sphere ==1 )
            {

```

```

distanceSRD(
    l_SRD_ptls_x,
    l_SRD_ptls_y,
    l_SRD_ptls_z, s_x, s_y, s_z,
    &l_dx, &l_dy, &l_dz, &l_dist);

rx = l_dx;
ry = l_dy;
rz = l_dz;
rotate_frame(&rx, &ry, &rz,
    molecule_q0[i], molecule_q1[i],
    molecule_q2[i], molecule_q3[i], 0);
if(rz < 0 && rz > -FORCE_RADIUS_F)
{
    FLOATTYPE l_one_over_r_length=
        1.0/sqrtf(l_dist) ;
    FLOATTYPE p_of_z= 1.0 +rz/FORCE_RADIUS_F;
    fdx=-(1.0-p_of_z)*
        MDforce* rx*l_one_over_r_length;
    fdy=-(1.0-p_of_z)*
        MDforce* ry*l_one_over_r_length;
    fdz=-p_of_z
        *MDforce* rz*l_one_over_r_length;
    rotate_frame(&fdx, &fdy, &fdz,
        molecule_q0[i], molecule_q1[i],
        molecule_q2[i], molecule_q3[i], 1);
}
else
{
    fdx=MDforce* molecule_e_x[i];
    fdy=MDforce* molecule_e_y[i];
    fdz=MDforce* molecule_e_z[i];
}
}
else if( is_sphere ==2 )
{
    distanceSRD(
        l_SRD_ptls_x,
        l_SRD_ptls_y,
        l_SRD_ptls_z, s_x2, s_y2, s_z2,
        &l_dx, &l_dy, &l_dz, &l_dist);

    rx = l_dx;
    ry = l_dy;
    rz = l_dz;
    rotate_frame(&rx, &ry, &rz,
        molecule_q0[i], molecule_q1[i],
        molecule_q2[i], molecule_q3[i], 0);

    if(rz > 0 && rz < FORCE_RADIUS_B)
    {
        FLOATTYPE l_one_over_r_length=
            1.0/sqrtf(l_dist);
        FLOATTYPE p_of_z= 1.0 - rz/FORCE_RADIUS_F;
        fdx=-(1.0-p_of_z)
            *MDforce* rx*l_one_over_r_length;
        fdy=-(1.0-p_of_z)
            *MDforce* ry*l_one_over_r_length;
        fdz=-p_of_z
            *MDforce* rz*l_one_over_r_length;
    }
}
}

```


Bibliography

- [1] Jörn Dunkel, Sebastian Heidenreich, Knut Drescher, Henricus H. Wensink, Markus Bär, and Raymond E. Goldstein, “Fluid dynamics of bacterial turbulence,” *Phys. Rev. Lett.* **110**, 228102 (2013), <https://link.aps.org/doi/10.1103/PhysRevLett.110.228102>
- [2] James E. Berleman, Jodie Scott, Tatiana Chumley, and John R. Kirby, “Pre-dataxis behavior in myxococcus xanthus,” *Proceedings of the National Academy of Sciences* **105**, 17127–17132 (2008), <http://www.pnas.org/content/105/44/17127>
- [3] A. Kamphuis, “Picture distributed under a cc by-sa 4.0 licence, bioconvection patterns of euglena gracilis in 5 petri dishes of different height and diameter, 2 time steps,” https://de.wikipedia.org/wiki/Biokonvektion#/media/File:Bioconvection_Euglena_5_Petri_Dishes_2_times_Colour.jpg
- [4] NASA Goddard Space Flight Center, “Credit: Usgs/nasa/landsat 7, licensed under the creative commons attribution 2.0 generic license..” https://commons.wikimedia.org/wiki/File:Van_Gogh_from_Space.jpg
- [5] Luanne Hall-Stoodley, J. William Costerton, and Paul Stoodley, “Bacterial biofilms: from the natural environment to infectious diseases,” *Nature reviews microbiology* **2**, 95 (2004)
- [6] E. Smith, L. Howard, and E. Dymek, “Dartmouth electron microscope facility, dartmouth college,” (2007), <http://remf.dartmouth.edu/images/algaeSEM/source/1.html>

- [7] Knut Drescher, Raymond E. Goldstein, Nicolas Michel, Marco Polin, and Idan Tuval, “Direct measurement of the flow field around swimming microorganisms,” *Phys. Rev. Lett.* **105**, 168101 (2010), <https://link.aps.org/doi/10.1103/PhysRevLett.105.168101>
- [8] E. H. White, Centers for Disease Control and Prevention(1995), <https://phil.cdc.gov/details.aspx?pid=9995>
- [9] Knut Drescher, Jörn Dunkel, Luis H. Cisneros, Sujoy Ganguly, and Raymond E. Goldstein, “Fluid dynamics and noise in bacterial cell–cell and cell–surface scattering,” *Proc. Natl. Acad. Sci. USA* **108**, 10940–10945 (2011), <http://www.pnas.org/content/108/27/10940.abstract>
- [10] Roman Stocker and Justin R. Seymour, “Ecology and physics of bacterial chemotaxis in the ocean,” *Microbiology and Molecular Biology Reviews* **76**, 792–812 (2012)
- [11] Gabriel S. Redner, Michael F. Hagan, and Aparna Baskaran, “Structure and dynamics of a phase-separating active colloidal fluid,” *Phys. Rev. Lett.* **110**, 055701 (2013), <https://link.aps.org/doi/10.1103/PhysRevLett.110.055701>
- [12] Clemens Bechinger, Roberto Di Leonardo, Hartmut Löwen, Charles Reichhardt, Giorgio Volpe, and Giovanni Volpe, “Active particles in complex and crowded environments,” *Rev. Mod. Phys.* **88**, 045006 (2016), <https://link.aps.org/doi/10.1103/RevModPhys.88.045006>
- [13] Xamm, “Picture distributed under a cc by-sa 4.0 licence,” <https://en.wikipedia.org/wiki/Squirmers>
- [14] Joakim Stenhammar, Cesare Nardini, Rupert W. Nash, Davide Marenduzzo, and Alexander Morozov, “Role of correlations in the collective behavior of microswimmer suspensions,” *Phys. Rev. Lett.* **119**, 028005 (2017), <https://link.aps.org/doi/10.1103/PhysRevLett.119.028005>
- [15] H.C. Berg, A. Borowski, and E.R. De Vivie, *E. coli in Motion*, Biological and Medical Physics, Biomedical Engineering (Springer, 2004) <https://books.google.de/books?id=qyVoI1iUiBkC>
- [16] Li Xie, Tuba Altindal, Suddhashil Chattopadhyay, and Xiao-Lun Wu, “Bacterial flagellum as a propeller and as a rudder for efficient chemotaxis,” *Proceedings of the National Academy of Sciences* **108**, 2246–2251 (2011), <http://www.pnas.org/content/108/6/2246>
- [17] William B. Whitman, David C. Coleman, and William J. Wiebe, “Prokaryotes: The unseen majority,” *Proceedings of the National Academy of Sciences* **95**, 6578–6583 (1998), <http://www.pnas.org/content/95/12/6578>

- [18] Ron Sender, Shai Fuchs, and Ron Milo, “Are we really vastly outnumbered? revisiting the ratio of bacterial to host cells in humans,” *Cell* **164**, 337–340 (2016), <http://www.sciencedirect.com/science/article/pii/S0092867416000532>
- [19] Marco G. Mazza, “The physics of biofilms-an introduction,” *Journal of Physics D: Applied Physics* **49**, 203001 (2016)
- [20] A. Garcimartín, J.M. Pastor, L.M. Ferrer, J.J. Ramos, C. Martín-Gómez, and I. Zuriguel, “Flow and clogging of a sheep herd passing through a bottleneck,” *Physical Review E* **91**, 022808 (2015)
- [21] Francesco Ginelli, Fernando Peruani, Marie-Helène Pillot, Hugues Chaté, Guy Theraulaz, and Richard Bon, “Intermittent collective dynamics emerge from conflicting imperatives in sheep herds,” *Proceedings of the National Academy of Sciences* **112**, 12729–12734 (2015)
- [22] Michele Ballerini, Nicola Cabibbo, Raphael Candelier, Andrea Cavagna, Evaristo Cisbani, Irene Giardina, Vivien Lecomte, Alberto Orlandi, Giorgio Parisi, Andrea Procaccini, *et al.*, “Interaction ruling animal collective behavior depends on topological rather than metric distance: Evidence from a field study,” *Proceedings of the national academy of sciences* **105**, 1232–1237 (2008)
- [23] Andrea Cavagna, Alessio Cimarelli, Irene Giardina, Giorgio Parisi, Raffaele Santagati, Fabio Stefanini, and Massimiliano Viale, “Scale-free correlations in starling flocks,” *Proceedings of the National Academy of Sciences* **107**, 11865–11870 (2010)
- [24] Daniel J.G. Pearce, Adam M Miller, George Rowlands, and Matthew S Turner, “Role of projection in the control of bird flocks,” *Proceedings of the National Academy of Sciences* **111**, 10422–10426 (2014)
- [25] Alessandro Attanasi, Andrea Cavagna, Lorenzo Del Castello, Irene Giardina, Tomas S. Grigera, Asja Jelić, Stefania Melillo, Leonardo Parisi, Oliver Pohl, Edward Shen, *et al.*, “Information transfer and behavioural inertia in starling flocks,” *Nature physics* **10**, 691 (2014)
- [26] Yael Katz, Kolbjørn Tunstrøm, Christos C. Ioannou, Cristián Huepe, and Iain D. Couzin, “Inferring the structure and dynamics of interactions in schooling fish,” *Proceedings of the National Academy of Sciences* **108**, 18720–18725 (2011)
- [27] Ivo Buttinoni, Julian Bialké, Felix Kümmel, Hartmut Löwen, Clemens Bechinger, and Thomas Speck, “Dynamical clustering and phase separation in suspensions of self-propelled colloidal particles,” *Phys. Rev. Lett.* **110**, 238301 (2013), <https://link.aps.org/doi/10.1103/PhysRevLett.110.238301>
- [28] Yaouen Fily and M. Cristina Marchetti, “Athermal phase separation of self-propelled particles with no alignment,” *Phys. Rev. Lett.* **108**, 235702 (2012), <https://link.aps.org/doi/10.1103/PhysRevLett.108.235702>

- [29] Julian Bialké, Hartmut Löwen, and Thomas Speck, “Microscopic theory for the phase separation of self-propelled repulsive disks,” *EPL (Europhysics Letters)* **103**, 30008 (2013), <http://stacks.iop.org/0295-5075/103/i=3/a=30008>
- [30] Joakim Stenhammar, Adriano Tiribocchi, Rosalind J. Allen, Davide Marenduzzo, and Michael E. Cates, “Continuum theory of phase separation kinetics for active brownian particles,” *Phys. Rev. Lett.* **111**, 145702 (2013), <https://link.aps.org/doi/10.1103/PhysRevLett.111.145702>
- [31] Adam Wysocki, Roland G. Winkler, and Gerhard Gompper, “Cooperative motion of active brownian spheres in three-dimensional dense suspensions,” *EPL (Europhysics Letters)* **105**, 48004 (2014), <http://stacks.iop.org/0295-5075/105/i=4/a=48004>
- [32] Antoine Bricard, Jean-Baptiste Caussin, Debasish Das, Charles Savoie, Vijayakumar Chikkadi, Kyohei Shitara, Oleksandr Chepizhko, Fernando Perarani, David Saintillan, and Denis Bartolo, “Emergent vortices in populations of colloidal rollers,” *Nature Communications* **6** (2015), doi:\bibinfo{doi}{10.1038/ncomms8470}, <https://doi.org/10.1038/ncomms8470>
- [33] Adam Wysocki, Jens Elgeti, and Gerhard Gompper, “Giant adsorption of microswimmers: Duality of shape asymmetry and wall curvature,” *Phys. Rev. E* **91**, 050302 (2015), <https://link.aps.org/doi/10.1103/PhysRevE.91.050302>
- [34] Mark J. Schnitzer, “Theory of continuum random walks and application to chemotaxis,” *Phys. Rev. E* **48**, 2553–2568 (1993), <https://link.aps.org/doi/10.1103/PhysRevE.48.2553>
- [35] J. Tailleur and M. E. Cates, “Statistical mechanics of interacting run-and-tumble bacteria,” *Phys. Rev. Lett.* **100**, 218103 (2008), <https://link.aps.org/doi/10.1103/PhysRevLett.100.218103>
- [36] J. Tailleur and M. E. Cates, “Sedimentation, trapping, and rectification of dilute bacteria,” *EPL (Europhysics Letters)* **86**, 60002 (2009), <http://stacks.iop.org/0295-5075/86/i=6/a=60002>
- [37] Florian Thüroff, Christoph A. Weber, and Erwin Frey, “Critical assessment of the boltzmann approach to active systems,” *Phys. Rev. Lett.* **111**, 190601 (2013), <https://link.aps.org/doi/10.1103/PhysRevLett.111.190601>
- [38] Florian Thüroff, Christoph A. Weber, and Erwin Frey, “Numerical treatment of the boltzmann equation for self-propelled particle systems,” *Phys. Rev. X* **4**, 041030 (2014), <https://link.aps.org/doi/10.1103/PhysRevX.4.041030>
- [39] Claudio Maggi, Filippo Saglimbeni, Michele Dipalo, Francesco De Angelis, and Roberto Di Leonardo, “Micromotors with asymmetric shape that efficiently

- convert light into work by thermocapillary effects,” *Nature Communications* **6** (2015)
- [40] Claudio Maggi, Juliane Simmchen, Filippo Saglimbeni, Jaideep Katuri, Michele Dipalo, Francesco De Angelis, Samuel Sanchez, and Roberto Di Leonardo, “Self-assembly of micromachining systems powered by janus micromotors,” *Small* **12**, 446–451 (2015), <https://doi.org/10.1002/smll.201502391>
- [41] H.C. Berg and L. Turner, “Chemotaxis of bacteria in glass capillary arrays. *escherichia coli*, motility, microchannel plate, and light scattering,” *Biophysical Journal* **58**, 919 – 930 (1990), <http://www.sciencedirect.com/science/article/pii/S000634959082436X>
- [42] Eric Lauga, Willow R. DiLuzio, George M. Whitesides, and Howard A. Stone, “Swimming in circles: motion of bacteria near solid boundaries,” *Biophys. J.* **90**, 400–412 (2006)
- [43] Allison P. Berke, Linda Turner, Howard C. Berg, and Eric Lauga, “Hydrodynamic attraction of swimming microorganisms by surfaces,” *Phys. Rev. Lett.* **101**, 038102 (2008), <https://link.aps.org/doi/10.1103/PhysRevLett.101.038102>
- [44] Aparna Baskaran and M. Cristina Marchetti, “Statistical mechanics and hydrodynamics of bacterial suspensions,” *Proc. Natl. Acad. Sci. USA* **106**, 15567–15572 (2009), <http://www.pnas.org/content/106/37/15567.abstract>
- [45] Takuji Ishikawa, J. T. Locsei, and T. J. Pedley, “Development of coherent structures in concentrated suspensions of swimming model micro-organisms,” *J. Fluid Mech.* **615**, 401–431 (2008)
- [46] Barath Ezhilan, Michael J. Shelley, and David Saintillan, “Instabilities and non-linear dynamics of concentrated active suspensions,” *Phys. Fluids* **25**, 070607 (2013), <http://dx.doi.org/10.1063/1.4812822>
- [47] David Saintillan and Michael J. Shelley, “Instabilities and pattern formation in active particle suspensions: Kinetic theory and continuum simulations,” *Phys. Rev. Lett.* **100**, 178103 (2008), <https://link.aps.org/doi/10.1103/PhysRevLett.100.178103>
- [48] Patrick T. Underhill, Juan P. Hernandez-Ortiz, and Michael D. Graham, “Diffusion and spatial correlations in suspensions of swimming particles,” *Phys. Rev. Lett.* **100**, 248101 (2008), <https://link.aps.org/doi/10.1103/PhysRevLett.100.248101>
- [49] Kwangmin Son, Jeffrey S. Guasto, and Roman Stocker, “Bacteria can exploit a flagellar buckling instability to change direction,” *Nature physics* **9**, 494 (2013)

- [50] Edward M. Purcell, “Life at low reynolds number,” *Am. J. Phys.* **45**, 3–11 (1977)
- [51] Marco Polin, Idan Tuval, Knut Drescher, J. P. Gollub, and Raymond E. Goldstein, “Chlamydomonas swims with two “gears” in a eukaryotic version of run-and-tumble locomotion,” *Science* **325**, 487–490 (2009), <http://science.sciencemag.org/content/325/5939/487>
- [52] G.D. Reilly, C.A. Reilly, E.G. Smith, and C. Baker-Austin, “Vibrio alginolyticus-associated wound infection acquired in british waters, guernsey, july 2011,” *Eurosurveillance* **16**, 19994 (2011)
- [53] Johannes Taktikos, Holger Stark, and Vasily Zaboruaev, “How the motility pattern of bacteria affects their dispersal and chemotaxis,” *PLOS ONE* **8**, 1–8 (2014), <https://doi.org/10.1371/journal.pone.0081936>
- [54] Vasily Kantsler, Jörn Dunkel, Marco Polin, and Raymond E. Goldstein, “Ciliary contact interactions dominate surface scattering of swimming eukaryotes,” *Proceedings of the National Academy of Sciences* **110**, 1187–1192 (2013), <http://www.pnas.org/content/110/4/1187>
- [55] Enkeleida Lushi, Vasily Kantsler, and Raymond E. Goldstein, “Scattering of biflagellate microswimmers from surfaces,” *Phys. Rev. E* **96**, 023102 (2017), <https://link.aps.org/doi/10.1103/PhysRevE.96.023102>
- [56] Willow R. DiLuzio, Linda Turner, Michael Mayer, Piotr Garstecki, Douglas B. Weibel, Howard C. Berg, and George M. Whitesides, “Escherichia coli swim on the right-hand side,” *Nature* **435**, 1271 (2005)
- [57] Eric Lauga and Thomas R. Powers, “The hydrodynamics of swimming microorganisms,” *Reports on Progress in Physics* **72**, 096601 (2009), <http://stacks.iop.org/0034-4885/72/i=9/a=096601>
- [58] Jens Elgeti, Roland G. Winkler, and Gerhard Gompper, “Physics of microswimmers—single particle motion and collective behavior: a review,” *Rep. Prog. Phys.* **78**, 056601 (2015)
- [59] Takuji Ishikawa, “Suspension biomechanics of swimming microbes,” *Journal of The Royal Society Interface*, rsif20090223(2009)
- [60] Alasdair G. Thompson, Julien Tailleur, Michael E. Cates, and Richard A. Blythe, “Lattice models of nonequilibrium bacterial dynamics,” *Journal of Statistical Mechanics: Theory and Experiment* **2011**, P02029 (2011)
- [61] Demian Levis and Ludovic Berthier, “Clustering and heterogeneous dynamics in a kinetic monte carlo model of self-propelled hard disks,” *Physical Review E* **89**, 062301 (2014)

- [62] Michael E. Cates and Julien Tailleur, “Motility-induced phase separation,” *Annu. Rev. Condens. Matter Phys.* **6**, 219–244 (2015)
- [63] D. Ray, C. Reichhardt, and C.J. Olson Reichhardt, “Casimir effect in active matter systems,” *Physical Review E* **90**, 013019 (2014)
- [64] Zahra Mokhtari, Timo Aspelmeier, and Annette Zippelius, “Collective rotations of active particles interacting with obstacles,” *EPL (Europhysics Letters)* **120**, 14001 (2017)
- [65] Fernando Peruani, Andreas Deutsch, and Markus Bär, “Nonequilibrium clustering of self-propelled rods,” *Phys. Rev. E* **74**, 030904 (2006), <https://link.aps.org/doi/10.1103/PhysRevE.74.030904>
- [66] H.H. Wensink and H. Löwen, “Emergent states in dense systems of active rods: from swarming to turbulence,” *Journal of Physics: Condensed Matter* **24**, 464130 (2012)
- [67] Aparna Baskaran and M Cristina Marchetti, “Hydrodynamics of self-propelled hard rods,” *Physical Review E* **77**, 011920 (2008)
- [68] H.H. Wensink, V. Kantsler, R.E. Goldstein, and J. Dunkel, “Controlling active self-assembly through broken particle-shape symmetry,” *Physical Review E* **89**, 010302 (2014)
- [69] Henricus H. Wensink, Jörn Dunkel, Sebastian Heidenreich, Knut Drescher, Raymond E. Goldstein, Hartmut Löwen, and Julia M. Yeomans, “Meso-scale turbulence in living fluids,” *Proc. Natl. Acad. Sci. USA* **109**, 14308–14313 (2012)
- [70] Andreas Zöttl and Holger Stark, “Hydrodynamics determines collective motion and phase behavior of active colloids in quasi-two-dimensional confinement,” *Phys. Rev. Lett.* **112**, 118101 (2014), <https://link.aps.org/doi/10.1103/PhysRevLett.112.118101>
- [71] Johannes Blaschke, Maurice Maurer, Karthik Menon, Andreas Zöttl, and Holger Stark, “Phase separation and coexistence of hydrodynamically interacting microswimmers,” *Soft Matter* **12**, 9821–9831 (2016)
- [72] Ricard Matas-Navarro, Ramin Golestanian, Tanniemola B. Liverpool, and Suzanne M. Fielding, “Hydrodynamic suppression of phase separation in active suspensions,” *Phys. Rev. E* **90**, 032304 (2014), <https://link.aps.org/doi/10.1103/PhysRevE.90.032304>
- [73] M. Theers, E. Westphal, K. Qi, R. G. Winkler, and G. Gompper, “Clustering of microswimmers: Interplay of shape and hydrodynamics,” *ArXiv e-prints*(2018), <http://adsabs.harvard.edu/abs/2018arXiv180701211T>

- [74] Matthew T. Downton and Holger Stark, “Simulation of a model microswimmer,” *J. Phys.: Condens. Matter* **21**, 204101 (2009), <http://stacks.iop.org/0953-8984/21/i=20/a=204101>
- [75] Ingo O. Götze and Gerhard Gompper, “Mesoscale simulations of hydrodynamic squirmer interactions,” *Phys. Rev. E* **82**, 041921 (2010), <https://link.aps.org/doi/10.1103/PhysRevE.82.041921>
- [76] Andreas Zöttl and Holger Stark, “Simulating squirmers with multiparticle collision dynamics,” *The European Physical Journal E* **41**, 61 (2018)
- [77] Anatoly Malevanets and Raymond Kapral, “Mesoscopic model for solvent dynamics,” *J. Chem. Phys.* **110**, 8605–8613 (1999), <http://dx.doi.org/10.1063/1.478857>
- [78] G. Gompper, T. Ihle, D. M. Kroll, and R. G. Winkler, *Multi-particle collision dynamics: a particle-based mesoscale simulation approach to the hydrodynamics of complex fluids*, Vol. Advanced computer simulation approaches for soft matter sciences III (Springer, 2009) pp. 1–87
- [79] David Saintillan and Michael J. Shelley, “Active suspensions and their nonlinear models,” *Comptes Rendus Physique* **14**, 497–517 (2013)
- [80] Tamás Vicsek, András Czirók, Eshel Ben-Jacob, Inon Cohen, and Ofer Shochet, “Novel type of phase transition in a system of self-driven particles,” *Physical review letters* **75**, 1226 (1995)
- [81] András Czirók and Tamás Vicsek, “Collective behavior of interacting self-propelled particles,” *Physica A: Statistical Mechanics and its Applications* **281**, 17–29 (2000)
- [82] Hugues Chaté, Francesco Ginelli, Guillaume Grégoire, Fernando Peruani, and Franck Raynaud, “Modeling collective motion: variations on the vicsek model,” *The European Physical Journal B* **64**, 451–456 (2008)
- [83] John Toner, Yuhai Tu, and Sriram Ramaswamy, “Hydrodynamics and phases of flocks,” *Annals of Physics* **318**, 170–244 (2005)
- [84] Yue-Xian Li, Ryan Lukeman, and Leah Edelstein-Keshet, “Minimal mechanisms for school formation in self-propelled particles,” *Physica D: Nonlinear Phenomena* **237**, 699–720 (2008)
- [85] Eric Bertin, Michel Droz, and Guillaume Grégoire, “Hydrodynamic equations for self-propelled particles: microscopic derivation and stability analysis,” *Journal of Physics A: Mathematical and Theoretical* **42**, 445001 (2009)
- [86] Rebekka E. Breier, Robin L.B. Selinger, Giovanni Ciccotti, Stephan Herminghaus, and Marco G. Mazza, “Spontaneous chiral symmetry breaking in collective active motion,” *Physical Review E* **93**, 022410 (2016)

- [87] Sriram Ramaswamy, “The mechanics and statistics of active matter,” *Annual Review of Condensed Matter Physics* **1**, 323–345 (2010), <https://doi.org/10.1146/annurev-conmatphys-070909-104101>
- [88] R. Kemkemer, D. Kling, D. Kaufmann, and H. Gruler, “Elastic properties of nematicoid arrangements formed by amoeboid cells,” *The European Physical Journal E* **1**, 215–225 (2000)
- [89] Vijay Narayan, Sriram Ramaswamy, and Narayanan Menon, “Long-lived giant number fluctuations in a swarming granular nematic,” *Science* **317**, 105–108 (2007)
- [90] Arshad Kudrolli, Geoffroy Lumay, Dmitri Volfson, and Lev S. Tsimring, “Swarming and swirling in self-propelled polar granular rods,” *Physical review letters* **100**, 058001 (2008)
- [91] Julia K. Parrish and William M. Hamner, *Animal groups in three dimensions: how species aggregate* (Cambridge University Press, 1997)
- [92] Xavier Serra-Picamal, Vito Conte, Romaric Vincent, Ester Anon, Dhananjay T. Tambe, Elsa Bazellieres, James P. Butler, Jeffrey J. Fredberg, and Xavier Trepat, “Mechanical waves during tissue expansion,” *Nature Physics* **8**, 628 (2012)
- [93] M. Cristina Marchetti, Jean-François Joanny, Sriram Ramaswamy, Tanniemola B. Liverpool, Jacques Prost, Madan Rao, and R. Aditi Simha, “Hydrodynamics of soft active matter,” *Reviews of Modern Physics* **85**, 1143 (2013)
- [94] Jonathan R. Howse, Richard A.L. Jones, Anthony J. Ryan, Tim Gough, Reza Vafabakhsh, and Ramin Golestanian, “Self-motile colloidal particles: from directed propulsion to random walk,” *Physical review letters* **99**, 048102 (2007)
- [95] Artur Erbe, Marcin Zientara, Larysa Baraban, Christian Kreidler, and Paul Leiderer, “Various driving mechanisms for generating motion of colloidal particles,” *Journal of Physics: Condensed Matter* **20**, 404215 (2008)
- [96] Shashi Thutupalli, Ralf Seemann, and Stephan Herminghaus, “Swarming behavior of simple model squirmers,” *New Journal of Physics* **13**, 073021 (2011)
- [97] Ralf Seemann, Jean-Baptiste Fleury, and Corinna C. Maass, “Self-propelled droplets,” *The European Physical Journal Special Topics* **225**, 2227–2240 (2016)
- [98] Stephan Herminghaus, Corinna C. Maass, Carsten Krüger, Shashi Thutupalli, Lucas Goehring, and Christian Bahr, “Interfacial mechanisms in active emulsions,” *Soft Matter* **10**, 7008–7022 (2014)
- [99] Carsten Krüger, Gunnar Klös, Christian Bahr, and Corinna C. Maass, “Curling liquid crystal microswimmers: A cascade of spontaneous symmetry breaking,” *Physical review letters* **117**, 048003 (2016)

- [100] Chenyu Jin, Carsten Krüger, and Corinna C. Maass, “Chemotaxis and autochemotaxis of self-propelling droplet swimmers,” *Proceedings of the National Academy of Sciences* **114**, 5089–5094 (2017)
- [101] Chenyu Jin, Babak V. Hokmabad, Kyle A. Baldwin, and Corinna C. Maass, “Chemotactic droplet swimmers in complex geometries,” *Journal of Physics: Condensed Matter* **30**, 054003 (2018)
- [102] Christina Kurzthaler, Clémence Devailly, Jochen Arlt, Thomas Franosch, Wilson C. K. Poon, Vincent A. Martinez, and Aidan T. Brown, “Spatiotemporal dynamics of catalytic janus particles,” (2017), arXiv:1712.03097, <https://arxiv.org/abs/1712.03097>
- [103] Francisco J. Sevilla and Mario Sandoval, “Smoluchowski diffusion equation for active brownian swimmers,” *Physical Review E* **91**, 052150 (2015)
- [104] Christina Kurzthaler, Sebastian Leitmann, and Thomas Franosch, “Intermediate scattering function of an anisotropic active brownian particle,” *Scientific Reports* **6**, 36702 (2016)
- [105] Christina Kurzthaler and Thomas Franosch, “Intermediate scattering function of an anisotropic brownian circle swimmer,” *Soft matter* **13**, 6396–6406 (2017)
- [106] E. Guyon, J.P. Hulin, L. Petit, and C.D. Matescu, *Physical Hydrodynamics* (Oxford University Press, 2015) <https://books.google.de/books?id=eYIwBgAAQBAJ>
- [107] G.J. Hancock, “The self-propulsion of microscopic organisms through liquids,” *Proc. R. Soc. Lond. A* **217**, 96–121 (1953)
- [108] S. Kim and S.J. Karrila, *Microhydrodynamics: Principles and Selected Applications*, Butterworth - Heinemann series in chemical engineering (Dover Publications, 2005)
- [109] Allen T. Chwang and T. Yao-Tsu Wu, “Hydromechanics of low-reynolds-number flow. part 2. singularity method for stokes flows,” *Journal of Fluid Mechanics* **67**, 787–815 (1975)
- [110] G.K. Batchelor, *An Introduction to Fluid Dynamics*, Cambridge Mathematical Library (Cambridge University Press, 2000) <https://books.google.de/books?id=R1a70ihRvUgC>
- [111] Hannes Risken, *The Fokker-Planck Equation* (Springer, 1984)
- [112] A. Einstein, “Über die von der molekularkinetischen theorie der wärme geforderte bewegung von in ruhenden flüssigkeiten suspendierten teilchen,” *Annalen der Physik* **322**, 549–560 (1905), <https://onlinelibrary.wiley.com/doi/abs/10.1002/andp.19053220806>

- [113] Marian von Smoluchowski, “Sur le chemin moyen parcouru par les molécules d’un gaz et sur son rapport avec la théorie de la diffusion,” *Bulletin International de l’Académie des Sciences de Cracovie* **1906**, 202 (1906)
- [114] Marian von Smoluchowski, “Zur kinetischen theorie der brownschen molekularbewegung und der suspensionen,” *Annalen der physik* **326**, 756–780 (1906)
- [115] Mike P. Allen and Dominic J. Tildesley, *Computer Simulation of Liquids* (Oxford University Press, 1989)
- [116] A.C. Brañka and D.M. Heyes, “Algorithms for brownian dynamics simulation,” *Phys. Rev. E* **58**, 2611–2615 (1998), <https://link.aps.org/doi/10.1103/PhysRevE.58.2611>
- [117] H. Goldstein, C. P. Poole, and J. L. Safko, *Classical Mechanics (3rd ed.)* (Addison-Wesley, 2001)
- [118] Igor P. Omelyan, “Algorithm for numerical integration of the rigid-body equations of motion,” *Phys. Rev. E* **58**, 1169–1172 (1998), <https://link.aps.org/doi/10.1103/PhysRevE.58.1169>
- [119] H. Noguchi, N. Kikuchi, and G. Gompper, “Particle-based mesoscale hydrodynamic techniques,” *Europhys. Lett.* **78**, 10005 (2007), <http://stacks.iop.org/0295-5075/78/i=1/a=10005>
- [120] Ingo O. Götze, Hiroshi Noguchi, and Gerhard Gompper, “Relevance of angular momentum conservation in mesoscale hydrodynamics simulations,” *Phys. Rev. E* **76**, 046705 (2007), <https://link.aps.org/doi/10.1103/PhysRevE.76.046705>
- [121] Hiroshi Noguchi and Gerhard Gompper, “Transport coefficients of off-lattice mesoscale-hydrodynamics simulation techniques,” *Phys. Rev. E* **78**, 016706 (2008), <https://link.aps.org/doi/10.1103/PhysRevE.78.016706>
- [122] Dan S. Bolintineanu, Jeremy B. Lechman, Steven J. Plimpton, and Gary S. Grest, “No-slip boundary conditions and forced flow in multiparticle collision dynamics,” *Phys. Rev. E* **86**, 066703 (2012), <https://link.aps.org/doi/10.1103/PhysRevE.86.066703>
- [123] John R. Platt, “"bioconvection patterns" in cultures of free-swimming organisms,” *Science* **133**, 1766–1767 (1961), <http://science.sciencemag.org/content/133/3466/1766>
- [124] Hugo Wioland, Francis G. Woodhouse, Jörn Dunkel, John O. Kessler, and Raymond E. Goldstein, “Confinement stabilizes a bacterial suspension into a spiral vortex,” *Phys. Rev. Lett.* **110**, 268102 (2013), <https://link.aps.org/doi/10.1103/PhysRevLett.110.268102>

- [125] H. Wioland, E. Lushi, and R. E. Goldstein, “Directed collective motion of bacteria under channel confinement,” *New J. Phys.* **18**, 075002 (2016), <http://stacks.iop.org/1367-2630/18/i=7/a=075002>
- [126] Lionel Ranjard and Agnès Richaume, “Quantitative and qualitative microscale distribution of bacteria in soil,” *Research in Microbiology* **152**, 707 – 716 (2001), <http://www.sciencedirect.com/science/article/pii/S0923250801012517>
- [127] Courtney K. Robinson, Jacek Wierzechos, Celeste Black, Alexander Crits-Christoph, Bing Ma, Jacques Ravel, Carmen Ascaso, Octavio Artieda, Sergio Valea, Mònica Roldán, Benito Gómez-Silva, and Jocelyne DiRuggiero, “Microbial diversity and the presence of algae in halite endolithic communities are correlated to atmospheric moisture in the hyper-arid zone of the atacama desert,” *Environmental Microbiology* **17**, 299–315 (2015), <https://onlinelibrary.wiley.com/doi/abs/10.1111/1462-2920.12364>
- [128] Rainer U. Meckenstock, Frederick von Netzer, Christine Stumpp, Tillmann Lueders, Anne M. Himmelberg, Norbert Hertkorn, Philipp Schmitt-Kopplin, Mourad Harir, Riad Hosein, Shirin Haque, and Dirk Schulze-Makuch, “Water droplets in oil are microhabitats for microbial life,” *Science* **345**, 673–676 (2014), <http://science.sciencemag.org/content/345/6197/673>
- [129] Joost de Graaf, Henri Menke, Arnold J. T. M. Mathijssen, Marc Fabritius, Christian Holm, and Tyler N. Shendruk, “Lattice-boltzmann hydrodynamics of anisotropic active matter,” *J. Chem. Phys.* **144**, 134106 (2016)
- [130] Lukas P. Fischer, Toni Peter, Christian Holm, and Joost de Graaf, “The raspberry model for hydrodynamic interactions revisited. i. periodic arrays of spheres and dumbbells,” *J. Chem. Phys.* **143**, 084107 (2015), <https://doi.org/10.1063/1.4928502>
- [131] Joost de Graaf, Toni Peter, Lukas P. Fischer, and Christian Holm, “The raspberry model for hydrodynamic interactions revisited. ii. the effect of confinement,” *J. Chem. Phys.* **143**, 084108 (2015), <https://doi.org/10.1063/1.4928503>
- [132] R. W. Nash, R. Adhikari, J. Tailleur, and M. E. Cates, “Run-and-tumble particles with hydrodynamics: Sedimentation, trapping, and upstream swimming,” *Phys. Rev. Lett.* **104**, 258101 (2010), <https://link.aps.org/doi/10.1103/PhysRevLett.104.258101>
- [133] R. W. Nash, R. Adhikari, and M. E. Cates, “Singular forces and pointlike colloids in lattice boltzmann hydrodynamics,” *Phys. Rev. E* **77**, 026709 (2008), <https://link.aps.org/doi/10.1103/PhysRevE.77.026709>

- [134] Juan P. Hernandez-Ortiz, Christopher G. Stoltz, and Michael D. Graham, “Transport and collective dynamics in suspensions of confined swimming particles,” *Phys. Rev. Lett.* **95**, 204501 (2005), <https://link.aps.org/doi/10.1103/PhysRevLett.95.204501>
- [135] Leonardo F. Valadares, Yu-Guo Tao, Nicole S. Zacharia, Vladimir Kitaev, Fernando Galembeck, Raymond Kapral, and Geoffrey A. Ozin, “Catalytic nanomotors: Self-propelled sphere dimers,” *Small* **6**, 565–572 (2010), <http://dx.doi.org/10.1002/sml1.200901976>
- [136] M. J. Lighthill, “On the squirring motion of nearly spherical deformable bodies through liquids at very small reynolds numbers,” *Commun. Pure Appl. Math.* **5**, 109–118 (1952)
- [137] J.R. Blake, “A spherical envelope approach to ciliary propulsion,” *J. Fluid Mech.* **46**, 199–208 (1971)
- [138] Takuji Ishikawa and T. J. Pedley, “Coherent structures in monolayers of swimming particles,” *Phys. Rev. Lett.* **100**, 088103 (2008), <https://link.aps.org/doi/10.1103/PhysRevLett.100.088103>
- [139] I. Llopis and I. Pagonabarraga, “Hydrodynamic interactions in squirmer motion: Swimming with a neighbour and close to a wall,” *J. Non-Newtonian Fluid Mech.* **165**, 946–952 (2010)
- [140] Arthur A. Evans, Takuji Ishikawa, Takami Yamaguchi, and Eric Lauga, “Orientational order in concentrated suspensions of spherical microswimmers,” *Phys. Fluids* **23**, 111702 (2011)
- [141] Andreas Zöttl and Holger Stark, “Nonlinear dynamics of a microswimmer in poiseuille flow,” *Phys. Rev. Lett.* **108**, 218104 (2012), <https://link.aps.org/doi/10.1103/PhysRevLett.108.218104>
- [142] Francisco Alarcón and Ignacio Pagonabarraga, “Spontaneous aggregation and global polar ordering in squirmer suspensions,” *J. Mol. Liq.* **185**, 56–61 (2013)
- [143] Kenta Ishimoto and Eamonn A. Gaffney, “Squirmer dynamics near a boundary,” *Phys. Rev. E* **88**, 062702 (2013), <https://link.aps.org/doi/10.1103/PhysRevE.88.062702>
- [144] John J. Molina, Yasuya Nakayama, and Ryoichi Yamamoto, “Hydrodynamic interactions of self-propelled swimmers,” *Soft Matter* **9**, 4923–4936 (2013)
- [145] Mario Theers, Elmar Westphal, Gerhard Gompper, and Roland G. Winkler, “Modeling a spheroidal microswimmer and cooperative swimming in a narrow slit,” *Soft Matter* **12**, 7372–7385 (2016), <http://dx.doi.org/10.1039/C6SM01424K>

- [146] Francisco Alarcon, Chantal Valeriani, and Ignacio Pagonabarraga, “Morphology of clusters of attractive dry and wet self-propelled spherical particle suspensions,” *Soft Matter* **13**, 814–826 (2017)
- [147] Takuji Ishikawa, J. T. Locsei, and T. J. Pedley, “Fluid particle diffusion in a semidilute suspension of model micro-organisms,” *Phys. Rev. E* **82**, 021408 (2010), <https://link.aps.org/doi/10.1103/PhysRevE.82.021408>
- [148] Gao-Jin Li and Arezoo M. Ardekani, “Hydrodynamic interaction of microswimmers near a wall,” *Phys. Rev. E* **90**, 013010 (2014), <https://link.aps.org/doi/10.1103/PhysRevE.90.013010>
- [149] Ignacio Pagonabarraga and Isaac Llopis, “The structure and rheology of sheared model swimmer suspensions,” *Soft Matter* **9**, 7174–7184 (2013), <http://dx.doi.org/10.1039/C3SM51258D>
- [150] David Saintillan and Michael J. Shelley, “Orientational order and instabilities in suspensions of self-locomoting rods,” *Phys. Rev. Lett.* **99**, 058102 (2007), <https://link.aps.org/doi/10.1103/PhysRevLett.99.058102>
- [151] Rajesh Singh, Somdeb Ghose, and R. Adhikari, “Many-body microhydrodynamics of colloidal particles with active boundary layers,” *Journal of Statistical Mechanics: Theory and Experiment* **2015**, P06017 (2015), <http://stacks.iop.org/1742-5468/2015/i=6/a=P06017>
- [152] James W. Swan, John F. Brady, Rachel S. Moore, and ChE 174, “Modeling hydrodynamic self-propulsion with stokesian dynamics. or teaching stokesian dynamics to swim,” *Physics of Fluids* **23**, 071901 (2011), <https://doi.org/10.1063/1.3594790>
- [153] David Saintillan and Michael J. Shelley, “Emergence of coherent structures and large-scale flows in motile suspensions,” *Journal of The Royal Society Interface*(2011)
- [154] Elizabeth H. Harris, David B. Stern, and George B. Witman, “Chapter 4 - motility and behavior,” in *The Chlamydomonas Sourcebook (Second Edition)* (Academic Press, London, 2009) second edition ed., pp. 89 – 117, <https://www.sciencedirect.com/science/article/pii/B9780123708731000046>
- [155] Peter S. Lovely and F.W. Dahlquist, “Statistical measures of bacterial motility and chemotaxis,” *Journal of Theoretical Biology* **50**, 477 – 496 (1975), <http://www.sciencedirect.com/science/article/pii/0022519375900946>
- [156] M. E. Cates and J. Tailleur, “When are active brownian particles and run-and-tumble particles equivalent? consequences for motility-induced phase separation,” *EPL (Europhysics Letters)* **101**, 20010 (2013), <http://stacks.iop.org/0295-5075/101/i=2/a=20010>

-
- [157] Julian Bialké, Thomas Speck, and Hartmut Löwen, “Crystallization in a dense suspension of self-propelled particles,” *Phys. Rev. Lett.* **108**, 168301 (2012), <https://link.aps.org/doi/10.1103/PhysRevLett.108.168301>
- [158] John D. Weeks, David Chandler, and Hans C. Andersen, “Role of repulsive forces in determining the equilibrium structure of simple liquids,” *J. Chem. Phys.* **54**, 5237–5247 (1971)
- [159] Christian Titus Kreis, Marine Le Blay, Christine Linne, Marcin Michal Makowski, and Oliver Bäumchen, “Adhesion of chlamydomonas microalgae to surfaces is switchable by light,” *Nature Physics* **14**, 45 (2018)
- [160] C.H. Ziener, M. Rückl, T. Kampf, W.R. Bauer, and H.P. Schlemmer, “Mathieu functions for purely imaginary parameters,” *Journal of Computational and Applied Mathematics* **236**, 4513–4524 (2012)
- [161] David R. Reichman and Patrick Charbonneau, “Mode-coupling theory,” *Journal of Statistical Mechanics: Theory and Experiment* **2005**, P05013 (2005), <http://stacks.iop.org/1742-5468/2005/i=05/a=P05013>
- [162] Christopher Battle, Chase P. Broedersz, Nikta Fakhri, Veikko F. Geyer, Jonathon Howard, Christoph F. Schmidt, and Fred C. MacKintosh, “Broken detailed balance at mesoscopic scales in active biological systems,” *Science* **352**, 604–607 (2016)

Acknowledgements

This thesis would not have been possible without a lot of people who I would like to thank. First, I thank Marco G. Mazza for being a wonderful supervisor, an outstanding scholar and great friend. He allowed me to do my PhD while always supporting my work, being ever helpful and taking care to keep me on the right track. I thank Stefan Herminghaus for the opportunity to work in his department and for creating an amazing working atmosphere. I thank Jan Cammann for his outstanding work as my bachelor student. I thank Tanya Ostapenko, Thomas J. Bøddeker, Christian Titus Kreis, and Oliver Bäumchen for a very fruitful collaboration. I thank Annette Zippelius and Jörg Enderlein for the helpful discussions and advise that I received in my thesis committee meetings.

I thank all the infrastructure people behind our work: Monika Teuteberg, Kristian Hantke, Thomas Eggers, Danny Fliegner, Hecke Schrobsdorff, and Guido Schriever.

I would like to thank my parents and siblings who supported me through my studies and always believed in me. I thank Jana Lasser and Mathias Hummel for the intriguing discussions in the morning or during coffee time. I want to thank my office mates for a wonderful time: Viktor Meiwes-Tourrion, Hannes Hornischer, Arne Zantop (also for climbing with me), Jens Lucht, Luis Miguel Ramos Henriques and Joscha Tabet. I thank all other NESM members, who I loved working with: Rebekka Breier, Thomas Breithaupt, Johannes Gräwer, Henning Zwirnmann, Shubhadeep Mandal, Chamkor Singh, Jérémy Vachier, Sebastian Mair, Vitali Telezki and Kuang-Wu Lee. I thank the entire DCF department for making my PhD such a great time. Finally, special thanks goes to Christine Linne.

Curriculum Vitae

Current address

Fabian Jan Schwarzendahl
Groner Landstraße 55b
37081 Göttingen
Germany

Personal Information

Date of birth January 12, 1990

Place of birth Gütersloh

Previous education

2013 – 2015 Physics Master at the Georg-August-Universität Göttingen

Thesis *Correlated emission and recoil effects in the QCD resummation of event-shape observables*

2009 – 2013 Physics Bachelor at the Georg-August-Universität Göttingen

Thesis *Interaction between Dirac fields and external fields*

Publications

Tanya Ostapenko, **Fabian Jan Schwarzendahl**, Thomas J. Böddeker, Christian Titus Kreis, Jan Cammann, Marco G. Mazza, and Oliver Bäümchen, *Curvature-Guided Motility of Microalgae in Geometric Confinement*, Physical Review Letters **120**, 068002 (2018).

Fabian Jan Schwarzendahl and Marco G. Mazza, *Maximum in density heterogeneities of active swimmers*, Soft Matter **14**, 4666-4678 (2018).